# Global investigation of marine atmospheric boundary layer rolls using Sentinel-1 SAR data

Chen Wang

## To cite this version:

Chen Wang. Global investigation of marine atmospheric boundary layer rolls using Sentinel-1 SAR data. Signal and Image Processing. Ecole nationale supérieure Mines-Télécom Atlantique, 2020. English. NNT : 2020IMTA0203 . tel-02940927v2

HAL Id: tel-02940927
https://theses.hal.science/tel-02940927v2

Submitted on 17 Sep 2020

# THÈSE DE DOCTORAT DE

L'ECOLE NATIONALE SUPÉRIEURE MINES-TÉLÉCOM
ATLANTIQUE BRETAGNE - PAYS DE LA LOIRE
DÉLIVRÉE CONJOINTEMENT AVEC
L'UNIVERSITE DE BRETAGNE OCCIDENTALE

ECOLE DOCTORALE N° 598
*Sciences de la Mer et du littoral*
Spécialité : Océanographie, Physique et Environnement

Par
**Chen Wang**

# Global Investigation of Marine Atmospheric Boundary Layer Rolls Using Sentinel-1 SAR data

**Thèse présentée et soutenue à Plouzane, le 30 Juillet, 2020**
**Unité de recherche : LabSTICC**
**Thèse N° : 2020IMTA0203**

**Rapporteurs avant soutenance :**

**Johnny A. Johannessen**
*Professor, Norway Nansen Environmental and Remote Sensing Center*

**Vladimir Kudryavtsev**
*Professor, Russian State Hydrometeorological University*

**Composition du Jury :**

**Johnny A. Johannessen**
*Professor, Norway Nansen Environmental and Remote Sensing Center/Rapporteur*

**Vladimir Kudryavtsev**
*Professor, Russian State Hydrometeorological University/Rapporteur*

**Florence Tupin**
*Professor, Télécom ParisTech/Présidente du jury*

**René GARELLO**
*Professor, IMT Atlantique/Directeur de thèse*

**Pierre Tandeo**
*Professor, IMT Atlantique/Co-Encadrant de thèse*

**Bertrand Chapron**
*Researcher, IFREMER/Co-Encadrant de thèse*

**Alexis Mouche**
*Researcher, IFREMER/Co-Encadrant de thèse*

# Global Investigation of Marine Atmospheric Boundary Layer Rolls Using Sentinel-1 SAR data

by

Chen WANG

Submitted for the Degree

Doctor of Philosophy

Supervised by René GARELLO

Co-supervised by Alexis MOUCHE,
Pierre TANDEO and Bertrand CHAPRON

University of IMT Atlantique
Institut français de recherche pour l'exploitation de la mer (IFREMER)

Brest, France
July 2020

# Abstract

Roll vortices are quasi-two-dimensional organized air flow eddies in the turbulent atmospheric boundary layer (ABL). They are usually formed and embedded within the whole ABL, and contribute significantly to the vertical exchanges of momentum, heat and moisture due to the additional non-local/non-gradient transport. Investigation of this typical boundary layer process has been conducted for decades, but mostly in the case studies. While the results have demonstrated a promising overview of the atmospheric conditions of roll occurrence (in near-neutral to slightly unstable stratification), and roll characteristics (2 to 5 km wavelengths and $\pm 25^\circ$ orientations relative to the mean flow direction), these roll features are not verified over the global oceans. For a higher level perspective, there are also needs for global and long-term climatology of roll-shaped ABL dynamics as well as annual and seasonal variability. Such climatology will no doubt advance the parameterization of roll dominated ABL, and hence improve the accuracy of numerical weather and climate model projections.

The thesis aims to exploit the global Sentinel-1 (S-1) wave mode (WV) synthetic aperture radar (SAR) data for Maine ABL roll investigations. Among the well-known practical means, spaceborne SAR holds the largest potential to achieve systematic observations of ABL rolls over the world's ocean. It is because SAR backscattering of ocean surface is independent of sunlight and most weather conditions, and is fundamentally sensitive to the roll-induced sea surface roughness changes. To automatically identify roll events from the S-1 WV SAR images, we train a deep-learning-based classification model based on the hand-curated dataset of TenGeoP-SARwv, namely CMwv. The independent and geophysical assessments show satisfactory and robust model performance. Global evaluation of the CMwv-identified roll WV images illustrates the sensitivity of SAR sensors in mapping ocean surface roll imprints. Much more and better roll events are visible at the 36° (WV2) than the 23.5° (WV1) incidence angle. SAR observations of roll imprints are found severely limited in low wind conditions ($<$ 3m/s) and when wind direction is perpendicular to the SAR antenna looking. Beyond this, the larger dataset also leads to a new result that, on average and across all wind speeds, ABL rolls drive surface wind variations about the mean flow of roughly 8% (±3.5%), and seldom exceeding 20%.

The global statistics of roll features have thus focused on the identified roll events from S-1 WV2 SAR data. Roll wavelength and orientation are extracted from each WV scene through the 2-D spectral analyses at ABL scales of 0.6-5 km. To quantify the atmospheric condition of roll occurrence, each WV SAR image is also collocated with the ERA5 surface variables. The major outcomes are: (1) up to 90% of roll events are occurred in the near-neutral to slightly unstable conditions, distinct from the overall average condition; (2) observed tiny seasonality in identified roll events and their atmospheric conditions; (3) roll dynamic seems stronger in the morning than evening due to more convection; (4) roll occurrence atmospheric condition is more unstable at low latitudes than mid-latitudes; (5) roll aspect ratios (roll wavelength divided by ABL height) are in lognormal distribution centered at 2.87; (6) roll orientations are in normal distribution, mostly within ±35°; (7) roll wavelength and orientation are weakly and strongly dependent on latitudes; (8) the dependence of roll orientation on Earth wind directions indicates the horizontal Coriolis force effects ABL roll dynamics.

Despite the fact that these highlighted results complement the understanding of ABL rolls with significant implications for both atmosphere and ocean studies, it is highly expected to extend the application of S-1 WV SAR data for other key ABL processes. One of the top interests is to understand the natural transition between ABL rolls, rain cells and convective cells. Moreover, there is a high possibility to project these ocean surface roughness images into air-sea interface stability, and then into surface fluxes, independently of individual sea surface temperature and near-surface air temperature measurements. This would aid the evaluation and improvement of ABL parameterization schemes (Eddy-diffusion mass-flux or similar) in different types of ABL. If these WV SAR data can be well processed to define the bottom properties of ABL. A full view of the ABL mean state would be obtained by including the low cloud measurements to define the top properties of ABL. It is the joint effort required to enhance the process-level knowledge of the Earth weather and climate system.

# Acknowledgments

First and foremost I want to acknowledge the financial support from China scholarship Council (CSC) for my PhD project at Ifremer and IMT-Atlantique, France. It opened my paths to study abroad and to pursue a career in scientific research that I dreamed for.

I am grateful to all the people who helped, encouraged and believed me in finishing the PhD study and dissertation. Their words and/or actions once inspired me to get through hard times and things, and will continue rising me up in my future life.

All the work involved in this thesis was under supervision of Drs. René Garello, Pierre Tandeo, Alexis Mouche and Bertrand Chapron. Their guidance has helped me to adapt the new culture and education, conduct my research and write this thesis for all the time. In particular, Drs. Alexis Mouche and Bertrand Chapron introduced me to the field of marine atmospheric boundary layer rolls, and guided me to work on this geophysical phenomenon with Sentinel-1 wave mode SAR data. Their expertise in SAR imaging mechanism, oceanography and boundary layer dynamic is an important guarantee for the success implement of my study. I can not finish the thesis in time and achieve relevant publications without their aid and advice.

I also would like to thank Dr. Douglas Vandemark (University of New Hampshire) and Dr. Ralph Foster (University of Washington), who get interested in my work in the early of 2017. Since then, they contributed to my study and thesis in data analysis and theoretical interpretation through a cooperated NASA projected with Ifremer. I learnt not only knowledge regarding air-sea interaction and boundary layer roll physics, but also attitudes and skills in doing science as well as writing academic papers.

My special thanks to Dr. Justin Stopa (University of Hawaii at Manoa), who gave me many help and advice in advancing my study and writing skills when he was working at Ifremer.

My sincere thanks also goes to all the colleagues in LOPS-SIAM, Ifremer, who provided a lot of helps after I joined the lab, and assistance in accessing the research facilities.

Lastly, I want to thank my family, close friends and fiancée Huimin Li for their selfless love and support during the past four years.

# TABLE OF CONTENTS

# Chapter 1 Introduction

## 1.1 Marine atmospheric boundary layer rolls

Marine atmospheric boundary layer (MABL) can be loosely defined as the lowest kilometer of Earth's atmosphere that has direct contacts with the wide-ranging ocean and responds to the surface forcings including frictional drag, evaporation and transpiration, heat transfer, and ocean waves et al (Stull, 1988; Garratt, 1994). It is a layer characterized by its air flow state, where the velocity, temperature, density and pressure fluctuate over scales ranging from less than one millimetre to several kilometres. The turbulent nature of MABL has been recognized with the great variability due to the thermodynamic and kinematic processes inside. These physical processes not only control the transport of heat, energy and momentum, the dispersion of pollutants and carbon dioxide, and but play important roles in the formation and interaction with low-level clouds in cloud-topped boundary layers (LeMone et al., 2018).

There has been increasing evidence that advanced understanding of the key MABL processes is far more fundamental for climate studies (Sherwood et al., 2014; Bony et al., 2015; Randall et al., 2018). Yet the physical processes related with the mean boundary layer state are not fully resolved in the present numerical models of either climate or weather (Bauer et al., 2015). Effort has been devoted to filling the knowledge gap of the MABL state. A workshop recently organized by the U.S. National Academy of Sciences Boards of 'Atmospheric Sciences and Climate', 'Ocean Surface Studies' and 'Life Sciences' recognized the implications of boundary layer processes in these fields (National Academies of Sciences, Engineering, and Medicine, 2018a). The most recent NASA Decadal Survey also identified boundary layer processes as one of the key missing observations in its earth satellite program (National Academies of Sciences, Engineering, and Medicine, 2018b).

Under near-neutral to slightly unstable conditions, air flows in the MABL are often organized into linear roll-shaped vortices (Brown, 1970, 1980; Brown & Liu, 1982). These vortices are in fact quasi two-dimensional organized eddies with its horizontal axis being approximately aligned with the mean flow (Etling & Brown, 1993; Young et al., 2002). The American Meteorological Society (AMS) Glossary defines this phenomenon as "counter-rotating horizontal vortices that commonly occur within the convective boundary layer" (`http://glossary.ametsoc.org/wiki/Horizontal_convective_rolls`). A schematic representation of the organized roll vortices embedded in the modified Ekman layer is given in Figure 1.1. It uses a two-layer similarity model to depict the dynamics of roll-shaped boundary layer. Other schematic plots of this secondary flow patterns are also available, e.g., Figure 5 of Brown (1980), Figure 1 of Alpers and Brümmer (1994), Figure 14.4 of Sikora and Ufermann (2004) and Figure 8 of Morrison, Businger, Marks, Dodge, and Businger (2005).

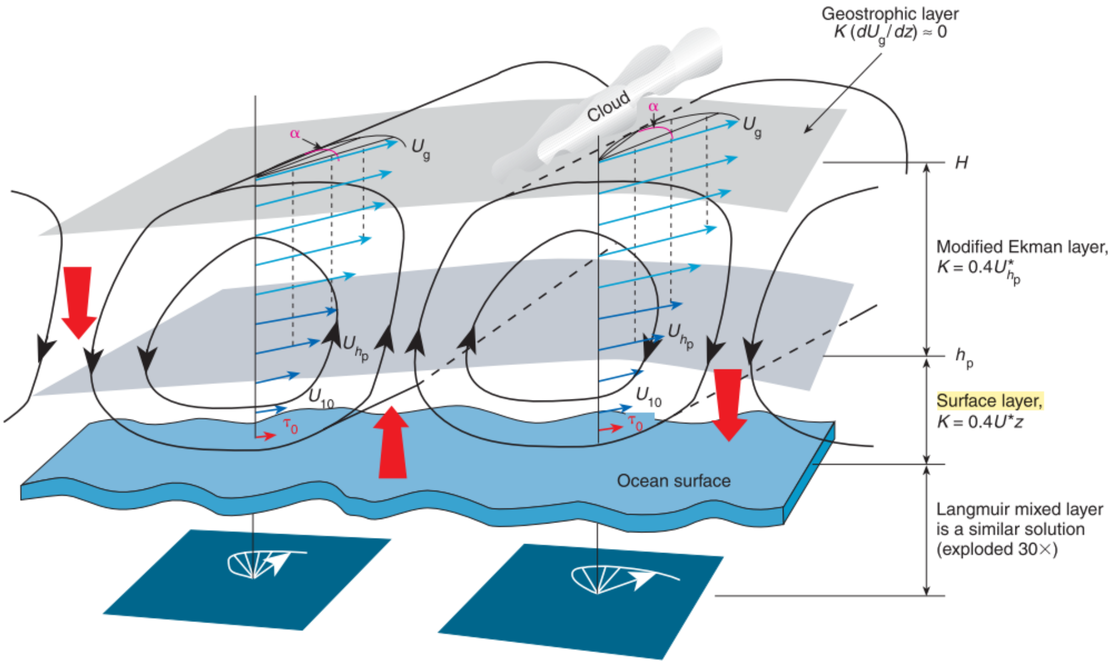

**Figure 1.1:** A schematic plot of typical roll vortices based on the two-layer similarity MABL model. $\tau_0$, $U_{10}$, $h_p$, $U_{h_p}$, $U_g$, $\alpha$, $K$, $H$ and $U^*$ are surface stress, 10-m wind, surface patch height, wind at the path height, geostrophic wind, angle of turning, eddy viscosity, height of the geostrophic layer and surface friction velocity, respectively. Black arrows and large red vectors indicate the roll circulation and direction of fluxes exchanges (After Brown (2000)).

There has been generally two types of theories for the generation of roll vortices. One relates to the thermal instability when the layer is heated from below or cooled from above and the other to the dynamic instability when the wind velocity changes with the height (Brown, 1980; Young et al., 2002). Roll vortices usually span the whole depth of boundary layer and form bands of overturning circulations with alternating linear regions of enhanced upward and downward perturbations between the counter-rotating roll circulations. The upward perturbation flow tends to be stronger and narrower than the downward one, leading to the enhanced and reduced surface wind convergence near the base of the updrafts and downdrafts, respectively. This net effect is an enhancement of the fluxes across the boundary layer that does not depend on the vertical gradients of the mean flow. It is therefore comprehensible how important it is to better understand the roll-shaped boundary layer, particularly its role to strengthen the air-sea interaction via its impact on the turbulent fluxes (e.g., Lemone, 1976; Atkinson & Wu Zhang, 1996; Weckwerth et al., 1997; Chen et al., 2001; Morrison et al., 2005; Brilouet et al., 2017).

MABL rolls are genuinely the same with rolls generated over land (Brown, 1980; Young et al., 2002). The differences only consists in the formation process of boundary layer over ocean vs. land. In specifics, the MABL develops via stability and sinking air (top-down process) whereas the land ABL develops in an opposite way, matured by destabilization and convection (bottom-up process). Over land, the surface ground warms and cools in response to the sunlight radiation in daytime and nighttime, which in turn destabilizes and stabilizes the above ABL. The land ABL thus forms largely depends on the diurnal cycle (Stull, 1988; LeMone et al., 2018). Switching gears, the MABL remains relatively stable regarding to the diurnal cycle, but allowing for a large amount of heat and moisture exchanges. Given the widespread coverage of the ocean (more than 70%) on Earth's surface, it is essential to devote more joint efforts for investigation of the MABL rolls and the associated physical processes.

In physics, roll vortices are manifestation of Ekman layer instabilities that can be described by the nonlinear Navier-Stokes equations when considering thermal and dynamic factors in a rotating system (Brown, 1980, 2002; Foster, 1996). The earlier theory of roll dynamics has focused on the linearization schemes and produced the representative solution of inflection-point (IP) instability (Asai, 1970; Brown, 1970, 1972). This theory predicts consistent roll characteristics with observations in terms of both aspect ratio and horizontal orientation. It is therefore widely adopted and extended by taking into account other effects, such as thermal wind (Brown, 1980; Foster, 1996), stratification (Asai & Nakasuji, 1973; Kaylor & Faller, 1972), baroclinicity (Foster, 1996; Foster & Levy, 1998), and nonlinear processes (Mourad & Brown, 1990). While in most of the IP-based studies, only the vertical component of Earth's rotation is considered. The horizontal one, however, is often neglected, though its importance in geophysical fluid dynamics has been clearly shown by several theoretical investigations. This is partially because of the lack of long-term and systematic observational dataset, which limits our understanding of roll features at the global scale.

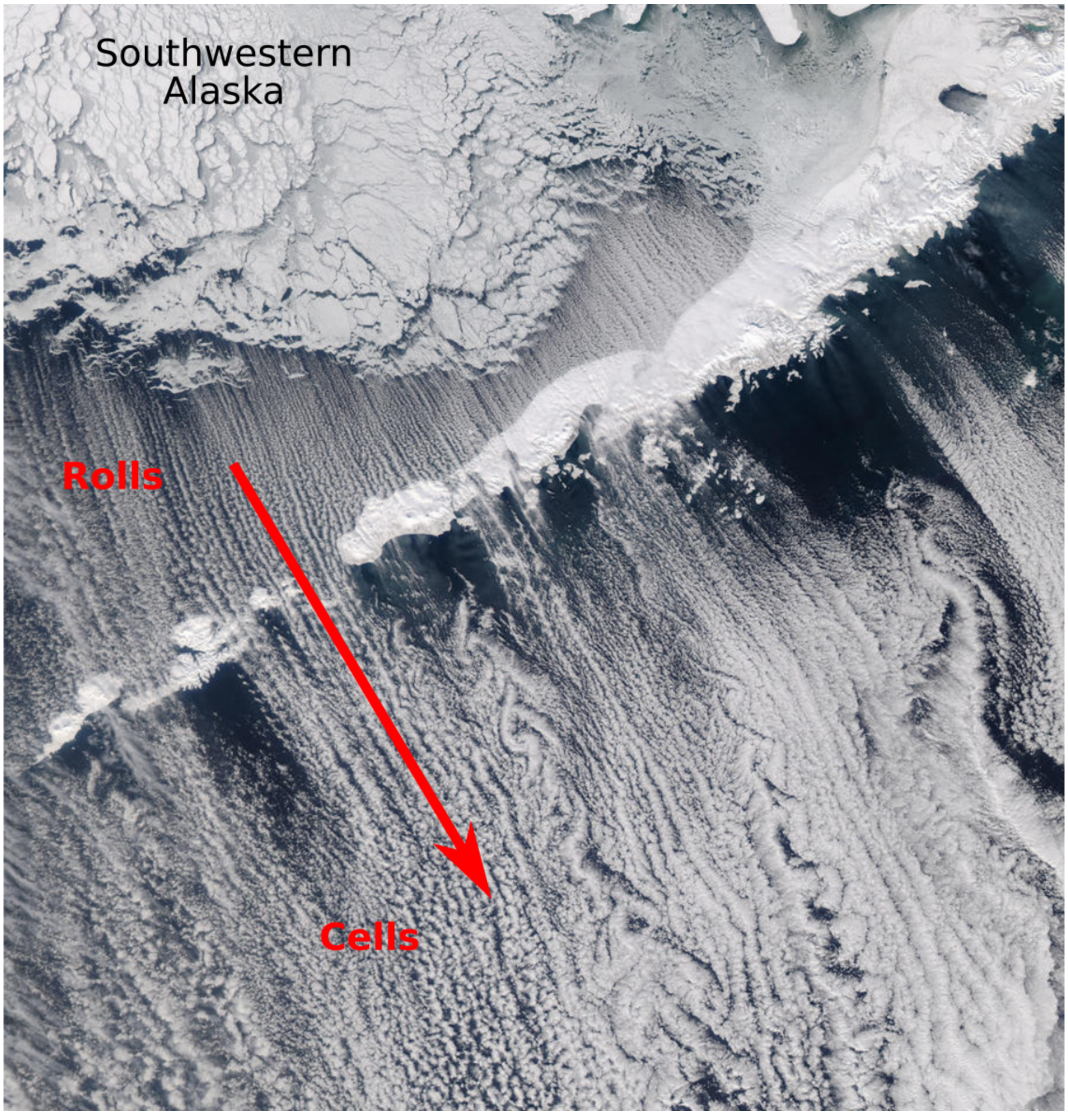

**Figure 1.2:** Moderate Resolution Imaging Spectroradiometer (MODIS) photograph of cloud streets and cells off the coast of southwestern Alaska on January 11, 2012. Wind is blowing from land to ocean, leading to the formation of linear clouds near the coast and cell-shaped clouds off the coastline.

On the top of roll-shaped boundary layer, condensation usually forms in the updraft parts of the roll circulations. This is associated with the rising warm air mass that gradually cools and condenses. Meanwhile, the sinking cool air in the downdrafts evaporates and creates cloud-free areas. These alternating rising and sinking air masses produce long rows of cumulus clouds that are oriented parallel with wind direction (Etling & Brown, 1993). These aligned lines of organized clouds are thus normally identified as "cloud streets" by human eyes (e.g., Hergesell, 1928; Walker, 1934; Kuettner, 1959) or on the satellite visible imageries (e.g., Streten, 1975; Weston, 1980; Mourad, 1996). In particular, the cloud streets are mostly visible over oceans in the winter when cold air over land moves towards the warmer ocean with rising thermals being organized by the prevailing offshore winds (Atlas et al., 1983, 1986). As the distance from the shoreline increases, roll-shaped clouds often transition into cell-shaped convection (Atkinson & Wu Zhang, 1996; Kristovich et al., 1999; Pithan et al., 2018). An example of roll-cell transition observed by the optical satellite image is given in Figure 1.2. Strong winds polished the snow of southwestern Alaska and stretched marine stratocumulus clouds into long, parallel streets near the coastline, and then into convective cells as air-sea temperature difference increases.

On the other hand, roll-generated overturning circulations dominate the pattern of wind perturbations near the surface. These band-shaped upward and downward perturbations are usually strong enough to modulate the cm-scale sea roughness, central to synthetic aperture radar (SAR) imaging of ocean surface (Alpers & Brümmer, 1994; Young, 2000; Vandemark et al., 2001). MABL rolls are thus also frequently captured and visible on the normalized radar cross-section (NRCS) images as alternative bright and dark linear features (Gerling, 1986; Alpers & Brümmer, 1994; Li et al., 2013). Figure 1.3 shows a ERS-1 SAR image example of roll imprints obtained in January 07, 1995 in the East of China Sea. The image is divided by a front line into two sections with quite different textures. On the right-hand, we can clearly see the transition of roll-shaped sea surface imprints at top to the cell-shaped textures at bottom of this image.

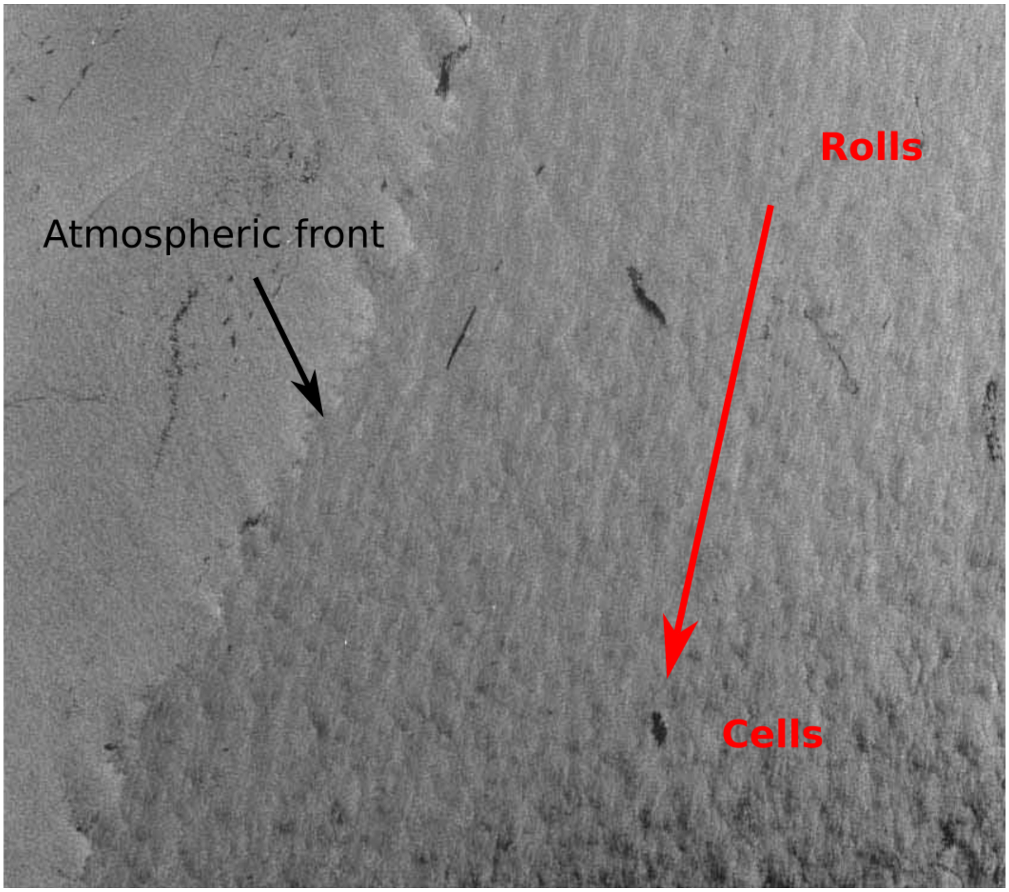

**Figure 1.3:** A SAR image example of roll transisition to cell-shaped convection. The image is acquired by ERS-1 on January 07, 1995 in the East Sea of China ( center geographic coordinate is 28°$N$, 122°$E$).

## 1.2 Literature review of roll studies

### 1.2.1 Early observational

The earliest notice of roll vortices in the turbulent atmospheric boundary layer came from glider pilots in the mid-twentieth century. Hergesell (1928) first discussed in his report the parallel and scale characteristics of the organized clouds, and their importance to aviation. Further efforts in understanding the relationship between the cloud rows and air currents have been made by the enthusiastic and idealistic individuals in long-distance soaring and flights (Walker, 1934; Brunt, 1938). The English gliders named the organized clouds as "wind (or cloud) streets" after realizing that these cloud rows are roughly parallel to the mean wind. Some practical experiments were led by Brunt (1938) attempting to illustrate the nature of atmospheric convection. Based on the result, he came up with the theory that the combined dynamic and thermal instabilities are the formation forces of cloud streets.

Though the roll vortices are mostly related to the visible cloud streets, later flights confirm their occurrence in cloud-free conditions. A more general description of this roll phenomenon and thorough understanding of its occurrence atmospheric condition is given by Kuettner (1959). The synoptic cloud analysis indicated that the roll-shaped structure of the atmosphere is more common than has been reported by the pilots. Some interesting highlights were noticed in a pilot's flight log: the downdraft between cloud rows were highly turbulent, strong downdrafts disappeared above $\sim$1 km and roll clouds cover more than hundred of km (Kuettner, 1959).

These observations encouraged the incredible gull field experiment by Woodcock (1940a, 1940b, 1942) over the Atlantic Ocean. The flight patterns of soaring birds were observed during two years on the sail-powered vessel from 16° to 42° N and within 600 miles off the US coast. It is noticed that soaring only occurred when the temperature of air was lower than the sea surface, and the soaring pattern also depends on the wind speed. The gull birds would rise in a corkscrew pattern whenever the surface wind speed was low but soar straightly along the upwind at high wind speeds (Woodcock, 1940b). Identification of the bird flight patterns immediately reminded Woodcock of their association with the newly reported helical vortices in the atmospheric boundary layer. It is speculated that the gulls are able and tend to exploit the updraft regions for extended soaring flights.

The synchronous measurements of wind speed and temperatures of air and sea surface made it possible to quantify the atmospheric condition under which various gull soaring patterns were observed (Woodcock, 1940a). Preference conditions of gull soaring (roll vortices probably occur) were at wind speed between 7 and 13 m/s with the air-sea temperature difference less than -4 $^{\circ}C$. This led to the first indication that roll vortices are closely involved with the air-sea momentum fluxes. Woodcock and Wyman (1947) further pursued the idea during a series of US Navy tests on smoke screens in the Gulf of Panama in 1945. While the smoke releases well visualized the air flows nearby airplane flights, the oblique photo views of sea surface captured clear alternating light and dark bands. These "seems to be due to systematic variation in the pattern of small waves on the surface, associated with a corresponding variation in wind speed" (Woodcock & Wyman, 1947). This interpretation is somewhat similar to SAR imaging of roll imprints on ocean surface, which will be described in section 1.3.1. As a matter of fact, the smoke visualization showed consistent results that the dark and light regions correspond to the downdrafts and updrafts of roll circulations, respectively.

### 1.2.2 Modern observational

Much more observations of roll vortices came after 1950s with new means of measurements such as radar, lidar and optical sensors. These instruments are equipped either on tower, ship or aircraft for field measurements or on space satellite for worldwide coverage. Investigations of rolls using these data were well summarised in the review articles of Etling and Brown (1993); Atkinson and Wu Zhang (1996); Weckwerth et al. (1997); Young et al. (2002). In the following, a brief introduction will be given in terms of roll occurrence, atmospheric conditions, roll structures (wavelength & orientation) and roll dynamic effect on fluxes. The goal is to focus on, but not limited to, the roll vortices over the wide-ranging ocean. In addition, the results covered in the introduction are inevitably subjective and eclectic given the massive amount of materials in this field.

**Roll occurrence**

A general difficulty in addressing the figure of roll occurrence is the lack of systematic means to observe and objectively identify roll events (Weckwerth et al., 1997). Nearly all the previous attempts have been restricted in fixed spots or areas. A first ground-based observational study on the occurrence of cloud streets was performed over Boston during 12 months between 1953-1954 (Kuettner, 1959). As the roll detection relied on the presence of clouds and observation for complete coverage was not ensured, it ended up with only 35 days when the roll occurrence is definite. Most of these days were in spring and fall, which indicated that the formation of cloud streets might be associated with the cold air advection. This very crude estimate led Kuettner to believe that "at least 30% of the cloud coverage existing over the world has a structure suitable for this kind of synoptic analysis" (Kuettner, 1959).

Consistent results were shown in a similar survey over British Isles. Yearlong satellite photographs were examined by Weston (1980) and the highest occurrence frequency of cloud streets is found in March and April of 1977. In another study based on the meteorological measurements taken at the Nlsudden wind turbine site, under slightly unstable conditions, horizontal roll vortices are observed over 55% of the study time (Smedman, 1991). All these investigations on cloud streets conveyed a strong message that roll vortices may occur most of the time and nearly everywhere.

To overcome the limitation of roll identification based on clouds, Levy (2001) attempted to ingest quantifies of roll vortices from the microwave SAR images over the Gulf of Alaska and Bering Sea. A total of 7150 SAR images with coverage of 100 Km by 100 km were analyzed in multiple ways to determine the occurrence of roll events at spatial scale. This dataset covered a three-year period between 1997 and 1999, but with missing data from June to October. The overall roll occurrence is about 33% with relatively higher number in winter months than in spring. Spatial map displays that roll occurrence can exceeds 60% in some areas. Recently, a close roll occurrence of 48% is reported based on analysis of 227 SAR images acquired by TerraSAR-X and TanDEM-X at three FiNO platforms in the North Sea and Baltic Sea (Zhao et al., 2016). Despite the spatial and temporal gaps, these SAR images provide great potential for systematic investigation of roll vortices over the global ocean.

In addition to regular conditions, SAR images have been demonstrated to well capture the roll structure in Tropical Cyclone (TC) conditions in recent years (Morrison et al., 2005; J. A. Zhang et al., 2008; Huang et al., 2018). The TC boundary layer was found favorable for roll formation (Foster, 2005). Despite specific statistics is not yet available, roll vortices are likely always present under TC condition based on the visual inspection of SAR images. Huang et al. (2018) analyzed the roll features using 16 SAR images acquired during three major hurricanes (Irma, Jose and Maria) during the 2017 Atlantic hurricane season. Other illustration can be referred to the SAR images in relevant hurricane studies (e.g. Xiaofeng Li et al., 2002; B. Zhang et al., 2014; A. Mouche et al., 2019).

Since the roll vortices are largely formed in marine cold air outbreaks, the climatology analysis of this weather event (Fletcher et al., 2016) gives an indirect demonstration of rolls occurrence at higher latitudes. The quantification, however, was dependent on the definition of cold air outbreaks, and may also be limited by the accuracy of used products. A more comprehensive climatology of the occurrence of rolls and convective cells has been given based on the 10-year warm-season observations in central Oklahoma (Banghoff et al., 2020). Roll events (including pure rolls, roll-to-cells, cell-to-rolls) were found to occur on 55% of all days. Together with the convective cells, organized features of the boundary layer appear over 92% of the days without precipitation during the observed warm season. Results also show that roll or cells normally form in mid-morning and may persist throughout the day or transition between each other before dissipating around sunset (Banghoff et al., 2020). This detailed documentation greatly advances out understanding of the occurrence of rolls and cells as well as their characteristics during the natural transitions over the central Oklahoma.

**Environmental conditions of roll occurrence**

The formation of roll vortices is in general thought to be dominated by wind shear and thermal convection of all situations (Brown, 1980; Etling & Brown, 1993). The Wind speed (or/and profile) and air-sea temperature difference are two useful parameters to characterize the environmental conditions for roll occurrence. In the earlier experiment of seagull soaring pattern (Woodcock, 1940b, 1942), these two parameters were also documented. Though the values are crude due to technical limitation back then, this trial yet served as a lighthouse for later investigations.

Aircraft photos and satellite pictures of cloud streets promoted roll related studies, particularly for the typical weather event of marine cold air outbreaks (e.g. Kuettner, 1959; Weston, 1980; Hein & Brown, 1988). The strong cold-air flows (usually in wintertime) from the polar regions towards the open ocean favors formation of the organized convective patterns in the atmosphere. Cloud streets associated with roll patterns are frequently observed over the first several hundred kilometres downwind of the sea-ice edge or coastline (Figure 1.2). At further downstream, cellular cloud structures gradually form with the decreased wind shear and increased convection. Numerous studies have been reported with focus on the roll- and cell-shaped cloud structures during cold-air outbreaks at different places over the world, such as in the Bering Sea (Weston, 1980), the East China Sea (Agee & Lomax, 1978; Miura, 1986), the American east coast (Atlas et al., 1986; Chou & Ferguson, 1991), the Great Lakes (Kelly, 1984; Agee & Gilbert, 1989), the Greenland and Barents Sea (Brümmer, 1996, 1999).

The balance between shear and thermal instabilities is fundamental for the formation of rolls (Brown, 1980; Etling & Brown, 1993; Brown, 2002). As such, analyses of atmospheric stability has to take both wind shear and thermal effects into consideration. Based on the observations of aircraft and tower data, LeMone (1973); Lemone (1976) found that roll occurrence is mostly at moderate winds (greater than 5 m/s) and slightly unstable stratification. The rolls have also been reported under near-neutral conditions over the ice-covered Bering sea during February (Walter & Overland, 1984). The stratification parameter of $z_i/L$ (where $z_i$ is the inversion height and $L$ is the Monin-Obukhov length) is commonly used to represent the atmospheric condition. Various values of this parameter have been observed for roll formation. For example, it is about -1.2 in Walter and Overland (1984), $-z_i/L < 21.4$ in Grossman (1982) and $3 < -z_i/L < 10$ in LeMone (1973). It should also be noted that very high values of $-z_i/L <$ (as large as 250) have been recorded (Christian & Wakimoto, 1989; Ferrare et al., 1991; Kristovich, 1993), which indirectly evidences the possible formation of rolls in extremely weather systems (Morrison et al., 2005; Huang et al., 2018). A statistical study of roll occurrence has been carried out that 67.3%, 20.0%, and 12.7% of observed rolls occurred under unstable, neutral, and stable atmospheric conditions, respectively (Zhao et al., 2016). Svensson et al. (2017) presented roll cases during a strongly stratified boundary layer using both SAR and aircraft observations.

Requirements of shear force for roll formation have also been documented that Christian and Wakimoto (1989) observed a minimum roll wind speed of 5 m/s. Slightly lower wind conditions (2-3.5 m/s) have been reported based on measurements from lidar, tower and aircraft radar (Ferrare et al., 1991; Wilczak & Businger, 1983). The statistical results further evidence the credibility of this low wind condition (<3 m/s) (Zhao et al., 2016). Most of the roll occurrence has been observed at medium winds with 5-11 m/s in (Hein & Brown, 1988), which is in agreement with the early study of 7-13 m/s (Woodcock, 1942). SAR imaging of roll imprints offers a new means for estimating the the wind speed fluctuations caused by roll vortices (Vandemark et al., 2001). It is promising that SAR-retrieved wind fluctuations of 7-10% are consistent with the aircraft measurements of the near-surface wind speed variations. This agreement shall facilitate statistical studies of roll-induced wind variation by taking advantage of the numerous SAR measurements at global scale.

In addition to the shear and thermal instabilities, there is a wide range of factors including the boundary layer height, baroclinicity, entrainment and the tangential component of the Coriolis force, can potentially affect the roll dynamics and organizations (Foster, 1996; Young et al., 2002; Salesky et al., 2017). The examination of roll (cloud streets) conditions over northern Germany confirmed the significance of the baroclinicity and convective effects (Müller et al., 1985). Foster (1996) theoretically exploited the sensitivity of roll dynamics to the atmospheric stratification and baroclinicity. As a matter of fact, investigations of these factor effects on roll circulations mostly remain in theoretical and numerical stage with a short review given in section 1.2.3.

**Roll characteristics**

The very two basic parameters to characterize the roll structures are the horizontal wavelength and orientation. Earlier visual inspections by the glider pilots remarks that roll wavelength normally ranges from hundreds to thousands meters, and the orientations are approximately aligned with the mean flow directions (Brunt, 1938; Kuettner, 1959). While in the modern observational era, roll wavelength is often scaled by the boundary layer depth, termed as aspect ratio ($AR$). Since no direct measurements of the boundary layer depth were available, it was often inferred from the height of capping inversion (Weckwerth et al., 1997; Young et al., 2002; LeMone et al., 2018). The roll orientation is usually presented with reference to the directions of surface wind, mean flow wind or/and the geostrophic wind (wind at the top of boundary layer).

Over the last decades, the investigations of roll structures have evolved from case study to statistical study. During the BOMEX project, Kuettner (1959, 1971) reported that the spacing between two cloud bands varies from 2 to 8 km. His measure of the aspect ratio was between 2 and 4, and the angle of cloud street orientation relative to the surface wind was nearly $0^\circ$. The

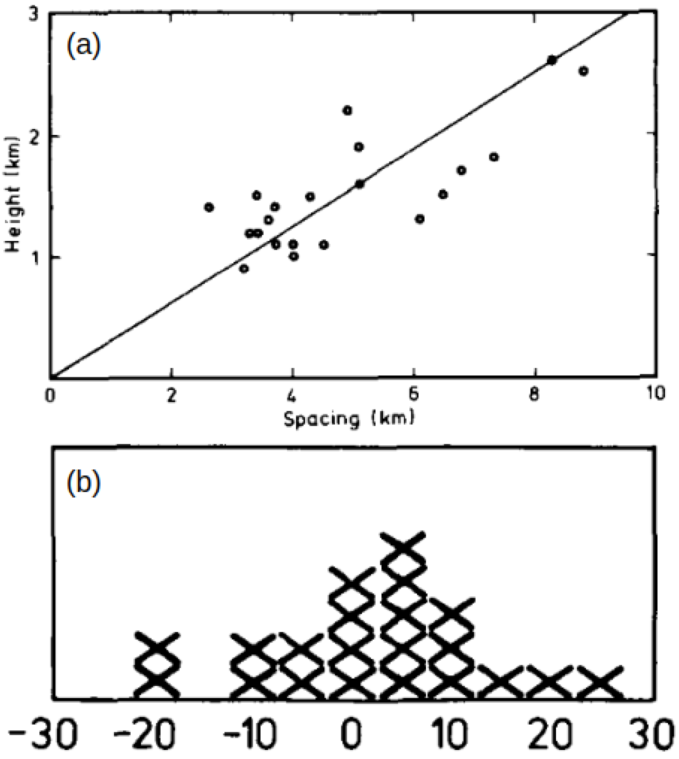

**Figure 1.4:** (a) Relationship between the spacing of cloud streets (roll wavelength) and the height of the boundary layer. The solid line indicates the average of aspect ration. (b) Angle deviation of cloud street orientation and the mean wind direction. Positive represents a clockwise rotation sense from the wind direction. (Reproduced from Weston (1980).)

later findings of LeMone (1973); Lemone (1976) were in broad agreement with Kuettner's results. The rolls were observed orientating to the left of the geostrophic wind by from 10 to 20°. The wavelengths is found to vary in the range of 1-7 km with aspect ratios of 2-6. The earliest statistics, to my knowledge, was provided by Weston (1980). He analysed 21 cases of cloud streets observed by optical images over British Isles land stations. It is documented that the typical roll wavelength is about 3-6 km and the boundary layer depth is around 1.5-2.5 km. The streets orientation was found within ±25° of the mean wind, most often around 10°. These observational cases were summarized in a diagram, reproduced here as Figure 1.4. Based on the 35-hours measurements by aircraft and radar over the Lake Michigan, Kelly (1984) recorded the roll wavelengths changed from 1.5 to 13.7 km and the boundary layer depth from 0.9 to 2.1 km. These resulted in the wider aspect ratio range of 1-9, and the roll orientation was ±10° within the geostrophic wind. Most of these studies have reported similar roll orientations and slightly different results for roll wavelengths.

In the situation of cold air outbreaks, rolls with relatively larger wavelength or aspect ratio have been observed. For example, Walter (1980); Walter and Overland (1984) reported the occurrence of cloud streets with large aspect ratio over the Bering Sea. Hein and Brown (1988) identified rolls with wavelengths of 2.3 and 5-6 km and proposed that the roll structure is largely determined by the dynamic instabilities which was modified and re-enforced by the thermal effects. Miura (1986) also observed rolls over the ocean with aspect ratios from 5 to 18 and the increasing trend of aspect ratio with further fetch towards the open ocean. Other notable observations of rolls include Asai (1966, 1970) who recorded rolls over the Sea of Japan with aspect ratios from 7 to 10, Kelly (1984); Kristovich (1993) who revealed the lake-effect boundary layer rolls with aspect rations of 9.1 and 6.7 and Brümmer (1999) who observed rolls with aspect ratios up to 6.7 based on satellite imagery of cloud patterns. Further reports of rolls with the aspect ratio larger than 5 are found in (Atlas et al., 1983; Holroyd, 1971; Kropfli & Kohn, 1978; Mourad, 1996).

All these observational results have been well summarized in (Atkinson & Wu Zhang, 1996; Weckwerth et al., 1997; Young et al., 2002). Two categories of narrow and wide rolls are reported. The narrow rolls with typical aspect ratio of 1-4 normally occur under the near-neutral to slightly unstable atmospheric conditions. Whereas the wider rolls that have aspect ratio larger than 10 are mostly associated with the strong weather events. Despite the fact that these two types of rolls are not yet well understood from theoretical point of view, a fundamental difference appears to be their interaction with the convective thermals (Atkinson & Wu Zhang, 1996; Young et al., 2002). In specifics, a single thermal band is usually associated with the updraft regions of the narrow rolls. By contrast, multiple bands are often observed within the wide roll updraft regions (Young et al., 2002).

As a matter of fact, existence of multi-scale rolls has been revealed in a number of roll observations. Holroyd (1971) suggested the presence of enhanced rolls on top of the smaller-scale roll vortices. Over the ice-covered Bering Sea, roll circulations on multiple scales of 1 to 2, 5 to 6, 12 to 15 and 25 to 30 km are simultaneously observed (Walter & Overland, 1984). Atlas et al. (1986) investigated the interactions between small-scale organized motions and the roll circulations with typical aspect ratios of 2–3. On the largest scale, Hein and Brown (1988) found the twofold hierarchy of circulations in well-developed cloud streets in the north of the Atlantic Ocean. The streets with wavelengths of 5-16 km superimposed upon a series of rolls with typical wavelengths of 2-3 km and aspect ratios of 3.3. Using satellite and aircraft observations, Mourad and Walter (1996); Mourad (1996) reported results that evidenced the superimposition of linear convective features with aspect ratios in the range of 3–8.

Though roll wavelengths in the hurricane system have been found to vary between 0.6 and 2 km with a typical aspect ratio of about 2.4 (Morrison et al., 2005; Huang et al., 2018), visual inspection of SAR images allows to identify larger-scale rolls. The missing identification is probably due to the inherent limitation of Fourier analyses. Nevertheless, the lognormal distributions of roll wavelength, boundary layer depth, aspect ratio, and roll orientation angle relative to the mean wind direction imply that the variable is exponentially dependent on another variable (Morrison et al., 2005). Huang et al. (2018) also illustrated that the spatial distribution of roll wavelengths around the eyes of tropical cyclones is asymmetrical, shortest roll wavelength was found around the storm center. These findings shall benefit the hurricane boundary layer model development given the outstanding roll effects on the air-sea energy and momentum exchanges.

The 10-year climatology analysis of warm-season roll features over the Oklahoma confirms that the narrow type of roll is more recurrent (Banghoff et al., 2020). Their radar observations disclose that the roll vortices can generally persist for 1-6 hours with wavelengths of 2-10 km and aspect ratios between 1 and 7. Most of the roll orientations are within ±10° of the mean wind direction, and only few up to 30° off the wind blowing. Of particular interests are the time-dependent aspect ratios within the day. It was found that the aspect ratio decreases early in the morning, remains constant during the afternoon and increases later in the evening. Although different from many previous field observations (Atkinson & Wu Zhang, 1996; Etling & Brown, 1993; Young et al., 2002), this varying aspect ratio manifests the natural evolution of roll circulations. The day-night contrast of aspect ratio implies the different boundary layer dynamics that might be associated with the diurnal fluctuations of multiple environmental variables.

### Roll impact on fluxes

It has been generally known that roll vortices produce extra-contribution (non-local or non-gradient) to the vertical transport of momentum, heat, moisture and chemical trace substances in the atmospheric boundary layer (Brown, 1980; Etling & Brown, 1993; Weckwerth et al., 1997). Size of the roll circulations lies in the range of spectral scales associated with the mass and energy turbulent exchanges (Lemone, 1976). The correlation analysis between the higher magnitudes of small-scale turbulent fluxes with the roll updrafts suggested minor exchanges (Lemone, 1976). While counter-gradient fluxes caused by roll vortices have been reported by (Rabin et al., 1982) based on the radar measurements. He concluded that the boundary layer parameterization of large-scale models was inadequate without accounting for the roll effect. This perspective was supported by the later aircraft flux measurements (Chou et al., 1986; Chou & Ferguson, 1991), showing that rolls are able to draw the smaller-scale eddies into the updraft regions. The transportation of turbulent kinetic energy is then enhanced across the boundary layer. Investigations into the roll-induced fluxes in the hurricane boundary layer provided further evidence. Morrison et al. (2005) utilized the covariance function between the horizontal and vertical components of wind fluctuations associated with rolls to calculate the momentum fluxes. It is found that the obtained fluxes are 2-3 times greater than that predicted by the parameterizations in the numerical weather models. Analysis of the airborne data suggested an increase of fluxed by about 50% due to the presence of rolls (J. A. Zhang et al., 2008). The affected flux exchanges of the boundary layer may provide a pathway to characterize the roll impact on the structure and intensification of hurricanes (Gao et al., 2017; Huang et al., 2018).

Roll circulation is also significant is to the horizontal air-mass transformation, especially between the Arctic and mid-latitudes due to the frequently occurred cold air outbreak weather events (Pithan et al., 2018). The extent of cold air outbreaks can reach up to 500-1000 km, with intensified fluxes exchanges and fast air-mass transformation from continents towards the ocean (Fletcher et al., 2016; Pithan et al., 2018). Further from the coast, the transition from a roll to a cell is accompanied by the shift of boundary layer state towards high convection. This is usually represented by the development from thin, elongated stratocumulus to deeper, dispersed cumulus clouds. The state variation often produced an increasing latent heat release in clouds relative to the surface heating (Brümmer, 1999; Atkinson & Wu Zhang, 1996).

While the significance of roll effects on surface heat and latent fluxes had been recognized, it is yet difficult to directly measure and quantify this non-local contributions. There has been dedicated efforts to introduce an diffusion parameterization related to this non-local effect in the flux modeling (Troen & Mahrt, 1986). Model simulations predicted an averaged increase of surface fluxes by 6% and surface stress by 15% due to the roll effects (Foster, 1996). Other effects on the flow in the boundary layer could be equally important and additional studies are supposed to advance our understanding (Foster, 1996; Foster & Levy, 1998). By that, new techniques and/or methods for the surface fluxes estimation are necessary to refine the future modeling. An interesting perspective is the use of ship-launched and ship-recovered Boeing–Insitu ScanEagle unmanned aerial vehicles (UAVs) for ocean surface processes study (Reineman et al., 2016). The UAVs measurements include atmospheric momentum and radiative, sensible, and latent heat fluxes, which can be complemented by measurements from ship-based instrumentation such as a foremast MABL eddy-covariance system, lidar altimeters, and a digitized X-band radar system (Reineman et al., 2016). These instruments shall provide sufficient observations for both atmospheric and oceanographic research, in spite of its weak competition of spatial coverage. For the airborne measurement, on the other hand, Brilouet et al. (2017) demonstrated that a correction of eddy covariance turbulent fluxes is necessary by taking into account the systematic and random errors due to sampling and data processing.

### 1.2.3 Theoretical and numerical

There has been a fairly long history of theoretical and numerical studies of roll vortices (Brown, 2002). According to the state of the art, several mechanisms have been proposed to interpret the generation of these quasi two-dimensional structures in the atmospheric boundary layer (Etling & Brown, 1993; Young et al., 2002). The mostly accepted theory is that rolls are driven by the shear instability, convective instability or the combinations of dynamics and stratification effects (Brown, 1980; Etling & Brown, 1993). Despite that the buoyancy contributions are able to modify roll structure, the shear dynamics is still the most basic factor for roll formation (Foster, 1996).

It has been assumed that the dynamic instabilities and thermal instabilities play their roles under certain situations (Etling & Brown, 1993). As summarized by Foster (1996), "A moderate amount of stable stratification will shut off the roll mechanism while slight to moderate unstable stratification will re-enforce it. For large enough thermal forcing, the dynamic instability is overwhelmed and the roll mechanism is inoperative. In this case there is a transition to a cellular convection pattern or to more unorganized convective turbulence." This remark is consistent with the simulation results of transitions between unorganized turbulence, organized rolls and cells (Salesky et al., 2017). The characteristic length scale and roll orientation are expected to vary with the dominant environmental forces.

All in all, the governing equations of this typical process are the Navier-Stokes equations including the thermal and dynamics effects in a rotating coordinate system (Brown, 1980). Instability analysis is expected to provide a solution or a representation for the mean flow subject to a normal mode perturbation. This method was initiated by Rayleigh (1916) to establish the criteria for the onset of convective and dynamic (inflection point) instabilities. Significance of the velocity profile was noticed in the atmospheric and oceanic boundary layer where horizontal layers can be readily distinguished by the differing speed and/or direction (Rayleigh, 1916). This again evidences the importance of the Coriolis force in rotating the air flow under balance with a horizontal density gradient (thermal wind) or with the viscous force in the Ekman layer (Brown, 1980).

Gregory, Stuart, Walker, and Bullard (1955) carried out the earlier theoretical analysis of the inflection point instability, producing rolls with wavelength six times of the boundary layer depth and orientation of 14° angle relative to the mean flow. While the basic mode was tested by Gregory, the inviscid instability equations still generated inaccurate prediction of roll wavelengths (Brown, 1972). Later, Lilly (1966) identified two instability modes from a neutrally stratified Ekman layer mean flow. One of the mode was referred to as the parallel instability because it extracts energy from the mean flow through shear production parallel to the roll axis. This energy transfer is dependent on the Coriolis term in the instability equations and is expected to not be able to persist towards the very high *Re* (Reynolds number) regime. The other mode is the so-called inflection point instability with its energy generation being associated with shear production near the inflection point in the mean velocity profile.

Since the solutions of inflection point instability predicted consistent values of roll formation, wavelength and orientation, it has been examined extensively in the earlier theoretical studies. Major progresses include the initial value calculation (Faller & Kaylor, 1966; Faller, 1967), stratification effects on the instability (Brown, 1972; Kaylor & Faller, 1972; Asai & Nakasuji, 1973), surface roughness (Etling & Wippermann, 1975) and variable eddy viscosity (Criminale & Spooner, 1981). In particular, the nonlinear analyses were also conducted to study the spectral property of roll development in neutral and unstably stratified conditions (Brown, 1970, 1972; Mourad & Brown, 1990; Haack & Shirer, 1992)

The influence of the horizontal component of the Coriolis force on the normal mode instability has been exploited by Etling (1971); Mason and Thomson (1987) and detained by Leibovich and Lele (1985). Results show that this horizontal component acts as a destabilizing agent that supports the northerly flows and reduces the growth rates of the southerly flows. The most unstable roll events is expected to be westerly. However, the horizontal Coriolis effects remains doubtful because direct observations evidence of this mechanism is not yet available. Both observational and theoretical efforts are required to better understand the role of the horizontal Coriolis force in the geophysical and astrophysical fluid dynamics (Gerkema et al., 2008; Glazunov, 2010; Liu et al., 2018).

The brief review above mostly concentrated on the theoretical analyses of roll vortices conducted in the late twentieth century. For more details, one can refer to the literature or review articles (Brown, 1980; Etling & Brown, 1993; Atkinson & Wu Zhang, 1996; Young et al., 2002). As a matter of fact, less progress in theory or model development of the boundary layer roll during the last two decades. This might be due to the lack of advanced observational means and new dataset. One exception is the increased attention towards the organized roll vortices in the hurricane boundary layer. Foster (2005) developed both the linear and nonlinear roll instability solutions to explain the rolls prevalence in hurricane weather systems. His predictions of roll orientation, wavelength and aspect ratio agree well with observations. The implications of roll effects on the boundary layer fluxes in terms of non-local and non-gradient contributions are also demonstrated. This shall provide guidance for parameterizing the roll effects on the hurricane boundary layer mean flow and fluxes.

## 1.3 SAR observation of MABL rolls

Since the launch of SEASAT in 1978, synthetic aperture radar (SAR) has become unique and irreplaceable tool for monitoring the global ocean surface (Lee-Lueng Fu & Holt, 1982). It is not only because of its weather and sunlight independence characteristics, but also due to its capability of resolving detailed features of various oceanic and atmospheric phenomena. The fundamental principles of a SAR system as well as the SAR imaging mechanism of ocean surface can be found in multiple textbooks (e.g. Lee-Lueng Fu & Holt, 1982; Jackson et al., 2004; Cumming & Wong, 2005) or literature (e.g. Hasselmann et al., 1985; Kudryavtsev, 2003a, 2003b; A. A. Mouche, Chapron, & Reul, 2007; Gens, 2008). Yet, it seems necessary to brief the state of the art of roll investigation using SAR observations.

### 1.3.1 SAR imaging of roll-impacted ocean surface

SAR is a side-looking imaging radar that transmits coherent pulses to illuminate the Earth surface (Stull, 1988; Jackson et al., 2004). These microwave pulses reflected to the radar are recorded in two dimensions with one along the radar looking direction (called range) and the other along the flight direction (called azimuth). SAR is competitive because of its high spatial resolution in comparison to other microwave systems, such as altimeters and scatterometers. Its range resolution is determined by reciprocal of the radar pulse bandwidth. In the azimuth direction, the antenna size is synthetically increased and resulting in high spatial resolution being half of the actual antenna length. Raw signal recorded by a SAR is processed and formed into an image, which can cover hundred kilometers of the Earth surface.

The SAR backscattering is commonly quantified by normalized radar cross-section

(NRCS). Its magnitude relies on radar configurations ( wavelength, polarization, geometry) and environmental conditions as well as the dielectric properties of sea surface. At moderate incidence angles, SAR signal can well be explained by the Bragg scattering theory. It tells that the incident radar pulses interact with the ocean surface roughness composed of short waves at comparable wavelengths. Of the multiple radar wavelengths, C-band SAR (radar wavelength around 5 cm) has been mostly exploited owing to its higher sensitivity to surface roughness. The roughness is usually wind-generated short waves ranging from capillary to gravity waves. While on the natural ocean surface, the longer waves/swell can modulate the short waves and therefore influence the ambient NRCS (Hasselmann et al., 1985; Kudryavtsev, 2003a, 2003b; Jackson et al., 2004; A. A. Mouche, Chapron, & Reul, 2007; A. A. Mouche, Chapron, Reul, Hauser, & Quilfen, 2007).

As SAR data are increasingly available, our understanding of SAR backscattering has been greatly advanced. It has been documented that the NRCS is composed of contribution not only from regular sea surface roughness, but also the breaking waves events (Kudryavtsev, 2003a; A. A. Mouche et al., 2006). These short waves are generated by the surface winds and mostly align with the local winds. By contrast, the scattering facets associated with the breaking waves are mostly isotropic. In the case of up-/downwind where wind blows against or into the SAR looking direction, the cm-scale waves are the prominent scatters. However, as wind direction changes towards the crosswind, the isotropic scatterers caused by intermediate breaking waves will instead take hold and reach the dominant. The backscattering contribution from cm-scale waves is therefore larger at up-/downwind than crosswind and stronger in VV polarization than HH, and in general increases with incidence angle.

The visibility of roll imprints on SAR images primarily depends on the modulation of roll-induced surface wind perturbation on sea surface roughness (Alpers & Brümmer, 1994; Young, 2000; Vandemark et al., 2001). To first-order, these wind perturbations are able to increase or decrease rapidly the population of cm-scale short waves, making roll imprints visible as alternative bright and dark wind streaks on SAR images (Jackson et al., 2004). This is particularly true at larger incidence angle and in the case of up-/downwind, where the directional cm-scale waves are the prominent scatters. By contrast at smaller incidence angle and crosswind, the SAR visible waves breakers can gradually grow only when the roll-induced wind perturbations are sufficiently stationary for a certain duration. As such, the stationarity of rolls and contribution of short wave scattering to the total NRCS are determinative for roll visibility on SAR images. Remarks on the later factor have been given by Alpers and Brümmer (1994), which is larger at up-/downwind than crosswind and stronger in VV polarization than HH, and in general increases with incidence angle. A following-on statistical assessment of SAR sensitivity to roll imprints is conducted in this thesis as one of the main results.

### 1.3.2 Roll investigations using SAR data

The first reported SAR observation of MABL rolls appeared during the Marineland Experiment in 1975 Thompson, Liu, and Weissman (1983). L-band SAR images were acquired over the Atlantic Ocean off the coast of Florida from a National Aeronautics and Space Administration (NASA) airplane with clear signatures of wind streaks at wavelength of 2-4 km. Flight observation also noticed that stronger roll features were present on SAR images when the radar was looking upwind with less prominent patterns at downwind. The roll signatures becomes almost invisible on SAR images when the radar was looking crosswind. These initial findings lay groundwork for later applications of SAR images for roll investigations, such as those from the SEASAT satellite (Lee-Lueng Fu & Holt, 1982; Gerling, 1986), and the space shuttle Columbia during the Shuttle Imaging Radar-A (SIR-A) experiment (Ford et al., 1983). The method to extract the direction of roll-associated wind streaks as well as its variability was proposed through the SAR image spectrum, which is still typical for roll investigation. Yet it should be pointed out that the failure of radar backscattering calibration prevented the retrieval of absolute wind speed from SAR images.

Since the 1990s, large volume of decent SAR images have been collected from multiple satellites such as ERS-1&2, RADARSAT-1&2, Envisat/ASAR and now Sentinel-1 A&B. Alpers and Brümmer (1994) investigated two MABL roll events observed by ERS-1 SAR over German Bight of the North Sea. The variations of SAR NRCS and SAR-retrieved surface wind speed associated with roll imprints were reported to be on the order of about 10%. The roll visibility on C-band SAR images were also noted back then including sensitivity changes versus radar antenna incidence angle, transmit frequency, and mean wind and direction. But such aspects have been seldom taken into account in the subsequent studies for SAR imaging of rolls, nor for wind direction retrieval (e.g. Chapron et al., 2001; Koch, 2004; Horstmann & Koch, 2005).

SAR-based investigation of MABL rolls almost remains in the phase of case studies. Mourad and Walter (1996) found comparable linear streaks in terms of the scale and orientation between Advanced Very High Resolution Radar (AVHRR) and SAR images simultaneously acquired over a region north of Alaska during a cold air outbreak. He also noted the multi-scale structure visible on SAR images, which might be associated with the fine-scale atmospheric microfronts and kilometer-scale roll vortices (Mourad, 1996). The wind streaks on SAR images were later evidenced as manifestation of MABL roll vortices by the consistent features obtained from the large-scale eddy simulations (G. Muller et al., 1999). Further supporting studies include roll feature observations by combining the aircraft data and RADARSAT-1 SAR images (Vandemark et al., 2001), roll coexistence with atmospheric gravity waves on SAR images (Li et al., 2013), and quantification of roll effects on the hydrodynamics (S. Muller et al., 2013).

Given the great potential of SAR providing high-resolution (1̃0 m) sea surface wind field, SAR measurements offer a new opportunity to diagnose the detailed structure of MABL rolls (Young, 2000). The spectra of SAR NRCS or derived winds are particularly effective for determining the basic characteristics of these organized flow patterns in the MABL (Young, 2000; Koch, 2004; Li et al., 2013; Zhao et al., 2016; Huang et al., 2018). It is also important to remind that long time series of SAR data will be accumulated to cover the temporal requirement for climate studies (Brown, 2000). This is guaranteed by the routine acquisition of wave mode (WV) SAR data during the European Remote Sensing (ERS-1/2) missions (1991–2003), Envisat/ASAR mission (2002–2012) and the current Sentinel-1A&B. Application of these WV SAR images and wide swath SAR images are expected to advance our understanding of the roll vortices.

Few attempts have been conducted to obtain statistical description of MABL rolls from

SAR observations. The first one is based on the RADARSAT-1 ScanSAR images over the Gulf of Alaska and the Bering sea in 1997-1999 (Levy, 2001). In total, 7150 100 km by 100 km images were categorized in different ways for occurrence statistics in both temporal and spatial scales. Significant variability was found on the spatial map of roll occurrence at grid of 2.5° by 2.5° boxes. Another statistical study focuses on the atmospheric conditions of roll occurrence (Zhao et al., 2016). In detail, 227 X-band SAR images acquired by TerraSAR-X and TanDEM-X over the North Sea and Baltic Sea are included. These SAR data are jointly analysed with the environmental variables measured from three FINO platforms. Results reports that 48% of these 227 SAR images have clear signatures of wind streaks, among which 67.3%, 20.0%, and 12.7% occurred under unstable, neutral, and stable atmospheric conditions, respectively. Although these two studies are still limited in either space coverage or time scale, they opened a new path for the SAR roll investigations at broader scope. It is worth noticing that both attempts rely on visual inspection to distinguish the presence of roll imprints on SAR images. Such manual classification approach is obviously impractical for the huge volume of WV SAR data obtained by ERS-1/2, Envisat ASAR and Sentinel-1. Thus, new methods to automatically identify roll events from SAR images are essential.

In addition to the statistical investigation of MABL rolls, efforts have been recently made to describe the roll structures observed by SAR images in hurricane weather system (Morrison et al., 2005; J. A. Zhang et al., 2008; Huang et al., 2018). The existence of intense, sub-kilometer-scale, boundary layer rolls that strongly modulated the near-surface wind speed was earlier revealed by the DopplerOnWheels(DOW) mobile weather radar (Wurman & Winslow, 1998). It was found that these roll structures are one cause of geographically varying surface damage patterns and much of the observed gustiness that can bring high-velocity air from aloft to the surface levels. While the length scale of roll observed in hurricane boundary layer is similar to the commonly visible rolls, the modulation of hurricane roll structures on air-sea momentum exchanges are more significant (Morrison et al., 2005; J. A. Zhang et al., 2008). Using 16 wide swath SAR images, Huang et al. (2018) illustrated the spatial distribution of roll length scale around the hurricane centers. He noticed the asymmetrical characteristic of roll wavelength and found it is overall shortest around the storm center, increase first and then decrease with the distance from storm center. The largest rolls were observed in the range of $d^* - 2d^*$, where $d^*$ is the distance to hurricane center normalized by the radius of maximum wind.

# Chapter 2 Scope of this thesis

## 2.1 Motivation and challenge

As briefly reviewed in Chapter 1, investigation of roll-shaped MABL has been conducted for decades, but mostly limited to case analyses (Brown, 1980; Etling & Brown, 1993; Atkinson & Wu Zhang, 1996; Young et al., 2002). These observational studies provide an overall panorama that rolls normally occur in near-neutral to moderately unstable atmospheric stratification. The typical characteristics of rolls include wavelengths of 1-5 km, aspect ratios (i.e., roll wavelength divided by boundary layer height, AR) between 1 and 7, and roll orientations of ±30° relative to the surface wind directions.

Although the dynamics of roll vortices are increasingly understood through extensive observations combined with theoretical studies and numerical modeling, systematic analyses of rolls over the global ocean have not yet been feasible. The primary difficulty is the lack of sufficient and comprehensive observations of roll events. As a result, the basic knowledge about MABL rolls such as characteristics, frequency of occurrence, and forcing mechanisms are not yet fully acknowledged. This further hinders the long-term and businesslike climatology establishment of roll-shaped ABL dynamics as well as its annual and seasonal variability. Such climatology will no doubt advance the parameterization of roll dominated ABL, and hence improve the accuracy of numerical weather and climate model projections.

In terms of the theory explorations, roll vortices are recognized as manifestation of the Ekman layer instability. Their formation can be described by the nonlinear Navier-Stokes equations when considering thermal and dynamic factors in a rotating system (Brown, 1980; Brown & Liu, 1982). The early theoretical investigations on roll dynamics have focused on the linearization schemes and produced the popular solution of inflection-point (IP) instability (e.g. Asai, 1970; Brown, 1970, 1972). This theory predicts consistent roll characteristics with observations in both aspect ratio and horizontal orientation. It is therefore widely adopted and extended by taking into account other effects such as thermal wind, stratification, baroclinicity, and nonlinear processes (Foster, 1996; Young et al., 2002). While in most of the IP-based studies, only the vertical component of Earth's rotation is considered. The horizontal one, however, is often neglected, though its significant impact on geophysical fluid dynamics has been clearly shown by multiple theoretical researches. Lack of observational evidence for influence of this factor is also one reason.

Over much of the world's oceans, the primary observational data used to study the mean state, characteristic and dynamic of the MABL is satellite visible imagery of the low clouds. This visualization is only possible when the MABL conditions are favorable for cloud formation and there are no intervening cloud layers. Another limitation of using visual satellite imagery to analyze the MABL is that the layer below the clouds is frequently decoupled from or only partially coupled with the cloudy layer. It seems that future improvements of MABL understanding will require new detailed global observations that are not subject to the presence or absence of clouds. They shall complement the MABL cloud measurements by providing information about the MABL processes that are tightly connected with the ocean surface. To this end, this thesis exploits the brand-new, ultra-high resolution SAR remote sensing data, which have the all-weather capability to characterize the MABL roll imprints on the ocean surface at climate time and space scales.

Ocean SAR imagery has been well-known to provide special insight into the MABL structures because of its high sensitivity to the wind-induced sea surface roughness change (e.g., Gerling, 1986; Alpers & Brümmer, 1994; Young, 2000; Li et al., 2013; Alpers et al., 2016). While until very recently it has been of limited use for meteorological and climate studies. The primary issues are that pervious SAR imagery was usually highly expensive (thousands of dollars per image) and did not provide coverage of the global oceans. These two issues have finally been resolved starting with the Sentinel-1 (S-1) A&B SAR missions launched by the European Space Agency (ESA) in 2014 and 2016, respectively (Salvi et al., 2012). It is important to note that ESA has planned SAR missions to keep the continuation into the foreseeable future. Secondly, technological advances also allowed the routine collection of sea surface roughness images by an improved Wave Mode (WV) with larger image size (20 km), finer spatial resolution (5 m), higher signal-to-noise (which reduces speckle noise), and increased global sampling.

These sea surface roughness SAR images capture a wide range of oceanic and atmospheric processes, making them a valuable asset for many geophysical applications. In the case of MABL rolls at scales of 1-5 km, the S-1 WV SAR data allow to decompose the quasi-periodic linear patterns for extraction of roll orientation and wavelength. It represents the first chance to exploit the surface manifestations of organized secondary wind fields introduced by MABL rolls over longer duration and larger spatial coverage. It is also feasible to move ocean SAR remote sensing forward by applying it for the air-sea interface, fluxes and MABL processes studies.

## 2.2 Objectives of the work

The novelty of this study is to take advantage of the newly global S-1 WV ocean SAR data set for MABL roll feature investigations. These small-sized SAR images are originally dedicated for directional ocean wave/swell spectra retrieval as part of ESA's operational Level-2 ocean product. While recent exploration of these WV SAR data have revealed the fact that a wide range of oceanic and atmospheric phenomena including MABL roll are also well captured. This poses a new and unique opportunity for extensive study of various significant ocean surface processes. While this thesis focuses on extending the ocean SAR data analysis strategies for deep investigation of the km-scale MABL rolls, which are significant to the air-sea interaction process.

Benefiting from the huge volume of SAR images acquired by S-1 WV, such data analyses in terms of roll features are allowed to move forward to nearly global, systematic and multi-annual investigations. To this end, the following questions have been formulated to be addressed during this thesis.

**Question 1:** How to efficiently categorize the huge S-1 WV SAR data ($\sim$120,000 per month) in terms of MABL rolls and/or other ocean surface phenomena?

**Question 2:** Is the SAR capability of resolving the km-scale MABL roll features well understood? towards identification methods and SAR sensitivity in mapping ocean surface roll imprints for different wind conditions?

**Question 3:** How is the the roll characteristics (orientation, length scale and structural content) derived from WV SAR images related to the spatial and temporal variation of MABL bulk properties, such as stability, wind shear, heat and momentum fluxes?

The proposed data exploitation assumes that significant average results will gain from the statistics of these huge roll WV images. While appropriate average and curve fit would reduce data noise, robust correlations and uncertainties with relevant controlling factors should be discussed. As a first step, we envision machine-based classification methods to automatically identify roll events from the massive S-1 WV SAR data. Then, substantial effort will be given to the signal processing of scene contrasts within the WV radar backscatter imagery to extract the desired roll information. These information shall serve the joint-analysis with ERA5 surface environmental variables for demonstration of global roll features. Thus, the specific objectives of this thesis are:

**1)** Collocate each WV SAR image with the ERA5 reanalysis product for potential required environmental variables.

**2)** To develop automatic methods for roll identification from S-1 WV SAR data. (**Question 1**)

**3)** To extract roll-relevant information from each identified WV SAR images, including orientation, wavelength, and roll-induced sea surface roughness modulation and wind perturbation.

**4)** To obtain statistical assessment of classified roll events, and roll-induced roughness modulation and wind perturbation at global scale. (**Question 2**)

**5)** To quantify the extracted roll characteristics and atmospheric conditions of roll occurrence at global scale. (**Question 3**)

**6)** To depict the relation between roll characteristics and environmental variables. (**Question 3**)

**7)** To validate the global findings and associate with the theoretical evidence. (**Question 3**)

## 2.3 List of publications

In achieving these objectives, the following papers have been published or are well prepared:

[1] Chen Wang, Alexis Mouche, Pierre Tandeo, Justin Stopa, Nicolas Longépé, Guillaume Erhard, Ralph Foster, Douglas Vandemark, and Bertrand Chapron, “Labeled SAR imagery dataset of ten geophysical phenomena from Sentinel-1 wave mode (TenGeoP-SARwv).” SEANOE, 2018.

[2] Chen Wang, Alexis Mouche, Pierre Tandeo, Justin Stopa, Bertrand Chapron, Ralph Foster, and Douglas Vandemark, “Automated Geophysical Classification of Sentinel-1 Wave Mode SAR Images Through Deep-Learning,” in IGARSS 2018 - 2018 IEEE International Geoscience and Remote Sensing Symposium, 2018, pp. 1776–1779.

[3] Chen Wang, Alexis Mouche, Pierre Tandeo, Justin Stopa, Nicolas Longépé, Guillaume Erhard, Ralph Foster, Douglas Vandemark, and Bertrand Chapron, “A labelled ocean SAR imagery dataset of ten geophysical phenomena from Sentinel-1 wave mode,” Geosci. Data J., vol. 0, no. 0, p. gdj3.73, Jul. 2019.

[4] Chen Wang, Pierre Tandeo, Alexis Mouche, Justin Stopa, Victor Gressani, Nicolas Longepe, Douglas Vandemark, Ralph Foster, and Bertrand Chapron, “Classification of the global Sentinel-1 SAR vignettes for ocean surface process studies,” Remote Sens. Environ., vol. 234, p. 111457, Dec. 2019.

[5] Chen Wang, Alexis Mouche, Ralph Foster, Douglas Vandemark, Justin Stopa, Pierre Tandeo, Nicolas Longepe, and Bertrand Chapron, “Characteristics of Marine Atmospheric Boundary Layer Roll Vortices from Sentinel-1 Sar Wave Mode,” in IGARSS 2019 - 2019 IEEE International Geoscience and Remote Sensing Symposium, 2019, pp. 7908–7911.

[6] Chen Wang, Douglas Vandemark, Alexis Mouche, Bertrand Chapron, Huimin Li and Ralph Foster, “An assessment of marine atmospheric boundary layer roll detection using Sentinel-1 SAR data,” Remote Sens. Environ., vol. 250, p. 112031, 2020.

[7] Chen Wang, Douglas Vandemark, Bertrand Chapron, Alexis Mouche and Ralph Foster, “Insights into the Global Feature of Marine Atmospheric Boundary Layer Rolls,” (To be submitted)

## 2.4 Summary of main results

This dissertation is dedicated to a observational investigation of MABL rolls using the new global S-1 WV SAR data. It is structured in the frame work of published articles and prepared manuscripts. While the papers are appended in Chapter 3, a summary of the main results are given in the following.

### 2.4.1 A labelled ocean SAR imagery dataset

As a first attempt to extend the global SAR application beyond ocean waves, much time at the beginning of this PhD project were devoted to the visual interpretation of the ocean surface processes observed by S-1 WV SAR images. I learnt myself during this activity that, except ocean waves/swell, the massive WV SAR images also capture a wide range of geophysical phenomena that are of significant interest in ocean-atmosphere interactions. And for most of the situation, there is only one individual phenomenon dominates across the 20 km by 20 km scenes. These suggest a new and unique opportunity for routine identification and study of a wide range of oceanic and atmospheric phenomena at global scale. The first challenge is to develop an efficient and accurate method to detect and classify key geophysical phenomena among the whole WV dataset.

To this end, a labelled dataset of ten geophysical phenomena from S-1A WV SAR images in VV polarization is established, namely TenGeoP-SARwv. This dataset consists of more than 37,000 SAR vignettes divided into ten pre-defined geophysical categories, including pure ocean waves (POW), wind streaks (WS), micro convective cells (MCC), rain cells (RC), biological slicks (BS), sea ice (SI), icebergs (IB), low wind areas (LWA), atmospheric fronts (AF) and oceanic fronts (OF). These images cover the entire open ocean and are manually selected from Sentinel-1A WV acquisitions throughout the year of 2016. For each image, only one prevalent geophysical phenomenon with its prescribed signature and texture is considered for labelling. All images are processed into a quick-look image provided in the formats of PNG and GeoTIFF as well as the associated labels. They are convenient for both visual inspection and can be used for training and validation of any candidate image analysis methods.

The proposed dataset is the first SAR image collection composed of multiple oceanic and atmospheric phenomena over the global open ocean. It seeks to foster the development of strategies or approaches for massive ocean SAR image analyses. A key objective is to allow exploiting the full potential of S-1 WV SAR acquisitions, which are about 60,000 images per satellite per month and freely available. Such a dataset shall be of great value to a wide range of users and communities in deep learning, remote sensing, oceanography and meteorology.

### 2.4.2 Automated classification of Sentinel-1 SAR images

Based on the labelled ocean SAR image dataset, we successfully applied the emerging deep learning approach to these WV SAR image classification tasks. In detail, a classification tool, called CMwv, is developed by fine-tuning the Inception v3 deep convolutional neural network (CNN). As SAR imaging sensitivity to ocean surface processes differs from low to a higher radar incidence angle, two CMwv models were built for VV-pol WV1 and WV2 data respectively. Both models are applicable for both S-1A and S-1B WV SAR data. This classification tool is able to distinguish the ten pre-defined geophysical phenomena, with assigning each WV image a probability score for the ten pre-defined classes. One image is sorted to be the class of the largest classification probability.

Performance of the developed classification tool is evaluated by using an independent labeled dataset. Results show satisfactory and robust classification results.The tool works properly, especially for six (WS, MCC, RC, BS, SI and LWA) of the ten classes. To further verify the classification results, we compare the classified rain cells and sea ice with rain precipitation from Global Precipitation Measurement (GPM) and sea ice concentration from Special Sensor Microwave Imager (SSMI). The geophysical patterns on global maps are qualitatively analyzed and found to be very consistent with independent remote sensing dataset. In addition, these high-resolution WV SAR data can resolve fine, sub-km scale, spatial structure of rain events and sea ice that complement other satellite measurements. This suggests that the S-1 WV data is an independent data source of small-scale phenomena at a global scale. Overall, such an automated ocean SAR image classification tool open paths for a broader geophysical application of maritime S-1 WV acquisitions. Although there is inevitable limitation for the CMwv tool, the amount of classified SAR images is sufficiently big to investigate global features of one phenomena, such as atmospheric conditions and characteristics of MABL rolls focused in this thesis.

### 2.4.3 Assessment of roll detection using Sentinel-1 SAR

Taking advantage of the new and large classified S-1 WV SAR dataset, we firstly examine the population of roll events. This is a complement to the classification model performance on identifying roll events from the global massive S-1 WV SAR images. In addition to that, SAR capability for mapping and characterizing roll imprints on SAR backscatter across the S-1 WV configurations is also examined for the first time at global scale. Data used in this separate study are the wave mode (WV) images collected by S-1 satellites in 2016-2017. These 20 km by 20 km SAR images are acquired at two incidence angles of 23 ° (WV1) and 36.5° (WV2) in VV or HH. In specific, $sim$1.37 million of automatically-classified WV scenes are examined. For each scene, we extract the roll-induced backscatter modulation and directional information for joint analysis with the collocated ERA5 winds.

The classification model is found has limitation in identifying weak roll imprints with a 4% baskscattering threshold for both WV1 and WV2 in VV and HH. This recalls the future model improvement by reinforcing the representative of the hand-selected training dataset. Statistics of the identified roll events show a low wind speed cut off near 2 m/s and the higher roll rates from WV2 SAR data and for up-/down wind situation. This is due to the fact that roll imprints are visible much clearer on images of WV2 and at up-/down winds based on the analysis of roll-induced NRCS variations. SAR retrieval of the wind speed variation caused by rolls confirms its higher values at crosswind and illustrates the first global estimation of about 8% (±3.5%) for average and across all wind speeds. These more stationary rolls observed in WV1 crosswind are mostly occur in more unstable atmospheric conditions, distinct from other relative wind directions. It implies that the SAR-imaged roll imprints are largely associated with roll vortex in various time and/or length scales. The 8% mean wind perturbation value was then used in the idealised GMF simulations to further assess the wind speed and direction dependence of S-1 SAR WV responses to roll modulation effects. All the highlights advance our understanding of SAR imaging sensitivity to the km-scale MABL rolls that has implications for SAR applications seeking wind direction estimates from roll imprints and, more broadly, boundary layer studies over the ocean.

### 2.4.4 Insights into the global feature of MABL rolls

The new classified S-1 WV SAR data provide quite valuable and detailed structure information of the atmospheric boundary layer at the bottom. As a preliminary step, we focus on the global feature of MABL rolls in terms of the synoptic conditions and their structural characteristics. More than 125, 000 roll events observed by S-1A WV2 in 2016-2018 are involved in the statistical analysis. Each image has been collocated in time and space with the ERA5 surface variables, and analysed in frequency domain for roll orientation and wavelength extractions.

As expected, up to 90% of roll events occur in slightly unstable to near-neutral atmospheric conditions, distinct from the total average. Quantitative examinations also unveiled the latitudinal dependence of atmospheric stratification using the bulk Richardson number, which is unstable in the tropics while near-neutral at mid-latitudes. Roll orientation is found to systematically swing between two angles with respect to the surface wind. One angle is presented towards and one away from the geostrophic winds with latitudes beyond and within $\pm 30^{\circ}$, respectively. The low- and mid-latitude angle contrast seems linked to the westerlies and trade wind belts, suggesting the significance of air flow directions in roll dynamics. This is expected to be explained by the horizontal Coriolis force effects on geophysical fluid dynamics as addressed in several theoretical investigations, but neglected in most. In terms of the multi-scale nature of roll vortices, our analysis shows nearly equal number of single-, double- and triple-length scales. Aspect ratio of these narrow rolls ranges from 0.5 to 8 with mean of 2.9, consistent with previous observations. Although gaps still exist in temporal and spatial coverage, it is the first time to condense MABL rolls at global scale. The statistical behavior of rolls summarized from the WV SAR measurements cannot be resolved by any other means.

## 2.5 Conclusions and perspectives

The present work in this thesis provides a basis to move application of ocean SAR remote sensing beyond ocean waves/swell and the case study stage. While only concentrated on the MABL rolls, these global WV SAR data has shown great potential for broader geophysical application, augmenting its operational role that supports ocean wave prediction systems.

The proposed SAR imagery dataset with individual annotations of oceanic or atmospheric phenomena allows new efforts to test, validate and benchmark different methods for the identification of key geophysical processes. It also supports limited statistical investigation of the geophysical properties for these ten pre-defined phenomena. Thus, such a dataset of labelled ocean SAR imagery is put forward for both scientific and engineering applications for different communities such as deep learning, remote sensing, oceanography and meteorology. Future work on the dataset are suggested to include more geophysical categories and introduce multi-labelling if multiple phenomena exist within one SAR image. The refinement of such a ocean SAR image dataset may need numerous researchers to work together for years from the experience of other image dataset collections.

The deep-learning technique provides a promising solution that advances the traditional way for automated classification of these massive S-1 WV SAR images. Our study demonstrates a typical procedure for training and validating a deep CNN model towards ocean SAR scene classification. While it muse be noted that the trained CNN model is somewhat dependent on the quality of the training dataset. This is because the ability of this deep CNN model to differentiate between phenomena in each SAR image relies on the efficient extraction of optimal features into convolutional layers, and then to amplify feature differences through pooled layers. That is, distinct image features cannot be extracted if the phenomena are insufficiently clear on SAR images. Therefore, one of important outlooks in improving the classification model performance is to refine the training dataset as mentioned above. Another perspective is to include the geographic information of SAR data in deep learning approaches. Latitude is just one of many possible important and obvious data inputs, helping for example, to limit sea ice and iceberg detection windows to cold waters. In addition, other deep learning techniques such as pixel-level based classification, object detection and image segmentation are expected to efficiently target the localized phenomena within each SAR scene.

Assessment of the classified roll events from S-1 WV SAR data confirmed the model limitation in identifying the weak roll imprints, and also advanced our understanding of C-band SAR sensitivity in mapping roll modulations on ocean surface. It also open avenues for further studies. On one hand, the revealed differences in SAR sensitivity to waves generated by roll impacts, particularly for crosswind views, should be further investigated. This may lead to new approaches for identifying unstable conditions, and Richardson number *RiB* retrieval methods. On the other hand, though the weak roll imprint cases are excluded in the present classified dataset, this S-1 SAR database is still state-of-the-art in terms of providing an overall global view of roll field characteristics (wavelength & orientation) as well as the ability to relate these data to near-surface forcing from the tropics to high latitudes. This massive classified WV SAR images can thus be used to support boundary layer studies over the world's ocean to advance our understanding of the km-scale MABL coherent roll structures on turbulent momentum fluxes.

Preliminary investigation focused on the global feature of MABL rolls. Statistics of the aspect ratio and the roll angle with respect to surface wind direction are in good alignment with reports from roll theoretical predictions and numerous field studies. More importantly, the latitudinal variations of roll occurrence atmospheric conditions and basic characteristics were evidenced, important findings to both roll-shaped boundary layer and related air-sea interaction studies. These suggest in-depth theoretical investigations of roll dynamics varying with latitudes. One starting point is to examine the horizontal Coriolis force effects on roll formation, which is often neglected in geophysical fluid problems. As such, roll-shaped boundary layer shall benefit and be extended to a broader range of applications across the global ocean.

Future work will also focus on the mapping of each classification category in time and space help to gain better understandings regarding air-sea interactions at scales of 5 m-10 km. Joint-analysis of MABL rolls with convective cells is interested to be performed. These two processes that are recognized as organized large eddies in the boundary layer can transition from one to another. Our experimental exploitation shows that the seasonal alternation between rolls and cells seems closely associated with the South Asia monsoon and Somalia ocean currents. The statistics of MABL rolls and cells should advance our knowledge of ABL dynamics, as well as the impacts of their presence on local and global climates. More broadly, the global C-band S-1 WV SAR data holds great potential to define the bottom properties of MABL without weather and sun light limitations. If linkages between SAR observed MABL imprints and atmospheric stratification can be quantified, it would be possible to retrieve the near-surface stratification parameter independently of individual sea surface temperature and near-surface air temperature measurements. The SAR-derived stratification should help constrain satellite-based surface flux estimates directly.

# Chapter 3 Publications

## 3.1 A labelled ocean SAR imagery dataset of ten geophysical phenomena from Sentinel-1 wave mode

Received: 28 September 2018 | Revised: 30 April 2109 | Accepted: 17 June 2019

DOI: 10.1002/gdj3.73

DATA PAPER

Geoscience Data Journal RMetS WILEY

# A labelled ocean SAR imagery dataset of ten geophysical phenomena from Sentinel-1 wave mode

**Chen Wang**[1,2] | **Alexis Mouche**[1] | **Pierre Tandeo**[2] | **Justin E. Stopa**[3] | **Nicolas Longépé**[4] | **Guillaume Erhard**[4] | **Ralph C. Foster**[5] | **Douglas Vandemark**[6] | **Bertrand Chapron**[1]

[1]Laboratoire d'Océanographie Physique et Spatiale (LOPS), IFREMER, University in Brest, CNRS, IRD, Brest, France

[2]Lab-STICC, IMT Atlantique, UBL, Brest, France

[3]Department of Ocean Resources and Engineering, University of Hawaii at Manoa, Honolulu, Hawaii, USA

[4]Space and Ground Segment, Collecte Localisation Satellites (CLS), Plouzané, France

[5]Applied Physics Laboratory, University of Washington, Seattle, Washington, USA

[6]Ocean Processes Analysis Laboratory, University of New Hampshire, Durham, New Hampshire, USA

**Correspondence**
Chen Wang, LOPS, IFREMER, Brest, France.
Email: chen.wang@ifremer.fr

**Funding information**
ESA Sentinel-1A Mission Performance Center, Grant/Award Number: 4000107360/12/I-LG; ESA S1-4SCI Ocean Study, Grant/Award Number: 4000115170/15/I-SBo; CNES TOSCA program; NASA Physical Oceanography, Grant/Award Number: NNX17AH17G; China Scholarship Council (CSC)

**Abstract**

The Sentinel-1 mission is part of the European Copernicus program aiming at providing observations for Land, Marine and Atmosphere Monitoring, Emergency Management, Security and Climate Change. It is a constellation of two (Sentinel-1 A and B) Synthetic Aperture Radar (SAR) satellites. The SAR wave mode (WV) routinely collects high-resolution SAR images of the ocean surface during day and night and through clouds. In this study, a subset of more than 37,000 SAR images is labelled corresponding to ten geophysical phenomena, including both oceanic and meteorologic features. These images cover the entire open ocean and are manually selected from Sentinel-1A WV acquisitions in 2016. For each image, only one prevalent geophysical phenomenon with its prescribed signature and texture is selected for labelling. The SAR images are processed into a quick-look image provided in the formats of PNG and GeoTIFF as well as the associated labels. They are convenient for both visual inspection and machine learning-based methods exploitation. The proposed dataset is the first one involving different oceanic or atmospheric phenomena over the open ocean. It seeks to foster the development of strategies or approaches for massive ocean SAR image analysis. A key objective was to allow exploiting the full potential of Sentinel-1 WV SAR acquisitions, which are about 60,000 images per satellite per month and freely available. Such a dataset may be of value to a wide range of users and communities in deep learning, remote sensing, oceanography and meteorology.

**Dataset**

Identifier: https://doi.org/10.17882/56796
Creator: Wang, C., Mouche, A., Tandeo, P., Stopa, J. E., Longépé, N., Erhard, G., Foster, R., Vandemark, D. and Chapron, B.
Title: Labelled SAR imagery dataset of ten geophysical phenomena from Sentinel-1 wave mode (TenGeoP-SARwv)
Publisher: Sea scientific open data publication (SEANOE)
Publication year: 2018
Resource type: Dataset
Version: 1.0

**KEYWORDS**
manual labelling, ocean surface phenomena, Sentinel-1 wave mode, Synthetic aperture radar

## 1 | INTRODUCTION

The world's ocean covers more than 70% of the Earth's surface, playing a crucial role in influencing the climate system. Comprehensive measurements and observations of ocean surface are essential to better understand air–sea interactions as well as to develop high-resolution climate models (Topouzelis and Kitsiou, 2015; Schneider *et al.*, 2017). Among the various space-borne sensors, Synthetic Aperture Radars (SAR) met both high-resolution and all weather day-and-night imaging criteria. SAR backscattering is very sensitive to the sea surface roughness composed of centimetre-scale waves. When air–sea interactions are strong enough to modulate these short waves, SAR can capture signatures of geophysical processes such as ocean waves (Ardhuin *et al.*, 2009; Collard *et al.*, 2009), atmospheric processes (Atkinson and Wu Zhang, 1996; Young *et al.*, 2005; Alpers *et al.*, 2016) and oceanic processes (Espedal *et al.*, 1996; Jia *et al.*, 2018). Therefore, SAR is a unique tool for extensive observation of ocean–atmosphere interactions at sub-km scales (Brown, 2000; Jackson and Apel, 2004).

SAR sensors have a variety of acquisition modes. A common one is wide-swath which provides data over several hundred kilometres. More specifically for Sentinel-1, wide-swath acquisitions in TOPS mode (De Zan and Monti Guarnieri, 2006) (Extended wide swath EW and Interferometric wide swath IW) are mainly used for monitoring of sea ice areas and coastal regions over the ocean. Due to power and data constraints of contemporary systems, the wide-swath mode with high-resolution capability is not able to collect data continuously and globally. The 'WaVe mode' (WV or WM), by contrast, is dedicated to measuring ocean waves from the global open ocean. This mode was firstly introduced on Earth observation mission by the European Space Agency (ESA) for the European Remote Sensing (ERS-1/2) missions (1991–2003) (Kerbaol *et al.*, 1998). Since then, acquisitions in WV have been pursued on Envisat advanced SAR (ASAR) mission (2002–2012) (Stopa *et al.*, 2016) and now Sentinel-1 (Torres *et al.*, 2012), providing more than 25 years of high-resolution observations of the world's ocean. The recent launches of Sentinel-1 (S-1) A and B in April 2014 and 2016 for the European Copernicus Program enable routine SAR WV acquisitions to be available. These two sensors collect nearly 120,000 WV vignettes with ocean surface imprints of 20 × 20 km in each month. Their spatial resolution is about 5 m. The primary intent of the small-sized vignettes is to provide ocean swell directional spectra as an ESA Level-2 ocean product (Torres *et al.*, 2012). However, they also capture a much wider range of geophysical processes that are of significant interest in ocean–atmosphere interactions. Global coverage is combined with high resolution and routine acquisitions in all weather conditions during day and night; and at such high resolution (5 m) make S-1 WV a presence and unique data source for new geophysical applications.

In this study, we define ten categories of different oceanic or atmospheric phenomena. These are the most common phenomena that can be observed in S-1 WV vignettes. The categories are pure ocean waves (POW), wind streaks (WS), micro convective cells (MCC), rain cells (RC), biological slicks (BS), sea ice (SI), icebergs (IB), low wind areas (LWA), atmospheric fronts (AF) and oceanic fronts (OF). Details on these definitions are introduced in Section 2. A labelled SAR WV dataset containing 37,553 images is then established. Within each image, only the prevalent geophysical phenomenon with clear signature and/or pattern is presented. The images are derived from the Single Look Complex (SLC) product of S-1 WV (Torres *et al.*, 2012), and provided in formats of Portable Network Graphics (PNG) and Georeferenced Tagged Image File Format (GeoTIFF). The proposed dataset, called TenGeoP-SARwv for 'Ten Geophysical Phenomena from SAR wave mode', is provided by IFREMER and publicly available at sea scientific open data publication (SEANOE): http://www.seanoe.org/data/00456/56796/. The methodology used to create the dataset is described in section 3. Such a labelled dataset could benefit the strategic development of massive ocean SAR data analysis. Deep learning signal processing algorithms that are now a common form of supervised learning may be exploited (LeCun *et al.*, 2015; Cheng *et al.*, 2017). In addition, this unique dataset is also significant to the communities of remote sensing, oceanography and meteorology. Discussion and perspectives regarding to potential applications and dataset refinement are given in section 4.

## 2 | GEOPHYSICAL PHENOMENA BY SENTINEL-1 WAVE MODE

The ESA S-1 mission is a constellation of two polar orbiting, sun-synchronous satellites (S-1 A and S-1 B) launched in April 2014 and 2016 respectively (Torres *et al.*, 2012). These two satellites both have a 12-day repeat cycle at the equator, and are phased at 180° to provide an effective 6-day repeat cycle. For each satellite, the expected life time is 7 years. Both carry a C-band SAR instrument with centre frequency of 5.405 GHz (5.5 cm wavelength). There are four exclusive imaging modes (Interferometric Wide swath, Extra Wide swath mode, Strip Map and Wave Mode[1]) for the S-1 SAR sensors. WV is the default operational mode over open ocean unless wide-swath SAR images are requested for particular applications. Note that, at present, there is no WV acquisition in the Arctic Ocean and closed seas such as Red, Black, Mediterranean and Caribbean seas. And in this study, we only use WV data acquired by Sentinel-1A in 2016. However, extensive validations have confirmed that SAR images acquired by S-1B are characteristic essentially equivalent to that from S-1A.

## 2.1 | Acquisitions

The vignettes of S-1 WV are collected in 20 × 20 km scenes at two alternate incidence angles of 23.8° (WV1) and 36.8° (WV2). They are acquired over the global open ocean with an along-track sampling separation of 100 km and an across-track distribution of roughly 200 km. Pixels within each vignette have 5 m ground resolution and can be obtained in VV (default) or HH polarization. For the polarization configurations, the first letter stands for the polarization of the emitting transmitter (as SAR is an active radar), whereas the second one is for the receiver polarization configuration. This study only relies on vignettes acquired in VV polarization as they account for more than 99% of all S-1 WV acquisitions. The S-1 WV backscatter consists of intensity and phase history and can be potentially processed into the SLC products for wave applications (Torres *et al.*, 2012). Using the digital number (DN) of these complex products and Look-Up-Table (*sigmaNaught*) annotated in the product, we compute the normalized radar cross section $\sigma_0$. This is the common radar parameter used to describe radar return backscattered by the ocean surface to the SAR sensors.

$$\sigma_0 = \frac{|\mathrm{DN}|^2}{sigmaNaught^2}. \tag{1}$$

## 2.2 | Ten geophysical phenomena

In this subsection, the ten defined oceanic or atmospheric phenomena are presented. Due to the 20-km WV image size, scales of observed geophysical phenomena are limited to about between 0.1 and 5 km. We focus on the prescribed ten geophysical phenomena because they are commonly observed by the S-1 WV SAR vignettes. It is worth noting that the WV can also capture signatures of other geophysical phenomena like internal waves (Jia *et al.*, 2018) and atmospheric gravity waves (Li *et al.*, 2013), and signatures of ships or platforms. While such phenomenaS are seldom seen in the open ocean, we may include those categories in this dataset in the near future.

### 2.2.1 | Pure ocean waves (POW)

Ocean waves including ocean swell and wind waves are the most prevalent feature in all SAR images (Fu and Holt, 1982; Jackson and Apel, 2004). Signatures of ocean waves often coexist with other oceanic and/or atmospheric phenomena. The short wind waves (centimetre to metre scale) are produced by local surface winds while ocean swell are longer (hundreds of metres) surface waves that are generated by distant weather systems such as storms or cyclones. These mechanical waves are propagating without any wind forcing after the wind blows for a period of time over a fetch of water (Ardhuin *et al.*, 2009). Ocean waves can be observed in all ocean basins, and their measurement with SAR relies on the theories of microwave scattering from rough sea surface (Hasselmann *et al.*, 1985; Collard *et al.*, 2009; Stopa *et al.*, 2016). SAR imaging of swell waves is typically influenced and distorted by different geophysical phenomena. This makes wave interpretation of SAR imagery difficult. Our definition of pure ocean waves (POW) is a SAR vignette that contains boundless ripples throughout the image, as displayed in Figure 1a. The following criteria are adopted for this category:

1. Periodic signatures of ocean waves dominate the whole image
2. Wavelengths are between 0.1 and 0.8 km
3. Intensity modulation within the scene is homogeneous
4. There is no other competing geophysical feature or pattern

### 2.2.2 | Wind streaks (WS)

Wind streaks are known to be the sea surface imprint of atmospheric boundary layer (ABL) rolls (Vandemark *et al.*, 2001). They usually occur in near-neutral to moderately unstable stratification conditions and span the whole depth of ABL. The approximately wind aligned wind streaks are the result of an embedded overturning coherent secondary circulation in the boundary layer that is induced by the vertical shear of the mean horizontal wind that can be further modified by the mean vertical stratification profile (Brown, 1980; Etling and Brown, 1993; Young *et al.*, 2002). The enhanced upward and downward wind perturbations near the surface between roll circulations are usually strong enough to modulate centimetre-scale waves and therefore induce organized imprints on the sea surface roughness. Consequently, wind streaks are frequently observed by SAR images as periodic, quasi two-dimensional and roll-shaped patterns (Alpers and Brümmer, 1994; Young *et al.*, 2002), as displayed in Figure 1b. It shows that the periodic pattern of wind streaks is superimposed at top signatures of ocean waves. In addition, some vignettes of wind streaks contain cell-shaped patterns (Micro

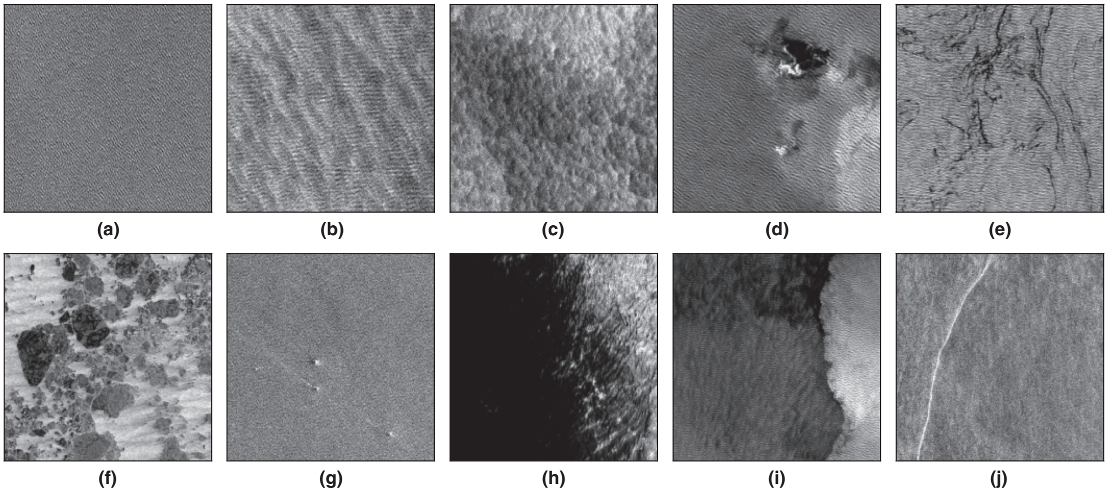

**FIGURE 1** From (a) to (g) are image examples of pure ocean waves, wind streaks, micro convective cells, rain cells, biological slicks, sea ice, icebergs, low wind area, atmospheric front and oceanic front

convective cells). This indicates the transition between two different regimes in the marine ABL (Atkinson and Wu Zhang, 1996; Jackson *et al.*, 2004). This transient stage can sometimes be tricky to decipher between the two classes. The criteria of wind streaks (WS) are:

1. Periodic linear features dominate the whole image
2. Wavelengths are between 0.8 and 5 km
3. Intensity modulation within the scene is homogeneous
4. Periodic signatures of ocean waves can coexist

### 2.2.3 | Micro convective cells (MCC)

Atmospheric convective cells are coherent structures of updrafts and downdrafts in the ABL (Khalsa and Greenhut, 1985; Atkinson and Wu Zhang, 1996). The local temperature difference between air and sea produces strong vertical exchange of heat. It creates cell-shaped rising/descending air, which leads to horizontal variability of sea surface wind speed. This wind variability modulates the centimetre-scale waves and thus the sea surface roughness. Therefore, coherent, periodic and cell-shaped patterns are normally visible on SAR images (Babin *et al.*, 2003). Note that the scale (radius) of atmospheric convective cells captured within these 20-by-20 km WV vignettes is about 1 km. It indicates that the cells here are mainly associated with shallow dry convection, where latent heat from condensation plays no role in the dynamics (Atkinson and Wu Zhang, 1996). This results in a category that we define as micro convective cells (MCC). However, roll-shaped pattern caused by wind streaks are also often visible in such vignettes. The key to distinguish between WS and MCC categories is based on which pattern dominates the image. An example of MCC vignette is displayed in Figure 1c. The criteria of this category are:

1. Coherent, periodic and cell-shaped features dominate the whole image
2. Scales are about 1 km
3. Intensity modulation within the scene is homogeneous
4. Periodic signatures of ocean waves can coexist, but they can be strongly distorted

### 2.2.4 | Rain cells (RC)

Rain can occur in many forms, such as downdraft, stratified rain, rain bands, squall lines and so on. Although the scattering mechanisms of C-band SAR for rain signatures are not fully understood, they can be generally characterized by high and low contrasts in backscatter (Alpers *et al.*, 2016). Here we only focus on the rain cells that are typically associated with downdraft patterns. Their signatures can be clearly captured by WV SAR vignettes. Our definition of rain cells (RC) largely concentrate on the vignettes containing circular- or semi-circular–shaped areas. This is typical signatures of wind gust fronts caused by the downdraft. Besides, bright and/or dark patches usually appear inside the circular areas. Dark patches are usually explained by signal attenuation due to rain droplets in the atmosphere. Bright areas are generally associated with splash due to the heavy rain impacts sea surface roughness. An example is given in Figure 1d. Note that the circular shape of RC is expected to be larger than that of MCC and may be sometimes larger than the vignette size. Our criteria for this category are:

1. Circular- or semi-circular–shaped areas are visible on SAR image
2. There are bright and/or dark patches inside the circular areas
3. Intensity modulation within the scene is heterogeneous
4. Periodic signatures of ocean waves can coexist with RC

### 2.2.5 | Biological slicks (BS)

Biological slicks (BS) in the ocean are natural films that accumulate at the water–air boundary (Jackson *et al.*, 2004). These surface slicks are typically only one molecular layer thick (approximately 3 nm) and consist of sufficiently hydrophobic substances. This thin film influences air–sea fluxes of momentum, heat and gas (Espedal *et al.*, 1996). Under low wind speeds, sea surface capillary and short gravity waves can be damped by the natural films. Thus, their signatures are usually visible as dark filaments on SAR images. The slicks captured by S-1 WV are generally randomly distributed over sea surface, see Figure 1e. Due to the coverage limitation of WV vignettes, the scale of slicks is hard to be quantified. However in some cases, they can be tracers of the ocean circulation such as surface currents, ocean fronts and eddies (Johannessen *et al.*, 1996). The following criteria are used to define this category:

1. Dark filaments are visible on SAR image
2. Intensity modulation within the scene is heterogeneous
3. Periodic signatures of ocean waves can coexist with BS, but they can be distorted

### 2.2.6 | Sea ice (SI)

Sea ice is defined as frozen ocean water which could be growing or melting. It is typically sorted according to whether or not it is attached to the shoreline, or described based on its development stages, such as new ice, nilas, young ice, first-year and old (Jackson *et al.*, 2004). SAR backscattering of sea ice essentially depends on the ice type, and therefore can be quite diverse due to the wide range of ice types. The textures of sea ice on SAR images are fairly complex. They can be roughly characterized by web shapes, three-dimensional structure, wiggly fractures, and high contrast (dark and bright patches) (Soh and Tsatsoulis, 1999). Our aim here was not to identify different sea ice types, but rather distinguish sea ice from open ocean water. Therefore, this category contains SAR vignettes of all ice types in the Southern Ocean near Antarctica. One sea ice example is shown in Figure 1f. The criteria of this category are:

1. Textural contexts are complex, which can be web-shaped, wiggly fractures, pebble-like, fractal and so on
2. Patches with sharp boundaries are usually visible on SAR image
3. There are strong intensity contrasts between different patches
4. Periodic signatures of ocean waves can coexist, but they can be severely distorted
5. Vignettes are mainly collected from the Southern Ocean near Antarctica

### 2.2.7 | Iceberg (IB)

Icebergs are large pieces of frozen freshwater that have broken off a glacier or an ice shelf and are floating freely in open water or sea ice area. They are categorized according to the size including growler (0–5 m), bergy bit (5–15 m), small berg (15–60 m), medium berg (60–120 m), large berg (120–220 m) and very large berg (>220 m), and/or with respect to their shape such as tabular, non-tabular, blocky, wedge, dry dock and pinnacle (Jackson *et al.*, 2004). In SAR images, icebergs appear as a cluster of pixels that have the uniformly high/low backscatter signals compared to the surroundings (sea water and sea ice). In our definition, the iceberg vignette contains one or several icebergs that are visible as bright targets. Possibly, there is a relatively dark shadow associated with the small bright cluster. This category focuses on the icebergs in the open sea water, as displayed in Figure 1g. Thus, the criteria of this category are:

1. Bright or Dark targets associated with dark shadows are visible on SAR image
2. Intensity modulation of the surroundings is homogeneous
3. Periodic signatures of ocean waves can coexist with IB
4. They are mainly distributed in the Southern Ocean near Antarctica

### 2.2.8 | Low wind areas (LWA)

When the local surface winds are too weak, sea state normally remains stationary for hours. Generally, there is no signature of ocean swell propagation and the small cm-scale roughness is absent too. Consequently, SAR backscatter from such sea surface is weak, resulting in dark areas on SAR images (Topouzelis and Kitsiou, 2015). Note that low wind condition is also necessary for the presence of biological slicks on SAR image. Thus, signatures of BS may exist at the boundaries of dark areas. In addition, LWA can also occur in areas where wind speed and/or direction suddenly change. Appearance of such LWA typically has a very large dark area accompanying by an atmospheric front. To distinguish from the definition of atmospheric front, the LWA category focuses on the vignettes that are dominated by a unique dark patch. An example is shown in Figure 1h. The criteria of LWA are:

1. A unique dark patch dominates the SAR image
2. Intensity modulation within the scene is heterogeneous
3. Periodic signatures of ocean waves are absent

### 2.2.9 | Atmospheric front (AF)

sAtmospheric fronts are associated with air mass boundaries and thus strong near-surface horizontal gradients of wind, temperature and/or humidity (Johannessen *et al.*, 1996). Unstable atmosphere conditions generally lead to occurrence of rain and low and high wind areas along the fronts. Therefore, signatures of atmospheric fronts observed by SAR are largely complex and have been called different names, including lobe, cleft, vortex, front and secluded front, based on their pattern (Young *et al.*, 2005). Figure 1i presents a vignette example of a typical atmospheric front observed by S-1 WV. This category is defined by the following criteria:

1. The edge of the front is typically not sharp, but rather a bit mottled or occluded
2. Besides the front, there are obvious intensity gradients
3. Intensity modulation of the surroundings is homogeneous
4. Periodic signatures of ocean waves can coexist with AF

### 2.2.10 | Oceanic front (OF)

Oceanic fronts are the boundaries between two distinct water masses that can be caused by a difference in oceanic temperature, salinity and/or density. The water masses near an oceanic front usually move in different directions, leading to downwelling or upwelling along the front and hence create a sea surface roughness anomaly (Rascle *et al.*, 2017). Enhanced or reduced sea surface roughness anomalies are visible as the bright or dark lines in SAR vignettes, as displayed in Figure 1g. Beside such lines, there are no obvious intensity gradients on the SAR image. This is the main distinction between OF and AF. The criteria of this category are:

1. A thin bright or dark mono-filament like linear feature is visible on SAR image
2. There is no obvious intensity gradient across the linear feature
3. Intensity modulation of the surroundings is homogeneous
4. Periodic signatures of ocean waves can coexist with OF

## 3 | DATASET CREATION

### 3.1 | SAR image processing

The 20 × 20 km image with 5 m resolution provides an image with more than 4,000 pixels in range and azimuth directions. This full-scale WV intensity image is not necessary for visual interpretation of oceanic or atmospheric phenomena. For instance, an example of a full resolution $\sigma_0$ image with features of wind streaks is shown in Figure 2a. It is clear that the wind streaks are concealed due to the low intensity contrast. In addition, the subplot of $\sigma_0$ mean values along range is displayed in Figure 2a*. It indicates that values of $\sigma_0$ slightly vary with different incidence angles within images. Therefore, three processing steps are applied to $\sigma_0$ images to enhance broad-scale features of oceanic and atmospheric phenomena.

### 3.1.1 | Re-calibration of $\sigma_0$

The $\sigma_0$ as measured by SAR over the ocean is highly dependent on the local ocean surface wind and viewing angles of the radar (incidence and azimuth angles). For a given wind speed, the overall $\sigma_0$ decreases along the range direction, as displayed in the inset plot of Figure 2a*. This decreasing trend in range is mainly associated with the increasing incidence angle, which is common to all C-band VV SAR imagery. The empirical geophysical model function, such as CMOD5.N for VV C-band SAR (Hersbach, 2010), models the $\sigma_0$ dependence on wind vector and radar incidence angle. To reduce the incidence angle effect, we use CMOD5.N to construct a reference factor by assuming a constant wind of 10 m/s at 45° relative to the antenna look angle. The $\sigma_0$ of each vignette can then be re-calibrated by dividing the reference factor. Note that the $\sigma_0$ values are in linear scale. Such re-calibrated $\sigma_0$ is referred as sea surface roughness (ssr) and is shown in Figure 2b. Specifically the ssr can be written:

$$\mathrm{ssr} = \frac{\sigma_0}{\mathrm{CMOD5.N(10,45,inc)}} \qquad (2)$$

where inc is the radar incidence angle for each pixel. The difference of intensity in ssr image between near (left) and far (right) field is significantly reduced (Figure 2b*.

### 3.1.2 | Downsampling

The fine-resolution SAR vignettes are not favourable for visual interpretation of larger scale geophysical features, especially since our category definitions focus on phenomena with scale of tens to thousands of metres. The expected length scales of larger phenomena corresponding to the category definition are from 100 m to 5 km. Therefore to better highlight the larger features, a moving averaging window of 10-by-10 pixels is applied to the ssr images. This averaging also reduces the speckle noise of SAR vignettes (Lee *et al.*, 1994). The ssr intensity images (Figure 2b) are then downsampled by 1/10 yielding a resolution of 50 m, as shown in Figure 2c. As shown, the pattern of wind streaks overlapping on ocean swell is appreciably highlighted. It is worth noticing that the spatial filtering applied in this study

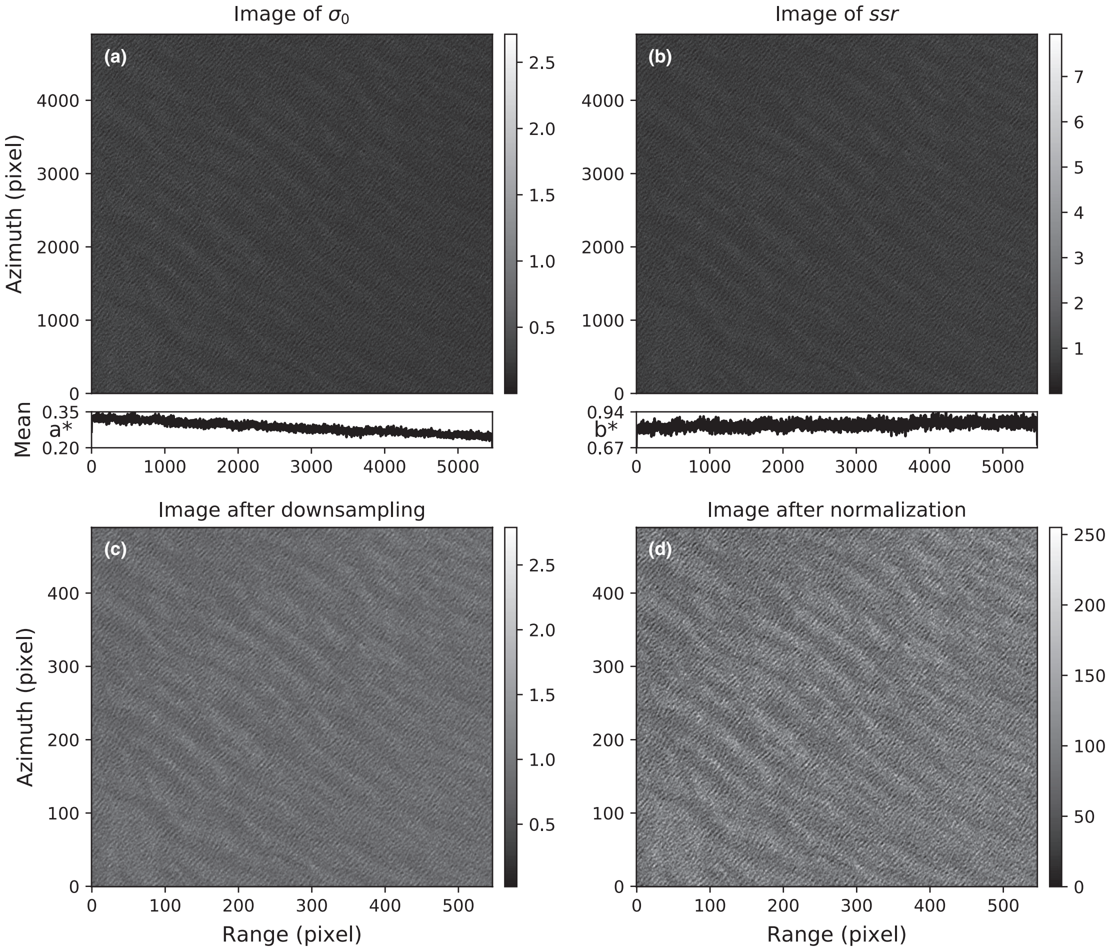

**FIGURE 2** SAR image processing of the case with wind streaks. (a) $\sigma_0$ image (b) image of sea surface roughness derived from $\sigma_0$ (c) intensity image down sampled from roughness (d) intensity image with enhanced contrast. Subplots of * in (a) and (b) are profiles of $\sigma_0$ and roughness images along the range direction

achieves similar results as for the classical SAR multi-look technique. But the later performs the filtering in the image spectral domain, which is relatively time-consuming.

### 3.1.3 | Normalization

1. **For human visual inspection** To enhance intensity contrast of the downsampled images, a statistical method of percentile is used to normalize each vignette. By sorting intensity values of an image, the proportion of principal data that falls between two given percentiles can be estimated (Natrella, 2013). For each image, this method split the ordered intensity values into hundredths, and pixel values between the 1st (minimum) and 99th (maximum) are normalized into a 8 bits grey scale ([0, 255]). With this processing, potential remaining anomaly (speckle noise) in the ssr values are effectively filtered. In Figure 2d, the image of wind streaks in grey scale after normalization is presented. It shows that the normalized image with enhanced contrast is better suited for visual interpretation of our identified oceanic and atmospheric phenomena.
2. **For machine learning-based exploitation** For the sake of machine learning approaches, another normalization process is also implemented. As opposed to the dataset used for human visualization where the retained minimum and maximum values are specific for each image, fixed values of 0 and 3 common to the entire database are applied to all downsampled ssr images. In between these two values, the quantization process is instead performed on 16 bits ([0, 65,535]) ensuring all texture and radiometric information are numerically maintained.

### 3.2 | TenGeoP-SARwv dataset

The TenGeoP-SARwv dataset is established based on the acquisitions of S-1A WV in VV polarization. This dataset consists of 37,553 SAR vignettes divided into our ten geophysical categories. For each category, the selection of SAR images covers the full year of 2016, and is manually labelled through visual inspection following the criteria documented in Section 2.2. Two screening standards are adopted. One is that only one individual geophysical phenomenon dominates across the whole vignette. The other one is that pattern structure of this phenomenon is clearly visible by human eye. Table 1 presents the counts of each category for each month. We attended to have 400 images labelled for each class in each month. However, we could not reach this number for the OF category. Moreover, only a few IB images were found in May to October due to the iceberg seasonality.

### 3.3 | Data format

The image patches are provided in formats of Portable Network Graphics (PNG) and Georeferenced Tagged Image File Format (GeoTIFF). PNG files are processed with floating normalization for better visualization of human eyes. While in GeoTIFF files, high precision values (16 bits) as well as the geographical information are kept for exploitation of machine learning-based approaches and geophysical application. In addition, text files containing description of categories and information for the file name, labelling, swath, capture time, and centre latitude and longitude of each image are also provided. These SLC products of S-1 WV are freely available at 'Sentinel open access hub' of ESA https://sentinel.esa.int/web/sentinel/sentinel-data-access. Notice that the GeoTIFF of TenGeoP-SARwv dataset is completely different from that of ESA SLC product. The latter contains original data and much more image processing information than this labelled dataset.

## 4 | DISCUSSION AND PERSPECTIVES

SAR images capture signatures of various geophysical phenomena that are associated with air–sea interactions. Most of them have been previously discussed to provide a comprehensive understanding of their imprints on SAR imagery (Alpers and Brümmer, 1994; Young *et al.*, 2005; Li *et al.*, 2013; Alpers *et al.*, 2016). Several of these phenomena factor significantly in the vertical transport of heat, moisture and momentum, and play key roles in the climate system (Khalsa and Greenhut, 1985; Ufermann and Romeiser, 1999; Vandemark *et al.*, 2001; Schneider *et al.*, 2017). Although understood, these manifestations of key geophysical phenomena are not systematically analysed or ingested in numerical models. In particular, automated detection and classification of these phenomena from the numerous SAR images is still challenging. The proposed SAR imagery dataset with individual annotations of oceanic or atmospheric phenomena should allow new efforts to test, validate and benchmark different methods for the identification of key geophysical processes. The annotations will allow massive classification of the data and open new perspectives for global or seasonal analysis of these phenomena. This work is a step towards broadening the scientific value of 25 years WV data acquired by ERS-1/2, Envisat ASAR and Sentinel-1 (Kerbaol *et al.*, 1998; Torres *et al.*, 2012; Stopa *et al.*, 2016). In addition, this labelled dataset can be directly used to statistically investigate the geophysical properties of the ten defined phenomena and characteristics of the imaged features. Therefore, such a dataset of labelled ocean SAR imagery is put forward for both scientific and engineering applications for different communities such as deep learning, remote sensing, oceanography and meteorology.

**TABLE 1** SAR image numbers of the labelled dataset for each class in every month of 2016

| | Jan | Feb | Mar | Apr | May | Jun | Jul | Aug | Sep | Oct | Nov | Dec | Total |
|---|---|---|---|---|---|---|---|---|---|---|---|---|---|
| POW | 406 | 407 | 408 | 409 | 406 | 408 | 410 | 409 | 409 | 409 | 408 | 411 | 4,900 |
| WS | 406 | 409 | 403 | 407 | 404 | 391 | 396 | 398 | 397 | 398 | 384 | 404 | 4,797 |
| MCC | 396 | 384 | 370 | 384 | 385 | 365 | 386 | 388 | 380 | 391 | 384 | 385 | 4,598 |
| RC | 398 | 399 | 398 | 395 | 398 | 391 | 395 | 393 | 393 | 396 | 394 | 390 | 4,740 |
| BS | 398 | 394 | 395 | 398 | 397 | 339 | 397 | 398 | 397 | 400 | 398 | 398 | 4,709 |
| SI | 387 | 150 | 282 | 396 | 396 | 392 | 393 | 393 | 396 | 396 | 396 | 393 | 4,370 |
| IB | 399 | 417 | 308 | 146 | 58 | 29 | 10 | 14 | 12 | 29 | 159 | 399 | 1,980 |
| LWA | 137 | 137 | 138 | 220 | 201 | 95 | 214 | 144 | 207 | 207 | 241 | 219 | 2,160 |
| AF | 360 | 282 | 301 | 348 | 363 | 234 | 361 | 377 | 378 | 367 | 364 | 365 | 4,100 |
| OF | 61 | 85 | 64 | 102 | 131 | 60 | 116 | 135 | 96 | 108 | 132 | 109 | 1,199 |
| Total | 3,348 | 3,064 | 3,067 | 3,205 | 3,139 | 2,704 | 3,078 | 3,049 | 3,065 | 3,101 | 3,260 | 3,473 | 37,553 |

### 4.1 | SAR image classification with deep learning

In recent years, state-of-the-art deep learning based techniques, for example Convolutional Neural Network (CNN), have been developed rapidly for image processing applications (LeCun *et al.*, 2015). CNN model is a deep multilayer architecture that can be trained to automatically extract the optimal image feature representations and amplify the discrimination between different classes (LeCun *et al.*, 2015). This new approach has been widely introduced to remote sensing (Zhang *et al.*, 2016; Chen *et al.*, 2016; Cheng *et al.*, 2017). However, a lack of high-quality labelled datasets limits further application and development of CNN models for ocean SAR images. The proposed TenGeoP-SARwv dataset could be used as a training dataset for the identification and classification of different key geophysical phenomena occurring over open ocean. It can be used to directly fine-tune existing CNN models for straightforward geophysical applications, or explore new CNN architectures to improve feature representations. In fact, one relevant work has been conducted and the preliminary result was presented at the International Geoscience and Remote Sensing Symposium (IGARSS) in 2018. We believe that the large number of images in each of these ten classes satisfy the requirement to train a deep CNN model. Moreover, unsupervised learning algorithms by combining deep learning and reinforcement learning will become far more important (LeCun *et al.*, 2015) and can also benefit from this dataset. However, there is still room in the proposed dataset for improvement. In the near future, more geophysical categories corresponding to other oceanic or atmospheric phenomena should be included. In addition, some of the vignettes contain multiple geophysical phenomena within the same scene even they are small-sized SAR images. Multi-labelling of those images is more of interest and important to the deep learning community for methodologies exploitation.

### 4.2 | Ocean SAR remote sensing

Space-borne SAR provides a unique means to observe the ocean surface. Despite the multi-scale nature of ocean surface waves, C-band SAR mainly responds to cm-scale sea surface roughness through Bragg resonant scattering (Alpers and Brümmer, 1994; Jackson *et al.*, 2004; Li *et al.*, 2013). While radar signal depends on radar properties (wavelength, polarization, and incidence and azimuth angles), ocean SAR imagery can be generally interpreted as variability in sea surface roughness. Different oceanic or atmospheric phenomena are frequently captured by SAR images owing to their modulations on near-surface wind stress as well as on cm-scale ocean waves (Vandemark *et al.*, 2001; Alpers *et al.*, 2016). How strong the modulations should be to make these phenomena visible on SAR images is still an open question from a statistical point of view. With the TenGeoP-SARwv dataset, one can potentially investigate the environmental conditions under which these phenomena occur. This would help to better understand their impact on sea surface roughness and therefore how they are imaged by SAR. In addition to that, ocean swell is of first interest as they are a fundamental phenomenon over the open ocean. The swell spectra inversion from SAR measurements are still distorted by the presence of various oceanic or atmospheric phenomena. The dataset of TenGeoP-SARwv can help us quantify the impact of these phenomena on SAR forward mapping from ocean wave spectrum to SAR image spectra. Therefore, it may be possible to recover more ocean swell estimation by taking their impact into account. This will benefit the study of global and local wave climate. Given the relatively small size of the WV vignette (20 km), the imaged area can be roughly assumed as homogeneous and often-time, only one phenomenon dominates. However, it should also be mentioned that the small and sparse vignette coverage restricts imaging of large-scale phenomena, such as upwelling, internal waves, hurricanes, among others.

### 4.3 | Geophysical investigation

SAR imagery yields high-resolution imprints of ocean surface and provides significant geophysical parameters for global weather and climate analysis, demonstrating its indispensable contributions to the Earth monitoring system (Brown, 2000). Investigation of key geophysical phenomena by utilizing SAR data, for example wind streaks and micro convective cells, has been performed for many years, mostly in the stage of case and field studies (Alpers and Brümmer, 1994; Vandemark *et al.*, 2001; Levy, 2001; Babin *et al.*, 2003; Li *et al.*, 2013). Statistical analysis of key geophysical phenomenon based on SAR data are barely attempted due to lack of reliable dataset. This proposed TenGeoP-SARwv dataset opens perspective to use S-1 WV acquisitions for global geophysical phenomena analysis. Combined with other environmental parameters, these labelled SAR vignettes can be used directly to address geophysical characteristics of the ten defined specific phenomena. The occurrence and atmospheric conditions of one specific phenomenon can be of particular interest (Levy, 2001). Furthermore, classification of the whole acquisitions of S-1 WV vignette based on the automated methodologies inspires us to map the monthly variations and seasonal changes of these geophysical phenomena in the context of climate modelling. However, the small footprint of S-1 WV limits the observation of larger scale geophysical phenomena. Some of the vignettes only capture part of the phenomena signatures, for instance, a corner of large-sized rain cell and a portion of atmospheric front or oceanic front.

## ACKNOWLEDGEMENTS

The authors would like to thank the anonymous reviewers for their helpful comments and suggestions regarding this manuscript. This image dataset is created thanks to Sentinel-1A data access via ESA and through Sentinel-1A Mission Performance Center (Contract No. 4000107360/12/I-LG). Copernicus data (2016) are used. A. Mouche, B. Chapron, N. LongÉpÉ and C. Wang were supported by S1-4SCI Ocean Study (Contract No. 4000115170/15/I-SBo) and CNES (TOSCA program, COWS project). R. Foster and D. Vandemark were supported by NASA Physical Oceanography grant NNX17AH17G. C. Wang also would like to acknowledge the financial support of China Scholarship Council (CSC) for his PhD study.

## OPEN PRACTICES

This article has earned an Open Data badge for making publicly available the digitally-shareable data necessary to reproduce the reported results. The data is available at https://doi.org/10.17882/ 56796 Learn more about the Open Practices badges from the Center for Open Science: https://osf.io/tvyxz/wiki.

## ORCID

*Chen Wang* https://orcid.org/0000-0002-0575-742X

## REFERENCES

Alpers, W., Zhang, B., Mouche, A., Zeng, K. and Chan, P.W. (2016) Rain footprints on C-band synthetic aperture radar images of the ocean - Revisited. *Remote Sensing of Environment*, 187, 169–185. ISSN 00344257. Available at: https://doi.org/10.1016/j.rse.2016.10.015.

Alpers, W. and Brümmer, B. (1994) Atmospheric boundary layer rolls observed by the synthetic aperture radar aboard the ers-1 satellite. *Journal of Geophysical Research: Oceans*, 99(C6), 12613–12621. ISSN 2156–2202. Available at: https://doi.org/10.1029/94JC00421.

Ardhuin, F., Chapron, B. and Collard, F. (2009) Observation of swell dissipation across oceans. *Geophysical Research Letters* ISSN: 00948276. Available at: https://doi.org/10.1029/2008GL037030.

Atkinson, B.W. and Wu Zhang, J. (1996) Mesoscale shallow convection in the atmosphere. *Reviews of Geophysics*, 34(4), 403. ISSN 8755–1209. Available at: https://doi.org/10.1029/96RG02623.

Babin, S.M., Sikora, T.D. and Winstead, N.S. (2003) A case study of satellite synthetic aperture radar signatures of spatially evolving atmospheric convection over the Western Atlantic Ocean. *Boundary-Layer Meteorology*, 106, 527–546. Available at: https://doi.org/10.1023/A:1021236600569.

Brown, R.A. (1980) Longitudinal instabilities and secondary flows in the planetary boundary layer: a review. *Reviews of Geophysics*, 18(3): 683–697. ISSN 19449208. Available at: https://doi.org/10.1029/RG018i003p00683.

Brown, R.A. (2000) Serendipity in the use of satellite scatterometer, SAR, and other sensor data. *Johns Hopkins APL Technical Digest (Applied Physics Laboratory)*, 21(1), 21–26. ISSN 02705214.

Chen, S., Wang, H., Xu, F. and Jin, Y.Q. (2016) Target classification using the deep convolutional networks for SAR images. *IEEE Transactions on Geoscience and Remote Sensing*, 54(8), 4806–4817. ISSN 0196–2892. Available at: https://doi.org/10.1109/TGRS.2016.2551720.

Cheng, G., Han, J. and Lu, X. (2017) Remote sensing image scene classification: benchmark and state of the art. *Proceedings of the IEEE*, 105(10), 1865–1883. ISSN 00189219. Available at: https://doi.org/10.1109/JPROC.2017.2675998.

Collard, F., Ardhuin, F. and Chapron, B. (2009) Monitoring and analysis of ocean swell fields from space: New methods for routine observations. *Journal of Geophysical Research: Oceans*. ISSN 21699291. Available at: https://doi.org/10.1029/2008JC005215.

Espedal, H.A., Johannessen, O.M. and Knulst, J. (1996) Satellite detection of natural films on the ocean surface. *Geophysical Research Letters*, 23(22), 3151–3154. ISSN 00948276. Available at: https://doi.org/10.1029/96GL03009.

Etling, D. and Brown, R.A. (1993) Roll vortices in the planetary boundary layer: a review. *Boundary-Layer Meteorology*, 65(3), 215–248. ISSN 1573–1472. Available at: https://doi.org/10.1007/BF00705527.

Hasselmann, K., Raney, R.K., Plant, W.J., Alpers, W., Shuchman, R.A., Lyzenga, D.R *et al*. (1985) Theory of synthetic aperture radar ocean imaging: a MARSEN view. *Journal of Geophysical Research: Oceans*, 90(C3), 4659–4686. ISSN 2156–2202. Available at: https://doi.org/10.1029/JC090iC03p04659.

Hersbach, H. (2010) Comparison of C-Band scatterometer CMOD5.N equivalent neutral winds with ECMWF. *Journal of Atmospheric and Oceanic Technology*, 27(4), 721–736. ISSN 07390572. Available at: https://doi.org/10.1175/2009JTECHO698.1.

Jackson, C.R. and Apel, J.R.eds (2004). Synthetic Aperture Radar Marine User's Manual. US Department of Commerce, National Oceanic and Atmospheric', Administration, National Environmental Satellite, Data, and Information Serve, Office of Research and Applications, Washington, DC.

Jia, T., Liang, J.J., Li, X.M. and Sha, J. (2018) SAR observation and numerical simulation of internal solitary wave refraction and reconnection behind the Dongsha Atoll. *Journal of Geophysical Research: Oceans*. ISSN: 21699291. Available at: https://doi.org/10.1002/2017JC013389.

Johannessen, J.A., Shuchman, R.A., Digranes, G., Lyzenga, D.R., Wackerman, C., Johannessen, O.M *et al*. (1996) Coastal ocean fronts and eddies imaged with ERS 1 synthetic aperture radar. *Journal of Geophysical Research*, 101(C3), 6651. ISSN 0148–0227. Available at: https://doi.org/10.1029/95JC02962.

Kerbaol, V., Chapron, B. and Vachon, P.W. (1998) Analysis of ERS-1/2 synthetic aperture radar wave mode imagettes. *Journal of Geophysical Research: Oceans*, 103(C4), 7833–7846. ISSN 2156–2202. Available at: https://doi.org/10.1029/97JC01579.

Khalsa, S.J.S. and Greenhut, G.K. (1985) Conditional sampling of updrafts and downdrafts in the marine atmospheric boundary layer. *Journal of the Atmospheric Sciences*, 42(23), 2550–2562. ISSN 0022–4928. Available at: https://doi.org/10.1175/1520-0469(1985)042<2550:CSOUAD>2.0.CO;2.

Soh, L.K. and Tsatsoulis, C. (1999) Texture analysis of sar sea ice imagery using gray level co-occurrence matrices. *IEEE Transactions on Geoscience and Remote Sensing*, 37(2 I), 780–795. ISSN 01962892. Available at: https://doi.org/10.1109/36.752194.

LeCun, Y., Bengio, Y. and Hinton, G. (2015) Deep learning. *Nature*, 521(7553), 436–444. ISSN 0028–0836. Available at: https://doi.org/10.1038/nature14539.

Lee, J.S., Jurkevich, L., Dewaele, P., Wambacq, P. and Oosterlinck, A. (1994) Speckle filtering of synthetic aperture radar images: a review. *Remote Sensing Reviews*, 8(4), 313–340. ISSN 02757257. Available at: https://doi.org/10.1080/02757259409532206.

Fu, L.-L. and Holt, B. (1982) Seasat views oceans and sea ice with synthetic-aperture radar, Vol 81. Pasadena, CA: California Institute of Technology, Jet Propulsion Laboratory.

Levy, G. (2001) Boundary layer roll statistics from SAR, *Geophysical Research Letters*, 28, 1993–1995. Available at: https://doi.org/10.1s029/2000GL012667.

Li, X., Zheng, W., Yang, X., Zhang, J.A., Pichel, W.G. and Ziwei, L. (2013) Coexistence of atmospheric gravity waves and boundary layer rolls observed by SAR*. *Journal of the Atmospheric Sciences*, 70(11), 3448–3459. ISSN0022–4928. Available at: https://doi.org/10.1175/JAS-D-12-0347.1.

Natrella, M. (2013)NIST/SEMATECH e-handbook of statistical methods. NIST/SEMATECH.

Rascle, N., Molemaker, J., Marié, L., Frédéric, N., Chapron, B., Lund, B *et al*. (2017) Intense deformation field at oceanic front inferred from directional sea surface roughness observations. *Geophysical Research Letters*, 44(11), 5599–5608. ISSN 19448007. Available at: https://doi.org/10.1002/2017GL073473.

Schneider, T., Teixeira, J., Bretherton, C.S., Brient, F., Pressel, K.G., Schar, C *et al*. (2017) Climate goals and computing the future of clouds. *Nature Climate Change*, 7(1), 3–5. ISSN 1758–678X. Available at: https://doi.org/10.1038/nclimate3190.

Stopa, J.E., Ardhuin, F., Husson, R., Jiang, H., Chapron, B. and Collard, F. (2016) Swell dissipation from 10 years of Envisat advanced synthetic aperture radar in wave mode, *Geophysical Research Letters*. ISSN: 19448007. Available at: https://doi.org/10.1002/2015GL067566.

Topouzelis, K. and Kitsiou, D. (2015) Detection and classification of mesoscale atmospheric phenomena above sea in SAR imagery. *Remote Sensing of Environment*, 160, 263–272. ISSN 00344257. Available at: https://doi.org/10.1016/j.rse.2015.02.006.

Torres, R., Snoeij, P., Geudtner, D., Bibby, D. and Davidson, M., Attema, E *et al*. (2012) GMES Sentinel-1 mission. *Remote Sensing of Environment*, 120, 9–24. ISSN 00344257. Available at: https://doi.org/10.1016/j.rse.2011.05.028.

Ufermann, S. and Romeiser, R. (1999) Numerical study on signatures of atmospheric convective cells in radar images of the ocean. *Journal of Geophysical Research: Oceans*, 104, 25707–25719. Available at: https://doi.org/10.1029/1999JC900224.

Vandemark, D., Mourad, P.D., Bailey, S.A., Crawford, T.l., Vogel, C.A., Sun, J *et al*. (2001) Measured changes in ocean surface roughness due to atmospheric boundary layer rolls. *Journal of Geophysical Research: Oceans*, 106(C3), 4639–4654. ISSN 01480227. Available at: https://doi.org/10.1029/1999JC000051.

Young, G.S., Kristovich, D.A.R., Hjelmfelt, M.R., Foster, R.C. (2002) Rolls, streets, waves, and more: a review of quasi-two-dimensional structures in the atmospheric boundary layer. *Bulletin of the American Meteorological Society*, 83(7), 997–1001. ISSN 00030007.

Young, G.S., Sikora, T.N. and Winstead, N.S. (2005) Use of synthetic aperture radar in finescale surface analysis of synoptic-scale fronts at sea. *Weather and Forecasting*, 20(3), 311–327. ISSN 0882–8156. Available at: https://doi.org/10.1175/WAF853.1.

De Zan, F. and Monti Guarnieri, A. (2006) TOPSAR: terrain observation by progressive scans. *IEEE Transactions on Geoscience and Remote Sensing*, 44(9), 2352–2360. Available at: https://doi.org/10.1109/tgrs.2006.873853.

Zhang, L., Zhang, L. and Bo, D. (2016) Deep learning for remote sensing data: a technical tutorial on the state of the art. *IEEE Geoscience and Remote Sensing Magazine*, 4(2), 22–40. ISSN 21686831. Available at: https://doi.org/10.1109/MGRS.2016.2540798.

**How to cite this article:** Wang C, Mouche A, Tandeo P, et al. A labelled ocean SAR imagery dataset of ten geophysical phenomena from Sentinel-1 wave mode. *Geosci Data J*. 2019;6:105–115. https://doi.org/10.1002/gdj3.73

## 3.2 Classification of the global Sentinel-1 SAR vignettes for ocean surface process studies

Remote Sensing of Environment 234 (2019) 111457

Contents lists available at ScienceDirect

Remote Sensing of Environment

journal homepage: www.elsevier.com/locate/rse

# Classification of the global Sentinel-1 SAR vignettes for ocean surface process studies

Chen Wang[a,b,*], Pierre Tandeo[b], Alexis Mouche[a], Justin E. Stopa[c], Victor Gressani[a], Nicolas Longepe[d], Douglas Vandemark[e], Ralph C. Foster[f], Bertrand Chapron[a]

[a] *IFREMER, Univ. Brest, CNRS, IRD, Laboratoire d'Oceanographie Physique et Spatiale (LOPS), Brest, France*
[b] *IMT Atlantique, Lab-STICC, UBL, Brest, France*
[c] *Department of Ocean Resources and Engineering, University of Hawaii at Manoa, Hawaii, USA*
[d] *Space and Ground Segment, Collecte Localisation Satellites (CLS), Plouzane, France*
[e] *Ocean Processes Analysis Laboratory, University of New Hampshire, New Hampshire, USA*
[f] *Applied Physics Laboratory, University of Washington, Seattle, USA*

ARTICLE INFO

*Keywords:*
Synthetic aperture radar (SAR)
Ocean surface phenomena
Sentinel-1 wave mode
Deep learning
Convolutional neural network (CNN)
Image classification

ABSTRACT

Spaceborne synthetic aperture radar (SAR) can provide finely-resolved (meters-scale) images of ocean surface roughness day-or-night in nearly all weather conditions. This makes it a unique asset for many geophysical applications. Initially designed for the measurement of directional ocean wave spectra, Sentinel-1 SAR wave mode (WV) vignettes are small 20 km scenes that have been collected globally since 2014. Recent WV data exploration reveals that many important oceanic and atmospheric phenomena are also well captured, but not yet employed by the scientific community. However, expanding applications of this whole massive dataset beyond ocean waves requires a strategy to automatically identify these geophysical phenomena. In this study, we propose to apply the emerging deep learning approach in ocean SAR scenes classification. The training is performed using a hand-curated dataset that describes ten commonly-occurring atmospheric or oceanic processes. Our model evaluation relies on an independent assessment dataset and shows satisfactory and robust classification results. To further illustrate the model performance, regional patterns of rain and sea ice are qualitatively analyzed and found to be very consistent with independent remote sensing datasets. In addition, these high-resolution WV SAR data can resolve fine, sub-km scale, spatial structure of rain events and sea ice that complement other satellite measurements. Overall, such automated SAR vignettes classification may open paths for broader geophysical application of maritime Sentinel-1 acquisitions.

## 1. Introduction

The spaceborne synthetic aperture radar (SAR) is a well-established technique to collect high-resolution sea surface backscatter data during day and night in most weather conditions. Over the ocean, SAR images provide an estimate of the sea surface roughness primarily through backscattering of short waves (Alpers et al., 1981; Hasselmann et al., 1985; Hasselmann and Hasselmann, 1991), where this small-scale (cm) roughness responds to the near-surface ocean winds (Lehner et al., 2000; Winstead et al., 2006; Mouche et al., 2012). In addition, these short waves are also modulated by ocean swell (Heimbach et al., 1998; Lehner et al., 2000; Collard et al., 2009), upper ocean processes (Johannessen et al., 1996; Rascle et al., 2017; Jia et al., 2018), and atmospheric phenomena (Alpers and Brümmer, 1994; Young et al., 2005; Winstead et al., 2006; Li et al., 2007, 2013; Alpers et al., 2016). Beginning with SEASAT in 1978, ocean SAR imagery has been widely used to examine numerous air-sea interaction processes (Meadows et al., 1983; Gerling, 1986; Carsey and Holt, 1987; Fu and Holt, 1982; Katsaros and Brown, 1991). Since then, ever-improving SAR data have been obtained by satellite missions that include ERS-1/2, Envisat/ASAR, RADARSAT-1/2, TerraSAR-X, TanDEM-X and Sentinel-1 constellation.

However, global-scale applications of ocean SAR data remain quite limited. This is largely because the wide swath SAR images are not routinely collected over the open ocean. These acquisitions mainly focus on land, Arctic regions, and near the coasts. Thus, most previous ocean SAR data investigations only involve limited regional or single SAR scene case study (Alpers and Brümmer, 1994; Babin et al., 2003;

---

[*] Corresponding author. IFREMER, Univ. Brest, CNRS, IRD, Laboratoire d'Oceanographie Physique et Spatiale (LOPS), Brest, France.
*E-mail address:* Chen.Wang@ifremer.fr (C. Wang).

https://doi.org/10.1016/j.rse.2019.111457
Received 27 February 2019; Received in revised form 24 September 2019; Accepted 30 September 2019

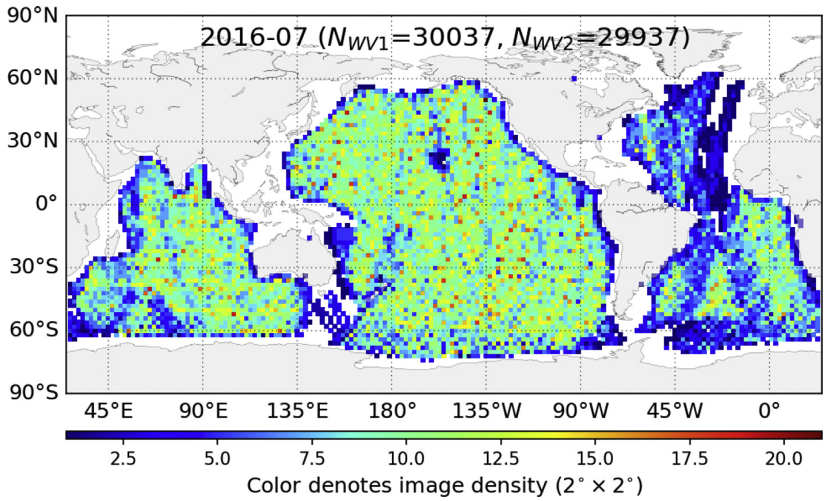

**Fig. 1.** Global distribution of the WV SAR data obtained by S-1A in July of 2016. Color is indicative of the SAR image density in 2° by 2° spatial grid. (For interpretation of the references to color in this figure legend, the reader is referred to the Web version of this article.)

Sikora et al., 2011; Li et al., 2013; Alpers et al., 2016). One exception is the wave mode (WV) dedicated to retrieving ocean wave proprieties at global scale (Kerbaol et al., 1998; Stopa et al., 2016). The WV has been developed for ERS-1/2 (1991–2003) and Envisat/ASAR (2002–2012), and now introduced to Sentinel-1 (2014-present) and Gaofen-3 (2016-present). It normally collects relative small SAR images (typically 5–10 km square) along the orbit with a distance of about 100 km in between. This is sufficient for ocean wave spectrum retrieval and empirically estimation of the total significant wave height (Heimbach et al., 1998; Collard et al., 2009; Stopa and Mouche, 2017), which can be used in wave forecasting. At present, the routine WV measurements are only available from the Sentinel-1 (S-1) A&B (Torres et al., 2012). It was improved upon Envisat and ERS by having finer spatial resolution (4 m), higher signal-to-noise (which reduces speckle noise), larger scene footprint (20 by 20 km), and increased global sampling.

Wang et al. (2019) demonstrated that the S-1 WV dataset has the potential for new studies on air-sea interactions at scales of 0.5–10 km. The primary advantage of the S-1 WV dataset is its ability of measuring high resolution sea surface roughness globally (∼120k images per month). However, without an automated means to identify the geophysical features captured by each image, the potential would remain untapped. For example, previous studies have relied solely on visual inspection to identify SAR images with wind streaks before performing statistical analysis or surface wind direction derivation (Lehner et al., 2000; Levy, 2001; Mouche et al., 2012; Zhao et al., 2016). Such manual classification approach is impractical for the huge volume of S-1 WV data. Similarly, dedicated classic machine learning algorithms have mostly been developed for specific applications such as detection of oil spills and ships. These methods depend on the empirically hand-crafted features, which are usually insufficient to generalize the local variations, shapes and structural patterns of different geophysical phenomena (Topouzelis and Kitsiou, 2015; Zhang et al., 2016).

This study attempts to train a deep convolutional neural network (CNN) to classify the ten prescribed geophysical phenomena seen in WV vignettes. Deep CNN models have been applied with great success in detection, segmentation, and recognition of objects, features, and textures within digital images (LeCun et al., 2015). They have also been applied to hyperspectral and optical remote sensing imagery (Zhao and Du, 2016; Li et al., 2017; Hu et al., 2015; Cheng and Han, 2016; Zhou et al., 2017). However, the primary use of CNN in ocean SAR application has mostly been for target recognition (Zhang et al., 2016; Zhu et al., 2017). In general, CNN is a multilayer architecture that can be trained to automatically extract the optimal image features and to amplify distinctions between images (LeCun et al., 2015; Zhang et al., 2016). A practical and effective way to develop a robust CNN for a specific application is to re-train an existing image recognition model. This so-called transfer-learning or fine-tuning strategy has been proven to be more efficient and practical than creating and training a new CNN architecture from scratch in the case of limited database (Yosinski et al., 2014; Zhu et al., 2017; Cheng et al., 2017; Too et al., 2018; Wang et al., 2018a).

In this paper, we adapt the Inception-v3 CNN (Szegedy et al., 2015) to train a model dedicated to the classification of S-1 WV vignettes, called CMwv. The involved datasets are described in section 2. Section 3 demonstrates the training process of CMwv and illustrates the model performance based on an independent assessment dataset. In section 4, we compare our classification results qualitatively with rain precipitation from Global Precipitation Measurement (GPM) and sea-ice concentration from Special Sensor Microwave Imager (SSM/I). Conclusions follow in section 5.

## 2. Datasets

This study uses ocean SAR vignettes from S-1 WV, precipitation data from GPM and sea ice concentration data from SSM/I. To train the CNN architecture, we create training datasets drawn from the labelled TenGeoP-SARwv database (Wang et al., 2018b). In addition, to assess and quantify the performance of CMwv, we build an assessment dataset of 10,000 visually verified images. All datasets are described in the following.

### 2.1. S-1 WV

The S-1 mission is a constellation of two (A&B) polar-orbiting, sun-synchronous SAR satellites (Torres et al., 2012). They were launched by European Space Agency (ESA) in April of 2014 and 2016, respectively. The two satellites share the same orbital plane, which crosses the equator at approximately 0600 or 1800 local time, with a 180° phase difference to provide an effective 6-day repeat cycle. The S-1 microwave SAR instruments have a 5.5 cm wavelength (C-band). WV is the default mode over the open ocean unless other imaging mode collections are requested. According to the defined Mission Operation Scenario, there is no WV acquisition in the Arctic Ocean, closed seas (Red, Black, Mediterranean and Caribbean seas) and coastal areas. Fig. 1

displays the spatial coverage of S-1A WV data acquired in July of 2016. Although only S-1A WV data is used in this study, S-1B images have essentially equivalent characteristics with S-1A. Thus, the combination of S-1A and S-1B will expand sampling in time and space for different geophysical phenomena applications. Moreover, the developed classification model and results presented hereafter are also applicable to S-1B.

S-1 WV vignettes are acquired in a ‘leapfrog’ pattern at two alternating center incidence angles of 23° (WV1) and 36.5° (WV2) every 100 km along the flight track. Each vignette has a 20 by 20 km footprint with 5 m spatial resolution. The default radar polarization is VV, though some HH images have been acquired. Combining both satellites and WV incidence angles, approximately 120,000 vignettes per month are acquired. This study focuses on the VV polarized SAR vignettes as they comprise more than 99% of acquisitions to date. Also, data quality control is carried out by removing data files with the following criteria:

- **HH polarization:** HH-polarized images are excluded.
- **Land contamination:** The distance of one vignette center (longitude and latitude) to the nearest coastline is calculated based on the dataset of Distance from Nearest Coastline (DNC). We filter out the vignettes if their center is over the land.
- **Low mean signal intensity:** We filter out the low-quality vignettes by limiting the mean Normalized Radar Cross Section (NRCS) to be larger than -22 dB, which is the Noise Equivalent Sigma Zero (Torres et al., 2012).

### 2.2. TenGeoP-SARwv dataset

TenGeoP-SARwv is a labelled dataset of more than 37k ocean SAR images corresponding to ten commonly-observed and expertly-defined geophysical phenomena (Wang et al., 2019). These ten choices, though somewhat subjective, were selected and defined after an extensive review of the S-1 WV data and with reference to past ocean SAR studies. This study denotes the classes as pure ocean waves (PureWave), wind streaks (WindStreak), micro-convective cells (WindCell), rain cells (RainCell), biological slicks (BioSlick), sea ice (SeaIce), icebergs (IceBerg), low wind areas (LowWind), atmospheric fronts (AtmFront), and oceanic fronts (OcnFront). Thousands of VV-polarized vignettes for each case were manually selected from the S-1A WV acquisitions in 2016. These vignettes are chosen with the criteria that within one scene, one geophysical phenomenon dominates with its specific signature or pattern. It is worth noticing that PureWave signatures normally exist in SAR images as background for other classes. Example vignettes of the ten defined classes are displayed in Fig. 2. These visually-identified and tagged SAR scenes, 37560 in total, are provided in formats of Portable Network Graphics (PNG) and Georeferenced Tagged Image File Format (GeoTIFF). Despite the fact that the GeoTIFF product maintains high precision of the original data, PNG files are more suitable for visual interpretation and satisfy the training input requirement for CNN models. Thus, PNG product is the dataset of interest in this study. It is important to note that the detectability of SAR on these phenomena, especially these modulations induced by the surface wind, can differ for WV1 versus WV2. Because the complex response of C-band radar scatter of the sea surface depends primarily on the incidence angle and the relative angle between the radar and the surface wind direction. Under some atmospheric conditions such as strong winds (>15 m/s), the backscatter is dominated by sea states (winds and waves). Consequently, other phenomena except ocean waves can not be well captured.

### 2.3. Assessment dataset

S-1 WV SAR vignettes are able to capture a wide range of ocean surface geophysical processes and the most common ten categories have been included in the TenGeoP-SARwv. To assess and quantify performance of the developed classification model on the whole WV database, an independent assessment dataset is thus created. 5000 WV1 and WV2 vignettes respectively were randomly selected from 2016 S-1A acquisitions and classified by visual inspection. A less strict criteria of PureWave was adopted to make this validation dataset representative of the actual WV measurements. We then apply the classification model to each of these scenes. The resulting class identifications were compared to visual results, which is a skill test commonly used in image classification modeling (Zhang et al., 2016; Cheng et al., 2017). For the vignettes that do not belong to any of the ten defined classes, we sort them into a special ‘The Other’ category (TheOther). These more infrequent phenomena include, but are not limited to, oceanic internal waves (Alpers and Huang, 2011; Jia et al., 2018), atmospheric gravity waves (Chunchuzov et al., 2000; Li et al., 2013), upwelling regions (Jackson and Apel, 2004), and irregular atmospheric patterns.

### 2.4. Rain precipitation from GPM and IMERG

The GPM mission is an international satellite network that provides global estimates of rainfall and snowfall from space (Hou et al., 2014). A primary instrument is the GPM Core Observatory that was launched

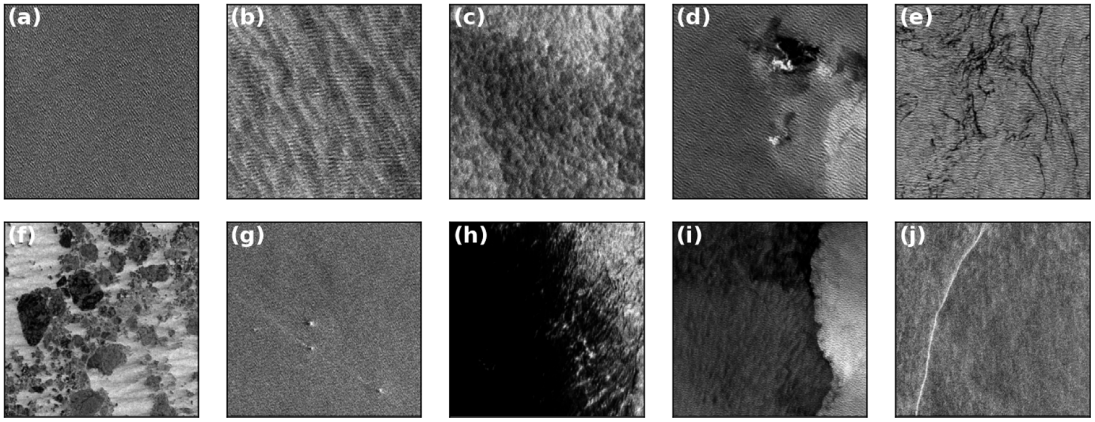

**Fig. 2.** Ten vignette examples of expertly-defined geophysical phenomena. From (a) to (j) are pure ocean waves (PureWave), wind streaks (WindStreak), micro convective cells (WindCell), rain cells (RainCell), biological slicks (BioSlick), sea ice (SeaIce), icebergs (IceBerg), low wind area (LowWind), atmospheric front (AtmFront) and oceanic front (OcnFront).

in February 2014 by the National Aeronautics and Space Administration (NASA) and the Japan Aerospace and Exploration Agency (JAXA). This Core Observatory carries the first dual-frequency (Ku-/Ka-band) precipitation radar (DPR) and a multichannel microwave imager (GMI). The Ku-band radar accurately measures moderate to heavy rain rates and the Ka-band radar can measure light rain and snowfall. They provide cross-track swaths of 245 km (Ku) and 120 km (Ka) with 5 km resolution. Retrieved precipitation estimates from the swath measurements are available at the NASA data center (https://pmm.nasa.gov/data-access/downloads/gpm). In addition, the Integrated Multi-satellitE Retrievals for GPM (IMERG) is a gridded precipitation product that combines all satellite precipitation measurements. In this study, we collocate GPM level-2 (swath) DPR Ku-only surface rain precipitation data with S-1A WV vignettes acquired from March 2016 to February 2017. Spatial and temporal collocation criteria of 35 km and less than 10 min are used and result in 2588 matched data pairs. The mean precipitation value for DPR measurements averaged across the 35 km square is used. We also use the IMERG 0.1°-monthly product to qualitatively validate the global and seasonal features of CMwv-classified rain events. Results and discussions are given in section 4.1.

### 2.5. Ice concentration from SSM/I

Sea ice concentration maps are produced by applying the Artist Sea Ice (ASI) algorithm to the brightness temperatures from Special Sensor Microwave Imager (SSM/I) radiometer (Ezraty et al., 2007). The concentration product has been operational since 1992 with 12.5 km spatial resolution. It is publicly available at ftp://ftp.ifremer.fr/ifremer/cersat/products/gridded/psi-concentration/. The seasonal sea ice concentration is computed based on the daily data, and compared with the CMwv-classified sea ice event occurrences (see section 4.2).

## 3. Automated ocean SAR scene classification

This section describes how the automated classifier for S-1 WV ocean SAR vignettes was developed by re-training the Inception-v3 CNN. The performance of this tool is evaluated and quantified using the independent assessment dataset described in section 2.3.

### 3.1. Inception-v3 and training strategies

Many successful CNN architectures have shown solid performance in the ImageNet large-Scale Visual Recognition Challenge (ILSVRC) (Russakovsky et al., 2015). In this study, we use the Inception-v3 architecture proposed by Google in 2015 (Szegedy et al., 2015, 2016) to demonstrate the potential of deep CNN in identifying and classifying geophysical phenomena from ocean SAR scenes. The Inception model was firstly introduced as GoogLeNet or Inception-v1 (Szegedy et al., 2015), a classic deep CNN architecture. The initial Inception architecture was refined in many ways. A first improvement was introduced in the Inception-v2 of batch normalization to accelerate the training process (Szegedy et al., 2016). While later, the Inception-v3 used additional factorization ideas to augment the number of convolutions without increasing the computational cost. It achieves remarkable performance with 94.4% top-5 accuracy on the ILSVRC 2012 classification dataset. We choose Inception-v3 in this study because of its promising performance and easy implementation with the python deep learning library of Keras (https://keras.io/). Also, at the time of starting this work, this model represented the good tradeoff between classification performance and huge parameters (Bianco et al., 2018).

The Inception-v3 architecture has 48 network layers with more than 23 million trainable weights. These layers are generally divided into feature extraction and classification parts. Weights of the feature extraction part are trained to describe common image characteristics such as curves, edges, gradients and particular patterns. These features are expected to be adopted to the task of ocean SAR vignette classification (Yosinski et al., 2014; Too et al., 2018; Wang et al., 2018a). The last layer of this CNN architecture represents the classification part, which is replaced with a new classification layer in our applications. Note that capability comparison of different CNN architectures may also be of interest, but it is beyond the scope of this work.

We examined two training strategies: transfer-learning and fine-tuning. The transfer-learning only trains the final classifier layer, while the fine-tuning adjusts all the layers in the CNN architecture. For each input image, Inception-v3 requires the image size to be 299 pixels for both height and width. Then, 2048 optimal features per image are extracted to construct the final classifier. As noted above, the sensitivity of SAR to different oceanic or atmospheric phenomena can be different for the two WV incidence angles. We therefore create separate training datasets for WV1 and WV2 (hereafter TDwv1 and TDwv2). To equalize the size of TDwv1 and TDwv2, 320 images per class are randomly selected from the labelled dataset of TenGeoP-SARwv (Wang et al., 2018b). For training Inception-v3, the input dataset is randomly split into training and validation subsets with proportions of 70% and 30%. Training subset is fed into the CNN to learn and extract image features. The validation subset, by contrast, is used to gauge the CNN model performance at each epoch (iteration of CNN optimization).

### 3.2. CMwv model

First, we compare results found for the transfer-learning versus fine-tuning training approaches. Based on TDwv1, the Overall Accuracy (OA, Stehman (1997)) is calculated within 500 epochs and is displayed in Fig. 3 (a). As shown, the OA of both transfer-learning (red lines) and fine-tuning (black lines) increases rapidly within the first 100 epochs, and then remains stable at around 89% and 97%, respectively. Fine-tuning is more accurate than transfer-learning and is therefore chosen in this study. Fig. 3 (b) displays the sensitivity assessment of the fine-tuning process to random training inputs. Random shuffling is repeated three times to generate different training and validation subsets drawn from TDwv1. Result shows no significant effect on OA due to different data draws. The impact of dataset size is also tested using image input datasets of 80, 160, 240 and 320 samples, respectively. All four models achieve comparable OA, as displayed in Fig. 3 (c). The largest training dataset converges most quickly and with the highest and most constant OA. In this paper, we use 320 images per class to train the final model. Fig. 3 (d) shows that OA improves rapidly with training epochs. The trained CNN weights at epochs 399 and 329 where OA reaches the maximum (blue and red vertical lines) are adopted in the final CMwv. This model has a OA of 98.5% and 98.3% for WV1 and WV2, respectively.

Misclassifications still occur even though the model OA is very high. With visual inspection of the misclassified images in the validation part, four representative examples with their classification probabilities are shown in Fig. 4. The red stars indicate the actual class. Ambiguous image features are one of the reasons leading to misclassification. For example in Fig. 4 (a), the linear feature of an oceanic front (OcnFront) looks more like the softer mottled linear features that we ascribed to the atmospheric front (AtmFront) class (Wang et al., 2019). Both cell-shaped features (WindCell) and the linear-shaped features (WindStreak) are visible in Fig. 4 (b), also resulting in an ambiguity within this vignette. Superimposition of these two phenomena is captured by the CMwv model with high classification probabilities in both classes. Indeed, the atmospheric coherent structures that generate the WindStreak signature often undergo a transition to the convective structures that generate the WindCell signature when the surface buoyancy increases (Atkinson and Wu Zhang, 1996). Another reason responsible for misclassifications is that multiple geophysical phenomena can coexist within the same vignette. Low wind area (LowWind) is often associated with wind gust fronts (AtmFront), as shown in Fig. 4 (c). Biological slicks (BioSlick) usually accompany the LowWind (Fig. 4 (d)) because they both occur in low wind conditions. Signatures of ocean waves are

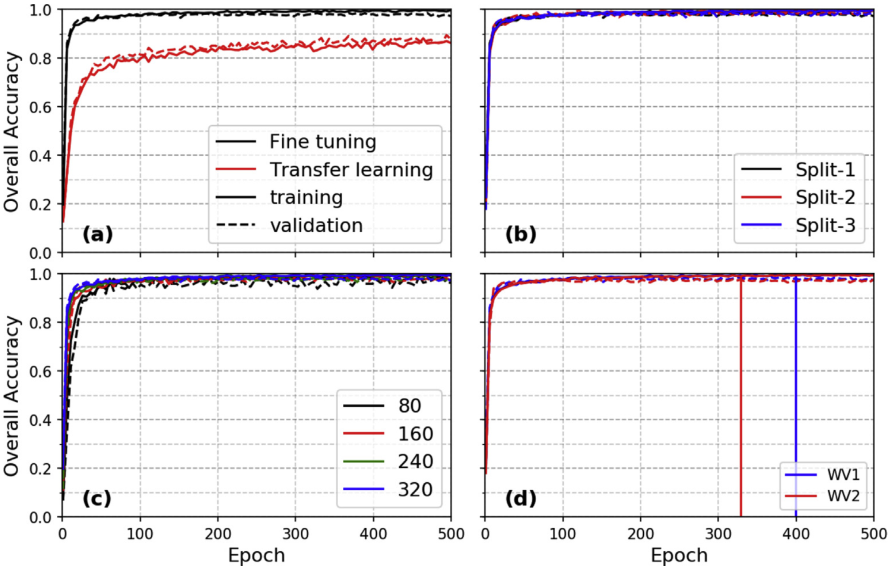

**Fig. 3.** Overall accuracy (OA) in each 5 epochs during the training of inception-v3. The first 500 epochs are shown for (a) comparison of transfer-learning and fine-tuning, (b) experiment of random splitting process, (c) experiment of the training dataset size and (d) the development of CMwv.

also clearly seen in the four examples. The PureWave classification probability for these scenes is nearly zero due to our imposed lowest ranking of ocean waves within these prelabelled events. In other words, the priority of other phenomena in the developed classification model is much higher. This corresponds to the fact that our definition of PureWave is a SAR image that only contains signature of ocean waves without any other geophysical phenomena. It is thus expected that adjustment of our model to address multi-labelling with equal weights for these multiple feature SAR images might improve future classification. To this end, the current classification probabilities can be further exploited to get more fuzzy probabilities or refine the training dataset. A thorough labeling strategy allowing the existence of multiple features is also demanded. In particular, wave detection shall facilitate the labeling of its coexistence with other phenomena.

### *3.3. CMwv model assessment*

To further assess the CMwv performance on the whole WV database, a quantitative figure was obtained through comparison against the independent assessment dataset introduced in Section 2.3. Fig. 5 provides the normalized confusion matrix. The rows and columns in the matrix indicate the truth (manually-labelled) and CMwv prediction, respectively. One image is assigned to be the class of the largest classification probability. As shown, most of the class identification skill results for both WV1 and WV2 cases show accuracy that exceeds 0.8. One exception is PureWave, this class being strongly influenced by IceBerg, AtmFront and OcnFront events. This leads to much lower PureWave classification accuracy of 47% and 39% for WV1 and WV2, respectively. It is likely because signatures of ocean waves are prevalent in

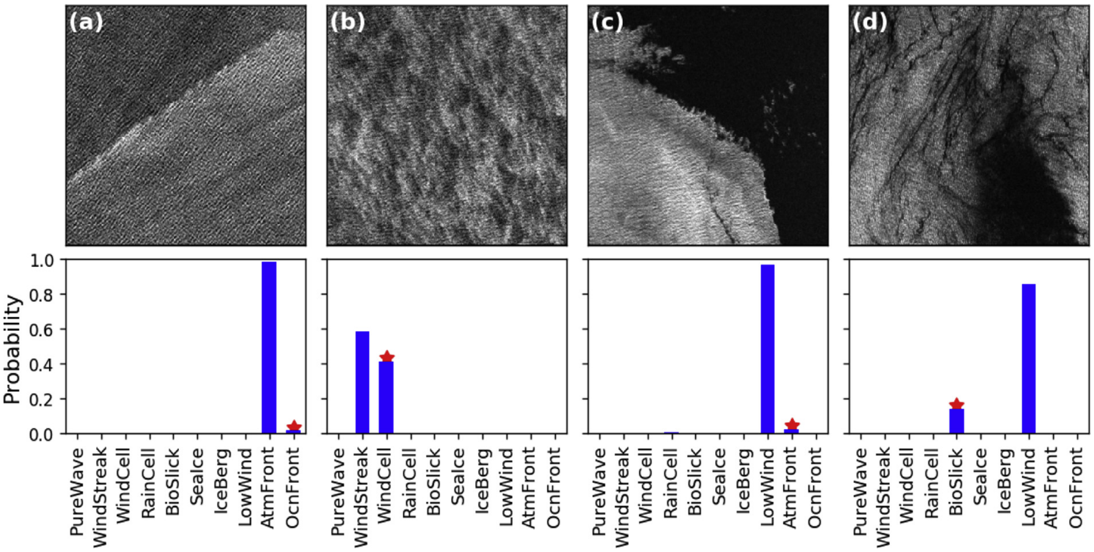

**Fig. 4.** Examples of misclassified WV images from CMwv along with the classification probability of each class. Red stars indicate the class determined visually (manually-labelled). (For interpretation of the references to color in this figure legend, the reader is referred to the Web version of this article.)

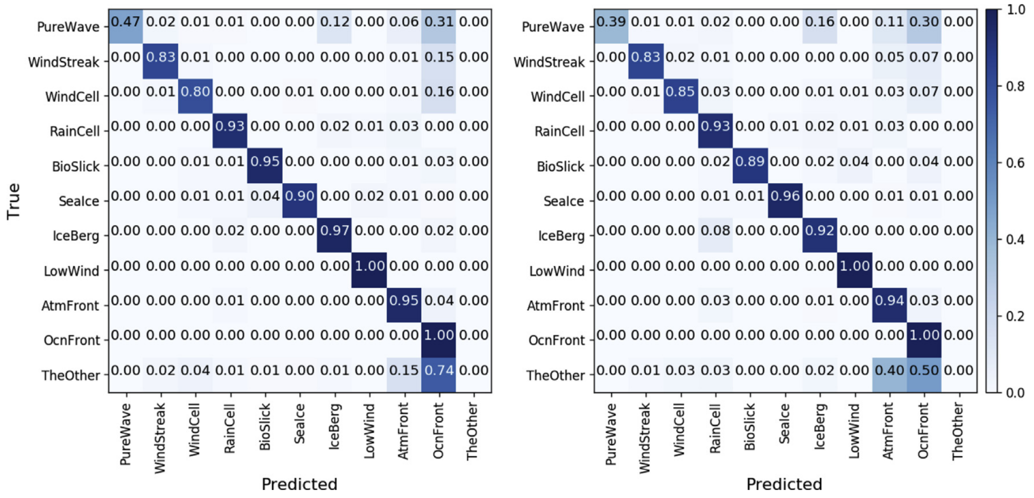

**Fig. 5.** CMwv normalized confusion matrix when the model is applied to the WV1 (left) and WV2 (right) independent verification data subsets.

most images and we choose a loose criteria for PureWave class in the assessment dataset. In addition, about 15% of WindStreak and WindCell images are misclassified as AtmFront and OcnFront, resulting in the relatively lower classification accuracy. Nearly 90% of the TheOther images are classified into categories of AtmFront and OcnFront. Overall, images of PureWave, IceBerg, AtmFront and OcnFront are often misclassified. To further quantify CMwv performance, recall, precision and F-score parameters (Sokolova and Lapalme, 2009) are calculated based on the confusion matrix:

$$Recall = \frac{number\ of\ correctly\ classified}{number\ of\ truth} \tag{1}$$

$$Precision = \frac{number\ of\ correctly\ classified}{number\ of\ classified} \tag{2}$$

$$F-score = \frac{2 \times precision \times recall}{precision + recall} \tag{3}$$

For given class, recall (also called sensitivity) is equivalent to the classification accuracy discussed above. Precision (also called positive predictability) indicates the model's internal accuracy or skill. The F-score takes both recall and precision into account as one comprehensive index for model performance. Values of these three parameters are all expected to be near one.

CMwv recall, precision and F-score results against the assessment dataset are given in Table 1. Results indicate a hierarchy in skill across classes where RainCell, BioSlick, SeaIce and LowWind classes show similarly highest levels of recall, precision and F-scores that exceed 85% in any measure, and for both WV1 and WV2 vignettes. A second tier with slightly lower skill is seen for WindStreak and WindCell with WV2 F-scores of nearly 0.9 and 0.8 for WV2 and WV1 respectively. The drop in WV1 F-score is due to nearly 20% lower precision in WV1 scene detection. This is due to the fact that ocean wave signatures are suppressed at higher incidence and other atmospheric phenomena are more pronounced. Overall, the results indicate robust CMwv model performance for these six phenomena. A next drop in skill is seen for the PureWave class. PureWave detection shows much lower recall levels of 47% and 39% for WV1 and WV2, respectively. Inspection found that this is because a large number of PureWave dominated SAR scenes are misclassified as IceBerg (12% and 16%), AtmFront (6% and 11%), and OcnFront (31% and 30%), as shown in Fig. 5. Yet, high PureWave precision suggests strong confidence when a PureWave detection occurs. The lowest performance tier is seen when CMwv is applied to detect icebergs, atmospheric, and ocean fronts (IceBerg, AtmFront and OcnFront). In these three classes, the model shows poor precision (i.e. an excess of false positives) caused by the misclassification of scenes that should have been ocean waves (PureWave) or more ambiguous events (TheOther).

Although time consuming, the visual classification provided by Wang et al. (2019) demonstrated the capabilities of S-1 WV to capture signatures of air-sea interactions. Above results suggest that an adapted deep CNN image recognition model can be trained for automated classification of the S-1 WV VV-polarized SAR vignettes. A brief summation of CMwv skill taken from these results suggests reasonable confidence levels for investigations that focus on six of the prescribed classes (WindStreak, WindCell, RainCell, BioSlick, SeaIce and LowWind), while CMwv refinements would be needed for OcnFront, AtmFront, IceBerg, and PureWave applications. Other deep learning techniques such as pixel-level based classification, object detection and image segmentation (Zhang et al., 2016; Cheng et al., 2017) are expected to efficiently target the localized phenomena (RainCell, IceBerg, AtmFront and OcnFront) within each scene. In addition, it will be beneficial to include the geographic and time information of SAR data in deep learning approaches. Latitude is just one of many possible important and obvious data inputs, helping for example, to limit sea ice and iceberg detection windows to cold waters.

**Table 1**
CMwv recall, precision and F-score metrics for each of the 10 geophysical categories when applied to WV1 (upper) and WV2 (lower) vignette detection.

| | PureWave | WindStreak | WindCell | RainCell | BioSlick | SeaIce | IceBerg | LowWind | AtmFront | OcnFront |
|---|---|---|---|---|---|---|---|---|---|---|
| **Recall** | 0.47 | 0.83 | 0.80 | 0.93 | 0.95 | 0.90 | 0.97 | 1.00 | 0.95 | 1.00 |
| | 0.39 | 0.83 | 0.85 | 0.93 | 0.89 | 0.96 | 0.92 | 1.00 | 0.94 | 1.00 |
| **Precision** | 1.00 | 0.77 | 0.76 | 0.88 | 0.88 | 0.96 | 0.16 | 0.87 | 0.39 | 0.02 |
| | 0.98 | 0.96 | 0.94 | 0.80 | 0.91 | 0.96 | 0.18 | 0.79 | 0.38 | 0.02 |
| **F-score** | 0.64 | 0.80 | 0.78 | 0.90 | 0.91 | 0.93 | 0.27 | 0.93 | 0.56 | 0.04 |
| | 0.56 | 0.89 | 0.89 | 0.86 | 0.90 | 0.96 | 0.30 | 0.88 | 0.54 | 0.04 |

## 4. Geophysical applications

As a first demonstration, the CMwv model was applied to all S-1A WV VV-polarized acquisitions from March 2016 to February 2017. We examine the images classified as rain cells (RainCell) and sea ice (SeaIce) as well as their occurrence in space and time. GPM and IMERG rain precipitation and SSM/I sea ice concentration data are used for comparison. Specifically, seasonal variations of these two phenomena are presented and discussed in the four seasons: March-April-May (MAM), June-July-August (JJA), September-October-November (SON) and December-January-February (DJF) from March 2016 to February 2017. There are more than 160k vignettes acquired globally by S-1A in each of these seasons.

### *4.1. Rain cells*

A detected RainCell in the S-1 vignettes has been defined as one or several km-scale circular- or semi-circular-shaped patches that may be either relatively bright or dark (Wang et al., 2019). These patches are typical signature of rain downdraft (Atlas, 1994; Alpers et al., 2016) in the convective rain cells (Houze, 1997). From March 2016 to February 2017, nearly 10% of S-1A images are classified as RainCell. The seasonal mapping of SAR-detected RainCell occurrence (fraction within 2° lat/lon bins) in the left panel of Fig. 6 indicates distinct spatial and temporal patterns. We also plot the seasonal maps of monthly averaged IMERG rain rate in the right panel of Fig. 6 for comparison. However, it must be noted here that the IMERG product aims at intercalibrating, merging, and interpolating satellite microwave precipitation estimates, together with microwave-calibrated infrared (IR) satellite estimates. This leads to different temporal and coverage resolution between SAR-detected RainCell occurrence and IMERG precipitation.

Across the whole tropical ocean (3 basins), SAR-detected rain events are found to be infrequent right along the equator with a band of strong occurrence north of the Equator. This band is clearly observed throughout the year and with the Inter-Tropical Convergence Zone (ITCZ). In the particular case of the Pacific ocean, strong occurrence of rain cells are also found in the South Pacific Convergence Zone. It is in good agreement with IMERG precipitation seasonal patterns. Significant differences are found in the subtropics between 10° and 30°. In the north hemisphere (Atlantic and Pacific), SAR-detected RainCell occurrence is high (>10%) whereas the rain precipitation from IMERG is low (<0.1 mm/h). In the south hemisphere, this is also observed in the east of the south Pacific, in the Atlantic and in the Indian ocean. In the extratropical areas (poleward of 30°N or 30°S), we observe the opposite trend. SAR results present lower occurrence of RainCell while IMERG measures comparatively higher precipitation rates.

Overall, most areas of higher SAR-detected RainCell occurrence are associated with high IMERG precipitation areas and consistent with the

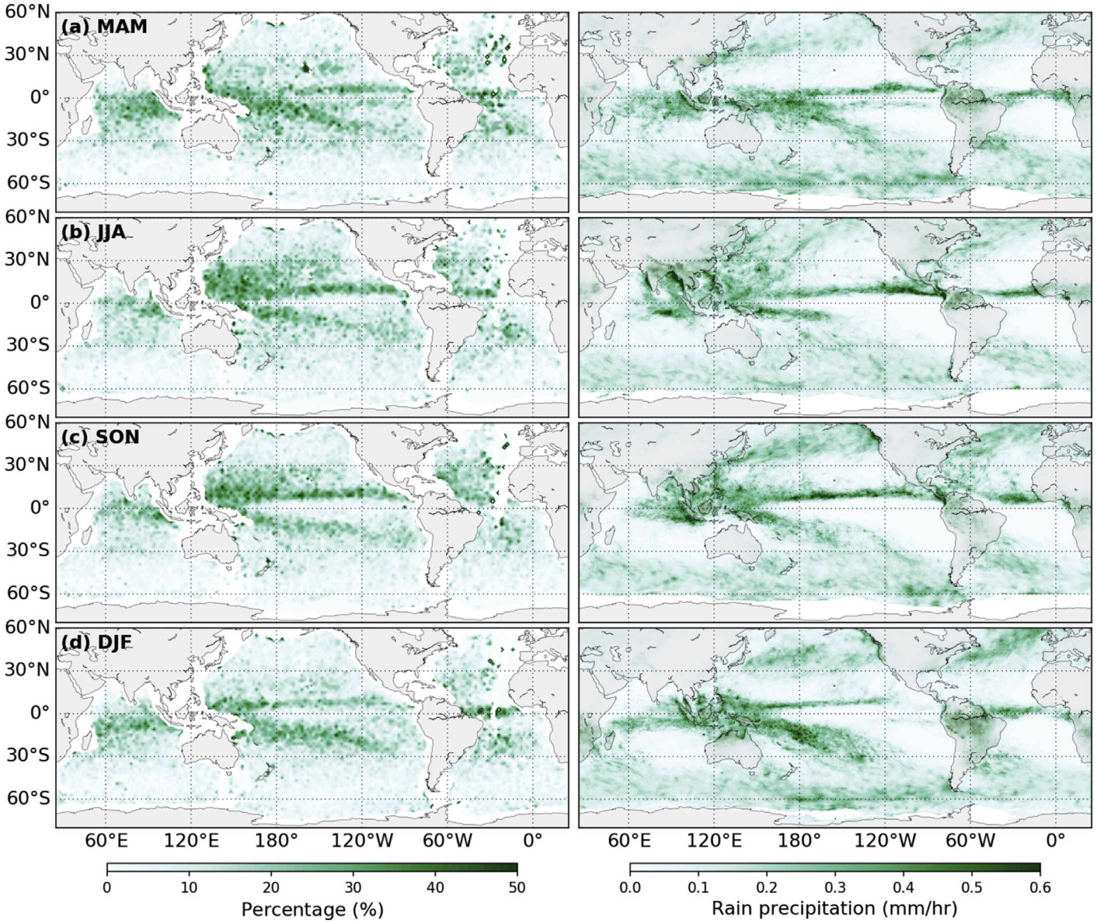

**Fig. 6.** Seasonal comparison of CMwv-detected S-1A rain cells (left) alongside GPM precipitation measurements (right). Rain occurrence percentages are calculated on a 2° by 2° spatial grid based on S-1A WV data from March 2016 to February 2017. The average monthly rain rate in MAM, JJA, SON and DJF are obtained from the IMERG 0.1°-monthly product.

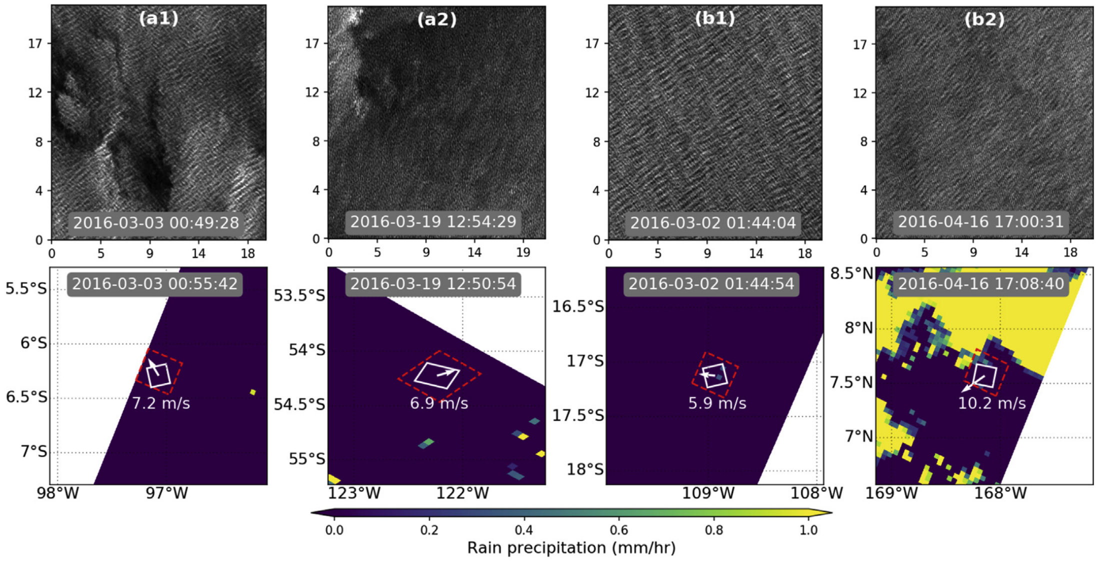

**Fig. 7.** Four cases of point-by-point comparison between classified rain cells and the collocated GPM level-2 DPR Ku-only surface rain precipitation. (a1) and (a2) are cases in which WV detects RainCell and GPM indicates no precipitation. (b1) and (b2) are cases in which WV did not detect RainCell and GPM measured precipitation. Upper panels are WV images, lower panels show the GPM rain rate swath data. In the lower panels, the WV outline is the white box and the collocation region is the red box. The vector indicates the sea surface wind. (For interpretation of the references to color in this figure legend, the reader is referred to the Web version of this article.)

rainfall climatology of previous studies (Kidd, 2001; Adler et al., 2003). However, disagreements are found as well. One of the reasons for this is due to the fact that IMEG products measure all types of rainfall and is not limited to rain cells. This certainly explains the agreement observed in the tropical area where the convective cells dominate (Houze, 1997). To further address the difference, a point-by-point collocation between S-1 WV SAR images and GPM level-2 DPR Ku-only surface rain precipitation is conducted. The collocation criteria is within 35 km in space and 10 min in time.

In total, there are 2588 matched data pairs with 286 SAR vignettes being classified as RainCell. For 63.4% of the RainCell-classified images, collocated GPM also reports precipitation. In the remaining cases, however, no precipitation is reported by GPM. Fig. 7 (a1) and (a2) display two examples of this situation that SAR detects rain events while GPM does not. The upper panel shows the SAR images and the bottom gives the precipitation. The red dashed box, white box and white arrow indicate the collocated area, image box and surface wind vector, respectively. As shown, these two SAR images exhibit clear RainCell signatures, confirming the credibility of RainCell classification results. The precipitation is not resolved by GPM, possibly because they are short-lived and/or weak rain events. For the images that are not classified as RainCell, 23.2% of the collocated GPM reports precipitation. With the visual inspection, we confirmed that most of these images do not have clear RainCell signature as defined in Wang et al. (2019). Two such examples are shown in Fig. 7 (b1) and (b2). RainCell signatures in SAR images are primarily caused by modulations of the surface waves due to rainfall, downdraft and also a direct attenuation of the signal by rain drops in the atmosphere (Alpers et al., 2016). However, we recall here that the first order impact on the sea surface roughness as detected by C-band active radar is the local wind. As a result, there is a competition between the ambient wind and possible rain impacts on the small-scale waves. Thus, we suspect that in situation where the wind speed is sufficiently high, the wind impact dominates the backscattering over the rain, yielding SAR scenes with hardly detectable rain signature. Fig. 8 further evidences this interpretation. It is the distribution of surface wind speed for the four possible situations (SAR-detected RainCell or not, GPM DPR-measured precipitation or not). As shown, SAR-detected RainCell (blue and orange lines) occurs mostly at intermediate wind speed of 3–10 m/s. By contrast, the wind distribution of the images with non-detected RainCell but precipitation as given by GPM (red line) centers at 12 m/s. This implies that when the backscattering is mainly impacted by the high wind speed, the detectability of rain cell signatures weakens.

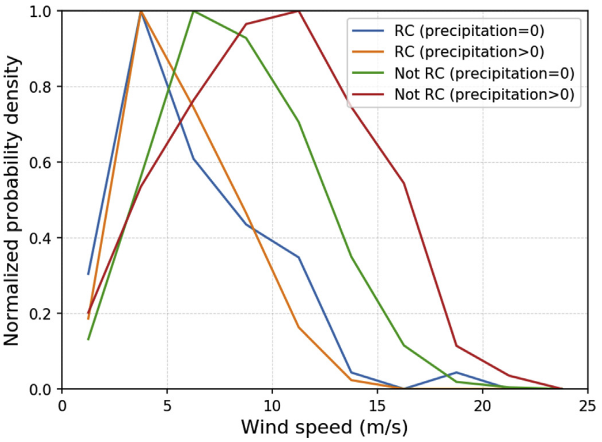

**Fig. 8.** Normalized probability density function of surface wind speed for the point-by-point comparisons with condition of rain cells are detected or not and precipitation is measurable or not.

From these comparisons, we conclude that Deep Learning methods can be used to automatically identify SAR images impacted by rain cells. As a matter of fact, the high resolution of SAR may complement the existing rainfall measurements available from space by detecting very short scale events. For now this potential seems limited to convective rain and is less relevant for high latitudes where sea state dominates the signature in SAR image, preventing for a reliable rain detection.

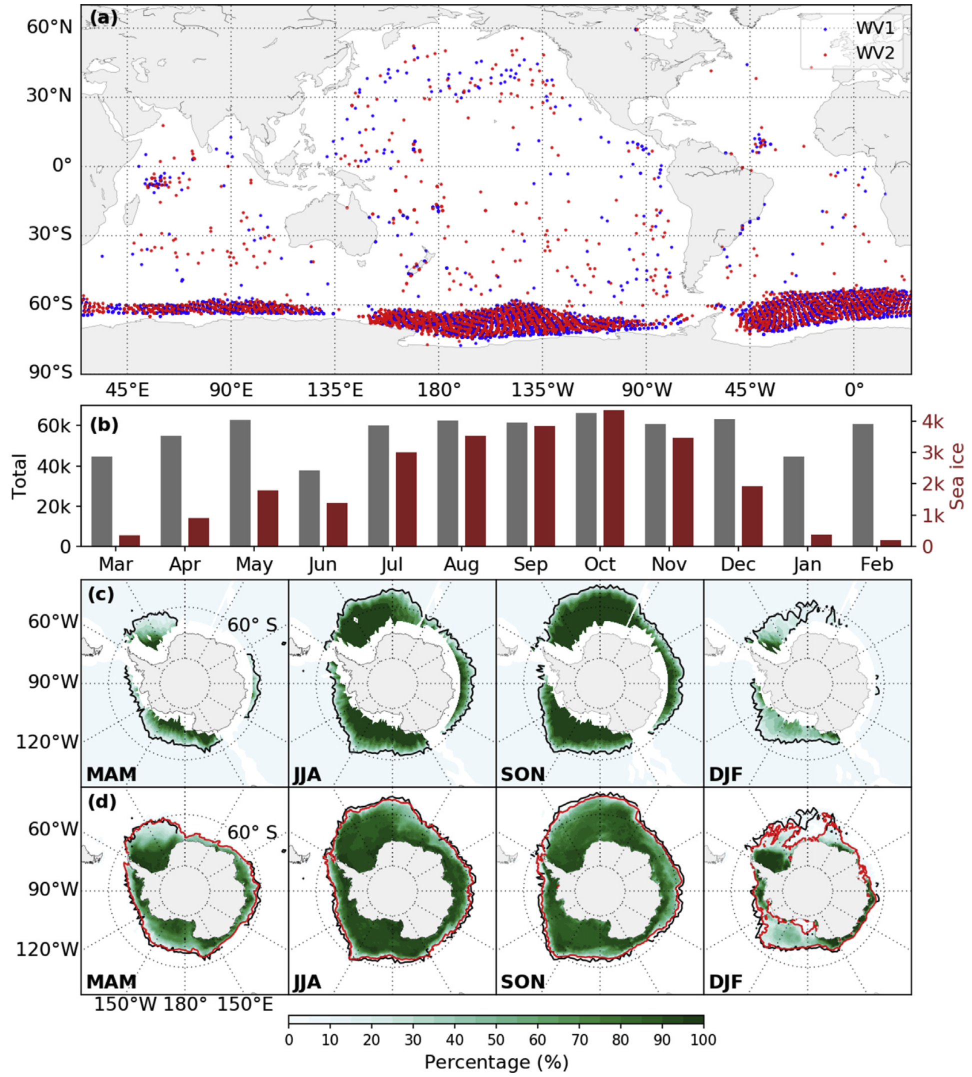

**Fig. 9.** Ocean sea ice around the Antarctica from March 2016 to February 2017. (a) displays the locations of classified sea ice vignettes with blue and red colors indicating WV1 and WV2, respectively. (b) presents the total number of S-1A and sea ice detected vignettes for each month. Sea ice coverage in four seasons derived from the classified SAR vignettes are shown in (c) with color representing the occurrence percentage in 2° boxes. (d) shows the mean sea ice concentration from the SSM/I daily product. Contour lines in (c) and (d) are calculated from the occurrence percentage (black, 10%) and sea ice concentration (red, 10%), denoting the ice-water boundaries. (For interpretation of the references to color in this figure legend, the reader is referred to the Web version of this article.)

### *4.2. Sea ice near Antarctica*

Interactions between sea ice, ocean, and the atmosphere in polar regions significantly impact global weather and climate systems (Fyke et al., 2018). Changing boundaries between the ocean and sea ice have dominant effects on marine ecosystem structure around the Antarctic (Tynan, 1998; Nicol et al., 2000). Monitoring of Southern Ocean sea ice has thus been of high interest among remote sensing and geoscience communities for many years. In this subsection, we assess sea ice (SeaIce) detected by CMwv near the Antarctica using S-1A WV SAR vignettes from March 2016 to February 2017. Note that our classification model distinguishes all type of SeaIce images from open ocean water.

In total, there are nearly 25k vignettes classified as SeaIce. As shown in Fig. 9 (a), most S-1A vignettes indicating SeaIce are distributed across the polar Southern Ocean. While the SeaIce subset mapping clearly shows a few misclassified cases of small islands, heavy rain and strong convection phenomena, the otherwise realistic geographic SeaIce distribution appears to confirm the high classification precision of 0.96 (see Table 1). Although the reason for misclassifications need further investigation, these misclassified SeaIce images can be easily filtered out according to the latitudes or SeaIce events occurrence map (see Fig. 9 (c)). Fig. 9 (b) provides the number of classified SeaIce SAR vignettes per month. As expected, the number of detected SeaIce vignettes has a clear seasonal variability, increasing from March to a maximum in October and subsequently decreasing. This variation is highly consistent with the seasonal cycle of Antarctic SeaIce extent (Doddridge and Marshall, 2017).

S-1A detected SeaIce occurrence is calculated on a 2° by 2° grid and shown in Fig. 9 (c). It illustrates the seasonal variation view of SeaIce coverage around the Antarctica. The SeaIce extent is also denoted by the contour lines where occurrence percentage is equal to 10%. In the austral summer (DJF and MAM), most of the classified SeaIce lies close to the Antarctica and is poleward of 60°S. It is also clear that the SeaIce extent is non-uniformly distributed along the Antarctic coasts, with more SeaIce from 0°-60°W, and from 120°W-150°E. Varied SeaIce coverage also exists in the Antarctic winter from JJA to SON. As shown in Fig. 9 (c), winter period SeaIce significantly expands in comparison to the austral summer. It even spreads north of 60°S between 10°E and 70°W during the summer. It is important to note that there is no WV SAR data acquired very close to the coast of or over Antarctica (Torres et al., 2012). This is the reason for the null/white space around the coastline in these maps. For comparison, seasonal maps of mean SeaIce concentration from the SSM/I daily product are provided in Fig. 9 (d). Contour lines of SeaIce edge calculated from both the occurrence percentage (black) and SeaIce concentration (red) are superimposed on these maps. As shown, the patterns seen on the SAR-detected SeaIce largely mirrors these SeaIce concentration maps where both systems collect data. Boundaries between ocean water and SeaIce from SAR and SSM/I data are highly consistent with each other. This agreement is another measure of CMwv credibility as an WV data classification tool.

As demonstrated, these high-resolution WV acquisitions of SeaIce are another data catalogue to monitor SeaIce edge boundaries around the Antarctica. In particular, they can benefit the survey of wave-ice interactions. Indeed, a new method has been recently developed to derive the directional wave spectrum in the sea-ice, from which wave heights, periods and directions can be derived (Ardhuin et al., 2015). Stopa et al. (2018) used these extensive information to address the wave forces on sea ice through break-up and rafting, advancing the knowledge of wave-ice dynamics. With respect of the waves and sea ice interactions, the use of sea-ice classification in combination with waves-in-ice algorithm is certainly a perspective.

## 5. Conclusions

The S-1 WV SAR vignette classification model (CMwv) has been successfully developed by a SAR-adaptation of the Inception-v3 CNN image recognition architecture. Experimental testing of the training process indicates that fine-tuning is a more effective approach than transfer-learning. The CMwv mode is able to identify and assign detection probabilities to ten geophysical phenomena that are pre-defined in a hand-labelled dataset (TenGeoP-SARwv, Wang et al. (2018b)). To evaluate and quantify the performance of CMwv, recall, precision and F-scores are calculated against an independent assessment dataset. Results show that this classification tool works well for classes of WindStreak (wind streaks), WindCell (micro-convective cells), RainCell (rain cells), BioSlick (biological slicks), SeaIce (sea ice) and LowWind (low wind area). However, classification of PureWave (pure ocean waves) is limited with very high precision, but low recall. Class detections for IceBerg (icebergs), AtmFront (atmospheric fronts) and OcnFront (oceanic fronts) are severely influenced by PureWave and the special category of TheOther. The developed classification model can directly be applied to S-1A&B WV datasets. In the near future, efforts to improve the classification of PureWave, IceBerg, AtmFront and OcnFront are necessary. In addition, the inclusion of new classes corresponding to other geophysical phenomena and the definition of a multi-labelled dataset would likely yield further improvements.

Two geophysical applications are demonstrated based on the classification results of S-1A WV vignettes from March 2016 to February 2017. Geophysical maps of classified rain cells and sea ice are qualitatively comparable to precipitation data from GPM and sea ice concentration from SSM/I. Results further verify the credibility of this classification tool. Moreover, once classified, access to the large catalogue of class-specific high-resolution WV vignettes may provide new and more detailed geophysical information to complement existing global ocean satellite measurements. The various geophysical phenomena captured within the massive S-1 A&B WV data suggest promise to further advance our understanding of air-sea interactions, particularly at sub-kilometer scales. Application of this CMwv tool to the growing three plus year of S-1 global ocean SAR data archive should allow, for the first time, access to the spatial (global and regional) and temporal (seasonal and inter-annual) statistics of numerous geophysical phenomena. This may, in turn, help to advance certain aspects of atmospheric and climate theory and numerical ocean and weather models.

This present work provides a basis to move application of ocean SAR remote sensing beyond the case study stage. It also demonstrates the potential of these global SAR WV mode vignettes for broader geophysical application, augmenting its operational role supporting ocean wave prediction systems. While this study is limited to the S-1 WV SAR acquisitions, the methodology could be applied to any other sub-scene (10–20 km) SAR data products from platforms such as ERS-1/2, Envisat/ASAR, TerraSAR-X, Gaofen-3 and CFOSAT. Similar exploitation of the full WV mode SAR data archive could provide a long-term (nearly 30 years) climatology including data on interannual and seasonal variability at global scale.

## Acknowledgements

The authors are grateful to NASA, IFREMER and ECMWF for providing the rain, sea ice and wind data that are used in this study. We acknowledge the Sentinel-1 SAR data access via ESA and through Sentinel-1A Mission Performance Center (4000107360/12/I-LG). This study is also supported by S1–4SCI Ocean Study (4000115170/15/I-SBo), CNES TOSCA program (COWS project) and NASA Physical Oceanography grant (NNX17AH17G). C. Wang thanks to the financial support of China Scholarship Council (CSC) for his PhD. Additionally, we would like to thank the anonymous reviewers for their constructive comments concerning this manuscript.

## Appendix A. Supplementary data

Supplementary data to this article can be found online at https://doi.org/10.1016/j.rse.2019.111457.

## References

Adler, R.F., Huffman, G.J., Chang, A., Ferraro, R., Xie, P.P., Janowiak, J., Rudolf, B., Schneider, U., Curtis, S., Bolvin, D., Gruber, A., Susskind, J., Arkin, P., Nelkin, E., 2003. The version-2 global precipitation climatology project (GPCP) monthly precipitation analysis (1979–present). J. Hydrometeorol. 4, 1147–1167.

Alpers, W., Brümmer, B., 1994. Atmospheric boundary layer rolls observed by the synthetic aperture radar aboard the ERS-1 satellite. J. Geophys. Res.: Oceans 99, 12613–12621.

Alpers, W., Huang, W., 2011. On the discrimination of radar signatures of atmospheric gravity waves and oceanic internal waves on synthetic aperture radar images of the sea surface. IEEE Trans. Geosci. Remote Sens. 49, 1114–1126.

Alpers, W., Zhang, B., Mouche, A., Zeng, K., Chan, P.W., 2016. Rain footprints on c-band synthetic aperture radar images of the ocean - revisited. Remote Sens. Environ. 187, 169–185.

Alpers, W.R., Ross, D.B., Rufenach, C.L., 1981. On the detectability of ocean surface waves by real and synthetic aperture radar. J. Geophys. Res.: Oceans 86, 6481–6498.

Ardhuin, F., Collard, F., Chapron, B., Girard-Ardhuin, F., Guitton, G., Mouche, A., Stopa, J.E., 2015. Estimates of ocean wave heights and attenuation in sea ice using the sar wave mode on sentinel-1a. Geophys. Res. Lett. 42, 2317–2325. https://agupubs.onlinelibrary.wiley.com/doi/pdf/10.1002/2014GL062940.

Atkinson, B.W., Wu Zhang, J., 1996. Mesoscale shallow convection in the atmosphere. Rev. Geophys. 34, 403.

Atlas, D., 1994. Origin of storm footprints on the sea seen by synthetic aperture radar. Science 266, 1364–1366.

Babin, S.M., Sikora, T.D., Winstead, N.S., 2003. A case study of satellite synthetic aperture radar signatures of spatially evolving atmospheric convection over the western atlantic ocean. Boundary-Layer Meteorol. 106, 527–546.

Bianco, S., Cadene, R., Celona, L., Napoletano, P., 2018. Benchmark analysis of representative deep neural network architectures. IEEE Access 6, 64270–64277.

Carsey, F., Holt, B., 1987. Beaufort-Chukchi ice margin data from seasat: ice motion. J. Geophys. Res.: Oceans 92, 7163.

Cheng, G., Han, J., 2016. A Survey on Object Detection in Optical Remote Sensing Images, vol. 1603. pp. 06201.

Cheng, G., Han, J., Lu, X., 2017. Remote sensing image scene classification: benchmark and state of the art. Proc. IEEE 105, 1865–1883 1703.00121.

Chunchuzov, I., Vachon, P.W., Li, X., 2000. Analysis and modeling of atmospheric gravity waves observed in RADARSAT SAR images. Remote Sens. Environ. 74, 343–361.

Collard, F., Ardhuin, F., Chapron, B., 2009. Monitoring and analysis of ocean swell fields from space: new methods for routine observations. J. Geophys. Res.: Oceans 114, C07023.

Doddridge, E.W., Marshall, J., 2017. Modulation of the seasonal cycle of Antarctic Sea ice extent related to the southern annular mode. Geophys. Res. Lett. 44, 9761–9768.

Ezraty, R., Girard-Ardhuin, F., Piolle, J.f., Kaleschke, L., Heygster, G., 2007. Arctic & Antarctic Sea Ice Concentration and Arctic Sea Ice Drift Estimated from Special Sensor MIcrowave Data - User's Manual V2, vol. 1.

Fu, L.L., Holt, B., 1982. Seasat Views Oceans and Sea Ice with Synthetic-Aperture Radar. Technical Report. California Institute of Technology, Jet Propulsion Laboratory.

Fyke, J., Sergienko, O., Löfverström, M., Price, S., Lenaerts, J., 2018. An overview of interactions and feedbacks between ice sheets and the Earth system. Rev. Geophys. 56, 361–408.

Gerling, T.W., 1986. Structure of the surface wind field from the Seasat SAR. J. Geophys. Res. 91, 2308.

Hasselmann, K., Hasselmann, S., 1991. On the nonlinear mapping of an ocean wave spectrum into a synthetic aperture radar image spectrum and its inversion. J. Geophys. Res.: Oceans 96, 10713–10729.

Hasselmann, K., Raney, R.K., Plant, W.J., Alpers, W., Shuchman, R.A., Lyzenga, D.R., Rufenach, C.L., Tucker, M.J., 1985. Theory of synthetic aperture radar ocean imaging: a MARSEN view. J. Geophys. Res.: Oceans 90, 4659–4686.

Heimbach, P., Hasselmann, S., Hasselmann, K., 1998. Statistical analysis and intercomparison of WAM model data with global ERS-1 SAR wave mode spectral retrievals over 3 years. J. Geophys. Res. 103, 7931–7977.

Hou, A.Y., Kakar, R.K., Neeck, S., Azarbarzin, A.A., Kummerow, C.D., Kojima, M., Oki, R., Nakamura, K., Iguchi, T., 2014. The Global Precipitation Measurement Mission. Bulletin of the American Meteorological Society.

Houze, R.A., 1997. Stratiform precipitation in regions of convection: a meteorological paradox? Bull. Am. Meteorol. Soc. 78, 2179–2196 arXiv:0801.1618v2.

Hu, F., Xia, G.S., Hu, J., Zhang, L., 2015. Transferring deep convolutional neural networks for the scene classification of high-resolution remote sensing imagery. Remote Sens. 7, 14680–14707.

Jackson, C.R., Apel, J.R. (Eds.), 2004. Synthetic Aperture Radar Marine User's Manual. US Department of Commerce, National Oceanic and Atmospheric Administration, National Environmental Satellite, Data, and Information Serve, Office of Research and Applications.

Jia, T., Liang, J.J., Li, X.M., Sha, J., 2018. SAR observation and numerical simulation of internal solitary wave refraction and reconnection behind the dongsha atoll. J. Geophys. Res.: Oceans 123, 74–89.

Johannessen, J.a., Shuchman, R.a., Digranes, G., Lyzenga, D.R., Wackerman, C., Johannessen, O.M., Vachon, P.W., 1996. Coastal ocean fronts and eddies imaged with ERS 1 synthetic aperture radar. J. Geophys. Res. 101, 6651.

Katsaros, K.B., Brown, R.A., 1991. Legacy of the Seasat Mission for Studies of the Atmosphere and Air-Sea-Ice Interactions. Bulletin of the American Meteorological Society.

Kerbaol, V., Chapron, B., Vachon, P.W., 1998. Analysis of ERS-1/2 synthetic aperture radar wave mode imagettes. J. Geophys. Res.: Oceans 103, 7833–7846.

Kidd, C., 2001. Satellite rainfall climatology: a review. Int. J. Climatol. 21, 1041–1066.

LeCun, Y., Bengio, Y., Hinton, G., 2015. Deep learning. Nature 521, 436–444 arXiv:1312.6184v5.

Lehner, S., Schulz-Stellenfleth, J., Schättler, B., Breit, H.H., Horstmann, J., 2000. Wind and wave measurements using complex ERS-2 SAR wave mode data. IEEE Trans. Geosci. Remote Sens. 38, 2246–2257.

Levy, G., 2001. Boundary layer roll statistics from SAR. Geophys. Res. Lett. 28, 1993–1995.

Li, W., Wu, G., Zhang, F., Du, Q., 2017. Hyperspectral image classification using deep pixel-pair features. IEEE Trans. Geosci. Remote Sens. 55, 844–853.

Li, X., Zheng, W., Pichel, W.G., Zou, C.Z., Clemente-Colón, P., 2007. Coastal katabatic winds imaged by SAR. Geophys. Res. Lett. 34.

Li, X., Zheng, W., Yang, X., Zhang, J.A., Pichel, W.G., Li, Z., 2013. Coexistence of atmospheric gravity waves and boundary layer rolls observed by SAR*. J. Atmos. Sci. 70, 3448–3459.

Meadows, G.A., Shuchman, R.A., Tseng, Y.C., Kasischke, E.S., 1983. Seasat synthetic aperture radar observations of wave-current and wave-topographic interactions. J. Geophys. Res. 88, 4393.

Mouche, A.A., Collard, F., Chapron, B., Dagestad, K.F., Guitton, G., Johannessen, J.A., Kerbaol, V., Hansen, M.W., 2012. On the use of Doppler shift for sea surface wind retrieval from SAR. IEEE Trans. Geosci. Remote Sens. 50, 2901–2909.

Nicol, S., Pauly, T., Bindoff, N.L., Wright, S., Thiele, D., Hosle, G.W., Strutton, P.G., Woehler, E., 2000. Ocean circulation off east Antarctica affects ecosystem structure and sea-ice extent. Nature 406, 504–507.

Rascle, N., Molemaker, J., Marié, L., Nouguier, F., Chapron, B., Lund, B., Mouche, A., 2017. Intense deformation field at oceanic front inferred from directional sea surface roughness observations. Geophys. Res. Lett. 44, 5599–5608.

Russakovsky, O., Deng, J., Su, H., Krause, J., Satheesh, S., Ma, S., Huang, Z., Karpathy, A., Khosla, A., Bernstein, M., Berg, A.C., Fei-Fei, L., 2015. ImageNet large scale visual recognition Challenge. Int. J. Comput. Vis. 1409, 0575.

Sikora, T.D., Young, G.S., Fisher, C.M., Stepp, M.D., 2011. A synthetic aperture radar-based climatology of open-cell convection over the northeast Pacific Ocean. J. Appl. Meteorol. Climatol. 50, 594–603.

Sokolova, M., Lapalme, G., 2009. A systematic analysis of performance measures for classification tasks. Inf. Process. Manag. 45, 427–437.

Stehman, S.V., 1997. Selecting and Interpreting Measures of Thematic Classification Accuracy. Remote Sensing of Environment.

Stopa, J.E., Ardhuin, F., Husson, R., Jiang, H., Chapron, B., Collard, F., 2016. Swell dissipation from 10 years of Envisat advanced synthetic aperture radar in wave mode. Geophys. Res. Lett. 43, 3423–3430.

Stopa, J.E., Mouche, A., 2017. Significant wave heights from Sentinel-1 SAR: validation and applications. J. Geophys. Res.: Oceans 122, 1827–1848.

Stopa, J.E., Sutherland, P., Ardhuin, F., 2018. Strong and Highly Variable Push of Ocean Waves on Southern Ocean Sea Ice. Proceedings of the National Academy of Sciences.

Szegedy, C., Liu, W., Jia, Y., Sermanet, P., Reed, S., Anguelov, D., Erhan, D., Vanhoucke, V., Rabinovich, A., 2015. Going deeper with convolutions. In: Proceedings of the IEEE Computer Society Conference on Computer Vision and Pattern Recognition, pp. 1–9 1409.4842.

Szegedy, C., Vanhoucke, V., Ioffe, S., Shlens, J., Wojna, Z., 2016. Rethinking the inception architecture for computer vision. In: 2016 IEEE Conference on Computer Vision and Pattern Recognition (CVPR), pp. 2818–2826.

Too, E.C., Yujian, L., Njuki, S., Yingchun, L., 2018. A Comparative Study of Fine-Tuning Deep Learning Models for Plant Disease Identification.

Topouzelis, K., Kitsiou, D., 2015. Detection and classification of mesoscale atmospheric phenomena above sea in SAR imagery. Remote Sens. Environ. 160, 263–272.

Torres, R., Snoeij, P., Geudtner, D., Bibby, D., Davidson, M., Attema, E., Potin, P., Rommen, B.r., Floury, N., Brown, M., Traver, I.N., Deghaye, P., Duesmann, B., Rosich, B., Miranda, N., Bruno, C., L'Abbate, M., Croci, R., Pietropaolo, A., Huchler, M., Rostan, F., 2012. GMES Sentinel-1 mission. Remote Sens. Environ. 120, 9–24.

Tynan, C.T., 1998. Ecological importance of the southern boundary of the antarctic circumpolar current. Nature, 0402594v3.

Wang, C., Mouche, A., Tandeo, P., Stopa, J., Chapron, B., Foster, R., Vandemark, D., 2018a. Automated geophysical classification of sentinel-1 wave mode SAR images through deep-learning. In: IGARSS 2018 - 2018 IEEE International Geoscience and Remote Sensing Symposium, IEEE, pp. 1776–1779.

Wang, C., Mouche, A., Tandeo, P., Stopa, J., Longépé, N., Erhard, G., Foster, R., Vandemark, D., Chapron, B., 2018b. Labeled SAR Imagery Dataset of Ten Geophysical Phenomena from Sentinel-1 Wave Mode. TenGeoP-SARwv).

Wang, C., Mouche, A., Tandeo, P., Stopa, J.E., Longépé, N., Erhard, G., Foster, R.C., Vandemark, D., Chapron, B., 2019. A labelled ocean SAR imagery dataset of ten geophysical phenomena from Sentinel1 wave mode. Geosci. Data J. 0 gdj3.73.

Winstead, N.S., Colle, B., Bond, N., Young, G., Olson, J., Loescher, K., Monaldo, F., Thompson, D., Pichel, W., 2006. Using Sar Remote Sensing, Field Observations, and Models to Better Understand Coastal Flows in the Gulf of alaska. Bulletin of the American Meteorological Society.

Yosinski, J., Clune, J., Bengio, Y., Lipson, H., 2014. How transferable are features in deep neural networks? In: In: Ghahramani, Z., Welling, M., Cortes, C., Lawrence, N.D., Weinberger, K.Q. (Eds.), Advances in Neural Information Processing Systems, vol. 27. Curran Associates, Inc., pp. 3320–3328.

Young, G.S., Sikora, T.N., Winstead, N.S., 2005. Use of synthetic aperture radar in finescale surface analysis of synoptic-scale fronts at sea. Weather Forecast. 20, 311–327.

Zhang, L., Zhang, L., Du, B., 2016. Deep learning for remote sensing data: a technical tutorial on the state of the art. IEEE Geosci. Remote Sens. Mag. 4, 22–40.

Zhao, W., Du, S., 2016. Spectral-spatial feature extraction for hyperspectral image classification: a dimension reduction and deep learning approach. IEEE Trans. Geosci. Remote Sens. 54, 4544–4554.

Zhao, Y., Li, X.M., Sha, J., 2016. Sea surface wind streaks in spaceborne synthetic aperture radar imagery. J. Geophys. Res.: Oceans 121, 6731–6741.

Zhou, W., Newsam, S., Li, C., Shao, Z., 2017. Learning low dimensional convolutional neural networks for high-resolution remote sensing image retrieval. Remote Sens. 9, 489.

Zhu, X.X., Tuia, D., Mou, L., Xia, G.S., Zhang, L., Xu, F., Fraundorfer, F., 2017. Deep Learning in Remote Sensing: A Comprehensive Review and List of Resources, vol. 1710. pp. 03959.

## 3.3 An assessment of marine atmospheric boundary layer roll detection using Sentinel-1 SAR data

Remote Sensing of Environment 250 (2020) 112031

Contents lists available at ScienceDirect

Remote Sensing of Environment

journal homepage: www.elsevier.com/locate/rse

# An assessment of marine atmospheric boundary layer roll detection using Sentinel-1 SAR data

Chen Wang[a,b,*], Douglas Vandemark[c], Alexis Mouche[a], Bertrand Chapron[a], Huimin Li[d], Ralph C. Foster[e]

[a] *IFREMER, Univ. Brest, CNRS, IRD, Laboratoire d'Oceanographie Physique et Spatiale (LOPS), Brest, France*
[b] *IMT Atlantique, Lab-STICC, UBL, Brest, France*
[c] *Ocean Processes Analysis Laboratory, University of New Hampshire, Durham, NH, USA*
[d] *School of Marine Sciences, Nanjing University of Information Science and Technology, Nanjing, China*
[e] *Applied Physics Laboratory, University of Washington, Seattle, WA, USA*

ARTICLE INFO

*Keywords:*
Marine atmospheric boundary layer rolls
Surface wind perturbation
Synthetic aperture radar (SAR)
Sentinel-1 wave mode
Imaging sensitivity

ABSTRACT

The ability of high-resolution synthetic aperture radar (SAR) to detect marine atmospheric boundary layer (MABL) roll-induced roughness modulation of the sea surface wave field is well known. This study presents SAR measurements of MABL rolls using global coverage data collected by the European Space Agency's C-band Sentinel-1A satellite in 2016–2017. An automated classifier is used to identify likely roll events from more than 1.3 million images that were acquired at two incidence angles of 23° and 36.5° in either VV or HH polarization. Characteristics of the detected rolls are examined for different wind speeds, polarizations, incidence and relative azimuth angles. Roll detection counts are much higher at the higher incidence angle and nearly equivalent for VV and HH polarizations. Detection depends strongly on the relative azimuth with roll detection rates at crosswind being 3–10 times lower than for up- or downwind. All data show a low wind speed threshold near 2 m s$^{-1}$ and that rolls are most commonly observed at wind speeds near 9 m s$^{-1}$. For all viewing configurations, we find that rolls induce a wide range of mean surface wind speed modulation with the most frequent value being 8% ( ± 3.5%). Roll detection at crosswind is associated with stronger roll-induced surface wind enhancement. Dependencies of roll detection on the incidence and relative azimuth angles are consistent with rapid short-scale wind-wave adjustments to the roll-induced surface wind gusts. These cm-scale waves are highly directional and provide limited crosswind backscatter at shallower incidence angles. The same roll-induced surface forcing is thus not equally detectable at all viewing geometries or polarizaions. Stronger and possibly longer-duration wind forcing is likely needed to produce detectable roll-induced modulations at crosswind.

## 1. Introduction

The mean flow in the marine atmospheric boundary layer (MABL) frequently includes an organized secondary circulation in the form of long helical rolls that are approximately aligned along the mean wind direction. They are sometimes made visible by the low-level cloud streets that form in the organized updrafts between rolls (Weston, 1980; Hein and Brown, 1988; Rowe and Houze, 2015). However, rolls are a common feature of the MABL when shear production of turbulence plays an important role and are thus frequently present in the absence of clouds. Investigation of the phenomenon extends back decades, including field, theoretical, numerical, and experimental efforts (Kuettner, 1959; LeMone, 1973; Brown, 1980; Etling and Brown, 1993; Atkinson and Wu Zhang, 1996; Young et al., 2002), and there is evidence that these coherent structures have a measurable impact on turbulent fluxes of heat and momentum across the MABL (Glendening, 1996; Zhang et al., 2008; Zhu, 2008; Brilouet et al., 2017). This inhomogeneous contribution is seldom included in the standard boundary layer parameterizations used in weather forecast and climate models. This is largely because the process occurs at small horizontal length scales that are within the so-called numerical modeling grey zone of 1–10 km (Shin and Hong, 2013; Bauer et al., 2015). Moreover, because they are often invisible to standard remote or in situ sensors, even basic measures of roll characteristics over the oceans have not been established. The fundamental particulars are the frequency of occurrence, strength, wave length, alignment direction, and formation conditions

---

* Corresponding author at: IFREMER & IMT Atlantique, Lab-STICC, UBL, Brest, France.
*E-mail address:* Chen.Wang@ifremer.fr (C. Wang).

https://doi.org/10.1016/j.rse.2020.112031
Received 3 April 2020; Received in revised form 1 August 2020; Accepted 3 August 2020

(Levy, 2001; Weckwerth et al., 1997; Zhao et al., 2016; Atkinson and Wu Zhang, 1996; Young et al., 2002).

Synthetic aperture radar (SAR) ocean imagery is able to resolve the parallel backscatter streaks that are associated with the roll-induced surface wind stress changes in day-and-night and most weather conditions (Gerling, 1986; Alpers and Brümmer, 1994; Young, 2000; Vandemark et al., 2001). Case studies using ocean SAR measurements have been conducted to examine MABL rolls in numerous air-sea investigations (Alpers and Brümmer, 1994; Li et al., 2013; Zhao et al., 2016; Babin et al., 2003; Sikora et al., 2011; Alpers et al., 2016). These applications have been limited in scope and mostly dedicated to coastal regions because wide-swath ocean SAR imagery is not acquired routinely nor globally. But a narrow swath option with nearly global coverage, sufficient resolution and scene size has been available from the Sentinel-1 SAR satellites since 2014 (Torres et al., 2012). The SAR Wave Mode (WV) extends a legacy of global ocean surface wave monitoring from previous satellite SAR missions. For the purposes of MABL studies, the two most important differences of S-1 WV compared to the legacy data is the increase in image size to 20 by 20 km, while retaining a high spatial resolution of 5 m pixels, and the addition of a higher incidence angle sample. The European Space Agency (ESA) currently operates two identical Sentinel-1 (S-1) satellites (A&B) for Copernicus that routinely collect ~130,000 images each month over most of the ocean surface. At the time of this writing, more than six million images have been acquired.

A required first step for MABL roll studies using SAR data is event detection (Weckwerth et al., 1997; Young et al., 2008). To date, visual inspection has been used to determine the presence of roll imprints in SAR images (e.g. Levy, 2001; Zhao et al., 2016). Given the large number of S-1 WV scenes, as automated method is required. A machine learning tool for S-1 WV image classification was developed from the Inception-v3 convolutional neural network (CNN) to classify each WV image into one of the ten different geophysical categories (Wang et al., 2019b). Note that this classifier very rarely tags non-roll events as rolls but can miss-categorize roll events into other classes. The present study uses only the images that are classified as roll events. More than 1.3 million WV SAR scenes collected in 2016–2017 were analyzed for the presence of MABL rolls, resulting in ~155,000 roll cases in total. This far surpasses the largest previous SAR MABL roll study of Levy (2001), for which, 7150 SAR images were examined.

The S-1 WV SAR images are acquired at two fixed incidence angles of 23° (WV1) and 36.5° (WV2), and with two transmit and receive linear polarization configurations, VV (default) and HH (experimental). This provides an opportunity for rigorous evaluation of C-band SAR detection and imaging of MABL rolls for varied wind speeds and radar viewing geometries. These characteristics have received limited attention in most previous SAR-based MABL roll investigations (Alpers and Brümmer, 1994; Young, 2000; Sikora and Ufermann, 2004; Li et al., 2013; Zhao et al., 2016), and in ocean SAR studies where the surface wind direction is inferred from roll imprint analyses (Gerling, 1986; Koch, 2004; Christiansen et al., 2006; Lin et al., 2008; Li and Lehner, 2014; Zecchetto, 2018). Alpers and Brümmer (1994) proposed that SAR backscatter due to the roll-induced wave-roughening can be interpreted using the empirical geophysical model functions (GMFs) that relate 20–40 km scale radar scatterometer measurements to surface wind speed and radar viewing geometry. However, field measurements have shown that surface wind-wave and radar backscatter changes during roll impacts are associated with short-duration and short length-scale wind forcing (Vandemark et al., 2001). These roll-induced forces primarily affect the shortest and highly directional wind waves, and not the whole spectrum of surface waves (LeMone, 1973; Lemone, 1976; Young, 2000; Mourad et al., 2000; Vandemark et al., 2001). This interpretation is used to explain the results regarding MABL roll detection and sea surface modulation using the global S-1 WV SAR data that are presented in this paper, and to explain the differences between WV observations and a GMF applied to these observations.

The paper is organized as follows. Data and methods are described in Section 2, including the S-1 WV SAR data, supporting surface environmental variables, and a description of the methods used to classify WV images and to estimate the radar backscatter modulation related to roll-induced wind perturbations. Statistics of the identified MABL roll events are given in Section 3. Section 4 provides analyses of the extracted roll modulation parameters, and compared them to a GMF simulation. Discussions and conclusions follow in Section 5.

## 2. Data and methods

### 2.1. Sentinel-1 WV

Sentinel-1 is a polar-orbiting, sun-synchronous SAR satellite constellation mission designed for long-term operation extending into the next decades. Currently, two satellites (A&B), which share the same orbital plane offset by a 180° phase difference, were launched in April of 2014 and 2016, respectively (Torres et al., 2012). The satellites are equipped with identical C-band SAR instruments that operate in four pre-programmed imaging modes: Interferometric Wide swath, Extra Wide swath, Strip Map and WaVe mode (WV). WV is the default mode over the world's ocean except in the Arctic, closed seas and coastal areas, or when S-1 has not been programmed to one of the other imaging modes. There is no WV data acquisition over land except the Amazon rainforest for calibration purposes. WV acquires small SAR image scenes (termed imagettes) at alternating incidence angles of 23° (WV1) and 36.5° (WV2). Both usually operate in linear vertical (VV) transmit and receive polarization and, during special phases, in horizontal (HH) polarization. Each WV image size is 20 km by 20 km, with 5 m pixel resolution. Neighboring images are spaced by 100–120 km. The orbital repeat cycle is 12 days. Approximately 65,000 imagettes per month are collected by each satellite. The S-1 WV SAR data used in this paper are the Level-1 Single Look Complex (SLC) repository, which are managed at IFREMER (http://www.ifremer.fr/datavore/exp/dvor/#/s1quicklook), and are also freely available at ESA's Sentinel Open Access Hub (https://sentinel.esa.int/web/sentinel/sentinel-data-access).

This study uses S-1A WV SAR data in VV polarization spanning 2016–2017, and S-1B WV data in HH polarization from 15 March to 01 July 2017. Inland, near-coastal and poleward of 55° to avoid possible sea ice images are removed. Fig. 1 illustrates the sample population for the VV and HH datasets on a 5° by 5° global spatial grid. The typical S-1 WV coverage is nearly complete over the Pacific, Indian and south Atlantic oceans. There is partial coverage for the eastern north Atlantic because, by default, other standard imaging modes are in operation. The total numbers of image evaluated from these S-1A and S-1B datasets are 1,182,540 and 197,442, respectively.

Each image is co-located in time and space with surface variables from the ERA5 hindcast model, including 10 m wind components, sea surface temperature, 2 m air temperature, 2 m dew-point temperature and surface pressure. ERA5 is the latest generation ECMWF reanalysis product and provides these environmental variables hourly on a global spatial grid of 0.25° by 0.25°. The data are publicly available at: https://cds.climate.copernicus.eu. From these variables, we estimate the bulk Richardson number $Ri_B$ at 10 m height, using the COARE 3.0 air-sea flux algorithm (Fairall et al., 2003).

### 2.2. Automated WV image classification

Oceanic SAR images have been used to identify numerous oceanic, atmospheric, and sea ice features (e.g. Jackson and Apel, 2004; Wang et al., 2019a, 2019b). The automated image classifier method applied to this WV data catalogue is briefly detailed here, with an emphasis on MABL roll identification (Wang et al., 2019a,). We first defined the ten most commonly observed geophysical phenomena in the WV image data (Wang et al., 2019a). These phenomena were ocean swell, wind streaks (induced by MABL rolls), micro-convective cells, rain cells, biological slicks, sea ice, icebergs, low wind areas, atmospheric fronts, and oceanic fronts. Visual selection was used to build a large representative collection for each class, leading to an open-access labelled database called TenGeoP-SARwv (Wang et al., 2018). We then developed an automated classification tool based on a

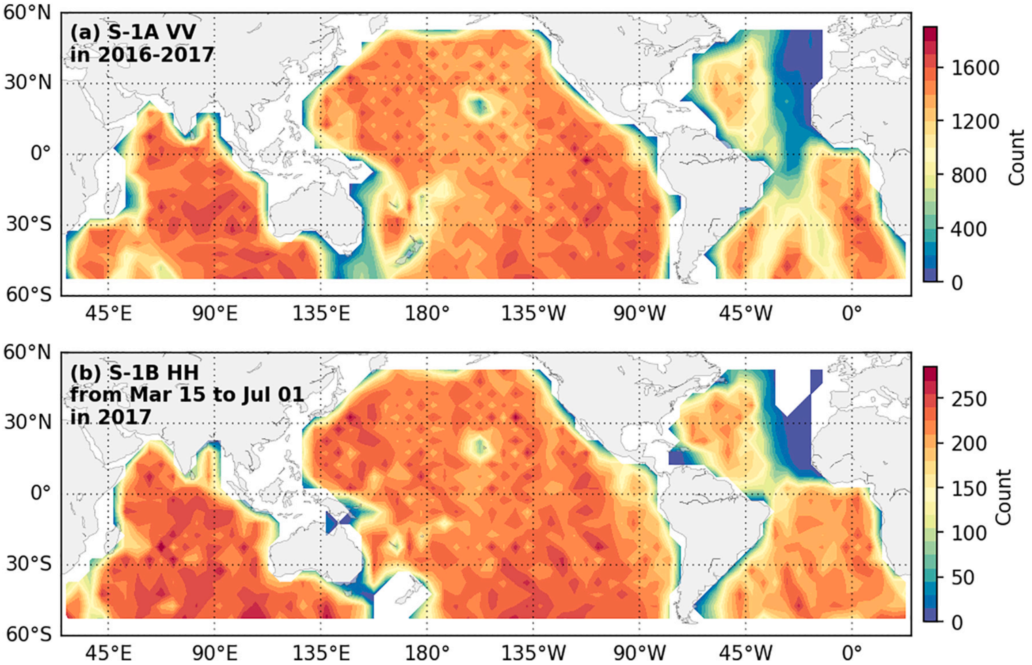

**Fig. 1.** Ocean SAR data coverage for S-1 study datasets, (a) S-1A in VV polarization in 2016–2017 and (b) S-1B in HH polarization, from 15 Mar to 01 Jul in 2017. Colour denotes the number of WV images within each 5° by 5° spatial bin. The total number of imagettes in these datasets is 1,182,540 and 197,442, respectively.

deep learning pattern recognition approach. The tool, namely CMwv, was created by fine-tuning the Inception-v3 deep convolutional neural network (CNN) to discriminate between the ten input training sets (Szegedy et al., 2016; Wang et al., 2019b). Separate CMwv models were built for VV-pol WV1 and WV2 data, which are applicable for both S-1A and S-1B WV SAR data. Although the model skill has only been formally evaluated for the VV-polarized SAR images, results suggested that it performs similarly for the HH SAR data, at least for the task of MABL roll identification and analyses presented in this study.

CMwv assigns each WV image probability scores for the ten pre-defined classes. These probabilities add up to 1, and a WV image is considered to represent a case of visually-distinct MABL roll impacts (i.e. wind streaks) if the roll class score is the largest among the ten. The quantified skill for this approach has a Recall (sensitivity) of 83% for both modes (WV1 and WV2), and Precision (positive detection rate) of 77% and 96% for WV1 and WV2, respectively (Wang et al., 2019b). The precision difference between WV1 and WV2 is likely due to a weaker MABL roll imprint in WV1 images, which is one focus of this study. Wang et al. (2019a, 2019b) documented that image contrasts due to roll imprints for WV2 were qualitatively stronger than for WV1 during the visual labelling procedure. Specific to the CMwv machine learning approach, the ability of this deep CNN model to differentiate between phenomena in each SAR image relies on the efficient extraction of optimal features into convolutional layers, and then to amplify feature differences through pooled layers (LeCun et al., 2015; Zhang et al., 2016). That is, distinct image features cannot be extracted if roll imprints are insufficiently clear. Even with these caveats, the overall CMwv precision scores are high. Potential study limitations due to the classification model are discussed in Section 5.

### *2.3. Extraction of roll-induced backscatter modulation amplitude and direction*

Prior to estimation of roll-induced SAR backscatter modulation for varying wind conditions, an objective SAR backscatter recalibration method is used to correct S-1 SAR normalized radar cross-section (NRCS, $\sigma^0$) as described in Li et al. (2019b). Specific details are provided in Appendix A.

Fig. 2 illustrates the process used to extract the roll-induced NRCS modulation from each WV roll imagette. The full resolution $\sigma^0$ image is box averaged to 200 m as shown in Fig. 2 (a), in order to filter out most of the ocean swell features. The chosen 200 m scale follows recommendations from previous studies (Koch, 2004; Horstmann and Koch, 2005; Christiansen et al., 2006). White and blue arrows in Fig. 2 (a) indicate North and the ERA5 10-m wind direction, respectively.

An image modulation spectrum $S(k_x, k_y)$ is calculated using a 2-D FFT over the full resolution $\sigma^0$ image. The spectrum $S(k_x, k_y)$ is converted from Cartesian to Polar coordinates, $S(k, \phi)$. Fig. 2 (b) displays the partial spectrum in the 0.8–4.0 km wavelengths band. The angle $\phi$ is in SAR image coordinates. $\phi = 0^\circ$ is in the increasing SAR azimuth direction along the satellite heading. $\phi = 90^\circ$ is in the increasing SAR range direction (S-1 looks to the right). Since there is a 180° direction ambiguity in wind streak orientation, the spectral energy peak maximises near $\phi = 140^\circ$ and $320^\circ$. Note that multiple peaks are visible, principally associated with irregularities in the main linear features throughout the image scene. Still a dominant azimuthal peak direction is apparent and similar FFT methodologies have been used to extract the dominant orientation of MABL rolls (Gerling, 1986; Mourad and Walter, 1996; Li et al., 2013; Huang et al., 2018). For the example case of Fig. 2, panel (c) shows the corresponding profile of $S(\phi) = \int_{k=2\pi/4000}^{k=2\pi/800} S(k, \phi) dk d\phi$ with the maximum shown as a red dot. The red arrow in Fig. 2 (a) defines this dominant roll direction $\phi_{WS}$ (with 180° ambiguity).

For each image, an estimate of the roll-induced $\sigma^0$ modulation along a 15 km transect is extracted. This $\sigma^0$ transect is located at the center of SAR scene and normal to the dominant wind streak direction, as shown in Fig. 2 (a). Five parallel lines (1 km width) of the backscatter are averaged and then smoothed using a Hanning window. As depicted in Fig. 2 (e), quasi-periodic $\sigma^0$ variations along the cross-roll transect are shown. The local maxima (red dots) and minima (blue dots) correspond to the alternating bright and dark bands on the backscatter image. The

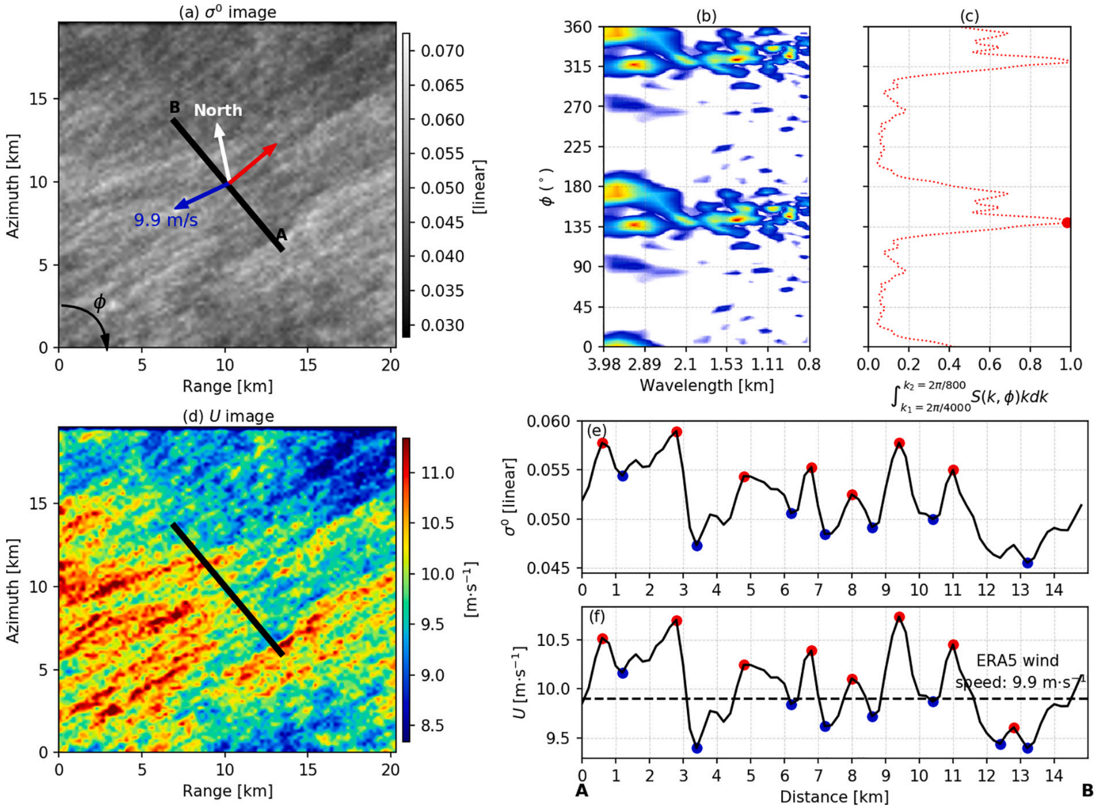

**Fig. 2.** Analysis of roll modulations in S-1 WV sea surface roughness images. Panel (a) is a typical roll image after smoothing to a 200-m pixel resolution $\sigma^0$ image. White, blue and red arrows indicate North, the ERA5 wind direction and extracted wind streak orientation, respectively. (b) 2-D FFT spectrum, $S(k, \phi)$, of the full resolution image within the expected wavenumber range of MABL patterns ($\lambda$ = 0.8 and 4 km). Angle $\phi$ is in SAR image coordinates, i.e. clockwise rotating from the azimuth to range direction. (c) Integral of S at each $\phi$, maximum marked as a red dot. (d) SAR-estimated wind speeds derived using the C-SARMOD GMF. (e) $\sigma^0$ transect profile along the black scan line in (a): from A to B. The profile (dashed line) has been smoothed with a 1 km length Hanning window. Red and blue dots indicate the detected local maximum and minimum. (f) similar to (e) but for SAR-retrieved local wind speed U. (For interpretation of the references to colour in this figure legend, the reader is referred to the web version of this article.)

distance between adjacent bright or dark (roll wavelength) varies from 1 to 3 km. It reveals local irregular roughness modulations with local changes of the surface wind intensity and/or direction, consistent with the multiple peaks present in the 2-D image spectrum. The modulation depth is defined as the difference between the mean bright ($\sigma_B^0$) and dark ($\sigma_D^0$) NRCS. The relative modulation depth, or contrast, is obtained after normalization by their average ($\sigma_B^0 + \sigma_D^0$)/2.

As shown in Fig. 2 (d), fine-scale (~200 m) surface wind speed is also retrieved from each down-sampled WV $\sigma^0$ imagette using the C-SARMOD GMF (Mouche and Chapron, 2015). Here we used the co-located ERA5 wind direction instead of the extracted roll direction as input to the GMF. Similar to above, a SAR-retrieved wind speed (U) cross-roll modulation transect is extracted and smoothed in Fig. 2 (f). The obtained wind variations range from 0.5–1.5 m s$^{-1}$.

In summary, the following parameters relevant to roll-induced impacts on sea surface roughness are extracted from each CMwv-identified MABL roll WV SAR scene:

1) $\phi_{WS}$ [°]: Roll orientation with 180° ambiguity in image coordinates: clockwise rotating from azimuth to range.
2) $\sigma_B^0$ [linear]: Mean NRCS for brightest roll modulation peaks.
3) $\sigma_D^0$ [linear]: Mean NRCS for the darkest roll modulation troughs.
4) $d\sigma^0 = \sigma_B^0 - \sigma_D^0$ [linear]: Modulation depth.
5) $d\sigma^0/\sigma^0 = d\sigma^0/[(\sigma_B^0 + \sigma_D^0)/2]$ [linear]: Roll-induced NRCS perturbation.
6) $U_B$ [$ms^{-1}$]: Mean of the wind speed peaks.
7) $U_D$ [$ms^{-1}$]: Mean of the wind speed troughs.
8) $dU/U = (U_B - U_D)/[(U_B + U_D)/2]$: SAR-derived wind speed perturbation due to rolls.

## 3. MABL roll occurrence rates

### 3.1. Occurrence statistics

The automated classification considers a SAR imagette as a MABL roll event if clear evidence of organized quasi-linear wind streaks can be distinguished, and they dominate scene compared to other possible geophysical phenomena. Fig. 3 shows the percentage of MABL roll events relative to the total number of WV scenes acquired in each month. The image count per month of approximately 20 k is about the same for WV1 and WV2. The overall fraction of identified roll events in WV2 is ~15%, while that for WV1 is ~9% with no apparent monthly variability in roll frequency observed for either WV1 or WV2. The higher identification rate for WV2 compared to WV1 is likely related to higher visibility of the roll-induced wind speed changes at the larger incidence angle. The percentages of CMwv-classified roll events using the much smaller S-1B HH SAR dataset are approximately 11% and 6% for WV2 and WV1, respectively (not shown). Note, these detection rates are significantly lower than the reported average of 40–50% using visually-selected images in coastal studies (Levy, 2001; Zhao et al., 2016).

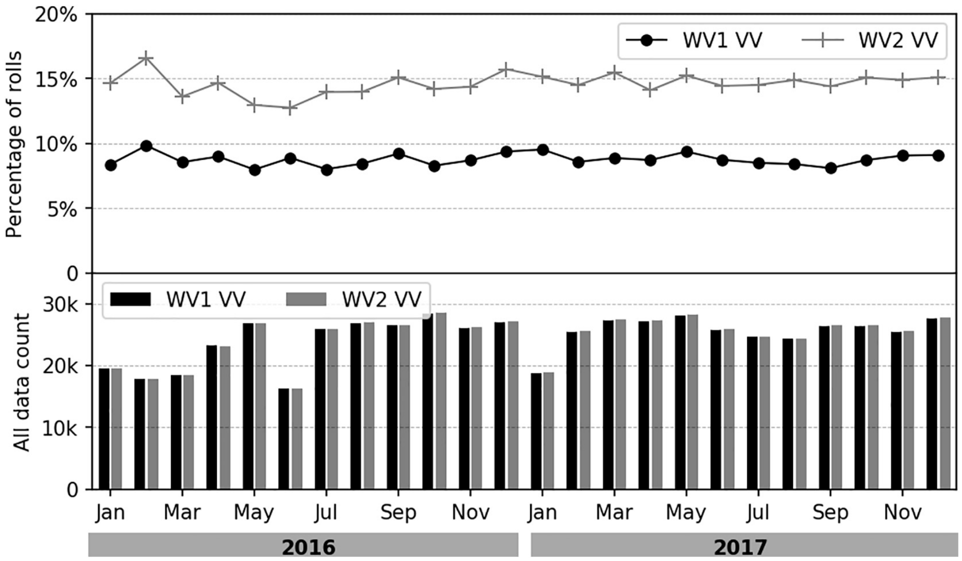

**Fig. 3.** Monthly statistics of detected roll events from all S-1A WV VV SAR imagettes. The top and bottom panels provide the percent-detected and the total number of imagettes examined in each month.

The probability density functions (PDFs) of the ERA5 surface wind speed when rolls were identified in the VV SAR data are shown in Fig. 4, along with the distribution for the entire S-1A WV dataset. The distributions for WV1 and WV2 roll events are similar. The most likely wind speed when rolls are identified is 9–10 m $s^{-1}$, which is higher than the 7 m $s^{-1}$ mode for the entire dataset. The low wind speed threshold for roll detection is near 2 to 3 m $s^{-1}$ for both WV1 and WV2. This is consistent with a postulated threshold of 3 m $s^{-1}$ (Weckwerth et al., 1997; Young et al., 2002; Zhao et al., 2016). The probability for roll detection rises rapidly with wind speed above this threshold. This is consistent with theoretical models that rolls usually form when shear production is an important aspect of the MABL dynamics (Brown, 1980; Etling and Brown, 1993).

MABL roll identification versus wind speed and relative azimuth, which is the angle between the radar beam and surface wind direction, is shown in Fig. 5. Data are averaged in 20° relative azimuth angle bins. Angles 0°, 90°/270° and 180° are indicative of upwind, crosswind and downwind radar viewing directions. The bottom panel of Fig. 5 shows the S-1A WV sampling as a function of relative azimuth. Because S-1 SAR is right-side-looking and in a polar orbit, more data are acquired in upwind and downwind looks compared to crosswind due to the prevailing low-latitude easterlies and mid-latitude westerlies. However, thousands of roll images are collected at crosswind, which are mostly associated with the meridional flow around low and high pressure centers in the mid-latitudes.

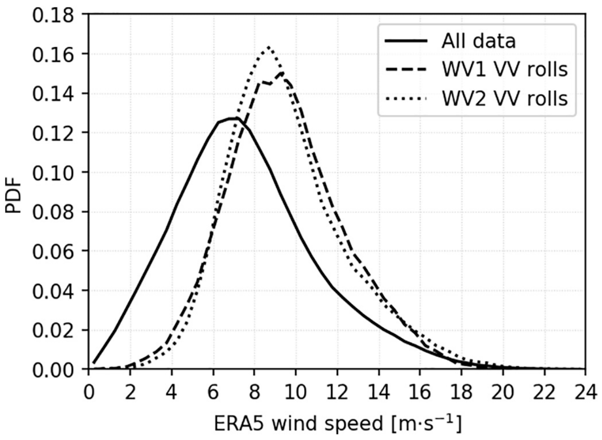

**Fig. 4.** Wind speed distributions of all S-1A WV VV SAR data and the CMwv-identified roll WV1 and WV2 data.

Fig. 5 (a, b) show that, for wind speeds above 6 m $s^{-1}$, roll event detection rates are dramatically lower at crosswind for both incidence angles. Note that the roll detection rates for either WV1 or WV2 can reach 25–35%, which are above the average 9% and 15% rates shown in Fig. 3 and are closer to the preciously reported detection rates (Levy, 2001; Zhao et al., 2016). While not shown, the detection rates of rolls from the smaller S-1B HH SAR dataset show similar behavior as S-1A VV for various wind speeds and relative azimuth. It is thus clear that the identification of roll events in S-1 SAR WV data depends strongly on all of incidence angle, wind speed and relative azimuth.

### 3.2. *Case study investigation*

To examine the MABL roll detection differences between WV1 and WV2, a section of Pacific Ocean (15°S-30°N, 170°E-180°E) data is extracted from a descending S-1A pass on Feb 2, 2017 (Fig. 6). The SAR look direction is 287° clockwise from North. Wind information from ERA5 shows that the wind field is fairly homogeneous at 9.5 m $s^{-1}$ and about 80° direction in meteorological convention, so the relative azimuth is 333°. The central locations of the WV1 and WV2 imagettes reflect the standard leap-frog acquisition pattern. Concentrating on the 5°N to 18°N region, seven consecutive WV2 imagettes are classified as rolls. The atmospheric stability parameter $Ri_B$ is slightly unstable at about $-0.006$, which indicates that conditions are favorable for MABL roll development (Brown, 1980; Etling and Brown, 1993; Young et al., 2002). Thus, one would expect S-1 to observe clear roll imprints in both WV1 and WV2. However, only one WV1 case is classified as a roll event.

Fig. 6 shows the three pairs of WV1 and WV2 images that were acquired within a 2 min span. WV2 images are displayed on the left column, and all these show clear periodic linear imprints of rolls. They have the same orientation, which is close to the ERA5 surface wind direction (blue arrows on images). In contrast, roll imprints are almost invisible on the three neighboring WV1 images shown in right column. Although one roll event was identified, the linear features on that image

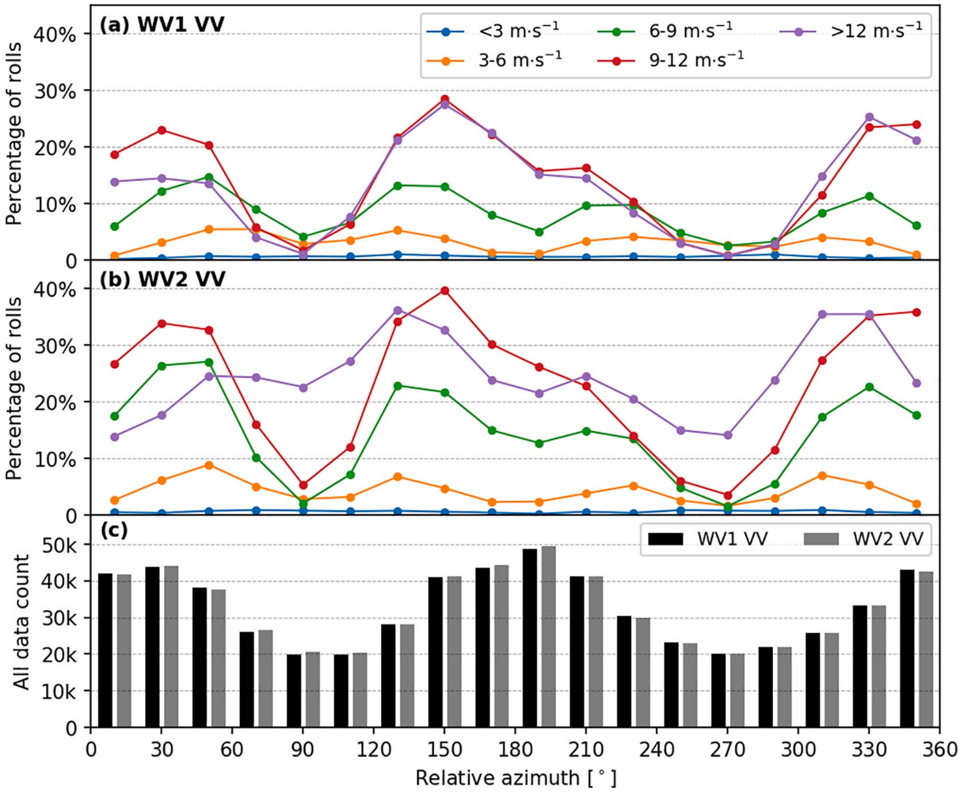

**Fig. 5.** Statistics of identified roll events from S-1A VV WV SAR images for different relative azimuth angles. (a) and (b) show the WV1 and WV2 percentages of identified rolls for selected wind speed ranges, and (c) gives the total of all images collected in each mode, respectively.

are weaker than those in the nearby WV2 images.

The computed image modulation parameters for these six cases are given in Table 1. The SAR-estimated wind speeds $U_B$ and $U_D$, corresponding to $\sigma_B^0$ and $\sigma_D^0$, are close to the mean ERA5 wind speed and approximately the same $dU$ levels are found in all six WV imagettes. However, the modulation depths, $d\sigma^0$, extracted from WV1 images are larger than that from WV2 data. When the modulation depth is normalized to contrast, $d\sigma^0/\sigma^0$, the three WV2 images have larger values than the three neighboring WV1 cases. This indicates that even though a smaller NRCS modulation is induced in WV2, it has a better roll detection capability than WV1 for the same wind conditions. Visually, roll imprints are more easily visible in WV2 than WV1 images as shown in Fig. 6. Roll detection is apparently sensitivity to the modulation contrast, which depends on the relative change in NRCS induced by small wind perturbation and the mean NRCS. These two variables both vary as a function of wind speed, incidence and relative azimuth angles. Note, however, that the sole WV1 image classified as rolls has the least $d\sigma^0/\sigma^0$ among the six cases. It implies that the explanation for different roll detection rates between WV1 and WV2 is not simple. A statistical analysis of roll-related modulation parameters is thus necessary and given in Section 4.

## 4. S-1 WV NRCS response to roll imprints

In this section, we take advantage of the large dataset to address the question of roll detection systematically. The parameters $d\sigma^0$, $d\sigma^0/\sigma^0$ and $dU/U$ are extracted from all the WV images that were identified as rolls by CMwv. The distributions of these quantities are binned as functions of ERA5 surface wind speed and relative azimuth for the different incidence angles and polarizations.

### 4.1. Wind speed dependence

The roll-induced modulation depth $d\sigma^0$ as a function of ERA5 wind speed for WV1 and WV2 in VV and HH polarization states are shown in Fig. 7 (a1,2). Box-plots are used to show the $d\sigma^0$ distribution in 2 m s$^{-1}$ bins from 3 to 19 m s$^{-1}$. Beyond this wind speed range, data are sparse particularly for HH. For both incidence angles and polarizations, $d\sigma^0$ increases with wind speed. WV1 $d\sigma^0$ values are clearly larger than for WV2 for both VV and HH measurements. For winds larger than 13 m s$^{-1}$, VV $d\sigma^0$ values exceed HH $d\sigma^0$. These observations consistently follow the fact that the implied slope, $\partial\sigma^0/\partial U$, is on average larger at the lower incidence angle for both VV and HH.

The SAR backscatter modulation contrast $d\sigma^0/\sigma^0$ is shown in Fig. 7 (b1,2). This roll-induced NRCS contrast is much less sensitive to surface wind speed than the modulation depth. One exception is the slightly larger values at low winds (3–7 m s$^{-1}$), particularly for HH data. This is likely because $\sigma^0$ can be very low in light winds even $d\sigma^0$ remains unchanged. A second observation is a likely roll identification threshold. For both WV1 and WV2 in either VV and HH polarization, the 10th percentile of $d\sigma^0/\sigma^0$ is almost constant near 0.04. We hypothesize that this value corresponds to the effective roll detection floor for the end-to-end S-1 SAR WV and automated CMwv model system. Roll cases with image contrasts below this 4% level might be discernible by trained eyes, but by design, the non-supervised CMwv model was trained to only identify clearly visible and delineated roll cases (Wang et al., 2019b).

Referring again to Fig. 7 (b1,2), it is clear that WV2 $d\sigma^0/\sigma^0$ levels are generally higher than these for WV1 in both VV and HH measurements. This difference is consistent with the detection rate differences shown in Fig. 3 and Fig. 5. This indicates that roll-induced SAR backscatter contrast is greater at the higher incidence angle, which improves the chances of CMwv to identify roll events. Regarding polarization

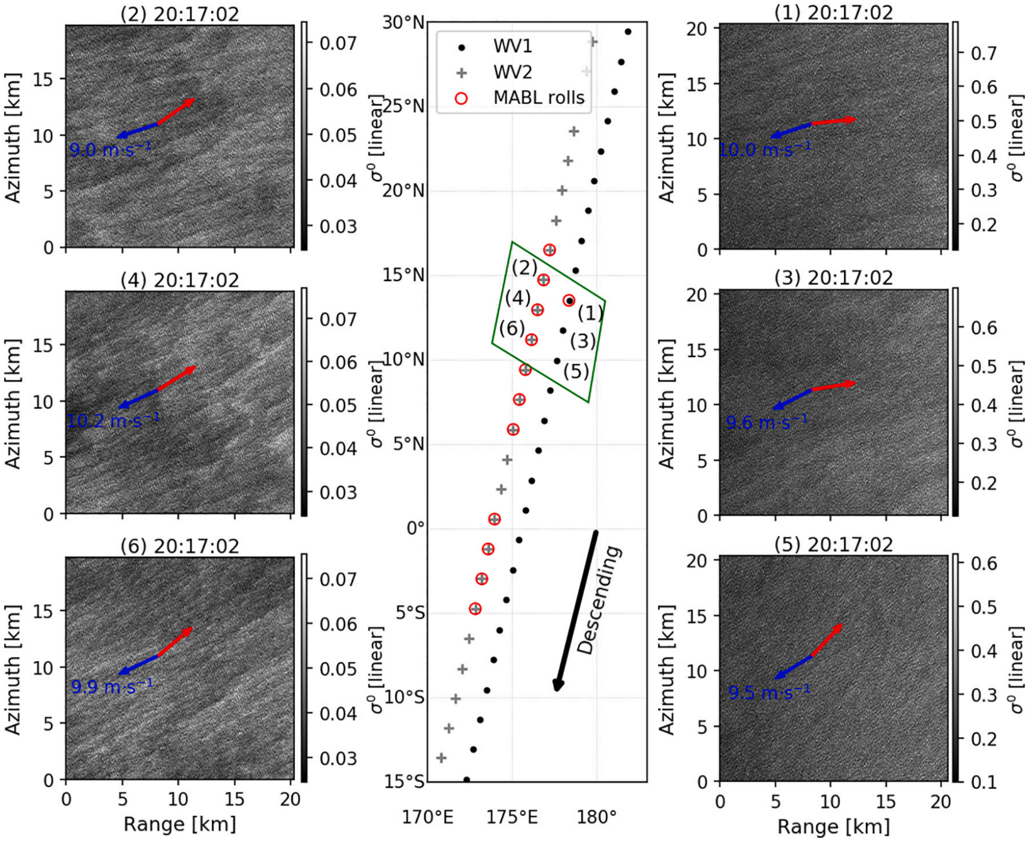

**Fig. 6.** Center panel shows center points of WV1 and WV2 acquisitions along an S-1A descending pass on 2017-02-02. Images identified by CMwv as roll events are shown with red circles. Three neighboring pairs WV2 and WV1 images (green box in the middle panel) are shown in the left and right panels. The blue and red arrows on the images indicate the ECMWF ERA5 surface wind and SAR backscatter-estimated roll directions, respectively. (For interpretation of the references to colour in this figure legend, the reader is referred to the web version of this article.)

dependencies in the S-1 data, there is little $d\sigma^0/\sigma^0$ difference between VV and HH measurements.

As noted earlier, ocean radar backscatter can be converted to wind speed using a GMF, which provides a means to normalize the results across the four WV mode incidence angle and polarization combinations. It also provides a geophysical quantification of MABL impact in terms of the surface wind speed perturbation. Global statistics of SAR-derived wind modulations ($dU/U$) versus mean wind speed are shown in Fig. 7 (c1) and (c2). Similar to the $d\sigma^0/\sigma^0$ measurements, $dU/U$ mean values for WV1 and WV2 in VV and HH are relatively constant with wind speed. The average level of wind perturbation is 8% (standard deviation of 3.5%). This value is consistent with previous field measurements of 7–10% obtained using low-level aircraft observations (Vandemark et al., 2001). The global ocean estimates show a slightly wider range of roll-induced wind perturbations, and the maximum wind perturbation seldom exceeds 15%. For both VV and HH, the $dU/U$ levels are slightly larger at low winds (3–7 m s$^{-1}$), which is similar to the $d\sigma^0/\sigma^0$ behavior. For wind speeds above 13 m s$^{-1}$, the detected rolls in WV1 (WV2) tend to be those with stronger (weaker) roll-induced wind perturbations.

### 4.2. Dependence of roll detection on relative azimuth

For a given wind speed, MABL roll event data show that the observed SAR backscatter and wind speed perturbation estimates depend

**Table 1**
Environmental variables and extracted roll modulation parameters for the six S-1A WV1 (23°) and WV2 (36.5°) image cases in Fig. 6. $U10$ and $\phi_{U10}$ are the ERA5 10 m wind speed and direction in meteorological convention. $Ri_B$ is the atmospheric stability parameter estimated from the ERA5 variables. $\phi_{WS}'$ is the extracted roll orientation in the same coordinate as $\phi_{U10}$. $\sigma^0_B$ and $\sigma^0_D$ are the mean NRCS over roll-induced bright and dark on SAR images. $d\sigma^0$, $d\sigma^0/\sigma^0$ and $dU/U$ represent the roll-induced NRCS variation, relative NRCS variation (image contrast) and surface wind perturbation.

| Case ID | Swath | $U10$ [m·s$^{-1}$] | $\phi_{U10}$ [°] | $Ri_B$ [$\times 10^{-3}$] | $\phi_{WS}'$ [°] | $\sigma^0_B$ [linear] | $\sigma^0_D$[linear] | $d\sigma^0$ [linear] | $\frac{d\sigma^0}{\sigma^0}$ | $U_B$ [m·s$^{-1}$] | $U_D$ [m·s$^{-1}$] | $\frac{dU}{U}$ |
|---|---|---|---|---|---|---|---|---|---|---|---|---|
| Fig. 6 (1) | WV1 | 10.0 | 84 | −6.98 | 96 | 0.346 | 0.326 | 0.021 | 0.06 | 10.35 | 9.82 | 0.05 |
| Fig. 6 (3) | WV1 | 9.6 | 75 | −5.56 | 93 | 0.339 | 0.307 | 0.032 | 0.10 | 10.44 | 9.61 | 0.08 |
| Fig. 6 (5) | WV1 | 9.5 | 70 | −6.99 | 55 | 0.302 | 0.278 | 0.024 | 0.08 | 9.54 | 8.99 | 0.06 |
| Fig. 6 (2) | WV2 | 9.0 | 84 | −7.38 | 67 | 0.051 | 0.046 | 0.005 | 0.10 | 9.58 | 9.05 | 0.06 |
| Fig. 6 (4) | WV2 | 10.2 | 77 | −6.29 | 70 | 0.053 | 0.047 | 0.006 | 0.12 | 10.09 | 9.39 | 0.07 |
| Fig. 6 (6) | WV2 | 9.9 | 77 | −6.36 | 62 | 0.056 | 0.049 | 0.007 | 0.12 | 10.34 | 9.68 | 0.07 |

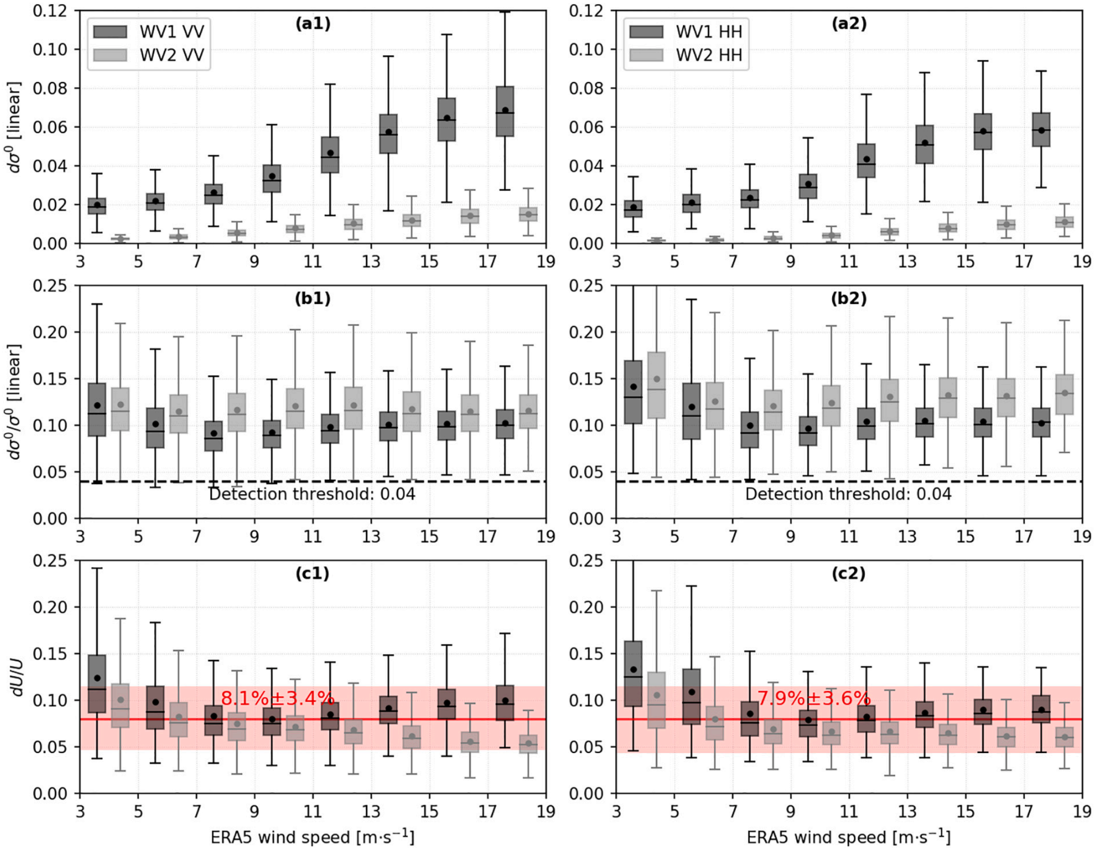

**Fig. 7.** Box plots of $d\sigma^0$, $d\sigma^0/\sigma^0$ and $dU/U$ for identified roll events from WV1 and WV2 in VV polarization (left panel) and HH (right panel). Statistics were conducted within each 2 m s$^{-1}$ bin from 3 to 19 m s$^{-1}$. Boxes indicate the 25th to 75th percentiles in each bin. Data mean and median are denoted using the point and line. The 10th and 90th percentiles are given by whiskers. The red line and shaded red in bottom panels represents the overall average and standard deviation of $dU/U$. (For interpretation of the references to colour in this figure legend, the reader is referred to the web version of this article.)

on the relative azimuth. Image contrast and wind perturbations within ± 15° of the up-, cross- and downwind sectors for different wind speeds are shown in Fig. 8. Up- and downwind $d\sigma^0/\sigma^0$ and $dU/U$ are comparable for all wind speeds. When the SAR view is crosswind, both parameters markedly increase, particularly for WV1 measurements. For winds below 10 m s$^{-1}$, the identified crosswind roll events are associated with perturbation levels twice these for up- and downwind. These differences are largest at lower wind speeds. In terms of wind perturbation, detected crosswind roll events suggest a level twice that for up/down looks at speeds of 6–8 m s$^{-1}$. It is worth noticing that the limited S-1B HH SAR data show similar results with S-1A VV and thus not shown in the paper. The explanation for this is mostly a combination of roll dynamics, SAR sampling and image processing. Most of the crosswind WV images come from the flow around mid-latitude highs and lows and hence are in different thermal advection regimes, which are known to affect the rolls differently (Foster and Levy, 1998). However, about 25% of crosswind roll detection with the strongest relative perturbation strength occur at very low latitudes.

It is likely that this strong difference in directional radar sensitivity is related to short wind-wave variability and Bragg-scattering from these waves, which is polarization dependent. Fig. 9 shows $d\sigma^0$ distributions in VV and HH for both WV1 and WV2 at 9 ± 1 m·s$^{-1}$. As expected, the difference between polarizations is much more distinct at 36° (WV2) than at 23° (WV1), and with larger NRCS variability at VV than at HH. The mean polarization difference (PD = $\sigma^0_{VV} - \sigma^0_{HH}$) is greater for WV2 observations (Quilfen et al., 1999; Kudryavtsev et al., 2013). This is consistent with the increasing impact of resonant small scatters that have short space-time relaxation scales, with increasing incidence angle (e.g. Mouche et al., 2007; Kudryavtsev et al., 2014). The differences between $d\sigma^0$ distributions at VV and HH are much less pronounced for crosswind configurations in the WV2 results.

Quantitatively, Fig. 9 shows that VV downwind $d\sigma^0$ levels are 3 times those of HH $d\sigma^0$ at 36° (WV2). This is consistent with the pure-Bragg wave scattering theory prediction of a four times VV-HH $\sigma^0$ difference according to typical scattering coefficient formulations (e.g. Eqs. 3 and 4 in Kudryavtsev (2003)). For WV1, pure-Bragg wave growth predicts a factor of 1.75 between VV and HH $\sigma^0$, which is consistent with the global downwind WV1 observations in Fig. 9. But at crosswind, the statistical distributions of HH and VV $d\sigma^0$ are similar, and the mean levels are much lower than the along-wind data. So for crosswind, the dominant radar scattering mechanism must be almost scalar. That is because non-polarized scatters control the C-band radar-detected contrasts at crosswind. These waves are likely to be steeper intermediate scale (10–50 cm) gravity waves that require much stronger and longer duration wind forcing than for cm-scale Bragg waves (Kudryavtsev, 2003; Kudryavtsev et al., 2014). The data then suggest that the roll-induced wind perturbations must be significantly enhanced when the S-1 SAR detects roll events in crosswind. This implication is that the crosswind roll detections are biased toward the strongest events.

### 4.3. Comparison with C-band GMF simulations

To further examine the C-band SAR NRCS response to rolls with respect to wind speed and relative azimuth, we interpret the S-1 WV $d\sigma^0$

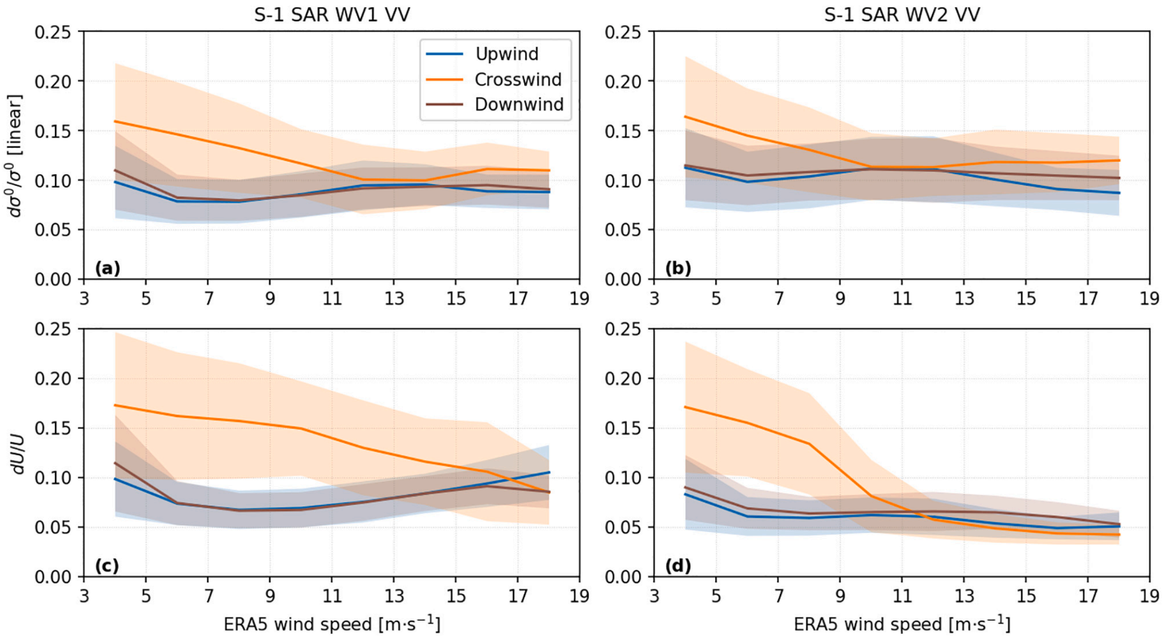

**Fig. 8.** Average $d\sigma^0/\sigma^0$ and $dU/U$ data from MABL roll events at up-, cross- and downwind SAR viewing angles as a function of wind speed. Data are from the 2016–2017 period with VV polarization. Statistics were computed for a ± 15° bin about the three relative azimuth angles, and within each 2 m s$^{-1}$ wind speed bin from 3 to 19 m s$^{-1}$. The line and shaded areas indicate the mean and one standard deviation.

measurements with a simple GMF simulation in the right column of Fig. 10. C-SARMOD calculations were performed assuming an 8% roll-induced wind speed change ($dU/U$) at each wind speed and direction for incidence angles of 23° and 36.5° over a wind speed range of 4.5 to 13.5 m s$^{-1}$ across the full range of relative azimuth angle.

Corresponding SAR measurement statistics are collected in 20°

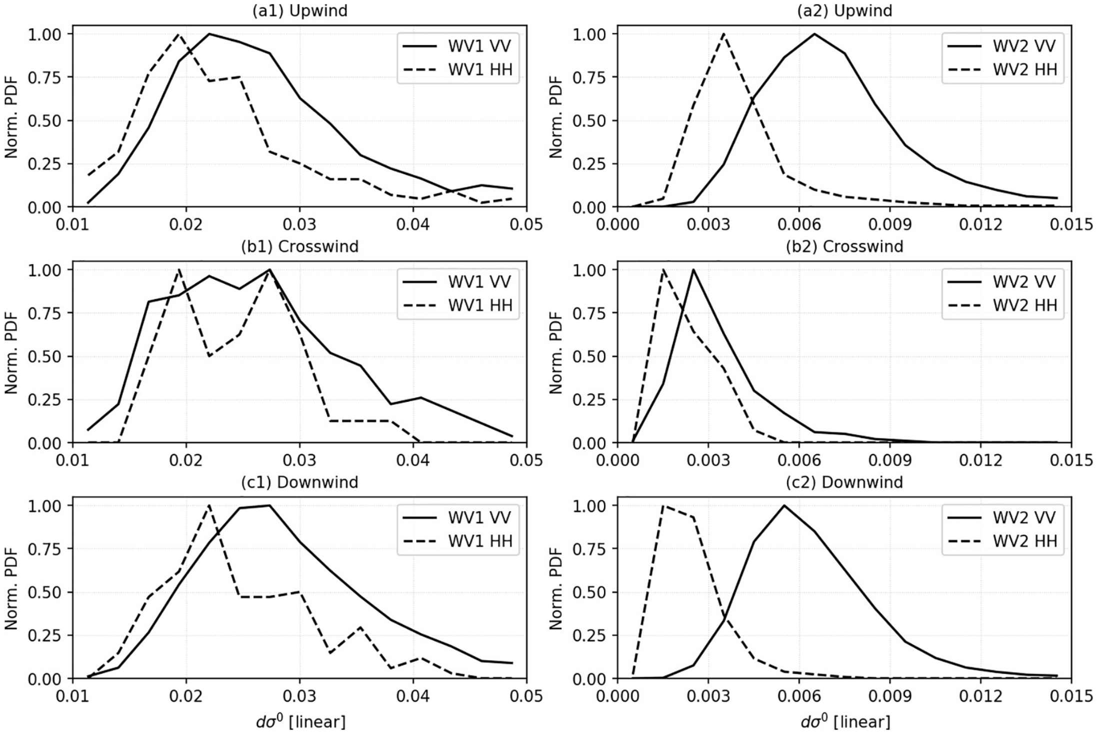

**Fig. 9.** $d\sigma^0$ distributions at up-, cross- and downwind ( ± 15° bin) for WV1 (left panel) and WV2 (right panel) in VV and HH with wind speed of 9 ± 1 m s$^{-1}$. Azimuth averaging is the same as for Fig. 8.

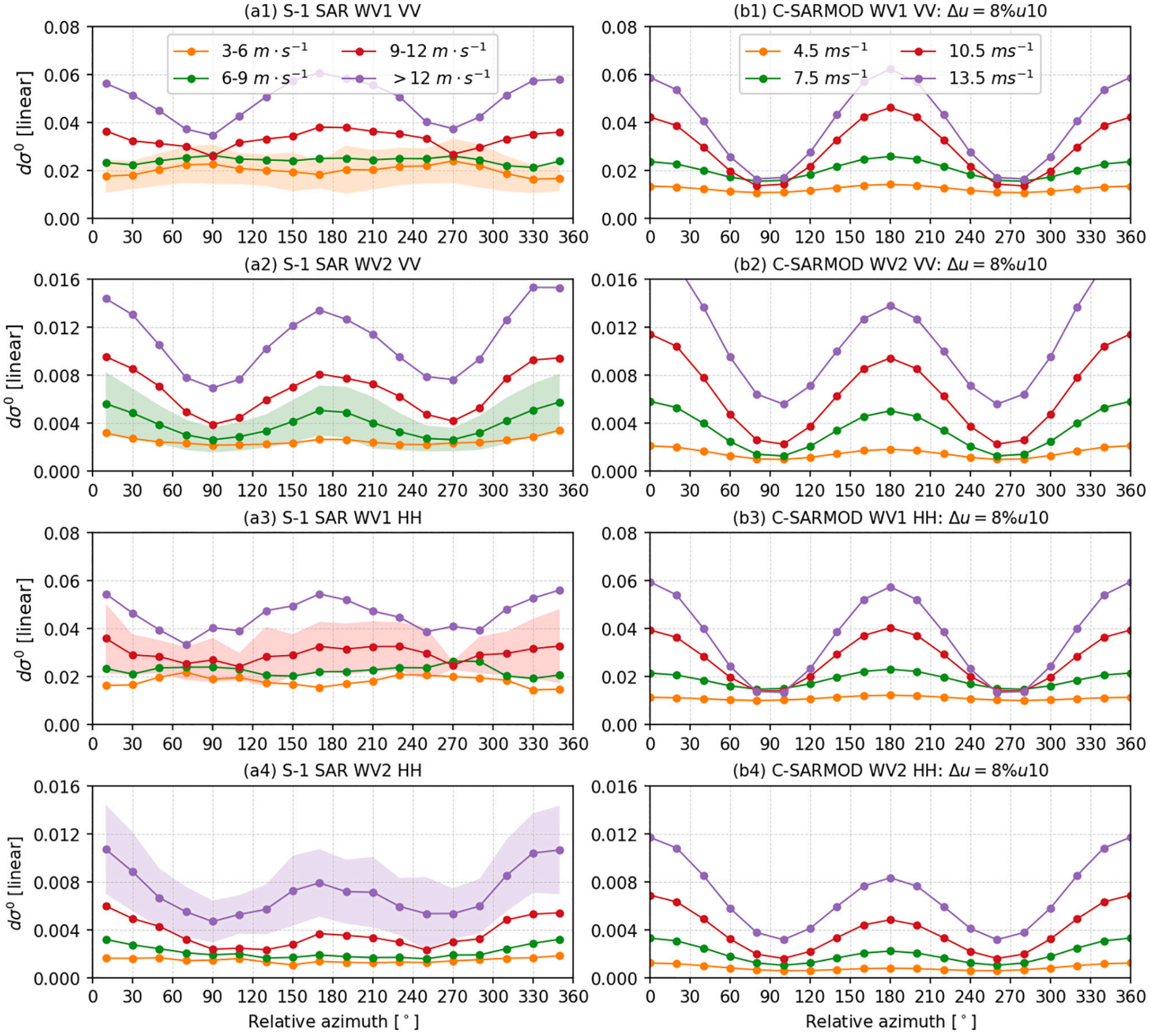

**Fig. 10.** Observed vs. predicted $d\sigma^0$ for roll events as function of wind speed and relative azimuth for WV1 and WV2 in VV and HH. Left panel are S-1 SAR WV results. Mean values are calculated for each 20° relative azimuth angle. For clarity, estimates of the standard deviation (shaded) are only shown for one wind speed in each panel. The right panel provides the C-SARMOD simulations under an assumed 8% wind speed change due to roll impacts.

relative azimuth and 3 m s$^{-1}$ wind speed bins (left column of Fig. 10). The modulation depth $d\sigma^0$ is largest at upwind and downwind. In light winds (3–6 m s$^{-1}$), WV1 and WV2 $d\sigma^0$ are nearly constant for both VV and HH with WV1 around 0.02 and WV2 about 0.002. With increasing wind speed, both VV and HH $d\sigma^0$ increase, with largest variations at up- and downwind.

The observed $d\sigma^0$ variations are generally similar, but there are some significant differences. In light winds (3–6 m s$^{-1}$), C-SARMOD $d\sigma^0$ is also nearly direction independent, but at a lower magnitude than the SAR measurements. For moderate wind speeds, C-SARMOD predicts a stronger $d\sigma^0$ dependence on the relative azimuth than we observe. For instance, within the 9–12 m s$^{-1}$ wind speed range, WV1 VV $d\sigma^0$ varies from 0.036 at upwind to about 0.026 at crosswind, and 0.037 at downwind. The corresponding C-SARMOD VV $d\sigma^0$ are 0.042, 0.013 and 0.046, respectively. Similar discrepancies are found for other wind speed ranges. These differences between S-1 WV and C-SARMOD simulations are larger for WV1 than for WV2 in both VV and HH, and increase with increasing wind speed.

As might be expected from the results discussed in Section 4.2, crosswind data show the largest differences with C-SARMOD. For WV1, the SAR $d\sigma^0$ is larger than 0.02, and increases with wind speed. In contrast, the C-SARMOD $d\sigma^0$ is less than 0.02, with no obvious wind speed trend. For WV2 at crosswind, both C-SARMOD and WV $d\sigma^0$ increase with wind speed, although C-SARMOD increases less rapidly. It should be noted that the constant 8% wind modulation due to rolls will not be valid across the full scope of the model-data comparison.

## 5. Discussions and conclusions

The combination of S-1 SAR WV data with automated image classification provides thousands of new MABL roll observations across most of the global ocean. Assessment results show that the 36° incidence angle measurements have a clear benefit for MABL roll investigations and improve on wave mode data from the earlier ERS and Envisat SAR ocean missions. In particular, there is a nearly 50% increase in event detection for WV2 compared to WV1. While more roll events are detected at the larger incidence angle, the two incidence angles show several important similarities for MABL roll remote sensing. First, they share a lower detection threshold near 4% in NRCS contrast at wind speeds from 3 to 19 m $s^{-1}$. Estimates of the roll-induced surface wind speed perturbations at both incidence angles fall in the range of 5–10%. Finally, WV1 and WV2 SAR roll event detection rates are 3–10 times greater for up- and down-wind compared to crosswind (Fig. 5). These results generally hold for both VV and HH, although WV2 VV is slightly more sensitive than HH to wind streak signatures as seen in Figs. 7 and 9. It is thus apparent that the best option for S-1 SAR measurements of this process is the WV2 VV-pol configuration. These findings suggest that any ocean SAR investigations of MABL rolls should carefully consider the relative azimuth and SAR incidence angles.

The central geophysical explanation for the observed radar dependencies under MABL roll forcing appears to be the combination of surface wind stress impacts and adjustment to this forcing by highly directional short wind waves. As discussed in Section 4.2, roll imprints are best captured by WV2 VV in the up and downwind configurations. It demonstrates that the local $d\sigma^0$ changes due to the roll field are significantly polarized. Short-scale polarizing surface structures correspond to the cm-scale Bragg waves. These waves have short relaxation times, and they quasi-instantaneously adjust to wind changes. Thus in the majority of cases, SAR-imaged rolls are likely to reflect this rapid adjustment in cm-scale waves for km-scale regions under the helical roll vortex field (Alpers and Brümmer, 1994; Young, 2000; Vandemark et al., 2001). Using a C-band radar GMF as a first-order model for this wind-wave adjustment, Fig. 7 (c1) and (c2) show that the global-averaged 8% ( ± 3.5) level for wind speed fluctuations does a reasonable job of explaining the roll-induced NRCS modulation depth. This appears to be a robust observation, valid across most wind speeds, and consistent with previous aircraft wind measurements showing a range of 7–10% (Vandemark et al., 2001). Results also indicate that the strength of the coherent secondary circulation scales with the intensity of the mean flow. These satellite-derived estimates of surface perturbation magnitude may help guide analytical and numerical models of eddy-impacted boundary layers.

An explanation for the largest difference of MABL roll detection between up and crosswind SAR viewing angles (see Figs. 5 and 8) is more nuanced. It is asserted that the dominant crosswind NRCS modulation mechanism under roll forcing must come from changes in steeper intermediate scale breaking or nearly breaking surface scattering facets (Kudryavtsev, 2003; Kudryavtsev et al., 2013). This conclusion is consistent with VV and HH pol differences observed in Fig. 9. Accordingly, and particularly at lower incidence angles, roll-induced surface wind variations must be increasingly vigorous in magnitude and duration for wind streak detection under crosswind conditions, as seen in Fig. 8.

Looking forward, this discrepancy in roll-field detection may be related to other environmental conditions that accompany events classified as MABL rolls using CMwv. Because S-1 is polar-orbiting and right-looking, roll observations at crosswind will be primarily associated with flows around mid-latitudinal lows and highs. These conditions are associated with particular thermal advection regimes that induce first-order modulations of the rolls. So, crosswind rolls present complication in both remote sensing and in geophysical interpretation. More generally, this reinforces the hypothesis that the forcing conditions needed to generate sufficient surface waves for wind streak detection may change, and be convolved with the SAR look direction and incidence angle. Further work is required to clarify this issue as it pertains to MABL roll process studies using S-1 data. Future investigations may also take advantage of these findings to focus on radar measurements under highly unstable atmospheric conditions, possibly using dual- and quad-polarized SAR measurements (Kudryavtsev et al., 2014, 2019; Fan et al., 2019).

It is certain that observed detection rates and thresholds depend to some extent on the performance of the CMwv automated image recognition algorithm. In the case of MABL rolls, the model was intentionally trained to find scenes that were clearly visible by eye. Given the consistent roll detection statistics and results in Fig. 7, this visibly-evident criterion corresponds to a 4% threshold in backscatter modulation. This implies that conditions with weaker, less visible, roll imprints are not captured in the present analysis and datasets. This limitation suggests that the overall percentage of occurrence rates for MABL rolls over the ocean seen in Figs. 3 and 5 represent conservative or lower-end estimates. In principle this may also affect the SAR-derived estimate of the low wind threshold for observed rolls (~2 m $s^{-1}$) shown in Fig. 4, but this value is consistent with previous estimates from theory and observations (Etling and Brown, 1993; Weckwerth et al., 1997). CMwv model limitations are not expected to impact the study conclusions drawn above pertaining to radar sensitivity to MABL roll impacts with changing incidence angle, relative azimuth, or polarization.

These new S-1 WV observations open avenues for further studies. On one hand, the revealed differences in SAR sensitivity to waves generated by roll impacts, particularly for crosswind views, should be further investigated. This may lead to new approaches for identifying unstable conditions, and $Ri_B$ retrieval methods. In that context, dual- and quad-polarized SAR observations (Fan et al., 2019), might be favored. In particular, short-scale polarized scatter contributions can be isolated to more precisely analyze local roll signatures. The growing number of quad-polarization observations, from Radarsat-2, Gaofen-3 and the new Radarsat Constellation Mission (RCM), are expected to serve this purpose. On the other hand, though the weak roll imprint cases are excluded in the present classified dataset, this S-1 SAR database is still state-of-the-art in terms of providing an overall global view of roll field characteristics (wavelength & orientation) as well as the ability to relate these data to near-surface forcing from the tropics to high latitudes. This massive classified WV SAR images can thus be used to support boundary layer studies over the world's ocean to advance understandings of km-scale MABL coherent roll structures on turbulent momentum fluxes.

## Declaration of Competing Interest

The authors declare that they have no known competing financial interests or personal relationships that could have appeared to influence the work reported in this paper.

## Acknowledgements

The authors would like to thank the anonymous reviewers for their constructive comments that improved the paper. This study is supported by ESA Sentinel-1 Mission Performance Center (4000107360/12/I-LG), ESA S1-4SCI Ocean Study (4000115170/15/I-SBo), and CNES TOSCA program (COWS) projects. Foster and Vandemark were supported by NASA Physical Oceanography grant NNX17AH17G. C. Wang is grateful for financial support from the China Scholarship Council (CSC) for his PhD, and the French ISblue project (ANR-17-EURE-0015) for this work.

## Appendix A. S-1 WV NRCS recalibration

For each WV SAR image, ESA's Level-1 SLC product provides the digital number $DN = \sqrt{I^2 + Q^2}$ per pixel ($I$ and $Q$ indicate the real and imaginary parts of SAR measurements). It can be used to compute the NRCS through radiometric calibration and noise correction:

$$\sigma^0_{ESA} = DN_i^2/A_i^2 - NESZ \quad [Linear]$$

where $A_i$ is the calibration lookup table (LUT) provided in the annotation files for each image pixel. NESZ is the noise equivalent $\sigma^0$ estimated from the mode of $DN_i^2/A_i^2$ histogram for wind speeds less than 1 m s$^{-1}$ (Li et al., 2019a, 2019b). The NESZ is 0.0014 and 0.0062 for S-1A WV1 and WV2 in VV, and 0.0012 and 0.0040 for S-1B WV1 and WV2 in HH.

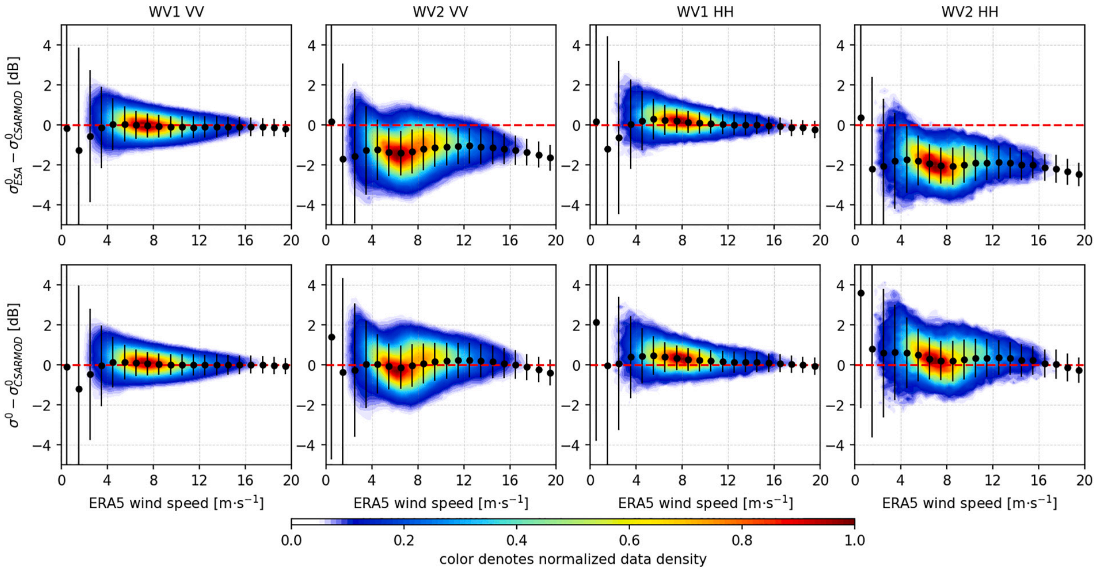

**Fig. A1.** NRCS residual of pre- and post-recalibration (top and bottom) as function of wind speed for WV1 and WV2 in VV and HH. VV data are for S-1A in 2016–2017 and HH data are for S-1B from 15 Mar to 01 Jul in 2017. Colour denotes the normalized data density. The red dashed line indicates the 0 dB baseline. Black dots are the mean residual within 1 m s$^{-1}$ bin and the error bars represent one standard deviation. The $\sigma^0$ reference comes from the C-SARMOD model noted in the text. (For interpretation of the references to colour in this figure legend, the reader is referred to the web version of this article.)

The chosen NRCS reference, or benchmark, is the C-band SAR GMF of C-SARMOD (Mouche et al., 2006). It is selected because of its applicable skill in both VV and HH polarizations. NRCS comparisons between standard ESA WV data ($\sigma^0_{ESA}$) and C-SARMOD predictions for WV1 and WV2 in VV and HH are given in the top panel of Fig. A1. We then computed the mean $\sigma^0_{ESA}$ per image for WV data and fed the collocated ERA5 wind speed and direction as well as image center incidence angle into C-SARMOD to derive the expected $\sigma^0_{C-SARMOD}$. Note that SAR data with mean $DN_i^2/A_i^2$ less than the NESZ are excluded. The error bar plots show the mean and 1st standard deviation within each 1 m s$^{-1}$ bin and the colour denotes the normalized data density. It is clear that the NRCS residual ($\sigma^0_{ESA}$-$\sigma^0_{C-SARMOD}$) for WV1 data in both VV and HH is nearly 0 dB for all wind speeds. However, the WV2 NRCS residual has a nearly constant negative bias at all wind speeds of about −1.6 dB for VV and − 2 dB for HH. This is consistent with the NRCS assessment that discrepancies exist between S-1 WV data (after built-in calibration processing) and CMOD5.N predictions, particularly for measurements at the WV2 incidence angle of 36° (Li et al., 2019b, 2019a).

A recalibration constant $C_{OC}$ is calculated for each 12 day repeat cycle using C-SARMOD and ERA5 wind direction. This factor is then used to correct the WV NRCS as $\sigma^0 = \sigma^0_{ESA}/C_{OC}$ in linear space. This procedure is applied for both WV1 and WV2 in VV and HH. The bottom panel of Fig. A1 displays the NRCS residuals after recalibration. As expected, the WV2 mean NRCS values now lie within 0.1–0.2 dB of the C-SARMOD prediction for most wind speeds.

## References

Alpers, W., Brümmer, B., 1994. Atmospheric boundary layer rolls observed by the synthetic aperture radar aboard the ERS-1 satellite. J. Geophys. Res. 99, 12613. https://doi.org/10.1029/94JC00421.

Alpers, W., Zhang, B., Mouche, A., Zeng, K., Chan, P.W., 2016. Rain footprints on C-band synthetic aperture radar images of the ocean - RRevisited. Remote Sensing of Environment 187, 169–185. URL. https://linkinghub.elsevier.com/retrieve/pii/S003442571630387X. https://doi.org/10.1016/j.rse.2016.10.015.

Atkinson, B.W., Wu Zhang, J., 1996. Mesoscale shallow convection in the atmosphere. Rev. Geophys. 34, 403–431. https://doi.org/10.1029/96RG02623.

Babin, S.M., Sikora, T.D., Winstead, N.S., 2003. A case study of satellite synthetic aperture radar signatures of spatially evolving atmospheric convection over the Western Atlantic Ocean. Bound.-Layer Meteorol. 106, 527–546. https://doi.org/10.1023/A:1021236600569.

Bauer, P., Thorpe, A., Brunet, G., 2015. The quiet revolution of numerical weather prediction. Nature 525, 47–55. http://www.nature.com/articles/nature14956 https://doi.org/10.1038/nature14956.

Brilouet, P., Durand, P., Canut, G., 2017. The marine atmospheric boundary layer under strong wind conditions: OOrganized turbulence structure and flux estimates by airborne measurements. J. Geophys. Res. Atmosph. 122, 2115–2130. URL. https://onlinelibrary.wiley.com/doi/abs/10.1002/2016JD025960. https://doi.org/10.1002/2016JD025960.

Brown, R.A., 1980. Longitudinal instabilities and secondary flows in the planetary boundary layer: A review. Rev. Geophys. 18, 683–697. URL. https://doi.org/10.1029/RG018i003p00683.

Christiansen, M.B., Koch, W., Horstmann, J., Hasager, C.B., Nielsen, M., 2006. Wind resource assessment from C-band SAR. Remote Sensing Environ. 105, 68–81. URL. http://www.sciencedirect.com/science/article/pii/S0034425706002239. https://doi.org/10.1016/j.rse.2006.06.005.

Etling, D., Brown, R.A., 1993. Roll vortices in the planetary boundary layer: AA review. Boundary-Layer Meteorology 65, 215–248. URL. http://link.springer.com/10.1007/BF00705527. https://doi.org/10.1007/BF00705527.

Fairall, C.W., Bradley, E.F., Hare, J.E., Grachev, A.A., Edson, J.B., 2003. Bulk parameterization of AirSea fluxes: Updates and verification for the COARE algorithm. J. Climate 16, 571–591.

Fan, S., Kudryavtsev, V., Zhang, B., Perrie, W., Chapron, B., Mouche, A., 2019. On C-Band Quad-Polarized Synthetic Aperture Radar Properties of Ocean Surface Currents. Remote Sensing 11, 2321. URL. https://www.mdpi.com/2072-4292/11/19/2321. https://doi.org/10.3390/rs11192321.

Foster, R.C., Levy, G., 1998. The contribution of organized roll vortices to the surface wind vector in Baroclinic conditions. J. Atmosph. Sci. 55, 1466–1472.

Gerling, T.W., 1986. Structure of the surface wind field from the Seasat SAR. J. Geophys. Res. 91, 2308. https://doi.org/10.1029/JC091iC02p02308.

Glendening, J.W., 1996. Lineal Eddy features under strong shear conditions. J. Atmosph.

Sci. 53, 3430–3449.

Hein, P.F., Brown, R.A., 1988. Observations of longitudinal roll vortices during arctic cold air outbreaks over open water. Boundary-Layer Meteorology 45, 177–199. URL. http://link.springer.com/10.1007/BF00120822. https://doi.org/10.1007/BF00120822.

Horstmann, J., Koch, W., 2005. Measurement of Ocean Surface Winds Using Synthetic Aperture Radars. IEEE Journal of Oceanic Engineering 30, 508–515. URL. http://ieeexplore.ieee.org/document/1593798/. https://doi.org/10.1109/JOE.2005.857514.

Huang, L., Li, X., Liu, B., Zhang, J.A., Shen, D., Zhang, Z., Yu, W., 2018. Tropical cyclone boundary layer rolls in synthetic aperture radar imagery. J. Geophys. Res. Oceans 123, 2981–2996. https://doi.org/10.1029/2018JC013755.

Jackson, C.R., Apel, J.R. (Eds.), 2004. Synthetic Aperture Radar Marine User's Manual. US Department of Commerce, National Oceanic and Atmospheric Administration, National Environmental Satellite, Data, and Information Serve. Office of Research and Applications.

Koch, W, 2004. Directional analysis of SAR images aiming at wind direction. IEEE Transactions on Geoscience and Remote Sensing 42, 702–710. URL. http://ieeexplore.ieee.org/document/1288365/. https://doi.org/10.1109/TGRS.2003.818811.

Kudryavtsev, V., 2003. A semiempirical model of the normalized radar cross-section of the sea surface 1. Background model. J. Geophys. Res. 108, 8054. https://doi.org/10.1029/2001JC001003.

Kudryavtsev, V.N., Chapron, B., Myasoedov, A.G., Collard, F., Johannessen, J.A., 2013. On Dual Co-Polarized SAR Measurements of the Ocean Surface. IEEE Geoscience and Remote Sensing Letters 10, 761–765. URL. http://ieeexplore.ieee.org/document/6377256/. https://doi.org/10.1109/LGRS.2012.2222341.

Kudryavtsev, V., Kozlov, I., Chapron, B., Johannessen, J.A., 2014. Quad-polarization SAR features of ocean currents. J. Geophys. Res. Oceans 119, 6046–6065. https://doi.org/10.1002/2014JC010173.

Kudryavtsev, V.N., Fan, S., Zhang, B., Mouche, A.A., Chapron, B., 2019. On Quad-Polarized SAR Measurements of the Ocean Surface. IEEE Transactions on Geoscience and Remote Sensing 57, 8362–8370. URL. https://ieeexplore.ieee.org/document/8742586/. https://doi.org/10.1109/TGRS.2019.2920750.

Kuettner, J., 1959. The Band Structure of the Atmosphere. Tellus 11, 267–294. URL. https://www.tandfonline.com/doi/full/10.3402/tellusa.v11i3.9319. https://doi.org/10.3402/tellusa.v11i3.9319.

LeCun, Y., Bengio, Y., Hinton, G., 2015. Deep learning. Nature 521, 436–444. URL. http://www.nature.com/doifinder/10.1038/nature14539. https://doi.org/10.1038/nature14539 arXiv:arXiv:1312.6184v5.

LeMone, M.A., 1973. The structure and dynamics of horizontal roll vortices in the planetary boundary layer. J. Atmosph. Sci. 30, 1077–1091.

Lemone, M.A., 1976. Modulation of turbulence energy by longitudinal rolls in an unstable planetary boundary layer. J. Atmosph. Sci. 33, 1308–1320.

Levy, G., 2001. Boundary layer roll statistics from SAR. Geophys. Res. Lett. 28, 1993–1995. https://doi.org/10.1029/2000GL012667.

Li, X.M., Lehner, S., 2014. Algorithm for Sea Surface Wind Retrieval From TerraSAR-X and TanDEM-X Data. IEEE Transactions on Geoscience and Remote Sensing 52, 2928–2939. URL. http://ieeexplore.ieee.org/document/6564437/. https://doi.org/10.1109/TGRS.2013.2267780.

Li, X., Zheng, W., Yang, X., Zhang, J.A., Pichel, W.G., Li, Z., 2013. Coexistence of Atmospheric Gravity Waves and Boundary Layer Rolls Observed by SAR. Journal of the Atmospheric Sciences 70, 3448–3459. URL. http://journals.ametsoc.org/doi/abs/10.1175/JAS-D-12-0347.1. https://doi.org/10.1175/JAS-D-12-0347.1.

Li, H., Mouche, A., Stopa, J.E., 2019a. Impact of Sea State on Wind Retrieval From sentinel-1 Wave Mode Data. IEEE J. Select. Topics Appl. Earth Observ. Remote Sensing 12, 559–566. URL. https://ieeexplore.ieee.org/document/8637022/. https://doi.org/10.1109/JSTARS.2019.2893890.

Li, H., Mouche, A., Stopa, J.E., Chapron, B., 2019b. CCalibration of the Normalized Radar Cross Section for sentinel-1 Wave Mode. IEEE Transactions on Geoscience and Remote Sensing 57, 1514–1522. URL. https://ieeexplore.ieee.org/document/8465988/. https://doi.org/10.1109/TGRS.2018.2867035.

Lin, H., Xu, Q., Zheng, Q., 2008. An overview on SAR measurements of sea surface wind. Progress in Natural Science 18, 913–919. URL. http://www.sciencedirect.com/science/article/pii/S1002007108001755. https://doi.org/10.1016/j.pnsc.2008.03.008.

Mouche, A., Chapron, B., 2015. Global C-band Envisat, RADARSAT-2 and Sentinel-1 SAR measurements in copolarization and cross-polarization. J. Geophys. Res. Oceans 120, 7195–7207. https://doi.org/10.1002/2015JC011149.

Mouche, A.A., Hauser, D., Kudryavtsev, V., 2006. Radar scattering of the ocean surface and sea-roughness properties: A combined analysis from dual-polarizations airborne radar observations and models in C band. J. Geophys. Res. 111, C09004. https://doi.org/10.1029/2005JC003166.

Mouche, A.A., Chapron, B., Reul, N., 2007. A simplified asymptotic theory for ocean surface electromagnetic wave scattering. Waves in Random and Complex Media 17, 321–341. URL. http://www.tandfonline.com/doi/abs/10.1080/17455030701230261. https://doi.org/10.1080/17455030701230261.

Mourad, P.D., Walter, B.a., 1996. Viewing a cold air outbreak using satellite-based synthetic aperture radar and advanced very high resolution radiometer imagery. J. Geophys. Res. Oceans 101, 16391–16400. https://doi.org/10.1029/96JC01123.

Mourad, P.D., Thompson, D.R., Vandemark, D.C., 2000. Extracting fine-scale wind fields from synthetic aperture radar images of the ocean surface. Johns Hopkins APL Technical Digest (Applied Physics Laboratory) 21 (1), 108–115.

Quilfen, Y., Chapron, B., Bentamy, A., Gourrion, J., El Fouhaily, T., Vandemark, D., 1999. Global ERS 1 and 2 and NSCAT observations: upwind/crosswind and upwind/downwind measurements. J. Geophys. Res. Oceans 104, 11459–11469. https://doi.org/10.1029/1998JC900113.

Rowe, A.K., Houze, R.A., 2015. Cloud organization and growth during the transition from suppressed to active MJO conditions. J. Geophys. Res. Atmospheres 120https://doi.org/10.1002/2014JD022948.. URL: https://onlinelibrary.wiley.com/doi/abs/10.1002/2014JD022948.

Shin, H.H., Hong, S.Y., 2013. Analysis of resolved and parameterized vertical transports in convective boundary layers at gray-zone resolutions. J. Atmos. Sci. 70, 3248–3261 URL: http://journals.ametsoc.org/doi/abs/10.1175/JAS-D-12-0290.1.

Sikora, T.D., Ufermann, S., 2004. Marine atmospheric boundary layer cellular convection and longitudinal roll vortices. In: Synthetic Aperture Radar Marine User's Manual. US Department of Commerce, National Oceanic and Atmospheric Administration, National Environmental Satellite, Data, and Information Serve. Chapter 14 Office of Research and Applications, pp. 266–290.

Sikora, T.D., Young, G.S., Fisher, C.M., Stepp, M.D., 2011. A Synthetic Aperture radar based Climatology of Open-Cell Convection over the Northeast Pacific Ocean. Journal of Applied Meteorology and Climatology 50, 594–603. URL. http://journals.ametsoc.org/doi/abs/10.1175/2010JAMC2624.1. https://doi.org/10.1175/2010JAMC2624.1.

Szegedy, C., Vanhoucke, V., Ioffe, S., Shlens, J., Wojna, Z., 2016. Rethinking the Inception Architecture for Computer Vision. In: 2016 IEEE CConference on CComputer VVision and PPattern RRecognition (CVPR). IEEE, pp. 2818–2826. URL. http://ieeexplore.ieee.org/document/7780677/. https://doi.org/10.1109/CVPR.2016.308.

Torres, R., Snoeij, P., Geudtner, D., Bibby, D., Davidson, M., Attema, E., Potin, P., Rommen, B., Floury, N., Brown, M., Traver, I.N., Deghaye, P., Duesmann, B., Rosich, B., Miranda, N., Bruno, C., L'Abbate, M., Croci, R., Pietropaolo, A., Huchler, M., Rostan, F., 2012. GMES Sentinel-1 mission. Remote Sensing of Environment 120, 9–24. URL. https://linkinghub.elsevier.com/retrieve/pii/S0034425712000600. https://doi.org/10.1016/j.rse.2011.05.028.

Vandemark, D., Mourad, P.D., Bailey, S.A., Crawford, T.L., Vogel, C.A., Sun, J., Chapron, B., 2001. Measured changes in ocean surface roughness due to atmospheric boundary layer rolls. J. Geophys. Res. Oceans 106, 4639–4654. https://doi.org/10.1029/1999JC000051.

Wang, C., Mouche, A., Tandeo, P., Stopa, J., Longépé, N., Erhard, G., Foster, R., Vandemark, D., Chapron, B., 2018. Labeled SAR imagery dataset of ten geophysical phenomena from Sentinel-1 wave mode (TenGeoP-SARwv). https://doi.org/10.17882/56796.

Wang, C., Mouche, A., Tandeo, P., Stopa, J.E., Longépé, N., Erhard, G., Foster, R.C., Vandemark, D., Chapron, B., 2019a. A labelled ocean SAR imagery dataset of ten geophysical phenomena from Sentinel1 wave mode. Geosci. Data J. https://doi.org/10.1002/gdj3.73.. 3.73. URL: https://onlinelibrary.wiley.com/doi/abs/10.1002/gdj3.73.

Wang, C., Tandeo, P., Mouche, A., Stopa, J.E., Gressani, V., Longepe, N., Vandemark, D., Foster, R.C., Chapron, B., 2019b. CClassification of the global Sentinel-1 SAR vignettes for ocean surface process studies. Remote Sensing of Environment 234, 111457 URL. https://www.sciencedirect.com/science/article/pii/S0034425719304766?dgcid=author. https://doi.org/10.1016/j.rse.2019.111457.

Weckwerth, T.M., Wilson, J.W., Wakimoto, R.M., Crook, N.A., 1997. Horizontal convective rolls: Determining the environmental conditions supporting their existence and characteristics. Monthly Weather Rev. 125, 505–526.

Weston, K.J., 1980. An observational study of convective cloud streets. Tellus 32, 433–438. URL. https://www.tandfonline.com/doi/full/10.3402/tellusa.v32i5.10598. https://doi.org/10.3402/tellusa.v32i5.10598.

Young, G.S., 2000. SAR signatures of the marine atmospheric boundary layer: Implications for numerical forecasting. Johns Hopkins APL Technical Digest (Applied Physics Laboratory) 21 (1), 27–31.

Young, G.S., Kristovich, D.A.R., Hjelmfelt, M.R., Foster, R.C., 2002. Rolls, streets, waves, and more: A review of quasi-two-dimensional structures in the atmospheric boundary layer. Bull. Am. Meteorol. Soc. 83, 997–1001.

Young, G., Sikora, T., Winstead, N., 2008. Mesoscale Near-Surface Wind Speed Variability Mapping with Synthetic Aperture Radar. Sensors 8, 7012–7034. URL. http://www.mdpi.com/1424-8220/8/11/7012. https://doi.org/10.3390/s8117012.

Zecchetto, S, 2018. Wind Direction extraction from SAR in Coastal Areas. Remote Sensing 10, 261. URL. http://www.mdpi.com/2072-4292/10/2/261. https://doi.org/10.3390/rs10020261.

Zhang, J.A., Katsaros, K.B., Black, P.G., Lehner, S., French, J.R., Drennan, W.M., 2008. Effects of Roll Vortices on Turbulent Fluxes in the Hurricane Boundary Layer. Boundary-Layer Meteorology 128, 173–189. URL. http://link.springer.com/10.1007/s10546-008-9281-2. https://doi.org/10.1007/s10546-008-9281-2.

Zhang, L.L., Zhang, L.L., Du, B., 2016. Deep Learning for Remote Sensing Data: AA Technical Tutorial on the State of the Art. IEEE Geosci. Remote Sens. Magaz. 4, 22–40. URL. http://ieeexplore.ieee.org/document/7486259/. https://doi.org/10.1109/MGRS.2016.2540798.

Zhao, Y., Li, X.M., Sha, J., 2016. Sea surface wind streaks in spaceborne synthetic aperture radar imagery. J. Geophys. Res. Oceans 121, 6731–6741. https://doi.org/10.1002/2016JC012040.

Zhu, P., 2008. Simulation and parameterization of the turbulent transport in the hurricane boundary layer by large eddies. J. Geophys. Res.arch 113, D17104. https://doi.org/10.1029/2007JD009643.

## 3.4 Insights into the Global Feature of Marine Atmospheric Boundary Layer Rolls

Manuscript prepared to *Geophysical Research Letters*

# Insights into the Global Feature of Marine Atmospheric Boundary Layer Rolls

**Chen Wang[1,2], Douglas Vandemark[3], Bertrand Chapron[1], Alexis Mouche[1], Ralph C. Foster[4],**

[1]IFREMER, Univ. Brest, CNRS, IRD, Laboratoire d'Oceanographie Physique et Spatiale (LOPS), Brest, France
[2]IMT Atlantique, LabSTICC, UBL, Brest, France
[3]Ocean Processes Analysis Laboratory, University of New Hampshire, USA
[4]Applied Physics Laboratory, University of Washington, USA

**Key Points:**

- New Sentinel-1 wave mode SAR data allows a first global view of the km-scale marine atmospheric boundary layer roll features
- Atmospheric condition of SAR-observed rolls show consistent results with previous, and latitudinal as well as diurnal variabilities
- Roll scale and orientation are extracted with findings of multi-scale organization and directional contrast between low- and mid-latitudes

---

Corresponding author: Chen Wang, `cwang@ifremer.fr`

## Abstract

This study demonstrates a pioneer global view of atmospheric boundary layer rolls over the world's ocean using the new classified Sentinel-1 wave mode SAR images. As expected, up to 90% of roll events occur in slightly unstable to near-neutral atmospheric conditions, distinct from the total average. Roll orientation is found to systematically swing between two angles with respect to the surface wind. One angle is presented towards and one away from the geostrophic winds with latitudes beyond and within ±30°, respectively. The low- and mid-latitude angle contrast seems linked to the westerlies and trade wind belts, suggesting the significance of air flow directions in roll dynamics. In terms of the multi-scale nature of roll vortices, analysis shows nearly equal number of single-, double- and triple-length scales. Aspect ratio of these narrow rolls ranges from 0.5 to 8 with mean of 2.9, consistent with previous observations.

## 1 Introduction

Roll vortices are an oft-observed feature of the turbulent marine atmospheric boundary layer (MABL) in near-neutral to moderately unstable conditions [*Brown*, 1980; *Etling and Brown*, 1993; *Atkinson and Wu Zhang*, 1996; *Young et al.*, 2002]. They are frequently visible as cloud streets when condensation occurs in the updraft bands [e.g. *Kuettner*, 1971; *Weston*, 1980; *Müller et al.*, 1985; *Wurman and Winslow*, 1998], and wind streaks over water due to the enhanced and reduced surface wind convergence [e.g. *Gerling*, 1986; *Alpers and Brümmer*, 1994; *Young*, 2000; *Li et al.*, 2013]. The horizontal extent of MABL rolls can be hundreds of kilometers, where the air-mass transformation along stream is significantly promoted [*Pithan et al.*, 2018]. Vertically, these organized secondary circulations usually span the whole depth of the MABL and form alternating bands of updrafts and downdrafts. The upward and downward flows are able to introduce a non-local net effect that is independent of the vertical gradient [e.g. *Lemone*, 1976; *Brooks and Rogers*, 1997; *Morrison et al.*, 2005]. This roll-associated extra-contribution to air-sea exchanges of momentum, heat, and water vapor is important but not fully resolved in current numerical models [*Bauer et al.*, 2015; *Bony et al.*, 2015], bringing about uncertainties in climate forcing, projection and sensitivity [*Sherwood et al.*, 2014].

Investigation of this fundamental physical process has been conducted for many decades through extensive observations [e.g. *Brunt*, 1938; *Kuettner*, 1959, 1971; *Weckwerth et al.*, 1997; *Levy*, 2001; *Zhao et al.*, 2016; *Huang et al.*, 2018], field experiments [e.g. *Walter and Overland*, 1984; *Chou and Ferguson*, 1991; *Vandemark et al.*, 2001], and numerical and theoretical analyses [e.g. *Brown*, 1970; *Lemone*, 1976; *Leibovich and Lele*, 1985; *Foster and Levy*, 1998; *Foster*, 2005; *Salesky et al.*, 2017]. Roll vortices are found to have typical length scale and orientation of 1-5 km and ±30° relative to the mean wind direction [*Etling and Brown*, 1993; *Atkinson and Wu Zhang*, 1996]. Although significant gain of roll physics has been obtained, little is known about their global features as well as annual and seasonal variations. The lack of efficient means to observe and objectively classify rolls is a main restriction for most of the relevant observational studies [*Weckwerth et al.*, 1997; *Levy*, 2001; *Zhao et al.*, 2016; *Banghoff et al.*, 2020]. To seek a longer-term climatology of roll vortices over the world's ocean, new detailed observations of the MABL structure are required. These data should be unaffected by the presence or absence of clouds and are able to achieve roll characterization at climate time and space scales.

Among the many techniques, spaceborne synthetic aperture radar (SAR) holds the largest potential to provide systematic measurements of roll imprints on the global ocean surface [*Brown*, 2000; *Young*, 2000; *Levy*, 2001]. While SAR backscattering is largely associated with the cm-scale ocean waves, the roll-induced wind modulations on these short waves are usually strong enough to produce linear dark and bright patterns on SAR images [*Alpers and Brümmer*, 1994; *Vandemark et al.*, 2001]. One example of such roll scene, chosen randomly from the Sentinel-1A (S-1A) SAR WaVe mode (WV) acquisitions, is given in Figure 1a. It clearly illustrates the km-scale roll imprints that have the orientation approximately aligning with the surface wind direction. This S-1 WV, inherited from ERS and Envisat SAR missions, collects 20×20 km SAR scenes routinely at two alternating incidence angles of 23° (WV1) and 36.5° (WV2) over the entire open ocean (see Supplementary Text S1). Except ocean waves, this global catalog of WV SAR data has been found to capture a wide range of ocean surface processes at scales of 0.5-10 km [*Wang et al.*, 2019a], providing an unprecedented opportunity for roll studies beyond case and region stages.

To automatically identify roll events from these massive WV SAR images, a classification tool based on deep learning techniques was developed [*Wang et al.*, 2019b]. Assessment of the classified roll events manifests that, compared to WV1, WV2 is more sensitive to roll-induced wind modulations on ocean surface and thus maps more and much clearer roll events [*Wang et al.*, 2020]. Here, we focus on the global feature of MABL rolls in terms of the synoptic conditions and their structural characteristics, using more than 125, 000 roll events observed by S-1A WV2 in 2016-2018. To this end, each image has been collocated in time and space with the ERA5 surface variables, and spectrally analysed for roll orientation and wavelength extractions (Supplementary Text S3). Although gaps still exist in temporal and spatial coverage, it is the first time to condense MABL rolls at global scale. The statistical behavior of rolls summarized from the WV SAR measurements cannot be resolved by any other means.

## 2 Atmospheric conditions of roll occurrence

One-day acquisition by S-1A SAR WV2 is given in Figure 1b. The images are acquired globally in ascending or descending passes that cross the equator at roughly 0600 or 1800 local time. Distances between two adjacent WV2 images along the orbit are roughly 100 km. In total, there are about 25k WV2 data per month obtained (Figure 1b), 15% of which are identified as roll events through our deep-learning classification tool. Despite the fact that weak roll imprints are not well detected due to the tool limitation (Wang et al., 2020), as expected, roll events are found across the whole ocean basin with the highest concentration in tropics alongside the rainfall belts (Supplementary Figure S1b). Given the short duration of the dataset under investigation, we observed relatively little seasonality in the number of detected rolls as well as their atmospheric conditions (Figure 1b and Supplementary Figure S4). Hence in the following analysis, we concentrate on and present only the mean statistical results of all identified roll events.

Both observational and numerical studies have demonstrated that MABL rolls are present under specific environmental conditions [*Etling and Brown*, 1993; *Atkinson and Wu Zhang*, 1996]. It has been continuously reported that the wind and convection are the prevalent driving force for roll formation. The two variables are usually incorporated by the bulk Richardson number. In this study, we define the neutral bulk Richardson number ($RiB_N$) with the neutral wind speed ($U10_N$) and virtual air-sea temperature difference ($\Delta T_V$) at 10-m height. The distributions of these three measures for detected rolls and all WV2 SAR data are given in Figure 1c. Indeed, the atmospheric conditions of MABL rolls are distinct from the overall average. In specific, the detected roll events are subject to higher wind speed in the range of 5-17 m·s$^{-1}$ and centered at around 9 m·s$^{-1}$. The air-sea temperature difference spans from $-4.5\,°$C to $0.5\,°$C and centers at $-2\,°$C. Extents of $U10_N$ and $\Delta T_V$ presented here cover almost all the previous roll observations, providing a first global view of atmospheric conditions for the majority of MABL roll events.

According to the bulk Richardson number, roll events identified from the SAR data are through slightly unstable to stable conditions with $RiB_N$ ranging from -0.02 to 0.005 and centering at -0.075. But the range of roll $RiB_N$ distribution is clearly narrower than that of the overall SAR acquisitions. This yet evidences the specific environmental conditions required for roll generation and also agrees well with the theoretical and experimen-

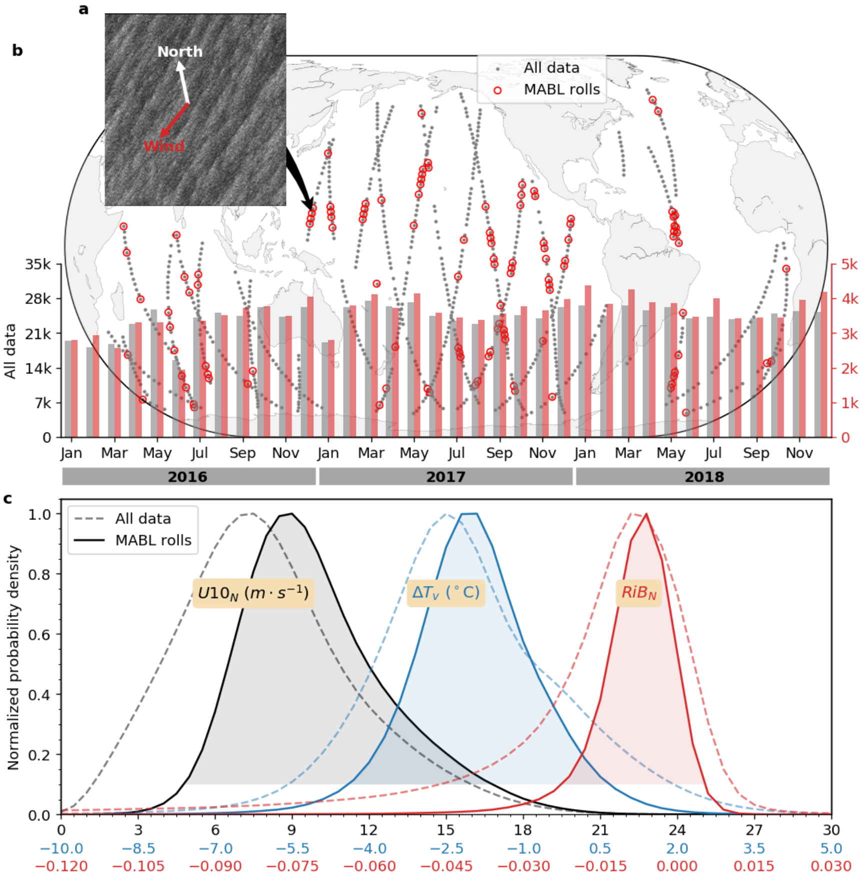

**Figure 1. Overall detection and atmospheric condition of MABL rolls from the global Sentinel-1 wave mode SAR data. a**, an example of sea surface roughness SAR image with the clear quasi-periodic linear roll imprints. The horizontal orientation is approximately aligned with the 10-m wind direction (red arrow). **b**, the map shows one-day (2016-12-29) sampling of Sentinel-1A WV2 acquisition and the identified roll events in red circles. Monthly numbers of total and roll data in 2016-2018 are given in the bar plot. **c**, the environmental conditions of the overall ocean surface and when rolls are formed, demonstrated by the normalized probability functions of $U10_N$, $\Delta T_V$, and $RiB_N$.

tal results [*Atkinson and Wu Zhang*, 1996; *Weckwerth et al.*, 1997; *Young et al.*, 2002]. In detail, 94% of the detected rolls take place in slightly unstable to near-neutral conditions, where either the wind or convection, or the combination of both are in effect. The other 6% of rolls that occur under stable conditions mostly position at high latitudes. These stable stratification are found to be closely associated with the poleward air flows. Warm air is brought in from the equator, leading to a positive $\Delta T_V$. This is manifested by the diagnosis of surface wind components at 50°S from unstable to stable conditions (Supplementary Figure S5). While the zonal wind conforms, the meridional wind exhibits an evident shift from 4.5 m·s$^{-1}$ (unstable) to -1.5 m·s$^{-1}$ (stable). The v-wind direction reversal causes the appearance of the warm advection from the equator to poles. In addition to the local stratification, the warm advection shall also modulate the thermal winds that is usually a constant shear added linearly into the mean wind profile. While the stratification and thermal winds are both significant to the roll dynamics at mid-latitudes, their modulation mechanisms on roll characteristics are not yet resolved. The huge SAR data seem able to provide an avenue to isolate thermal wind effects on roll dynamics. It is beyond the scope of this paper and will be thoroughly addressed in a parallel study.

As a matter of fact, the atmospheric condition of detected roll events is not uniformly distributed across the globe and found to be latitudinal dependent. As shown in Figure 2, $RiB_N$ decreases from nearly 0 at high latitude to -0.02 near the equator, corresponding to the stratification change from near-neutral to slightly unstable. At low latitude (30°S-30°N), the majority of detected rolls occur under unstable conditions. It implies that roll vortices are predominantly driven by the thermal convection. This is additionally featured by the stronger air-sea temperature difference as well as the weaker wind speed as given in Figure 2. Towards the higher latitudes, wind force gradually takes over and dominates the dynamic of roll-shaped boundary layer. This actually echoes the prevalent role of the thermal wind near the polar region as discussed above. In addition to that, the change in the driving force is also reflected by the varying skewness in $RiB_N$ from near zero at high latitude to obvious negative values at the equator.

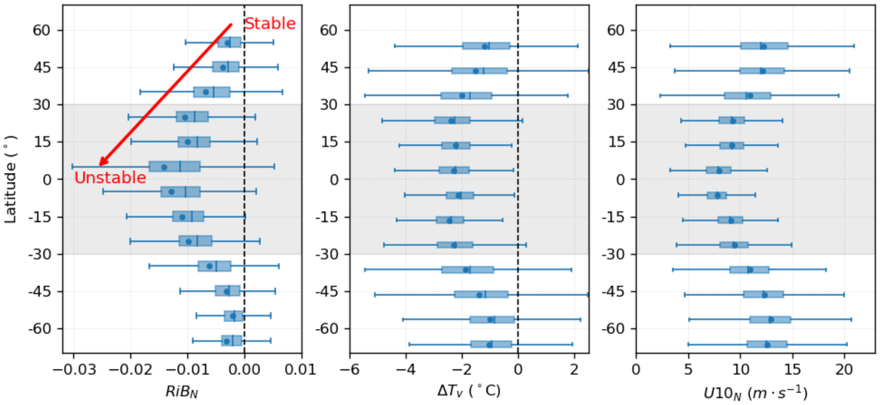

**Figure 2. Latitudinal statistics of $RiB_N$, $\Delta T_V$ and $U10_N$ of identified MABL rolls from the Sentinel-1 WV2 SAR data in 2016-2018.** Box plots are made in each 10° latitude bin from 70°S to 60°N.

## 3 Roll characteristics

While environmental conditions of roll occurrence are certainly important, detailed investigation of roll characteristics is essential towards a better understanding of roll dynamics. One typical roll feature is the horizontal orientation relative to the directions of surface wind or the aloft geostrophic wind. The other key feature is the horizontal roll wavelength ($\lambda$) scaled by the boundary layer height ($h$). In this study, we extract the dominant roll orientation through spectral method from each identified WV roll image. The horizontal wavelength of roll vortices is collected by searching the local peaks within the spectral band determined by the roll orientation angle. Roll wavelengths corresponding to the most three energetic peaks are recorded for the following analysis. The extraction procedure is detailed in Supplementary Text S3.

### 3.1 Horizontal orientation

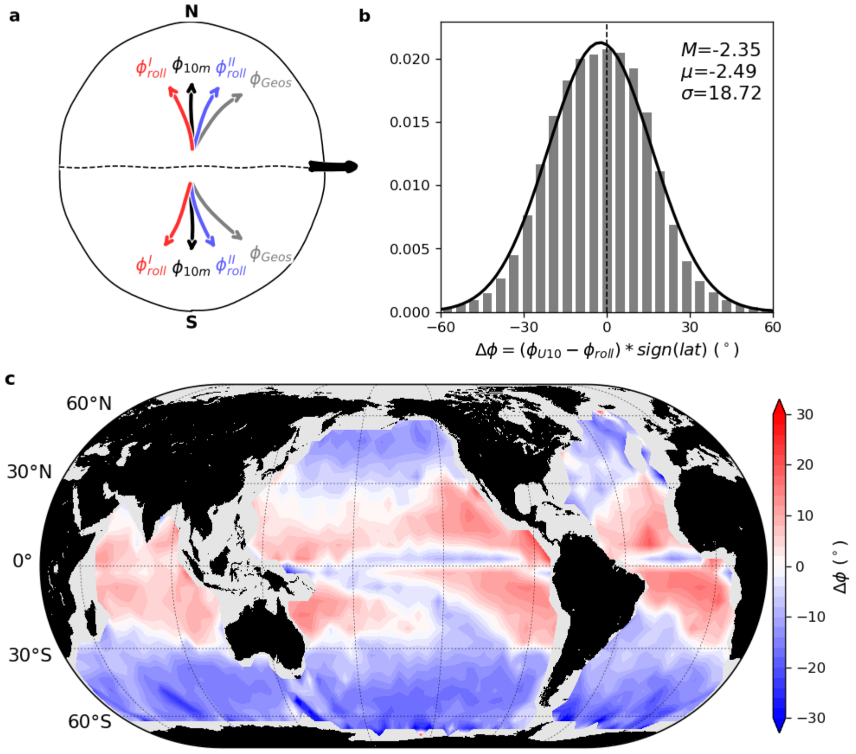

**Figure 3. Global view of roll orientation relative to the surface U10 wind direction. a**. demonstration of roll orientation relation with the surface wind and geostrophic wind directions. **b**. distribution of the angle deviation ($\Delta\phi$) between surface wind direction and roll orientation, sign flips in the southern hemisphere. **c**. global map of the mean $\Delta\phi$ in 5° by 5° grid boxes.

Figure 3a gives an illustration of the horizontal roll orientation with respect to the surface wind and the aloft geostrophic wind. Although roll orientation is roughly in alignment with the mean flow direction, both theoretical and observational investigations have evidenced significance of the angle between roll orientation and the reference wind. The fact that a roll forms within the Ekman spiral determines roll is supposed to orient on the left/right of the geostrophic wind in the northern/southern hemisphere. The angle between roll orientation and the geostrophic wind has been found to vary in a wide range [*Etling and Brown*, 1993; *Atkinson and Wu Zhang*, 1996; *Weckwerth et al.*, 1997]. In the case of small angle deviation, the roll axes fall between the geostrophic wind and surface wind (blue curve in Figure 3a). While roll orientation can be up to 30° relative to the geostrophic wind [e.g. *Brown*, 1970], ending up on the left/right of the surface wind in the northern/southern hemisphere (red curve in Figure 3a). Despite this behavior of roll orientation has been reported in numerous case studies, its statistics is yet to be further explored at both local and global scale.

Here, we choose the 10-m winds from ERA5 as reference to calculate the angle deviation between roll orientation and surface wind direction $\Delta\phi = (\phi_{u10} - \phi_{roll}) \times sign(lat)$.

The results obtained from the new global WV SAR data is presented in Figure 3b. As shown, PDF of the angle deviation roughly follows a normal distribution with the mean of -2.49° and standard deviation of 18.72°. The tiny shift from 0° to negative value is due to the unbalanced data quantity between two hemispheres. It is also worth noting that PDFs of the angle deviation in the northern and southern hemisphere resemble the total with the mean of 0.38° and -4.06°, respectively (Supplementary Figure S6). Overall, 90% of the data lies within the range of [-30°, 30°] that is generally consistent with previous results [*Morrison et al.*, 2005]. The other 9.6% data beyond ±30° may encompass higher uncertainty due to inaccurate model winds and/or the direction errors in the spectral analysis.

Benefiting from the huge dataset, the global signature of roll orientation is readily manifested in Figure 3c. For demonstration, the $\Delta\phi$ is averaged over 5° by 5° latitude and longitude grids. Red color represents that roll orientation is left/right of the surface wind in the northern/southern hemisphere. While the blue color indicates the opposite trend for roll orientation relative to the surface winds. It is surprising to notice that the global map of $\Delta\phi$ can be categorized into two sectors. The anticyclonic roll roll orientation in blue color dominates at high latitudes beyond ±30°. This has been well predicted by the popular roll theories regarding inflection-point and thermal instabilities [*Brown*, 1980; *Etling and Brown*, 1993; *Young et al.*, 2002]. The cyclonic roll orientation in red color, however, prevails at low latitude within 30°S and 30°N, implying that another mechanism for roll dynamic might be in effect. It appears that roll orientation might be related with the absolute wind directions at the global scale. We speculate that the opposite angle deviation from trade winds to the westerlies might be due to impacts of the horizontal Coriolis force on roll dynamics, which is neglected in most of the current theoretical investigations [*Gerkema et al.*, 2008]. In addition, the peculiar strip of negative $\Delta\phi$ near the equator results from the inaccurate surface wind direction of ERA5. Moreover, the leftward roll orientation extends up to the polar region near 60°S, while there is no evident signature in the Arctic due to lack of data acquisition.

### 3.2 Roll length scale

While well organized, roll imprints seen on the SAR images are in fact irregular linear features and exhibit multi-length scales [*Mourad and Walter*, 1996; *Young*, 2000; *Mourad et al.*, 2000]. To extract the dominant wavelengths of roll vortices from each WV imageete, we adopt the 2-D spectral method as detailed in the Supplementary Text S3. The local spectral peaks are extracted and retained according to their energetic significance. 33.9%, 31.7% and 34.4% of the roll events are labeled as single-, double- and triple-scales, respectively (Figure 4a). Note that the proportion of these three types of rolls changes with the energetic threshold chosen to characterize the peak significance (Supplementary Table S1). In the following, the threshold of 50% is applied as we found there is little difference in the aspect ratio statistics for different thresholds. Despite the mutli-scale nature of roll vortices, our results shown here represent a first statistical view of the roll horizontal lengths over the global ocean. But it has to be remarked that large-wavelength rolls, usually occurring in the cold-air-outbreaks [e.g. *Miura*, 1986; *Brümmer*, 1999], can not be addressed by these small WV images. As such, the nonlinear interactions between resonant triads of instabilities proposed in *Mourad and Brown* [1990] are not further resolved in the present work.

As a measure of the vertical shape of roll vortices, the aspect ratio ($AR$) is in parallel examined. It is defined as the roll wavelength scaled by the atmospheric boundary layer height [e.g. *Young et al.*, 2002]. Distribution of $AR$ calculated using the extracted wavelength from the most energetic spectral peak is given in Figure 4a. As shown, the PDF that in black color roughly follows a lognormal curve with a 0.47 geometric standard deviation, s, ranges from 0.2 to 1 for the lognormal distribution [*Morrison et al.*, 2005]. The mean and median are correspondingly 2.91 and 2.64, in good alignment with theoretical predictions [e.g. *Kuettner*, 1971; *Brown*, 1980] and previous observations [*Atkinson*

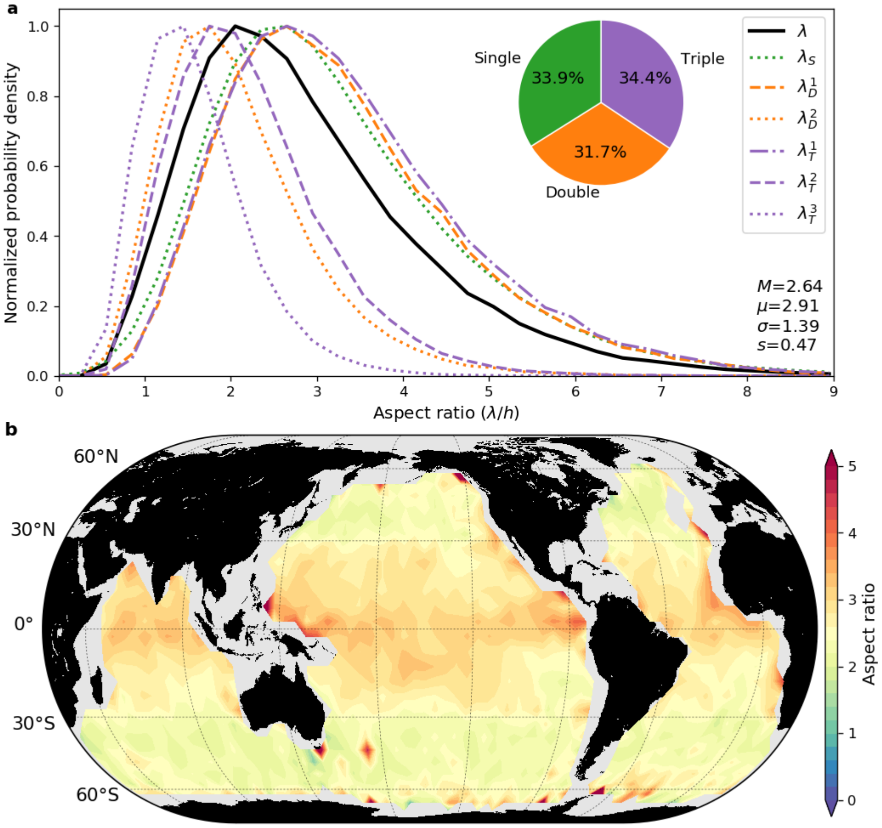

**Figure 4. Global view of roll aspect ratio (*AR*=$\lambda/h$, roll wavelength divided by the boundary layer height). a**. Normalized probability density functions of *AR* for the extracted roll wavelengths from SAR images. Spectral analysis (method supporting information) show that 33.9%, 31.7% and 34.4% of the classified rolls are single-, double- and triple-scales based on the significance of the detected spectrum peaks. $\lambda$ represents the wavelength of the most energetic peak for all the data. For multi-scales cases, $\lambda$ is sorted with decreasing wavelength with $\lambda_D^1 > \lambda_D^2$, $\lambda_T^1 > \lambda_T^2 > \lambda_T^3$. **b**. global map of the mean *AR* for the most energetic peak in 5° by 5° grid boxes.

*and Wu Zhang*, 1996, e.g., 2-5 in]. We also examined the *AR* PDFs of roll events with single-, double- and triple-length scales. For multi-scale cases, the wavelengths are arranged in decreasing order, that is $\lambda_D^1 > \lambda_D^2$ and $\lambda_T^1 > \lambda_T^2 > \lambda_T^3$. All corresponding PDFs are in lognormal distributions. In detail, the *AR* PDFs of $\lambda_S$, $\lambda_D^1$ and $\lambda_T^1$ are quite similar with the *AR* PDF using the most energetic peak, but a bit shifted on the right. The *AR* PDFs of $\lambda_D^2$ and $\lambda_T^2$ are obviously narrower than the black *AR* PDF curve and are also located slightly left of the curve. The PDF of $\lambda_T^3$ is the narrowest and on the leftmost of all PDF curves. By comparison, the *AR* PDF using the most energetic peak covers nearly all *AR* values from the shortest to largest wavelengths for single-, double- and triple-scale roll cases. In other words, the most energetic peak can either be the peaks of short, median or large wavelengths for multi-scale roll events. As the most energetic peak also corresponds to the dominant length scale of roll structures, its *AR* PDF holds the largest representative for all the identified roll cased from the global WV SAR data.

The global map of roll *AR* associated with the most energetic peak is then presented in Figure 4b. It illustrates that rolls in the tropics have a larger *AR* than those in the extratropics. This implies that rolls at low latitude hold a different vertical shape with rolls formed at high latitudes. According to the *AR* PDFs of multi-scale rolls in Figure 4a, it can be deduced that most of the single-scale cases are located in the tropics. However, the global distribution of the most energetic peak roll wavelength is unlike that of the *AR* or roll orientation, showing irregular signatures from the tropics to the high latitudes in both hemispheres (Supplementary Figure S7). This low-to-high latitude contrast of *AR* is closely associated with the global pattern of atmospheric boundary layer height. In addition, we also found that the rolls occurring in the coastal region tend to show higher AR, which is due to the decreasing boundary layer height as well.

## 4 Discussion and conclusion

Benefiting from the newly built dataset of Sentinel-1A WV SAR images with roll imprints, both the atmospheric conditions and roll characteristics are examined on a statistical basis in this paper. Our results across the major ocean basins confirmed the statement that roll vortices are indeed mostly generated at slightly unstable to near-neutral conditions [*Etling and Brown*, 1993; *Atkinson and Wu Zhang*, 1996; *Weckwerth et al.*, 1997; *Young et al.*, 2002]. Also as foreseeable, quantitative examinations unveiled the latitudinal dependence of atmospheric stratification using the bulk Richardson number, which is unstable in the tropics while near-neutral at mid-latitudes. It must be noted that the SAR images of MABL rolls are classified by the pre-developed deep-learning-based classification tool [*Wang et al.*, 2019b]. The tool was created with a limitation of identifying weak roll imprints, and thus may result in bias in the atmospheric condition analysis, particularly for light winds [*Wang et al.*, 2020]. Rejection of the weak roll cases also constrains the examination of roll occurrence at global scale, which is roughly 10%-30% (Supplementary Figure S1b), lower than the two relevant coastal results of 40%-50% in *Levy* [2001]; *Zhao et al.* [2016].

It is certain that the angle accuracy of roll orientation relative to the surface winds to some extent depends on the spectral analysis and the quality of ERA5 variables. Our inspection finds that the spectral method fails to extract the right roll orientation when roll imprints are less visible or there are other phenomena on the WV SAR images. Combining with the possible errors in ERA5 model winds, it is reasonable to observe a small proportion (3.4%) of angle deviation that is beyond ±40°. It is important to emphasize that the majority of the angle of roll orientations relative to the surface wind are trustworthy within ±30°, constituting the new finding that roll orientation systematically differs from low- to mid-latitudes (Figure 3c). This directional contrast must somewhat be linked to the global stratification behavior that changes from unstable near equator to near-neutral at the higher latitudes (Figure 2). Despite that, other factors such as the air flow directions that are overall eastern in tropics while western in extratropics, should also play non-negligible roles in generating the orientation contrast.

In addition to the orientation, the multi-scale roll vortices visible on the high-resolution WV SAR images are examined in terms of their wavelengths. Our extraction of roll wavelength is directly from the local peaks detected within the predominant spectral band as detailed in Supplementary Text S3. It is no doubt that the extraction algorithm can be further refined, we maintain high confidence in the obtained roll wavelengths from a statistical point of view. In determining if one roll event is a single-, double- or triple-scale case, an objective threshold of the relative peak energy is used. Albeit the proportion of these three types varies with choice of the threshold, we found that PDF of their aspect ratio barely changes. Regarding the global feature, roll wavelength of the most energetic peak that corresponds to the strongest component of roll imprints displays a dissimilar spatial pattern as roll orientation. The aspect ratio is, however, found larger at low- than mid-latitudes, similar to the low-high latitude contrast of roll orientation. All these imply that roll dynamics differ from the tropics to extratropics, one aspect that has so far been untapped in the state-of-the-art roll theory.

The latitudinal variations of roll atmospheric condition and basic characteristics evidenced here are both important to studies of roll-shaped boundary layer and related air-sea interactions. Statistics of the aspect ratio and the roll angle with respect to surface wind direction are in good alignment with reports from roll theoretical predictions and numerous field studies. Yet challenges remain. The deep learning tool used to identify rolls from SAR data shall be refined to address the occurrence of MABL rolls by possibly combining the acquisitions from multiple in-orbit SAR satellites. More importantly, in-depth theoretical investigations are essential to advance our understanding of the latitudinal dependence of roll dynamics. One starting point is to examine the horizontal Coriolis force effects on roll formation, which is often neglected in geophysical fluid problems. As such, roll theory studies shall benefit and be extended to a broader range of applications across the global ocean.

## Acknowledgments

This study is supported by ESA Sentinel-1 Mission Performance Center (4000107360/12/I-LG), ESA S1-4SCI Ocean Study (4000115170/15/I-SBo), and CNES TOSCA program (COWS) projects. Foster and Vandemark were supported by NASA Physical Oceanography grant NNX17AH17G. C. Wang is grateful for financial support from the China Scholarship Council (CSC) for his PhD, as well as from the ISblue project Interdisciplinary graduate school for the blue planet (ANR-17-EURE-0015) and the French government program "Investments for the Future".

## References

Alpers, W., and B. Brümmer (1994), Atmospheric boundary layer rolls observed by the synthetic aperture radar aboard the ERS-1 satellite, *Journal of Geophysical Research*, *99*(C6), 12,613, doi:10.1029/94JC00421.

Atkinson, B. W., and J. Wu Zhang (1996), Mesoscale shallow convection in the atmosphere, *Reviews of Geophysics*, *34*(4), 403–431, doi:10.1029/96RG02623.

Banghoff, J. R., J. D. Sorber, D. J. Stensrud, G. S. Young, and M. R. Kumjian (2020), A 10-Year Warm-Season Climatology of Horizontal Convective Rolls and Cellular Convection in Central Oklahoma, *Monthly Weather Review*, *148*(1), 21–42, doi:10.1175/MWR-D-19-0136.1.

Bauer, P., A. Thorpe, and G. Brunet (2015), The quiet revolution of numerical weather prediction, *Nature*, *525*(7567), 47–55, doi:10.1038/nature14956.

Bony, S., B. Stevens, D. M. W. Frierson, C. Jakob, M. Kageyama, R. Pincus, T. G. Shepherd, S. C. Sherwood, A. P. Siebesma, A. H. Sobel, M. Watanabe, and M. J. Webb (2015), Clouds, circulation and climate sensitivity, *Nature Geoscience*, *8*(4), 261–268, doi:10.1038/ngeo2398.

Brooks, I. M., and D. P. Rogers (1997), Aircraft Observations of Boundary Layer Rolls off the Coast of California, *Journal of the Atmospheric Sciences*, *54*(14), 1834–1849, doi: 10.1175/1520-0469(1997)054<1834:AOOBLR>2.0.CO;2.

Brown, R. A. (1970), A Secondary Flow Model for the Planetary Boundary Layer, *Journal of the Atmospheric Sciences*, *27*(5), 742–757, doi:10.1175/1520-0469(1970)027<0742:ASFMFT>2.0.CO;2.

Brown, R. A. (1980), Longitudinal instabilities and secondary flows in the planetary boundary layer: A review, *Reviews of Geophysics*, *18*(3), 683–697, doi: 10.1029/RG018i003p00683.

Brown, R. A. (2000), Serendipity in the use of satellite scatterometer, SAR, and other sensor data, *Johns Hopkins APL Technical Digest (Applied Physics Laboratory)*, *21*(1), 21–26.

Brümmer, B. (1999), Roll and cell convection in wintertime arctic cold-air outbreaks, *Journal of the Atmospheric Sciences*, *56*(15), 2613–2636, doi:10.1175/1520-0469(1999)056<2613:RACCIW>2.0.CO;2.

Brunt, D. (1938), Gliding and Soaring Flight*, *Nature*, *141*(3573), 712–716, doi: 10.1038/141712a0.

Chou, S. H., and M. P. Ferguson (1991), Heat fluxes and roll circulations over the western Gulf Stream during an intense cold-air outbreak, *Boundary-Layer Meteorology*, *55*(3), 255–281, doi:10.1007/BF00122580.

Etling, D., and R. A. Brown (1993), Roll vortices in the planetary boundary layer: A review, *Boundary-Layer Meteorology*, *65*(3), 215–248, doi:10.1007/BF00705527.

Foster, R. C. (2005), Why Rolls are Prevalent in the Hurricane Boundary Layer, *Journal of the Atmospheric Sciences*, *62*(8), 2647–2661, doi:10.1175/JAS3475.1.

Foster, R. C., and G. Levy (1998), The Contribution of Organized Roll Vortices to the Surface Wind Vector in Baroclinic Conditions, *Journal of the Atmospheric Sciences*, *55*(8), 1466–1472, doi:10.1175/1520-0469(1998)055<1466:TCOORV>2.0.CO;2.

Gerkema, T., J. T. F. Zimmerman, L. R. M. Maas, and H. van Haren (2008), Geophysical and astrophysical fluid dynamics beyond the traditional approximation, *Reviews of Geophysics*, *46*(2), RG2004, doi:10.1029/2006RG000220.

Gerling, T. W. (1986), Structure of the surface wind field from the Seasat SAR, *Journal of Geophysical Research*, *91*(C2), 2308, doi:10.1029/JC091iC02p02308.

Huang, L., X. Li, B. Liu, J. A. Zhang, D. Shen, Z. Zhang, and W. Yu (2018), Tropical Cyclone Boundary Layer Rolls in Synthetic Aperture Radar Imagery, *Journal of Geophysical Research: Oceans*, *123*(4), 2981–2996, doi:10.1029/2018JC013755.

Kuettner, J. (1959), The Band Structure of the Atmosphere, *Tellus*, *11*(3), 267–294, doi: 10.3402/tellusa.v11i3.9319.

Kuettner, J. P. (1971), Cloud bands in the earth's atmosphere: Observations and Theory, *Tellus*, *23*(4-5), 404–426, doi:10.3402/tellusa.v23i4-5.10519.

Leibovich, S., and S. K. Lele (1985), The influence of the horizontal component of Earth's angular velocity on the instability of the Ekman layer, *Journal of Fluid Mechanics*, *150*, 41–87, doi:10.1017/S0022112085000039.

Lemone, M. A. (1976), Modulation of Turbulence Energy by Longitudinal Rolls in an Unstable Planetary Boundary Layer, *Journal of the Atmospheric Sciences*, *33*(7), 1308–1320, doi:10.1175/1520-0469(1976)033<1308:MOTEBL>2.0.CO;2.

Levy, G. (2001), Boundary layer roll statistics from SAR, *Geophysical Research Letters*, *28*(10), 1993–1995, doi:10.1029/2000GL012667.

Li, X., W. Zheng, X. Yang, J. A. Zhang, W. G. Pichel, and Z. Li (2013), Coexistence of Atmospheric Gravity Waves and Boundary Layer Rolls Observed by SAR*, *Journal of the Atmospheric Sciences*, *70*(11), 3448–3459, doi:10.1175/JAS-D-12-0347.1.

Miura, Y. (1986), Aspect ratios of longitudinal rolls and convection cells observed during cold air outbreaks., *Journal of the Atmospheric Sciences*, *43*(1), 26–39, doi: 10.1175/1520-0469(1986)043<0026:AROLRA>2.0.CO;2.

Morrison, I., S. Businger, F. Marks, P. Dodge, and J. A. Businger (2005), An Observational Case for the Prevalence of Roll Vortices in the Hurricane Boundary Layer*, *Journal of the Atmospheric Sciences*, *62*(8), 2662–2673, doi:10.1175/JAS3508.1.

Mourad, P. D., and R. A. Brown (1990), Multiscale Large Eddy States in Weakly Stratified Planetary Boundary Layers, *Journal of the Atmospheric Sciences*, *47*(4), 414–438, doi:10.1175/1520-0469(1990)047<0414:MLESIW>2.0.CO;2.

Mourad, P. D., and B. A. Walter (1996), Viewing a cold air outbreak using satellite-based synthetic aperture radar and advanced very high resolution radiometer imagery, *Journal of Geophysical Research: Oceans*, *101*(C7), 16,391–16,400, doi:10.1029/96JC01123.

Mourad, P. D., D. R. Thompson, and D. C. Vandemark (2000), Extracting fine-scale wind fields from synthetic aperture radar images of the ocean surface, *Johns Hopkins APL Technical Digest (Applied Physics Laboratory)*.

Müller, D., D. Etling, C. Kottmeier, and R. Roth (1985), On the occurrence of cloud streets over Northern Germany, *Quarterly Journal of the Royal Meteorological Society*, *111*(469), 761–772, doi:10.1002/qj.49711146906.

Pithan, F., G. Svensson, R. Caballero, D. Chechin, T. W. Cronin, A. M. L. Ekman, R. Neggers, M. D. Shupe, A. Solomon, M. Tjernström, and M. Wendisch (2018), Role of air-mass transformations in exchange between the Arctic and mid-latitudes, *Nature Geoscience*, *11*(11), 805–812, doi:10.1038/s41561-018-0234-1.

Salesky, S. T., M. Chamecki, and E. Bou-Zeid (2017), On the Nature of the Transition Between Roll and Cellular Organization in the Convective Boundary Layer, *Boundary-Layer Meteorology*, *163*(1), 41–68, doi:10.1007/s10546-016-0220-3.

Sherwood, S. C., S. Bony, and J.-L. Dufresne (2014), Spread in model climate sensitivity traced to atmospheric convective mixing, *Nature*, *505*(7481), 37–42, doi:10.1038/nature12829.

Vandemark, D., P. D. Mourad, S. A. Bailey, T. L. Crawford, C. A. Vogel, J. Sun, and B. Chapron (2001), Measured changes in ocean surface roughness due to atmospheric boundary layer rolls, *Journal of Geophysical Research: Oceans*, *106*(C3), 4639–4654, doi:10.1029/1999JC000051.

Walter, B. A., and J. E. Overland (1984), Observations of Longitudinal Rolls in a Near Neutral Atmosphere, *Monthly Weather Review*, *112*(1), 200–208, doi:10.1175/1520-0493(1984)112<0200:OOLRIA>2.0.CO;2.

Wang, C., A. Mouche, P. Tandeo, J. E. Stopa, N. Longépé, G. Erhard, R. C. Foster, D. Vandemark, and B. Chapron (2019a), A labelled ocean SAR imagery dataset of ten geophysical phenomena from SentinelâĂŘ1 wave mode, *Geoscience Data Journal*, *0*(0), gdj3.73, doi:10.1002/gdj3.73.

Wang, C., P. Tandeo, A. Mouche, J. E. Stopa, V. Gressani, N. Longepe, D. Vandemark, R. C. Foster, and B. Chapron (2019b), Classification of the global Sentinel-1 SAR vignettes for ocean surface process studies, *Remote Sensing of Environment*, *234*, 111,457, doi:10.1016/j.rse.2019.111457.

Wang, C., D. Vandemark, A. Mouche, B. Chapron, H. Li, and R. C. Foster (2020), Global assessment of marine atmospheric boundary layer roll detection using Sentinel-1 SAR data, *Remote Sensing of Environment*.

Weckwerth, T. M., J. W. Wilson, R. M. Wakimoto, and N. A. Crook (1997), Horizontal Convective Rolls: Determining the Environmental Conditions Supporting their Existence and Characteristics, *Monthly Weather Review*, *125*(4), 505–526, doi:10.1175/1520-0493(1997)125<0505:HCRDTE>2.0.CO;2.

Weston, K. J. (1980), An observational study of convective cloud streets, *Tellus*, *32*(5), 433–438, doi:10.3402/tellusa.v32i5.10598.

Wurman, J., and J. Winslow (1998), Intense sub-kilometer-scale boundary layer rolls observed in hurricane Fran, *Science*, *280*(5363), 555–557, doi:10.1126/science.280.5363.555.

Young, G. S. (2000), SAR signatures of the marine atmospheric boundary layer: Implications for numerical forecasting, *Johns Hopkins APL Technical Digest (Applied Physics Laboratory)*.

Young, G. S., D. A. R. Kristovich, M. R. Hjelmfelt, and R. C. Foster (2002), Rolls, Streets, Waves, and More: A Review of Quasi-Two-Dimensional Structures in the Atmospheric Boundary Layer, *Bulletin of the American Meteorological Society*, *83*(7), 997–1001, doi:10.1175/1520-0477(2002)083<0997:RSWAMA>2.3.CO;2.

Zhao, Y., X.-M. Li, and J. Sha (2016), Sea surface wind streaks in spaceborne synthetic aperture radar imagery, *Journal of Geophysical Research: Oceans*, *121*(9), 6731–6741, doi:10.1002/2016JC012040.

# Supporting Information for "Insights into the Global Feature of Marine Atmospheric Boundary Layer Rolls"

**Chen Wang**[1,2], **Douglas Vandemark**[3], **Bertrand Chapron**[1], **Alexis Mouche**[1], **Ralph C. Foster**[4],

[1]IFREMER, Univ. Brest, CNRS, IRD, Laboratoire d'Oceanographie Physique et Spatiale (LOPS), Brest, France
[2]IMT Atlantique, LabSTICC, UBL, Brest, France
[3]Ocean Processes Analysis Laboratory, University of New Hampshire, USA
[4]Applied Physics Laboratory, University of Washington, USA

## Contents

1. Text S1 to S3
2. Figures S1 to S7
3. Tables S1

## Text S1. Sentinel-1 wave mode SAR data

Sentinel-1 (S-1) is a polar-orbiting, sun-synchronous C-band SAR satellite constellation mission [*Torres et al.*, 2012]. It is designed for long-term operation extending into the next decades. Two satellites (A&B), sharing the same orbital plane offset by a 180° phase difference, have been launched in April of 2014 and 2016, respectively. Both satellites are equipped with identical SAR instruments operating in pre-programmed modes of Interferometric Wide swath (IW), Extra Wide swath mode (EW), Strip Map (SM) and WaVe mode (WV). Among which, WV is the default mode over global oceans except the Arctic, closed seas and coastal areas. WV mode is specialized to acquire small SAR image scenes (termed images) at two alternating incidence angles of 23° (WV1) and 36.5° (WV2), both operated in linear vertical (VV) transmit and receive (default) polarization, and during special phases in horizontal (HH) polarization. Each WV image size is 20 km by 20 km, with 5 m pixel resolution. The acquisition is step-wise, with spacing between two neighboring images being between 100-120 km, and with nearly exact repeat sampling of each 12 days. On average, more than 30,000 images per month are collected by each satellite at each incidence angle. The WV SAR data repository of the Level-1 Sin-

---

Corresponding author: Chen Wang, `cwang@ifremer.fr`

gle Look Complex (SLC) product is managed at IFREMER (`http://www.ifremer.fr/datavore/exp/dvor/#/s1quicklook`), and also at ESA's Sentinel Open Access Hub (`https://sentinel.esa.int/web/sentinel/sentinel-data-access`).

In this study, we use S-1A WV2 SAR data spanning 2016-2018, all acquired in VV polarization. All inland and coastal images are filtered out for this analysis and ocean data are limited to have the surface temperature larger than 0 °C to avoid possible sea ice impact. Figure S1a illustrates the sample population of these images on a 5° by 5° global spatial grid. Data coverage is nearly complete over the Pacific, Indian and south Atlantic oceans while partial for the eastern north Atlantic ocean because, by default, other standard imaging modes are in operation. The total number of images evaluated within these S-1A WV2 dataset is 868,878 in total.

Each image is colocated in time and space with the surface variables from the ERA5, including 10 meter wind components ($u10$, $v10$), sea surface temperature ($SST$), 2 meter air temperature ($T2m$), 2 meter dew-point temperature ($d2m$) and surface pressure ($sp$). ERA5 is the latest generation of the European Centre for Medium-Range Weather Forecasts (ECMWF) reanalysis products that provide the environmental variables hourly and on a global spatial grid of 0.25° by 0.25°. The data are publicly available at `https://cds.climate.copernicus.eu`. Based on these variables, the atmospheric parameters of the neutral bulk Richardson number ($RiB_N$), the neutral wind speed ($U10_N$) and virtual air-sea temperature difference ($\Delta T_V$) at 10 meter height are derived, using the COARE 3.0 air-sea turbulent flux algorithm [*Fairall et al.*, 2003].

## Text S2. Automated identification of roll events

To extend application of these global S-1 WV SAR data beyond ocean waves, an automated image classification tool has been recently created [*Wang et al.*, 2019a,b]. We briefly describe this work here with an emphasis on the MABL roll identification. The top ten common geophysical phenomena seen in the WV image data was firstly defined [*Wang et al.*, 2019a]. They were ocean swell, wind streaks, micro-convective cells, rain cells, biological slicks, sea ice, icebergs, low wind areas, atmospheric fronts, and oceanic fronts. Visual selection was then used to build a large representative collection for each class, leading to an open-access labelled database called TenGeoP-SARwv [*Wang et al.*, 2018]. It has supported our training and validating of the automated classification tool, which is developed from the deep Inception-v3 convolutional neural network (CNN) [*Szegedy et al.*, 2015; *Wang et al.*, 2019b]. This tool, namely CMwv, is able to discriminate the input WV scene for the ten defined geophysical classes. In detail, CMwv assigns each WV image a probability score for each class. These probabilities add up to 1, and a WV image is considered to represent a case of visually-distinct MABL roll impacts (i.e. wind streaks) if the roll class score is the largest among the ten. The quantified skill of this tool has a Recall (sensitivity) of 83% and Precision (positive detection rate) of 96% for WV2 data [*Wang et al.*, 2019b]. More details and discussion about CMwv and its performance on classification of MABL rolls are documented in *Wang et al.* [2019b, 2020].

## Text S2. Extraction of roll orientation and wavelength from SAR images

While might be irregular, roll imprints visible on SAR images are usually organized linear features. This coherent and periodic structure can be well analyzed by the spectral method, i.e. two-dimensional Fourier transform (2-D FFT). In many relevant studies, the approach has been proven to be effective in extracting the roll orientation and/or wavelengths from ocean SAR images [*Gerling*, 1986; *Mourad and Walter*, 1996; *Lehner et al.*, 1998; *Li et al.*, 2013]. Here, we describe the specific procedures of this spectral method dedicated for S-1 WV SAR image. Two examples are demonstrated in detail with one being recognized as a single-scale roll event and another as a multi-scale roll case.

Figure S2a illustrates the normalized radar cross-section ($\sigma^0$) image that is already shown in Figure 1a. For better visualization, resolution of this image was down-sampled to be 1/10 of the original using a box average. This process filters out small ocean wave/swell features, outstanding the roll signatures. The white and red arrows on the image indicate North and ERA5 10-m wind direction. One can clearly notice that the roll linear features are approximately aligned with the surface winds.

The image spectrum $S(k_x, k_y)$ is calculated using the 2-D FFT algorithm over the whole $\sigma^0$ image, and then converted from Cartesian to Polar coordinates, $S(k, \phi)$. Figure S2b displays the spectral part for wavelength ($\lambda$=$2\pi/k$) between 0.8 and 6 km. Angle $\phi$ is in SAR image coordinate with 0° being the positive azimuth and rotating to the range direction. As there is a 180° direction ambiguity, the spectral energy is concentrated in two clusters located near $\phi$=117° and 297° in the case of Figure S2a. These spectral clusters correspond to the periodic roll signatures in spatial domain. To objectively extract the dominant roll orientation, we draw the integrated spectral profile of $s(\phi) = \int_{k=2\pi/4000}^{k=2\pi/800} s(k,\phi)dkd\phi$ in Figure S2c, with the maximum marked as a red dot at $\phi_0$=117°. A narrower spectral section is adopted here to avoid any impacts of spectral energy generated by the non-roll features. From $\phi_0$, we can calculate the roll orientation $\phi_{roll}$= $\phi_0$+$\phi_h$+$\pi/2$, in geographic coordinate (clockwise relative to the North). Where $\phi_h$ represents the angle of SAR image heading. Noticing that the 180° ambiguity of $\phi_{roll}$ can be removed by referring to the collocated ERA5 10-m height surface wind direction.

Once the dominant roll orientation is locked, one can define the specific spectrum band for MABL roll structures. The band width is determined by the relative spectral energy as shown in Figure S2c, 50% of the maximum. We then extract the local peaks within the limited spectrum band (dashed red box in Figure S2b), and record the top three most energetic ones. Energy level of these peaks decides a roll case is single-scale or multi-scale. In detail in this work, the peaks are sorted in decreasing spectral energy with $E_1$>$E_2$>$E_3$. A roll case is recognized as single-, double- or triple-scales only when $E_2$<f*$E_1$, $E_2$>f*$E_1$ & $E_3$<f*$E_2$ or $E_3$>f*$E_2$, respectively. The f indicates a percentage threshold, and we see that the cases in Figure S2 and Figure S3 are recognized as single- and triple-scale roll events with f=50%. A detailed proposition change of single-, double- and triple-scale rolls with different thresholds is given in Table S1. Roll wavelengths thus can easily be read from these extracted peaks. Wavelength of the most energetic peak is donated as $\lambda$. Wavelengths of the multi-scale rolls are donated by $\lambda_S$, $\lambda_D^i$ and $\lambda_T^i$ (i=1,2,3), all sorted in decreasing order, i.e. $\lambda_D^1$>$\lambda_D^2$ and $\lambda_T^1$>$\lambda_T^2$>$\lambda_T^3$.

## References

Fairall, C. W., E. F. Bradley, J. E. Hare, A. A. Grachev, and J. B. Edson (2003), Bulk Parameterization of AirâĂŞSea Fluxes: Updates and Verification for the COARE Algorithm, *Journal of Climate*, *16*(4), 571–591, doi:10.1175/1520-0442(2003)016<0571:BPOASF>2.0.CO;2.

Gerling, T. W. (1986), Structure of the surface wind field from the Seasat SAR, *Journal of Geophysical Research*, *91*(C2), 2308, doi:10.1029/JC091iC02p02308.

Lehner, S., J. Horstmann, W. Koch, and W. Rosenthal (1998), Mesoscale wind measurements using recalibrated ERS SAR images, *Journal of Geophysical Research: Oceans*, *103*(C4), 7847–7856, doi:10.1029/97JC02726.

Li, X., W. Zheng, X. Yang, J. A. Zhang, W. G. Pichel, and Z. Li (2013), Coexistence of Atmospheric Gravity Waves and Boundary Layer Rolls Observed by SAR*, *Journal of the Atmospheric Sciences*, *70*(11), 3448–3459, doi:10.1175/JAS-D-12-0347.1.

Mourad, P. D., and B. A. Walter (1996), Viewing a cold air outbreak using satellite-based synthetic aperture radar and advanced very high resolution radiometer imagery, *Journal of Geophysical Research: Oceans*, *101*(C7), 16,391–16,400, doi:10.1029/96JC01123.

Szegedy, C., Wei Liu, Yangqing Jia, P. Sermanet, S. Reed, D. Anguelov, D. Erhan, V. Vanhoucke, and A. Rabinovich (2015), Going deeper with convolutions, in *2015 IEEE Conference on Computer Vision and Pattern Recognition (CVPR)*, vol. 07-12-June, pp. 1–9, IEEE, doi:10.1109/CVPR.2015.7298594.

Torres, R., P. Snoeij, D. Geudtner, D. Bibby, M. Davidson, E. Attema, P. Potin, B. Rommen, N. Floury, M. Brown, I. N. Traver, P. Deghaye, B. Duesmann, B. Rosich, N. Miranda, C. Bruno, M. L'Abbate, R. Croci, A. Pietropaolo, M. Huchler, and F. Rostan (2012), GMES Sentinel-1 mission, *Remote Sensing of Environment*, *120*(Supplement C), 9–24, doi:10.1016/j.rse.2011.05.028.

Wang, C., A. Mouche, P. Tandeo, J. Stopa, N. Longépé, G. Erhard, R. Foster, D. Vandemark, and B. Chapron (2018), Labeled SAR imagery dataset of ten geophysical phenomena from Sentinel-1 wave mode (TenGeoP-SARwv), doi:10.17882/56796.

Wang, C., A. Mouche, P. Tandeo, J. E. Stopa, N. Longépé, G. Erhard, R. C. Foster, D. Vandemark, and B. Chapron (2019a), A labelled ocean SAR imagery dataset of ten geophysical phenomena from SentinelâĂŘ1 wave mode, *Geoscience Data Journal*, *0*(0), gdj3.73, doi:10.1002/gdj3.73.

Wang, C., P. Tandeo, A. Mouche, J. E. Stopa, V. Gressani, N. Longepe, D. Vandemark, R. C. Foster, and B. Chapron (2019b), Classification of the global Sentinel-1 SAR vignettes for ocean surface process studies, *Remote Sensing of Environment*, *234*, 111,457, doi:10.1016/j.rse.2019.111457.

Wang, C., D. Vandemark, A. Mouche, B. Chapron, H. Li, and R. C. Foster (2020), Global assessment of marine atmospheric boundary layer roll detection using Sentinel-1 SAR data, *Remote Sensing of Environment*.

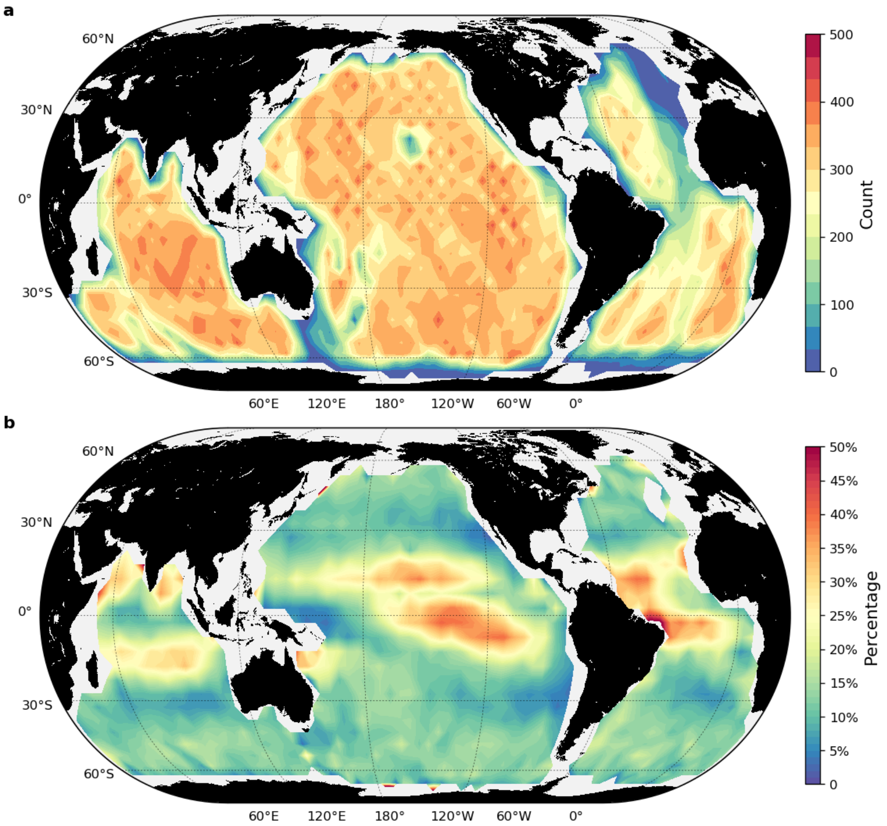

**Figure S1.** Spatial gridded statistics of, **a**, Sentinel-1A WV2 SAR images in 2016-2018 and, **b**, the percentage of identified roll events in 5° by 5° grid boxes.

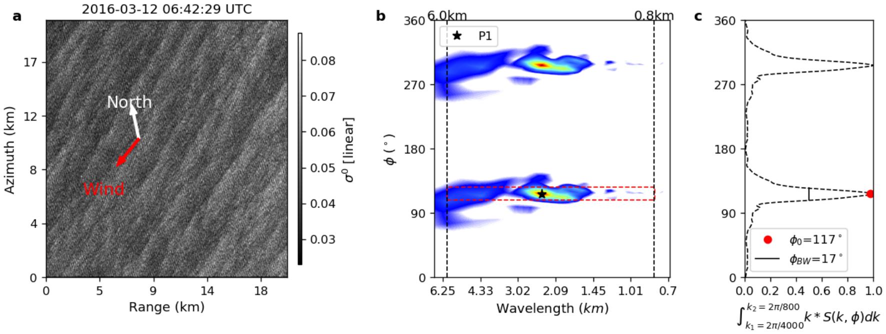

**Figure S2.** Demonstration roll orientation and wavelength extraction from the Sentinel-1 WV SAR image in terms of a single-scale roll case. **a**. A typical WV SAR image with km-scale linear rol features being clearly visible. The white and red arrows indicate North and the ERA5 wind direction. **b**. The 2-D FFT image spectrum, $S(k,\phi)$, within the expected wavelength ($\lambda$=$2\pi/k$) range of 0.8-6 km for MABL roll structures. The Angle $\phi$ is in SAR image coordinates, i.e. relative to the azimuth rotating from 0° to range. The colored star indicates the detected local spectrum peaks within the dashed red spectrum band. **c**. Integral of the spectrum $S(k,\phi)$ at each $\phi$ and wavenumber between $2\pi/4000$ and $2\pi/800$, maximum marked as a red dot and noted as $\phi_0$. Vertical line indicates the width of the spectral band ($\phi_{BW}$) associated with the roll structures.

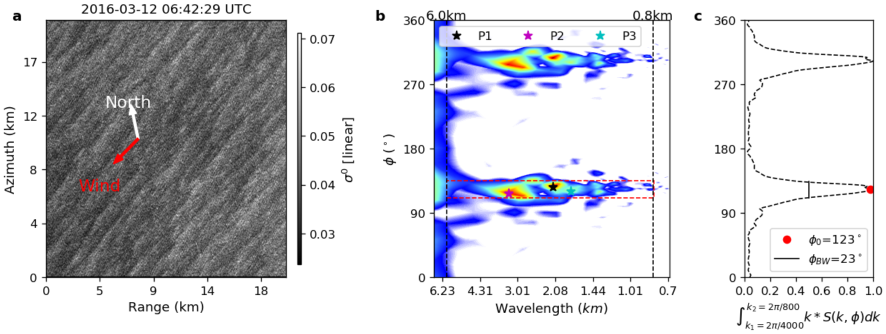

**Figure S3.** Similar to Figure S2 but for a multi-scale roll case.

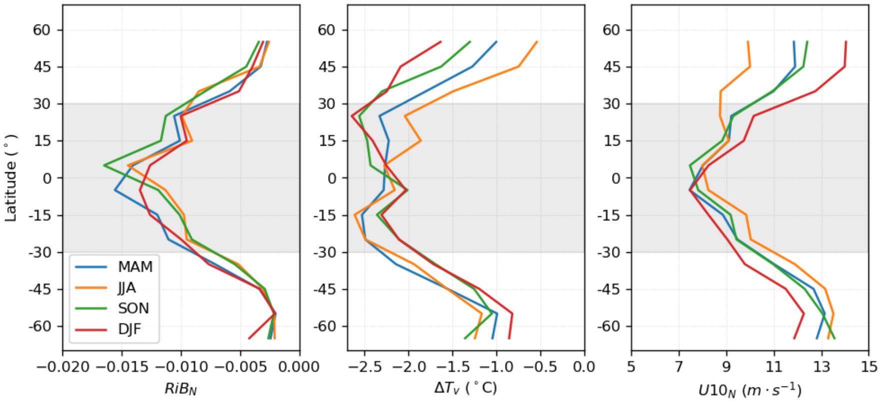

**Figure S4.** Latitudinal statistics of $RiB_N$, $\Delta T_V$ and $U10_N$ of all Sentinel-1 WV2 acquisitions in 2016-2018. Box plots are made in each 10° latitude bin from 70° S to 60° N.

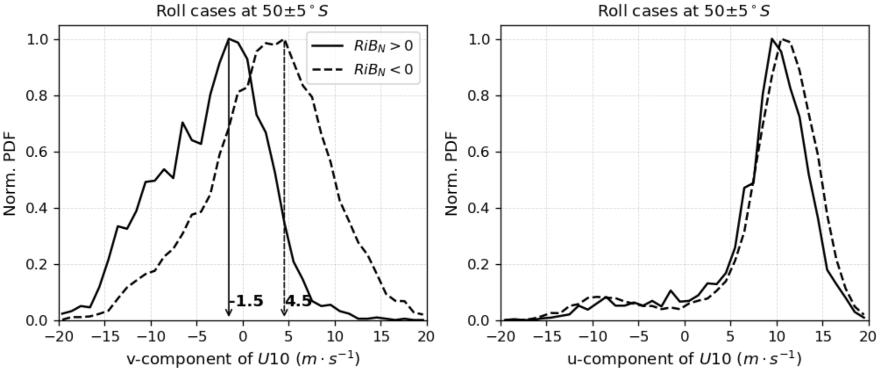

**Figure S5.** Comparisons of v- and u-component for stable ($RiB_N$>0) and near-neutral to unstable ($RiB_N$<0) rolls at 50° southern ocean.

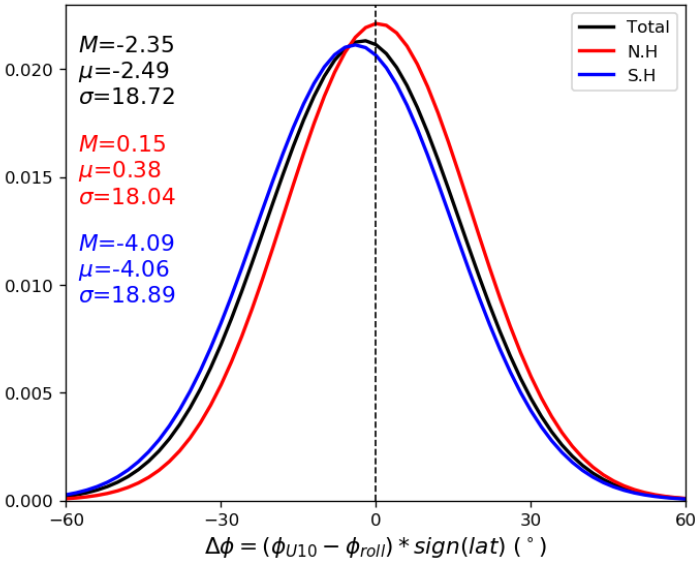

**Figure S6.** Distribution of the angle deviation ($\Delta\phi$) from roll orientation to ERA5 surface wind direction for total, northern hemisphere (N.H) and southern hemisphere (S.H), respectively.

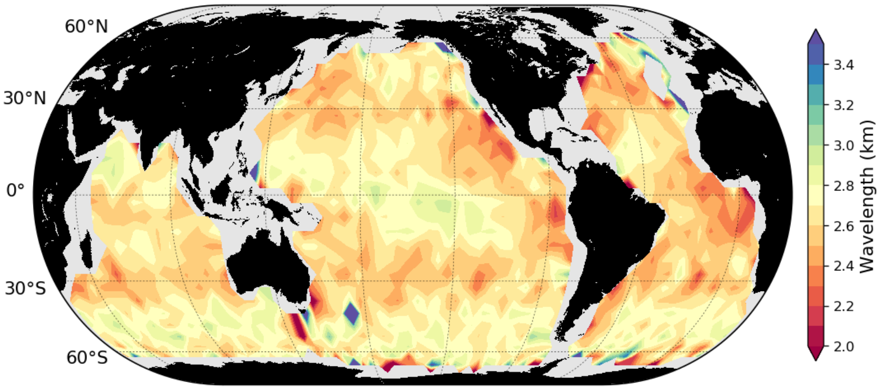

**Figure S7.** Global distribution of the extracted roll wavelength from the most energetic peak of the identified WV SAR images. Color donates the average in 5° by 5° grid boxes.

**Table S1.** Proportion changes of single-, double- and triple-scale roll events with increasing threshold.

| Threshold | single-scale | double-scale | triple-scale |
|---|---|---|---|
| 10% | 1.41% | 5.08% | 93.50% |
| 20% | 6.63% | 14.69% | 78.68% |
| 30% | 14.31% | 23.18% | 62.51% |
| 40% | 23.54% | 28.82% | 47.64% |
| 50% | 33.90% | 31.73% | 34.37% |
| 60% | 44.92% | 31.95% | 23.13% |
| 70% | 56.89% | 29.41% | 13.70% |
| 80% | 69.89% | 23.68% | 6.43% |
| 90% | 83.83% | 14.35% | 1.82% |

# References

Agee, E. M., & Gilbert, S. R. (1989). An Aircraft Investigation of Mesoscale Convection over Lake Michigan during the 10 January 1984 Cold Air Outbreak. *Journal of the Atmospheric Sciences*, *46*(13), 1877–1897. doi: 10.1175/1520-0469(1989)046<1877:AAIOMC>2.0.CO;2

Agee, E. M., & Lomax, F. E. (1978). Structure of the Mixed Layer and Inversion Layer Associated with Patterns of Mesoscale Cellular Convection During AMTEX 75. *Journal of the Atmospheric Sciences*, *35*(12), 2281–2301. doi: 10.1175/1520-0469(1978)035<2281:SOTMLA>2.0.CO;2

Alpers, W., & Brümmer, B. (1994). Atmospheric boundary layer rolls observed by the synthetic aperture radar aboard the ERS-1 satellite. *Journal of Geophysical Research*, *99*(C6), 12613. doi: 10.1029/94JC00421

Alpers, W., Zhang, B., Mouche, A., Zeng, K., & Chan, P. W. (2016). Rain footprints on C-band synthetic aperture radar images of the ocean - Revisited. *Remote Sensing of Environment*, *187*, 169–185. doi: 10.1016/j.rse.2016.10.015

Asai, T. (1966). Cloud Bands over the Japan Sea off the Hokuriku District during a Cold Air Outburst. *Papers in Meteorology and Geophysics*, *16*(3-4), 179–194. doi: 10.2467/mripapers1950.16.3-4_179

Asai, T. (1970). Stability of a Plane Parallel Flow with Variable Vertical Shear and Unstable Stratification. *Journal of the Meteorological Society of Japan. Ser. II*, *48*(2), 129–139. doi: 10.2151/jmsj1965.48.2_129

Asai, T., & Nakasuji, I. (1973). On the Stability of Ekman Boundary Layer Flow with Thermally Unstable Stratification. *Journal of the Meteorological Society of Japan. Ser. II*, *51*(1), 29–42. doi: 10.2151/jmsj1965.51.1_29

Atkinson, B. W., & Wu Zhang, J. (1996). Mesoscale shallow convection in the atmosphere. *Reviews of Geophysics*, *34*(4), 403–431. doi: 10.1029/96RG02623

Atlas, D., Chou, S.-H., & Byerly, W. P. (1983). The Influence of Coastal Shape on Winter Mesoscale Air-Sea Interaction. *Monthly Weather Review*, *111*(2), 245–252. doi: 10.1175/1520-0493(1983)111<0245:TIOCSO>2.0.CO;2

Atlas, D., Walter, B., Chou, S.-H., & Sheu, P. J. (1986). The Structure of the Unstable Marine Boundary Layer Viewed by Lidar and Aircraft Observations. *Journal of the Atmospheric Sciences*, *43*(13), 1301–1318. doi: 10.1175/1520-0469(1986)043<1301:TSOTUM>2.0.CO;2

Banghoff, J. R., Sorber, J. D., Stensrud, D. J., Young, G. S., & Kumjian, M. R. (2020). A 10-Year Warm-Season Climatology of Horizontal Convective Rolls and Cellular Convection in Central Oklahoma. *Monthly Weather Review*, *148*(1), 21–42. doi: 10.1175/MWR-D-19-0136.1

Bauer, P., Thorpe, A., & Brunet, G. (2015). The quiet revolution of numerical weather prediction. *Nature*, *525*(7567), 47–55. doi: 10.1038/nature14956

Bony, S., Stevens, B., Frierson, D. M. W., Jakob, C., Kageyama, M., Pincus, R., … Webb, M. J. (2015). Clouds, circulation and climate sensitivity. *Nature Geoscience*, *8*(4), 261–268. doi: 10.1038/ngeo2398

Brilouet, P., Durand, P., & Canut, G. (2017). The marine atmospheric boundary layer under strong wind conditions: Organized turbulence structure and flux estimates by airborne measurements. *Journal of Geophysical Research: Atmospheres*, *122*(4), 2115–2130. doi: 10.1002/2016JD025960

Brown, R. A. (1970). A Secondary Flow Model for the Planetary Boundary Layer. *Journal of the Atmospheric Sciences*, *27*(5), 742–757. doi: 10.1175/1520-0469(1970)027<0742:asfmft>2.0.co;2

Brown, R. A. (1972). On the Inflection Point Instability of a Stratified Ekman Boundary Layer. *Journal of the Atmospheric Sciences*, *29*(5), 850–859. doi: 10.1175/1520-0469(1972)029<0850:OTIPIO>2.0.CO;2

Brown, R. A. (1980). Longitudinal instabilities and secondary flows in the planetary boundary layer: A review. *Reviews of Geophysics*, *18*(3), 683–697. doi: 10.1029/RG018i003p00683

Brown, R. A. (2000). Serendipity in the use of satellite scatterometer, SAR, and other sensor data. *Johns Hopkins APL Technical Digest (Applied Physics Laboratory)*, *21*(1), 21–26.

Brown, R. A. (2002). Scaling effects in remote sensing applications and the case of organized large eddies. *Canadian Journal of Remote Sensing*, *28*(3), 340–345. doi: 10.5589/m02-033

Brown, R. A., & Liu, W. T. (1982). An Operational Large-Scale Marine Planetary Boundary Layer Model. *Journal of Applied Meteorology*, *21*(3), 261–269. doi: 10.1175/1520-0450(1982)021<0261:aolsmp>2.0.co;2

Brümmer, B. (1996). Boundary-layer modification in wintertime cold-air outbreaks from the Arctic sea ice. *Boundary-Layer Meteorology*, *80*(1-2), 109–125. doi: 10.1007/BF00119014

Brümmer, B. (1999). Roll and Cell Convection in Wintertime Arctic Cold-Air Outbreaks. *Journal of the Atmospheric Sciences*, *56*(15), 2613–2636. doi: 10.1175/1520-0469(1999)056<2613:RACCIW>2.0.CO;2

Brunt, D. (1938). Gliding and Soaring Flight*. *Nature*, *141*(3573), 712–716. doi: 10.1038/141712a0

Chapron, B., Johnsen, H., & Garello, R. (2001). Wave and wind retrieval from sar images of the ocean. *Annales Des Télécommunications*, *56*(11), 682–699. doi: 10.1007/BF02995562

Chen, W., Banner, M. L., Walsh, E. J., Jensen, J. B., & Lee, S. (2001). The Southern Ocean Waves Experiment. Part II: Sea Surface Response to Wind Speed and Wind Stress Variations. *Journal of Physical Oceanography*, *31*(1), 174–198. doi: 10.1175/1520-0485(2001)031<0174:TSOWEP>2.0.CO;2

Chou, S.-H., Atlas, D., & Yeh, E.-n. (1986). Turbulence in a Convective Marine Atmospheric Boundary Layer. *Journal of the Atmospheric Sciences*, *43*(6), 547–564. doi: 10.1175/1520-0469(1986)043<0547:TIACMA>2.0.CO;2

Chou, S. H., & Ferguson, M. P. (1991). Heat fluxes and roll circulations over the western Gulf Stream during an intense cold-air outbreak. *Boundary-Layer Meteorology*, *55*(3), 255–281. doi: 10.1007/BF00122580

Christian, T. W., & Wakimoto, R. M. (1989). The relationship between radar reflectivities and clouds associated with horizontal roll convection on 8 August 1982. *Monthly Weather Review*. doi: 10.1175/1520-0493(1989)117<1530:TRBRRA>2.0.CO;2

Criminale, W. O., & Spooner, G. F. (1981). Maintenance of oscillations in a turbulent Ekman layer. *Boundary-Layer Meteorology*, *21*(4), 407–421. doi: 10.1007/BF02033591

Cumming, I. G., & Wong, F. H.-c. (2005). *Digital processing of synthetic aperture radar data*. Artech House.

Etling, D. (1971). The stability of an ekman boundary layer flow as influenced by thermal stratification. *Beitr. Phys. Atmos.*, *44*, 168–186.

Etling, D., & Brown, R. A. (1993). Roll vortices in the planetary boundary layer: A review. *Boundary-Layer Meteorology*, *65*(3), 215–248. doi: 10.1007/BF00705527

Etling, D., & Wippermann, F. (1975). On the instability of a planetary boundary layer with Rossby-number similarity. *Boundary-Layer Meteorology*, *9*(3), 341–360. doi: 10.1007/BF00230775

Faller, A. J. (1967). Instability of the Ekman Spiral with Applications to the Planetary Boundary Layers. *Physics of Fluids*, *10*(9), S212. doi: 10.1063/1.1762452

Faller, A. J., & Kaylor, R. E. (1966). A Numerical Study of the Instability of the Laminar Ekman Boundary Layer. *Journal of the Atmospheric Sciences*, *23*(5), 466–480. doi: 10.1175/1520-0469(1966)023<0466:ANSOTI>2.0.CO;2

Ferrare, R. A., Schols, J. L., Eloranta, E. W., & Coulter, R. (1991). Lidar Observations of Banded Convection during BLX83. *Journal of Applied Meteorology*, *30*(3), 312–326. doi: 10.1175/1520-0450(1991)030<0312:LOOBCD>2.0.CO;2

Fletcher, J., Mason, S., & Jakob, C. (2016). The Climatology, Meteorology, and Boundary Layer Structure of Marine Cold Air Outbreaks in Both Hemispheres. *Journal of Climate*, *29*(6), 1999–2014. doi: 10.1175/JCLI-D-15-0268.1

Ford, J. P., Elachi, C., & Cimino, J. B. (1983). *Space shuttle columbia views the world with imaging radar: the sir-a experiment*. Pasadena, Calif.: NASA, Jet Propulsion Laboratory.

Foster, R. C. (1996). *An analytic model for planetary boundary layer roll vortices* (Doctoral dissertation). University of Washington, WA.

Foster, R. C. (2005). Why Rolls are Prevalent in the Hurricane Boundary Layer. *Journal of the Atmospheric Sciences*, *62*(8), 2647–2661. doi: 10.1175/JAS3475.1

Foster, R. C., & Levy, G. (1998). The Contribution of Organized Roll Vortices to the Surface Wind Vector in Baroclinic Conditions. *Journal of the Atmospheric Sciences*, *55*(8), 1466–1472. doi: 10.1175/1520-0469(1998)055<1466:TCOORV>2.0.CO;2

Gao, K., Ginis, I., Doyle, J. D., & Jin, Y. (2017). Effect of Boundary Layer Roll Vortices on the Development of an Axisymmetric Tropical Cyclone. *Journal of the Atmospheric Sciences*, *74*(9), 2737–2759. doi: 10.1175/JAS-D-16-0222.1

Garratt, J. R. (1994). Review: the atmospheric boundary layer. *Earth Science Reviews*. doi: 10.1016/0012-8252(94)90026-4

Gens, R. (2008). Oceanographic Applications of SAR Remote Sensing. *GIScience & Remote Sensing*, *45*(3), 275–305. doi: 10.2747/1548-1603.45.3.275

Gerkema, T., Zimmerman, J. T. F., Maas, L. R. M., & van Haren, H. (2008). Geophysical and astrophysical fluid dynamics beyond the traditional approximation. *Reviews of Geophysics*, *46*(2), RG2004. doi: 10.1029/2006RG000220

Gerling, T. W. (1986). Structure of the surface wind field from the Seasat SAR. *Journal of Geophysical Research*, *91*(C2), 2308. doi: 10.1029/JC091iC02p02308

Glazunov, A. V. (2010). On the effect that the direction of geostrophic wind has on turbulence and quasiordered large-scale structures in the atmospheric boundary layer. *Izvestiya, Atmospheric and Oceanic Physics*, *46*(6), 727–747. doi: 10.1134/S0001433810060058

Gregory, N., Stuart, J. T., Walker, W. S., & Bullard, E. C. (1955). On the stability of three-dimensional boundary layers with application to the flow due to a rotating disk. *Philosophical Transactions of the Royal Society of London. Series A, Mathematical and Physical Sciences*, *248*(943), 155-199. doi: 10.1098/rsta.1955.0013

Grossman, R. L. (1982). An analysis of vertical velocity spectra obtained in the bomex fair-weather, trade-wind boundary layer. *Boundary-Layer Meteorology*, *23*(3), 323–357. doi: 10.1007/BF00121120

Haack, T., & Shirer, H. N. (1992). Mixed Convective–Dynamic Roll Vortices and Their Effects on Initial Wind and Temperature Profiles. *Journal of the Atmospheric Sciences*, *49*(14), 1181–1201. doi: 10.1175/1520-0469(1992)049<1181:MCRVAT>2.0.CO;2

Hasselmann, K., Raney, R. K., Plant, W. J., Alpers, W., Shuchman, R. A., Lyzenga, D. R., … Tucker, M. J. (1985). Theory of synthetic aperture radar ocean imaging: A MARSEN view. *Journal of Geophysical Research*, *90*(C3), 4659. doi: 10.1029/JC090iC03p04659

Hein, P. F., & Brown, R. A. (1988). Observations of longitudinal roll vortices during arctic cold air outbreaks over open water. *Boundary-Layer Meteorology*, *45*(1-2), 177–199. doi: 10.1007/BF00120822

Hergesell, H. (1928). The observation of clouds with special reference to the safety of aviation. *Quarterly Journal of the Royal Meteorological Society*, *54*(226), 128–132. doi: 10.1002/qj.49705422611

Holroyd, E. W. (1971). Lake-Effect Cloud Bands as Seen From Weather Satellites. *Journal of the Atmospheric Sciences*. doi: 10.1175/1520-0469(1971)028<1165:lecbas>2.0.co;2

Horstmann, J., & Koch, W. (2005). Measurement of Ocean Surface Winds Using Synthetic Aperture Radars. *IEEE Journal of Oceanic Engineering*, *30*(3), 508–515. doi: 10.1109/JOE.2005.857514

Huang, L., Li, X., Liu, B., Zhang, J. A., Shen, D., Zhang, Z., & Yu, W. (2018). Tropical Cyclone Boundary Layer Rolls in Synthetic Aperture Radar Imagery. *Journal of Geophysical Research: Oceans*, *123*(4), 2981–2996. doi: 10.1029/2018JC013755

Jackson, C. R., Apel, J. R., & Editors. (2004). *Synthetic Aperture Radar Marine User's Manual*. National Environmental Satellite, Data, and Information Serve.

Kaylor, R., & Faller, A. J. (1972). Instability of the Stratified Ekman Boundary Layer and the Generation of Internal Waves. *Journal of the Atmospheric Sciences*, *29*(3), 497–509. doi: 10.1175/1520-0469(1972)029<0497:IOTSEB>2.0.CO;2

Kelly, R. D. (1984). Horizontal Roll and Boundary-Layer Interrelationships Observed over Lake Michigan. *Journal of the Atmospheric Sciences*, *41*(11), 1816–1826. doi: 10.1175/1520-0469(1984)041<1816:HRABLI>2.0.CO;2

Koch, W. (2004). Directional analysis of SAR images aiming at wind direction. *IEEE Transactions on Geoscience and Remote Sensing*, *42*(4), 702–710. doi: 10.1109/TGRS.2003.818811

Kristovich, D. A. R. (1993). Mean circulations of boundary-layer rolls in lake-effect snow storms. *Boundary-Layer Meteorology*, *63*(3), 293–315. doi: 10.1007/BF00710463

Kristovich, D. A. R., Laird, N. F., Hjelmfelt, M. R., Derickson, R. G., & Cooper, K. A. (1999). Transitions in Boundary Layer Meso- $\gamma$ Convective Structures:An Observational Case Study. *Monthly Weather Review*, *127*(12), 2895–2909. doi: 10.1175/1520-0493(1999)127<2895:TIBLMC>2.0.CO;2

Kropfli, R. A., & Kohn, N. M. (1978). Persistent Horizontal Rolls in the Urban Mixed Layer as Revealed by Dual-Doppler Radar. *Journal of Applied Meteorology*, *17*(5), 669–676. doi: 10.1175/1520-0450(1978)017<0669:PHRITU>2.0.CO;2

Kudryavtsev, V. (2003a). A semiempirical model of the normalized radar cross-section of the sea surface 1. Background model. *Journal of Geophysical Research*, *108*(C3), 8054. doi: 10.1029/2001JC001003

Kudryavtsev, V. (2003b). A semiempirical model of the normalized radar cross section of the sea surface, 2. Radar modulation transfer function. *Journal of Geophysical Research*, *108*(C3), 8055. doi: 10.1029/2001JC001004

Kuettner, J. (1959). The Band Structure of the Atmosphere. *Tellus*, *11*(3), 267–294. doi: 10.3402/tellusa.v11i3.9319

Kuettner, J. (1971). Cloud bands in the earth's atmosphere: Observations and Theory. *Tellus*, *23*(4-5), 404–426. doi: 10.3402/tellusa.v23i4-5.10519

Lee-Lueng Fu, & Holt, B. (1982). *Seasat views oceans and sea ice with synthetic aperture radar* (Vol. 81; Tech. Rep.). Pasadena, California: California Institute of Technology, Jet Propulsion Laboratory.

Leibovich, S., & Lele, S. K. (1985). The influence of the horizontal component of Earth's angular velocity on the instability of the Ekman layer. *Journal of Fluid Mechanics*, *150*, 41–87. doi: 10.1017/S0022112085000039

LeMone, M. A. (1973). The Structure and Dynamics of Horizontal Roll Vortices in the Planetary Boundary Layer. *Journal of the Atmospheric Sciences*, *30*(6), 1077–1091. doi: 10.1175/1520-0469(1973)030<1077:TSADOH>2.0.CO;2

Lemone, M. A. (1976). Modulation of Turbulence Energy by Longitudinal Rolls in an Unstable Planetary Boundary Layer. *Journal of the Atmospheric Sciences*, *33*(7), 1308–1320. doi: 10.1175/1520-0469(1976)033<1308:MOTEBL>2.0.CO;2

LeMone, M. A., Angevine, W. M., Bretherton, C. S., Chen, F., Dudhia, J., Fedorovich, E., … Weil, J. (2018). 100 Years of Progress in Boundary Layer Meteorology. *Meteorological Monographs*, *59*, 9.1–9.85. doi: 10.1175/AMSMONOGRAPHS-D-18-0013.1

Levy, G. (2001). Boundary layer roll statistics from SAR. *Geophysical Research Letters*, *28*(10), 1993–1995. doi: 10.1029/2000GL012667

Li, X., Zheng, W., Yang, X., Zhang, J. A., Pichel, W. G., & Li, Z. (2013). Coexistence of Atmospheric Gravity Waves and Boundary Layer Rolls Observed by SAR*. *Journal of the Atmospheric Sciences*, *70*(11), 3448–3459. doi: 10.1175/JAS-D-12-0347.1

Lilly, D. K. (1966). On the Instability of Ekman Boundary Flow. *Journal of the Atmospheric Sciences*, *23*(5), 481–494. doi: 10.1175/1520-0469(1966)023<0481:otioeb>2.0.co;2

Liu, J., Liang, J.-H., McWilliams, J. C., Sullivan, P. P., Fan, Y., & Chen, Q. (2018). Effect of Planetary Rotation on Oceanic Surface Boundary Layer Turbulence. *Journal of Physical Oceanography*, *48*(9), 2057–2080. doi: 10.1175/JPO-D-17-0150.1

Mason, P. J., & Thomson, D. (1987). Large-eddy simulations of the neutral-static-stability planetary boundary layer. *Quarterly Journal of the Royal Meteorological Society*, *113*(476), 413–443.

Miura, Y. (1986). Aspect Ratios of Longitudinal Rolls and Convection Cells Observed during Cold Air Outbreaks. *Journal of the Atmospheric Sciences*, *43*(1), 26–39. doi: 10.1175/1520-0469(1986)043<0026:AROLRA>2.0.CO;2

Morrison, I., Businger, S., Marks, F., Dodge, P., & Businger, J. A. (2005). An Observational Case for the Prevalence of Roll Vortices in the Hurricane Boundary Layer*. *Journal of the Atmospheric Sciences*, *62*(8), 2662–2673. doi: 10.1175/JAS3508.1

Mouche, A., Chapron, B., Knaff, J., Zhao, Y., Zhang, B., & Combot, C. (2019). Copolarized and Cross-Polarized SAR Measurements for High-Resolution Description of Major Hurricane Wind Structures: Application to Irma Category 5 Hurricane. *Journal of Geophysical Research: Oceans*. doi: 10.1029/2019JC015056

Mouche, A. A., Chapron, B., & Reul, N. (2007). A simplified asymptotic theory for ocean surface electromagnetic wave scattering. *Waves in Random and Complex Media*, *17*(3), 321–341. doi: 10.1080/17455030701230261

Mouche, A. A., Chapron, B., Reul, N., Hauser, D., & Quilfen, Y. (2007). Importance of the sea surface curvature to interpret the normalized radar cross section. *Journal of Geophysical Research*, *112*(C10), C10002. doi: 10.1029/2006JC004010

Mouche, A. A., Hauser, D., & Kudryavtsev, V. (2006). Radar scattering of the ocean surface and sea-roughness properties: A combined analysis from dual-polarizations airborne radar observations and models in C band. *Journal of Geophysical Research*, *111*(C9), C09004. doi: 10.1029/2005JC003166

Mourad, P. D. (1996). Inferring multiscale structure in atmospheric turbulence using satellite-based synthetic aperture radar imagery. *Journal of Geophysical Research: Oceans*, *101*(C8), 18433–

18449. doi: 10.1029/96JC00920

Mourad, P. D., & Brown, R. A. (1990, feb). Multiscale Large Eddy States in Weakly Stratified Planetary Boundary Layers. *Journal of the Atmospheric Sciences*, *47*(4), 414–438. doi: 10.1175/1520-0469(1990)047<0414:MLESIW>2.0.CO;2

Mourad, P. D., & Walter, B. A. (1996). Viewing a cold air outbreak using satellite-based synthetic aperture radar and advanced very high resolution radiometer imagery. *Journal of Geophysical Research: Oceans*, *101*(C7), 16391–16400. doi: 10.1029/96JC01123

Müller, D., Etling, D., Kottmeier, C., & Roth, R. (1985). On the occurrence of cloud streets over Northern Germany. *Quarterly Journal of the Royal Meteorological Society*, *111*(469), 761–772. doi: 10.1002/qj.49711146906

Muller, G., Brummer, B., & Alpers, W. (1999). Roll Convection within an Arctic Cold-Air Outbreak: Interpretation of In Situ Aircraft Measurements and Spaceborne SAR Imagery by a Three-Dimensional Atmospheric Model. *Monthly Weather Review*, *127*(3), 363–380. doi: 10.1175/1520-0493(1999)127<0363:RCWAAC>2.0.CO;2

Muller, S., Stanev, E. V., Schulz-Stellenfleth, J., Staneva, J., & Koch, W. (2013). Atmospheric boundary layer rolls: Quantification of their effect on the hydrodynamics in the German Bight. *Journal of Geophysical Research: Oceans*, *118*(10), 5036–5053. doi: 10.1002/jgrc.20388

National Academies of Sciences, Engineering, and Medicine. (2018a). *The future of atmospheric boundary layer observing, understanding, and modeling* (L. Everett, Ed.). Washington, D.C.: National Academies Press. doi: 10.17226/25138

National Academies of Sciences, Engineering, and Medicine. (2018b). *Thriving on our changing planet: A decadal strategy for earth observation from space*. Washington, D.C.: National Academies Press. doi: 10.17226/25437

Pithan, F., Svensson, G., Caballero, R., Chechin, D., Cronin, T. W., Ekman, A. M. L., … Wendisch, M. (2018). Role of air-mass transformations in exchange between the Arctic and mid-latitudes. *Nature Geoscience*, *11*(11), 805–812. doi: 10.1038/s41561-018-0234-1

Rabin, R. M., Doviak, R. J., & Sundara-Rajan, A. (1982). Doppler Radar Observations of Momentum Flux in a Cloudless Convective Layer With Rolls. *Journal of the Atmospheric Sciences*, *39*(4), 851–863. doi: 10.1175/1520-0469(1982)039<0851:DROOMF>2.0.CO;2

Randall, D. A., Bitz, C. M., Danabasoglu, G., Denning, A. S., Gent, P. R., Gettelman, A., … Thuburn, J. (2018). 100 Years of Earth System Model Development. *Meteorological Monographs*, *59*, 12.1–12.66. doi: 10.1175/AMSMONOGRAPHS-D-18-0018.1

Rayleigh, L. (1916). On convection currents in a horizontal layer of fluid, when the higher temperature is on the under side. *The London, Edinburgh, and Dublin Philosophical Magazine and Journal of Science*, *32*(192), 529–546.

Reineman, B. D., Lenain, L., & Melville, W. K. (2016). The use of ship-launched fixed-wing UAVs for measuring the marine atmospheric boundary layer and ocean surface processes. *Journal of Atmospheric and Oceanic Technology*, *33*(9), 2029–2052. doi: 10.1175/JTECH-D-15-0019.1

Salesky, S. T., Chamecki, M., & Bou-Zeid, E. (2017). On the Nature of the Transition Between Roll and Cellular Organization in the Convective Boundary Layer. *Boundary-Layer Meteorology*, *163*(1), 41–68. doi: 10.1007/s10546-016-0220-3

Salvi, S., Stramondo, S., Funning, G. J., Ferretti, A., Sarti, F., & Mouratidis, A. (2012). The Sentinel-1 mission for the improvement of the scientific understanding and the operational monitoring of the seismic cycle. *Remote Sensing of Environment*. doi: 10.1016/j.rse.2011.09.029

Sherwood, S. C., Bony, S., & Dufresne, J.-L. (2014). Spread in model climate sensitivity traced to atmospheric convective mixing. *Nature*, *505*(7481), 37–42. doi: 10.1038/nature12829

Sikora, T., & Ufermann, S. (2004). Marine atmospheric boundary layer cellular convection and longitudinal roll vortices. In *Synthetic Aperture Radar Marine User's Manual* (p. 321-330). National Environmental Satellite, Data, and Information Serve.

Smedman, A. S. (1991). Occurrence of roll circulations in a shallow boundary layer. *Boundary-Layer Meteorology*, *57*(4), 343–358. doi: 10.1007/BF00120053

Streten, N. A. (1975). Cloud cell size and pattern evolution in Arctic air advection over the North Pacific. *Archiv für Meteorologie, Geophysik und Bioklimatologie Serie A*, *24*(3), 213–228. doi: 10.1007/BF02245365

Stull, R. B. (1988). *An Introduction to Boundary Layer Meteorology* (R. B. Stull, Ed.). Dordrecht: Springer Netherlands. doi: 10.1007/978-94-009-3027-8

Svensson, N., Sahlée, E., Bergström, H., Nilsson, E., Badger, M., & Rutgersson, A. (2017). A Case Study of Offshore Advection of Boundary Layer Rolls over a Stably Stratified Sea Surface. *Advances in Meteorology*, *2017*, 1–15. doi: 10.1155/2017/9015891

Thompson, T. W., Liu, W. T., & Weissman, D. E. (1983). Synthetic aperture radar observation of ocean roughness from rolls in an unstable marine boundary layer. *Geophysical Research Letters*, *10*(12), 1172–1175. doi: 10.1029/GL010i012p01172

Troen, I. B., & Mahrt, L. (1986). A simple model of the atmospheric boundary layer; sensitivity to surface evaporation. *Boundary-Layer Meteorology*, *37*(1-2), 129–148. doi: 10.1007/BF00122760

Vandemark, D., Mourad, P. D., Bailey, S. A., Crawford, T. L., Vogel, C. A., Sun, J., & Chapron, B. (2001). Measured changes in ocean surface roughness due to atmospheric boundary layer rolls. *Journal of Geophysical Research: Oceans*, *106*(C3), 4639–4654. doi: 10.1029/1999JC000051

Walker, G. (1934). Recent Gliding Performances and their Meteorological Conditions. *Nature*, *134*(3384), 347–349. doi: 10.1038/134347a0

Walter, B. A. (1980). Wintertime Observations of Roll Clouds over the Bering Sea. *Monthly Weather Review*, *108*(12), 2024–2031. doi: 10.1175/1520-0493(1980)108<2024:WOORCO>2.0.CO;2

Walter, B. A., & Overland, J. E. (1984). Observations of Longitudinal Rolls in a Near Neutral Atmosphere. *Monthly Weather Review*, *112*(1), 200–208. doi: 10.1175/1520-0493(1984)112<0200:OOLRIA>2.0.CO;2

Weckwerth, T. M., Wilson, J. W., Wakimoto, R. M., & Crook, N. A. (1997). Horizontal Convective Rolls: Determining the Environmental Conditions Supporting their Existence and Characteristics. *Monthly Weather Review*, *125*(4), 505–526. doi: 10.1175/1520-0493(1997)125<0505:HCRDTE>2.0.CO;2

Weston, K. J. (1980). An observational study of convective cloud streets. *Tellus*, *32*(5), 433–438. doi: 10.3402/tellusa.v32i5.10598

Wilczak, J. M., & Businger, J. A. (1983). Thermally Indirect Motions in the Convective Atmospheric Boundary Layer. *Journal of the Atmospheric Sciences*, *40*(2), 343–358. doi: 10.1175/1520-0469(1983)040<0343:TIMITC>2.0.CO;2

Woodcock, A. H. (1940a). Convection and soaring over the open sea. *J. Mar. Res*, *3*, 248–253.

Woodcock, A. H. (1940b). Observations on Herring Gull Soaring. *The Auk*, *57*(2), 219–224. doi: 10.2307/4078746

Woodcock, A. H. (1942). Soaring over the Open Sea. *The Scientific Monthly*, *55*, 226–232.

Woodcock, A. H., & Wyman, J. (1947). CONVECTIVE MOTION IN AIR OVER THE SEA. *Annals of the New York Academy of Sciences*, *48*(8), 749–776. doi: 10.1111/j.1749-6632.1947.tb38488.x

Wurman, J., & Winslow, J. (1998). Intense sub-kilometer-scale boundary layer rolls observed in hurricane Fran. *Science*, *280*(5363), 555–557. doi: 10.1126/science.280.5363.555

Xiaofeng Li, Pichel, W., Mingxia He, Wu, S., Friedman, K., Clemente-Colon, P., & Chaofang Zhao. (2002). Observation of hurricane-generated ocean swell refraction at the Gulf Stream north wall with the RADARSAT-1 synthetic aperture radar. *IEEE Transactions on Geoscience and Remote Sensing*, *40*(10), 2131–2142. doi: 10.1109/TGRS.2002.802474

Young, G. S. (2000). SAR signatures of the marine atmospheric boundary layer: Implications for numerical forecasting. *Johns Hopkins APL Technical Digest (Applied Physics Laboratory)*.

Young, G. S., Kristovich, D. A. R., Hjelmfelt, M. R., & Foster, R. C. (2002). Rolls, Streets, Waves, and More: A Review of Quasi-Two-Dimensional Structures in the Atmospheric Boundary Layer. *Bulletin of the American Meteorological Society*, *83*(7), 997–1001. doi: 10.1175/1520-0477(2002)083<0997:RSWAMA>2.3.CO;2

Zhang, B., Perrie, W., Zhang, J. A., Uhlhorn, E. W., & He, Y. (2014). High-Resolution Hurricane Vector Winds from C-Band Dual-Polarization SAR Observations. *Journal of Atmospheric and Oceanic Technology*, *31*(2), 272–286. doi: 10.1175/JTECH-D-13-00006.1

Zhang, J. A., Katsaros, K. B., Black, P. G., Lehner, S., French, J. R., & Drennan, W. M. (2008). Effects of Roll Vortices on Turbulent Fluxes in the Hurricane Boundary Layer. *Boundary-Layer Meteorology*, *128*(2), 173–189. doi: 10.1007/s10546-008-9281-2

Zhao, Y., Li, X.-M., & Sha, J. (2016). Sea surface wind streaks in spaceborne synthetic aperture radar imagery. *Journal of Geophysical Research: Oceans*, *121*(9), 6731–6741. doi: 10.1002/2016JC012040

# Analyse globale des rouleaux de la couche limite atmosphérique marine à l'aide de données SAR Sentinel-1

**Par Chen WANG**

**Thèse présentée et soutenue à Plouzane, le 30 Juillet, 2020**

**Unité de recherche : LabSTICC**

**Thèse N° : 2020IMTA0203**

**Mots clés:**
Radar à ouverture synthétique, Couche limite atmosphérique marine, Tourbillons de roulis, Classification, Apprentissage profond

**Résumé:**

La couche limite atmosphérique marine (MABL) est le kilomètre le plus bas de l'atmosphère terrestre qui est en contact direct avec le vaste océan et réagit aux forçages de surface, notamment la traînée de frottement, l'évaporation et la transpiration, le transfert de chaleur et les vagues océaniques. C'est une couche caractérisée par son état d'écoulement d'air, où la vitesse, la température, la densité et la pression fluctuent sur des échelles allant de moins d'un millimètre à plusieurs kilomètres. La nature turbulente du MABL a été reconnue avec une grande variabilité en raison des processus thermodynamiques et cinétiques à l'intérieur. Ces processus physiques contrôlent non seulement le transport de la chaleur, de l'énergie et de l'élan, la dispersion des polluants et du dioxyde de carbone, mais jouent un rôle important dans la formation et l'interaction avec les nuages de bas niveau dans les couches limites surmontées de nuages. Il y a de plus en plus de preuves qu'une compréhension avancée des processus clés du MABL est beaucoup plus fondamentale pour les études climatiques. Pourtant, les processus physiques liés à l'état moyen de la couche limite ne sont pas entièrement résolus dans les modèles numériques actuels du climat ou du temps.

Dans des conditions quasi-neutres à légèrement instables, les flux d'air dans le MABL sont souvent organisés en tourbillons linéaires en forme de rouleau. Ces tourbillons sont en fait des

tourbillons organisés quasi bidimensionnels dont l'axe horizontal est approximativement aligné avec l'écoulement moyen. Ils sont généralement formés et intégrés dans l'ensemble de l'ABL, et généralement interprétés par deux types de théories. L'un concerne l'instabilité thermique lorsque la couche est chauffée par le bas ou refroidie par le haut et l'autre l'instabilité dynamique lorsque la vitesse du vent change avec la hauteur. Les tourbillons de rouleaux couvrent généralement toute la profondeur de la couche limite et forment des bandes de circulations de retournement avec des régions linéaires alternées de perturbations ascendantes et descendantes améliorées entre les circulations de rouleaux contrarotatives. L'écoulement de perturbation vers le haut a tendance à être plus fort et plus étroit que celui vers le bas, conduisant à une convergence accrue et réduite du vent de surface près de la base des courants ascendants et descendants, respectivement. Cet effet net est une amélioration des flux à travers la couche limite qui ne dépend pas des gradients verticaux de l'écoulement moyen. On comprend donc à quel point il est important de mieux comprendre la couche limite en forme de rouleau, en particulier son rôle pour renforcer l'interaction air-mer via son impact sur les flux turbulents.

Les rouleaux MABL sont vraiment les mêmes avec les rouleaux générés sur terre. Les différences résident uniquement dans le processus de formation de la couche limite entre l'océan et la terre. Dans les détails, le MABL se développe via la stabilité et l'air descendant (processus top-down) alors que le terrain ABL se développe de manière opposée, mûri par déstabilisation et convection (processus bottom-up). Au-dessus de la terre, la surface du sol se réchauffe et se refroidit en réponse au rayonnement solaire de jour et de nuit, ce qui à son tour déstabilise et stabilise l'ABL ci-dessus. Le terrain que forme ABL dépend donc en grande partie du cycle diurne. En cas de changement de vitesse, le MABL reste relativement stable par rapport au cycle diurne, mais permettant une grande quantité d'échanges de chaleur et d'humidité. Compte tenu de la couverture étendue de l'océan (plus de 70%) à la surface de la Terre, il est essentiel de consacrer davantage d'efforts conjoints à l'étude des rouleaux MABL et des processus physiques associés.

En physique, les tourbillons de roulis sont la manifestation des instabilités de couche d'Ekman qui peuvent être décrites par les équations non linéaires de Navier-Stokes lorsqu'on considère les facteurs thermiques et dynamiques dans un système rotatif. La théorie antérieure de la dynamique du roulis s'est concentrée sur les schémas de linéarisation et a produit la solution représentative de l'instabilité du point d'inflexion (IP). Cette théorie prédit des caractéristiques de roulis cohérentes avec des observations en termes de rapport hauteur / largeur et d'orientation horizontale. Elle est donc largement adoptée et étendue en prenant en compte d'autres effets, tels que le vent thermique, la stratification, la baroclinicité et les processus non linéaires. Alors que dans la plupart des études basées sur la propriété intellectuelle, seule la composante verticale de la rotation de la Terre est prise en compte. L'horizontale, cependant, est souvent négligée, bien que son importance dans la dynamique des fluides géophysiques ait été clairement démontrée par plusieurs recherches théoriques. Cela est en partie dû au manque d'ensembles de données d'observation systématiques et à long terme, ce qui limite notre compréhension des caractéristiques des rouleaux à l'échelle mondiale.

Sur le dessus de la couche limite en forme de rouleau, de la condensation se forme généralement dans les parties de courant ascendant des circulations de rouleaux. Ceci est associé à l'augmentation de la masse d'air chaud qui se refroidit et se condense progressivement. Pendant ce temps, l'air frais qui descend dans les courants descendants s'évapore et crée des zones sans nuages. Ces masses d'air ascendantes et descendantes alternées produisent de longues rangées de cumulus orientés parallèlement à la direction du vent. Ces lignes alignées de nuages organisés sont donc normalement identifiées comme des «rues de nuages» par les yeux humains ou sur les images visibles du satellite. En particulier, les rues nuageuses sont surtout visibles au-dessus des océans en hiver lorsque l'air froid au-dessus de la terre se déplace vers l'océan plus chaud, la hausse des températures étant organisée par les vents dominants au large. À mesure que la distance du rivage augmente, les nuages en forme de rouleau se transforment souvent en convection en forme de cellule. Un exemple de transition roll-cell observée par l'image satellite optique est donné dans la figure ci-dessous. Des vents violents ont poli la neige du sud-ouest de l'Alaska et étiré les nuages stratocumulus marins en longues rues parallèles près de la côte, puis en cellules convectives à mesure que la différence de température air-mer augmente.

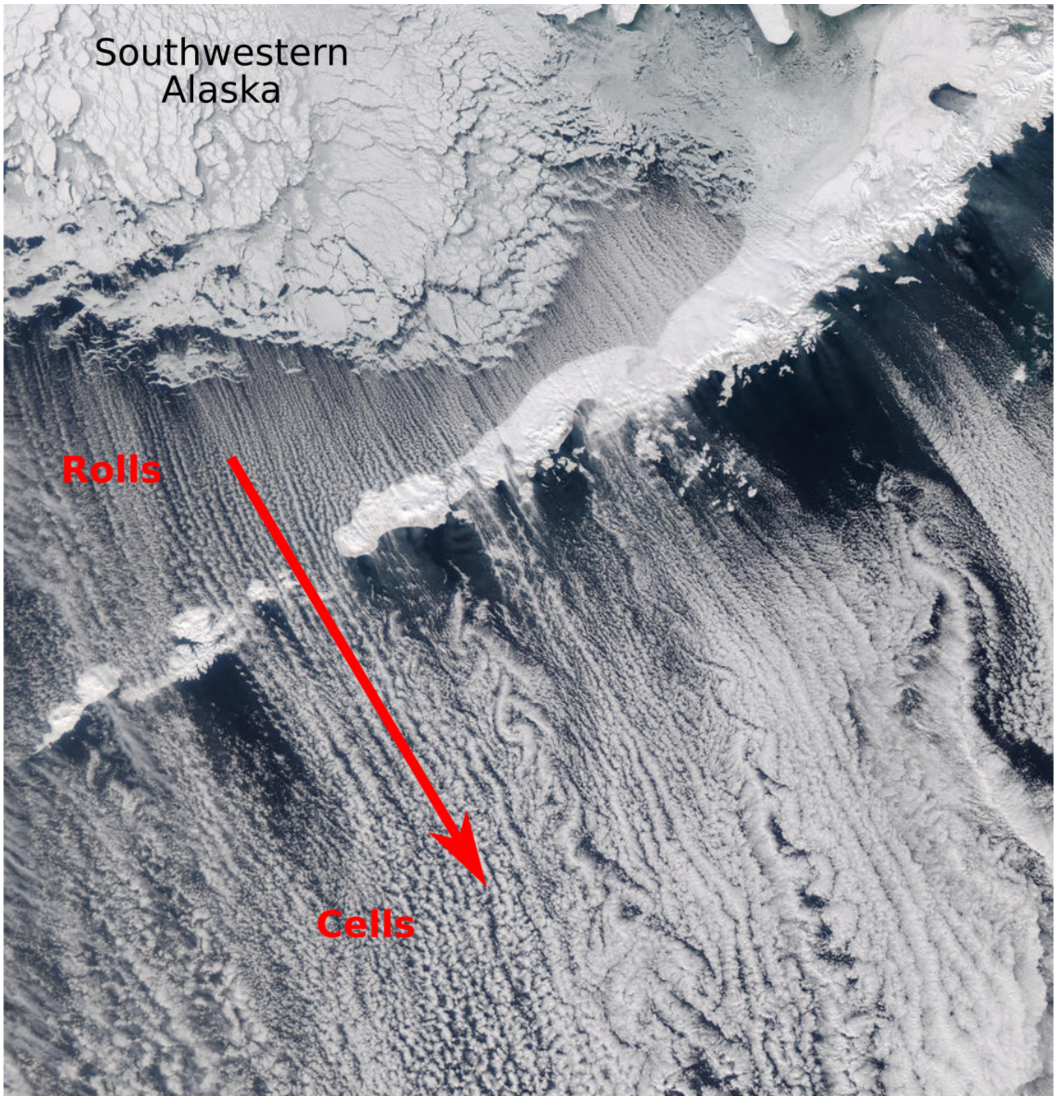

**Figure**. Spectroradiomètre imageur à résolution modérée (MODIS) photographie de rues et de cellules de nuages au large de la côte sud-ouest de l'Alaska le 11 janvier 2012. Le vent souffle de terre en océan, conduisant à la formation de nuages linéaires près de la côte et de nuages en forme de cellules au large. le littoral.

L'étude de ce processus typique de couche limite a été menée pendant des décennies, mais principalement dans les études de cas. Alors que les résultats ont démontré une vue d'ensemble prometteuse des conditions atmosphériques d'occurrence du roulis (dans une stratification quasi neutre à légèrement instable) et des caractéristiques du roulis (longueurs d'onde de 2 à 5 km et orientations de ± 25 ° par rapport à la direction moyenne de l'écoulement), ces les caractéristiques ne sont pas vérifiées sur les océans mondiaux. Pour une perspective de plus haut niveau, il existe également des besoins en climatologie globale et à long terme de la dynamique ABL en forme de rouleau ainsi que de la variabilité annuelle et saisonnière. Une telle climatologie fera sans aucun doute progresser la paramétrisation de la LBA dominée par le roulis, et améliorera donc la précision des projections numériques des modèles météorologiques et climatiques. La thèse vise à exploiter les données globales de radar à ouverture synthétique (SAR) en mode d'onde Sentinel-1 (S-1) (WV) pour les enquêtes de roulis ABL dans le Maine. Parmi les moyens pratiques bien connus, la SAR spatiale recèle le plus grand potentiel pour réaliser des observations systématiques des rouleaux ABL au-dessus de l’océan mondial. C'est parce que la rétrodiffusion SAR de la surface de l'océan est indépendante de la lumière du soleil et de la plupart des conditions météorologiques, et est fondamentalement sensible aux changements de rugosité de la surface de la mer induits par le roulis.

Cependant, l'expansion des applications de cet ensemble massif de données au-delà des vagues océaniques nécessite une stratégie pour identifier ces phénomènes géophysiques. Pour identifier automatiquement les événements de roulis à partir des images SAR S-1 WV, nous proposons d'appliquer l'approche émergente d'apprentissage en profondeur dans la classification des scènes SAR océaniques. La formation est effectuée à l'aide d'un ensemble de données triées sur le volet défini pour décrire dix processus atmosphériques ou océaniques courants. L'évaluation de notre modèle repose sur un ensemble de données d'évaluation indépendant et montre des résultats de classification satisfaisants et robustes. Pour illustrer davantage les performances du modèle, les modèles régionaux de pluie et de glace de mer sont analysés qualitativement et se révèlent très cohérents avec les ensembles de données de télédétection auxiliaires et indépendants. En outre, ces données WV SAR haute résolution peuvent résoudre à une échelle fine, inférieure au km, la structure spatiale des événements de pluie et la glace de mer qui complète d'autres mesures par satellite. Une telle classification automatisée de vignettes SAR ouvre la voie à une application géophysique plus large des acquisitions maritimes Sentinel-1.

L'empreinte des rouleaux de la couche limite atmosphérique marine organisée (MABL) à la surface de l'océan peut être détectée par un radar à synthèse d'ouverture (SAR). Cette capacité SAR de cartographie des signatures de rouleau est examinée pour la première fois à l'échelle mondiale à l'aide des observations en mode vague (WV) recueillies par les deux satellites Sentinel-1 (S-1) de l'ESA en 2016-2017. Le S-1 WV acquiert des images SAR de 20 km sur 20 à deux angles d'incidence de 23 ° (WV1) et 36,5 ° (WV2) en VV ou HH. Plus précisément, 1,37 million de ~ de scènes WV classées automatiquement sont examinées. Pour chaque scène, nous extrayons la modulation de rétrodiffusion induite par le roulis et les informations directionnelles pour une analyse conjointe avec les vents de surface ERA5 colocalisés. Les résultats montrent une sensibilité WV2 plus forte à la modulation du roulis et une coupure de vitesse du vent faible pour l'observation du roulis près de 2 ms-1 aux deux angles d'incidence. La modulation NRCS induite par le roulis diminue fortement lorsque le SAR regarde l'océan par vent de travers, ce qui réduit la détection SAR des événements de roulis. En moyenne et à toutes les vitesses de vent, les rouleaux MABL produisent des variations de vent de surface autour du débit moyen d'environ 8% (± 3,5%) et dépassent rarement 20%. La vitesse du vent et la dépendance relative de la direction du vent des réponses du NRCS WV1 et WV2 aux empreintes de roulis sont en outre évaluées avec une fonction de modèle géophysique de vent océanique SAR. L'interprétation globale de ces résultats implique à la fois la sensibilité SAR au changement de rugosité de la surface de la mer induit par le roulis et la limitation du modèle de classification dans l'identification des empreintes de roulis faibles. Il suggère que les réponses SAR aux perturbations des ondes de vent induites par le roulis sont largement associées au vortex de roulis à diverses échelles de temps et de longueur. Ces résultats ont des implications pour les applications SAR recherchant des estimations de la direction du vent à partir des empreintes de roulis et, plus largement, des études de couche limite au-dessus de l'océan.

Les statistiques globales des caractéristiques de roulis se sont donc concentrées sur les événements de roulis identifiés à partir des données SAR S-1WV2. La longueur d'onde et l'orientation du rouleau sont extraites de chaque scène WV par le biais des analyses spectrales

2D à des échelles ABL de 0,6 à 5 km. Pour quantifier les conditions atmosphériques d'occurrence de roulis, chaque image WV SAR est également co-localisée avec les variables de surface ERA5. Les principaux résultats sont: (1) jusqu'à 90% des événements de roulis se produisent dans des conditions quasi-neutres à légèrement instables, distinctes de la condition moyenne globale; (2) une minuscule saisonnalité observée dans les événements de roulis identifiés et leurs conditions atmosphériques; (3) la dynamique de roulis semble plus forte le matin que le soir en raison d'une convection plus importante; (4) les conditions atmosphériques d'occurrence de roulis sont plus instables aux basses latitudes qu'aux latitudes moyennes; (5) les rapports d'aspect de roulis (longueur d'onde de roulis divisée par la hauteur ABL) sont dans une distribution log-normale centrée à 2,87; (6) les orientations de roulis sont dans une distribution normale, principalement à ± 35 °; (7) la longueur d'onde et l'orientation du roulis dépendent faiblement et fortement des latitudes; (8) la dépendance de l'orientation du roulis aux directions du vent terrestre indique les effets de la force de Coriolis horizontale sur la dynamique du roulis ABL.

Malgré le fait que ces résultats mis en évidence complètent la compréhension des rouleaux ABL avec des implications significatives pour les études sur l'atmosphère et l'océan, il est fortement attendu d'étendre l'application des données SAR S-1 WV à d'autres processus ABL clés. L'un des principaux intérêts est de comprendre la transition naturelle entre les rouleaux ABL, les cellules de pluie et les cellules de convection. De plus, il existe une forte possibilité de projeter ces images de rugosité de surface de l'océan dans la stabilité de l'interface air-mer, puis dans les flux de surface, indépendamment de la température de surface de la mer individuelle et des mesures de température de l'air près de la surface. Cela faciliterait l'évaluation et l'amélioration des schémas de paramétrage ABL (Eddy-diffusion mass-flux ou similaire) dans différents types d'ABL. Si ces données WV SAR peuvent être bien traitées pour définir les propriétés inférieures d'ABL. Une vue complète de l'état moyen ABL serait obtenue en incluant les mesures des nuages bas pour définir les propriétés supérieures d'ABL. Il s'agit de l'effort conjoint requis pour améliorer la connaissance au niveau des processus du système météorologique et climatique de la Terre.

UNIVERSITE SCIENCES
BRETAGNE DE LA MER
LOIRE ET DU LITTORAL

IMT Atlantique
Bretagne-Pays de la Loire
École Mines-Télécom

Université de Bretagne Occidentale

## Titre : Analyse globale des rouleaux de la couche limite atmosphérique marine à l'aide de données SAR Sentinel-1

**Mots clés :** Radar à ouverture synthétique, Couche limite atmosphérique marine, Tourbillons de roulis, Classification, Apprentissage profond

**Résumé :** Cette thèse exploite les données globales du radar à ouverture synthétique (SAR) Sentinel-1 (S-1) pour l'étude des rouleaux de la couche limite atmosphérique marine (MABL). Un modèle basé sur l'apprentissage en profondeur a été développé pour identifier automatiquement les rouleaux à partir des images massives S-1 WV. L'évaluation prouve que des rouleaux plus nombreux et plus clairs sont visibles à un angle d'incidence plus grand avec une limitation à des vitesses de vent très basses et lorsque la direction du vent est perpendiculaire à l'antenne SAR. Au-delà de cela, les énormes données conduisent à un nouveau résultat qui, en moyenne et à toutes les vitesses de vent, les rouleaux MABL induisent des variations de vent de surface de ~ 8% (± 3,5%) le débit moyen, dépassant rarement 20%.

Les statistiques mondiales ont confirmé dans des études antérieures que jusqu'à 90% des rouleaux identifiés se produisent dans des conditions quasi neutres à légèrement instables. La longueur d'onde et l'orientation du roulis sont extraites avec des résultats d'organisation multi-échelles et de contraste directionnel entre les latitudes basses et moyennes. La distribution systématique de l'orientation des rouleaux par rapport au vent de surface des tropiques aux extra-tropiques rappelle l'importance de la force de Coriolis horizontale sur les rouleaux. Malgré l'importance de ces faits saillants pour les études sur l'atmosphère et l'océan, il est très probable que les données SAR S-1 WV presque globales soient étendues aux rouleaux, aux cellules convectives et à d'autres processus air-mer clés. Les résultats devraient être comparés, expliqués et complétés dans un proche avenir par des études théoriques et numériques approfondies.

## Title : Global Investigation of Marine Atmospheric Boundary Layer Rolls Using Sentinel-1 SAR data

**Keywords :** Synthetic aperture radar (SAR), Marine atmospheric boundary layer (MABL), Roll vortices, Classification, Deep learning

**Abstract :** This thesis exploits the global Sentinel-1 (S-1) wave mode (WV) synthetic aperture radar (SAR) data for marine atmospheric boundary layer (MABL) roll studies. A deep-learning-based model was developed to automatically identify rolls from the massive S-1 WV images. Valuation evidences that more and clearer rolls are visible at the larger incidence angle with limitation in very low wind speeds and when wind direction being perpendicular to the SAR antenna looking. Beyond this, the huge data leads to a new result that, on average and across all wind speeds, MABL rolls induce surface wind variations of ~8% (±3.5%) the mean flow, seldom exceeding 20%.

Global statistics confirmed with previous studies that up to 90% of the identified rolls occur in near-neutral to slightly unstable conditions. Roll wavelength and orientation are extracted with findings of multi-scale organization and directional contrast between low- and mid-latitudes. The systematical distribution of roll orientation with respect to the surface wind from tropics to extra-tropics recalls the importance of horizontal Coriolis force on rolls. Despite the significance of these highlights for both atmosphere and ocean studies, it is highly expected to extend the nearly global S-1 WV SAR data for rolls, convective cells and other key air-sea processes. Results should be compared, explained, and complemented in the near future with in-depth theoretical and numerical studies.